UNIVERSITY OF CALIFORNIA, SAN DIEGO

Development of new analytical techniques for measuring radiosulfur in terrestrial samples to understand the present-day and Archean atmospheric sulfur cycles

A dissertation submitted in partial satisfaction of the
requirement for the degree of doctor of philosophy

in

Chemistry

by

Mang Lin

Committee in charge:

Professor Mark H. Thiemens, Chair
Professor John Crowell
Professor Jeff Severinghaus
Professor Amitabha Sinha
Professor William Trogler

2018

The dissertation of Mang Lin is approved, and it is acceptable in quality and form for publication on microfilm and electronically:

_____

_____

_____

_____

_____

Chair

University of California, San Diego

2018

DEDICATION

To my parents Huaxuan Lin and Siu Kin Lam for their unconditional love.

To the late Karl Turekian for his pioneer works on atmospheric radiosulfur measurements.

EPIGRAPH

"Out of Tao, One is born; Out of One, Two; Out of Two, Three; Out of Three, the created Universe. The created Universe carries the Yin at its back and the Yang in front; Through the union of the pervading principles it reaches harmony."

Laozi, *Tao Te Ching*, the 6th century BCE. Translated by Lin, Yutang.

"It has been said that astronomy is a humbling and character-building experience. There is perhaps no better demonstration of the folly of human conceits than this distant image of our tiny world."

Carl Sagan, *Pale Blue Dot*, 1994

"Find an important subject that is not yet interesting to others; otherwise the big guys, with their big labs, will get there before you. Don't go with the mainstream."

Avram Hershko, 2004 Nobel laureate in chemistry, in the 2017 Lindau Nobel Laureate Meetings

TABLE OF CONTENTS

LIST OF FIGURES

LIST OF TABLES

ACKNOWLEDGEMENTS

I owe my sincerest gratitude to my Ph.D. advisor, scientific role model, colleague, and friend Prof. Mark Thiemens. We first met in my hometown Guangzhou nine years ago, when I just got my Bachelor degree and worked as a fulltime research assistant in Sun Yat-sen University. I was impressed by Mark's broad interests and accomplishments in physical/analytical chemistry and Earth/atmospheric/planetary sciences, especially the discovery of mass-independent isotopic fractionation and its applications to the understanding of the origin of life and of the solar system. Since then I had been dreaming to join Mark's lab as a Ph.D. student and this came true in 2013. Mark is a terrific mentor in many ways. At the start of my time at UCSD, I asked him what project I should do. He told me that there were many options but I should think about what I was interested in and then propose my own project myself. The freedom and autonomy he gave is crucial for me to quickly grow as a self-motivated and independent scientist at the very beginning of my PhD training. Mark never pushed me, but he was always available when I needed advice. He was in the lab almost every day so that I could discuss with him at any time. Instead of handing me the fish directly, he always led me to think and learn how to fish. In almost every conversion, he asked me a host of questions that I could hardly answer. This teaching style makes me always critically think about problems and solve them myself. Mark really cares about his students. As far as I know, Mark is the only Ph.D. advisor who always replies students' emails and revises their manuscripts in one day. When Mark revised my first paper in my Ph.D. project, he was sitting on a pineapple cake box at a bus stop in Taiwan! I love field works, and so does Mark. As a part of my Ph.D. research, we went together to the Mount Everest. During the trip, I noticed that Mark could propose many new ideas based on what he saw in fields. His vast knowledge, vision, and creativity is probably rooted in the fact that he reads more than 100 papers every week. I learned from him and started to read papers in a wide variety of research fields. This habit has been driving me to think how to apply my chemistry knowledge and technique into other new and important research areas. I must also thank Teresa ("Terri") Jackson, the lab manager of Mark's lab. Terri is an extremely careful (in her words: "sometime paranoid") analytical chemist, and a diligent

and responsible individual. In my first year, I virtually had no experience in stable isotope analysis. Terri trained me hand by hand and shared all her more-than-40-year experience to me. I would say she was my informal mentor in analytical chemistry because my troubleshooting skills were largely learned from her. Mark and Terri's great help in training me as an independent scientist has been invaluable.

It has been always my honor to be a part of Mark's lab, the birth place of mass-independent isotopic fractionation research. I would want to thank all my other lab-mates: Robina Shaheen, Subrata Chakraborty, Antra Priyadarshi, Gerardo Dominguez, Jason Hill-Falkenthal, Morgan Nunn, Daniel Crocker, and many other undergraduate and visiting students. Their works cover a wide variety of research topics such as sea-spray aerosols, South Pole ice records, nuclear reactions, lunar water, meteorites, planetary atmospheres, solar winds, and the origin of the solar system. I really enjoyed discussing these topics with them and Mark's lab is a truly extraordinary environment to work in. I would also like to thank my collaborators Yanan Shen, Shichang Kang, Xiaolin Zhang, Zhisheng Zhang, Lin Su, Kun Wang and many others. I had many wonderful discussions with them during collaboration and our conversions include, but are not limit to, the origin of life, Cambrian explosion, "Big Five" extinction events, and glacier retreat. Without their inputs and inspiring thoughts, this Ph.D. project cannot be done.

When I was a visiting scholar in Yale in 2009, Mark asked me to visit his scientific grandfather, the late Karl Turekian. I was privileged to meet and discuss with him at his famous Yale coffee hour. I would probably not go into this research field without Karl's pioneering work of atmospheric radiosulfur measurements. His famous saying, "It's one more data point than anyone else has!", has been inspiring me to explore the unknown and carefully consider what each new measurement may mean. Special thanks go to my high school chemistry and mathematics teachers, Huabin Liu and Min Liu, respectively, and my previous research advisor Chuen-Yu "John" Chan. When I was a high school student, I was not interested in studying at all, but Huabin and Min seemed to know that I could learn well and they helped me feel that being a smart and knowledgeable guy could be very cool. In the senior year of my undergraduate study, I was very confused about which career path to pursue, and John was the one showing me how fascinating

and exciting the world of scientific research can be. John is not an isotope geochemist, but he introduced me to isotope geochemistry (and Mark) because he felt that this research field was interesting and that I would love it. As it turned out he was right.

Last but certainly not the least, I would like to thank my parents, Huaxuan Lin and Siu Kin Lam, who always support me to do academic research even though they don't exactly understand what I am doing. Financial support from the Guangzhou Elite Project, the Chinese Government Award for Outstanding Self-Financed Students Abroad, and the Distinguished Graduate Student Fellowship from the Department of Chemistry and Biochemistry is greatly acknowledged.

Chapter 2, in full, is a reprint of the material "Accurate quantification of radiosulfur in chemically complex atmospheric samples" as it appears in Analytical Chemistry 2018. Lin, Mang; Thiemens, Mark H., American Chemical Society, 2018. The dissertation author was the primary investigator and author of this paper.

Chapter 3, in full, is a reprint of the material "Simple method for high-sensitivity determination of cosmogenic ^{35}S in snow and water samples collected from remote regions" as it appears in Analytical Chemistry 2017. Lin, Mang; Wang, Kun; Kang, Shichang; Thiemens, Mark H., American Chemical Society, 2017. The dissertation author was the primary investigator and author of this paper.

Chapter 4, in full, is a reprint of the material "Detection of deep stratospheric intrusions by cosmogenic ^{35}S" as it appears in Proceedings of the National Academy of Sciences of the United States of America 2016. Lin, Mang; Su, Lin; Shaheen, Robina; Fung; Jimmy C.H.; Thiemens, Mark H., National Academy of Sciences of the United States of America 2016. The dissertation author was the primary investigator and author of this paper.

Chapter 5, in full, is a reprint of the material "Quantification of gas-to-particle conversion rates of sulfur in the terrestrial atmosphere using high-sensitivity measurements of cosmogenic ^{35}S" as it appears in

ACS Earth and Space Chemistry 2017. Lin, Mang; Biglari, Saman; Thiemens, Mark H., American Chemical Society, 2017. The dissertation author was the primary investigator and author of this paper.

Chapter 6, in full, is a reprint of the material "Unexpected high ^{35}S concentration revealing strong downward transport of stratospheric air during the monsoon transitional period in East Asia" as it appears in Geophysical Research Letters 2016. Lin, Mang; Zhang, Zhisheng; Su, Lin; Su, Binbin; Liu, Lanzhong; Tao, Jun; Fung; Jimmy C.H.; Thiemens, Mark H., American Geophysical Union, 2016. The dissertation author was the primary investigator and author of this paper.

Chapter 7, in full, is a reprint of the material "Vertically uniform formation pathways of tropospheric sulfate aerosols in East China detected from triple stable oxygen and radiogenic sulfur isotopes" as it appears in Geophysical Research Letters 2017. Lin, Mang; Biglari, Saman; Zhang, Zhisheng; Crocker, Daniel; Jun, Tao; Su, Binbin; Liu, Lanzhong; Thiemens, Mark H., American Geophysical Union, 2017. The dissertation author was the primary investigator and author of this paper.

Chapter 8, in full, is a reprint of the material "Resolving the impact of stratosphere-to-troposphere transport on the sulfur cycle and tropospheric ozone level over the Tibetan Plateau using a cosmogenic ^{35}S tracer" as it appears in Journal of Geophysical Research: Atmosphere, 2016. Lin, Mang; Zhang, Zhisheng; Su, Lin; Hill-Falkenthal, Jason; Priyadarshi, Antra; Zhang, Qianggong; Zhang, Guoshuai; Kang, Shichang; Chan, Chuen-Yu; Thiemens, Mark H., American Geophysical Union, 2016. The dissertation author was the primary investigator and author of this paper.

Chapter 9, in full, has been submitted for publication of the material "Five-S-isotope evidence of two distinct mass-independent sulfur isotope effects and its consequence for the Archean record" as it may appear. Lin, Mang; Zhang, Xiaolin; Li, Menghan; Xu, Yilun; Zhang, Zhisheng; Tao, Jun; Su, Binbin; Liu, Lanzhong; Shen, Yanan; Thiemens, Mark H. The dissertation author was the primary investigator and author of this paper.

Chapter 10, in full, has been submitted for publication of the material "Atmospheric sulfur isotopic anomalies recorded at Mt. Everest across the Anthropocene" as it may appear. Lin, Mang; Kang, Shichang; Shaheen, Robina; Li, Chaoliu; Hsu, Shih-Chieh; Thiemens, Mark H. The dissertation author was the primary investigator and author of this paper.

VITA

2008	B.Sc., Environmental Science, Sun Yat-sen University
2008-2011	Research Assistant (fulltime), School of Environmental Science and Engineering, Sun Yat-sen University
2009	Summer School Student (IsoCamp: Stable Isotope Biogeochemistry and Ecology), Stable Isotope Ratio Facility for Environmental Research, University of Utah
2009	Visiting Scholar, Yale School of Forestry and Environmental Studies, Yale University
2011	Visiting Scholar, Department of Chemistry and Biochemistry, University of California San Diego
2011-2013	Graduate Research Assistant, School of Environmental Science and Engineering, Sun Yat-sen University
2012	Visiting Scholar, Research Center for Environmental Changes and Institute of Earth Sciences, Academia Sinica
2013	M.Sc., Environmental Science (Atmospheric Chemistry), Sun Yat-sen University
2013-2018	Graduate Research Fellow, Department of Chemistry and Biochemistry, University of California San Diego
2014-2015	Teaching Assistant, Department of Chemistry and Biochemistry, University of California San Diego
2018	Ph.D., Chemistry, University of California San Diego

PUBLICATIONS

Lin, M., S. Kang, R. Shaheen, C. Li, S.-C. Hsu, and M.H. Thiemens (2018). Atmospheric sulfur isotopic anomalies recorded at Mt. Everest across the Anthropocene. Under review.

Lin, M., X. Zhang, M. Li, Y.Xu, Z. Zhang, J. Tao, B. Su, L. Liu, Y. Shen, M.H. Thiemens (2018). Five-S-isotope evidence of two distinct mass-independent sulfur isotope effects and its consequence for the Archean record. Under review.

Lin, M., M.H. Thiemens (2018). Rapid sample pretreatment and accurate quantification of radiosulfur in chemically complex atmospheric samples. Analytical Chemistry. doi: 10.1021/acs.analchem.7b05079.

Lin, M., S. Biglari and M.H. Thiemens (2017). Quantification of gas-to-particle conversion rates of sulfur in the terrestrial atmosphere using high-sensitivity measurements of cosmogenic ^{35}S. ACS Earth and Space Chemistry. doi: 10.1021/acsearthspacechem.7b00047.

Lin, M., S. Biglari, Z. Zhang, D. Crocker, J. Tao, B. Su, L. Liu, M.H. Thiemens (2017). Vertically uniform formation pathways of tropospheric sulfate aerosols in East China detected from triple stable oxygen and radiogenic sulfur isotopes. Geophysical Research Letters. doi:10.1002/2017GL073637.

Lin, M., K. Wang, S. Kang, M.H. Thiemens (2017). Simple method for high-sensitivity determination of cosmogenic ^{35}S in snow and water samples collected from remote regions. Analytical Chemistry. doi: 10.1021/acs.analchem.6b05066.

Lin, M., L. Su, R. Shaheen, J.C.H. Fung, M.H. Thiemens (2016). Detection of deep stratospheric intrusions by cosmogenic ^{35}S. Proceedings of the National Academy of Sciences of the United States of America. doi: 10.1073/pnas.1609919113.

Lin, M., Z. Zhang, L. Su, B. Su, L. Liu, J. Tao, J.C.H. Fung, M.H. Thiemens (2016). Unexpected high ^{35}S concentration revealing strong downward transport of stratospheric air during the monsoon transitional period in East Asia. Geophysical Research Letters. doi: 10.1002/2016GL068194.

Lin, M., Z. Zhang, L. Su, J. Hill-Falkenthal, A. Priyadarshi, Q. Zhang, G. Zhang, S. Kang, C.Y. Chan, M.H. Thiemens (2016). Resolving the impact of stratosphere-to-troposphere transport on the sulfur cycle and tropospheric ozone level over the Tibetan Plateau using a cosmogenic ^{35}S tracer. Journal of Geophysical Research - Atmosphere. doi: 10.1002/2015JD023801

Priyadarshi, A., J. Hill-Falkenthal, M. Thiemens, Z. Zhang, **M. Lin**, C. Chan, S. Kang (2014). Cosmogenic ^{35}S measurements in the Tibetan Plateau to quantify glacier snowmelt. Journal of Geophysical Research - Atmosphere. doi:10.1002/2013JD019801.

FIELDS OF STUDY

Major Field: Analytical and Atmospheric Chemistry

Studies in Isotope Geochemistry

Professor Mark Thiemens

Studies in Earth, Atmospheric, and Planetary Sciences

Professor Mark Thiemens

ABSTRACT OF THE DISSERTATION

Development of new analytical techniques for measuring radiosulfur in terrestrial samples to understand the present-day and Archean atmospheric sulfur cycles

by

Mang Lin

Doctor of Philosophy in Chemistry

University of California, San Diego, 2018

Professor Mark H. Thiemens, Chair

Sulfur, the 10th most abundance element in the universe, has variable valence states (from -2 to +6) and therefore actively participates in a host of biogeochemical processes in nature. Since the earliest geological record of the primitive Earth, sulfur has been ubiquitous and has played an important role in the evolution of life and the ability to track its origin. In the present-day Earth, interest in the terrestrial sulfur

cycle predominantly stems from anthropogenic influences on the atmospheric sulfur budget and the key role of sulfate in affecting climate. To understand a wide range of physical, chemical, and biological processes involved in the aforementioned topics, measurements of quadruple stable sulfur isotopes (^{32}S, ^{33}S, ^{34}S, and ^{36}S) in terrestrial samples (e.g., rocks, ice cores, aerosols) have been utilized. However, cosmogenic ^{35}S, the only radioactive sulfur isotope with an ideal half-life (~87 days) for tracking atmospheric, hydrological, and biogeochemical processes, is seldom measured because of its low-energy decay, low abundance in nature, and associated analytical difficulties. In this dissertation, new analytical techniques were developed for accurate quantification of ^{35}S in atmospheric, cryospheric, and hydrospheric samples using an ultra-low-level liquid scintillation spectrometer (chapters 2 and 3). Based on these newly developed analytical methods, I measured ^{35}S in varying natural samples collected around the Northern Hemisphere to explore the use of ^{35}S in the Earth, atmospheric, and planetary sciences. I demonstated that ^{35}S is a highly sensitive tracer for quantifying the downward transport of high-altitude air masses and gas-to-particle conversion rates of sulfur in the terrestrial atmosphere, and provided new insights into atmospheric vertical mixing (from the boundary layer to stratosphere) and sulfur chemistry over the Pacific Rim, Himalayas and Tibetan Plateau (chapters 4-8). Using simultaneous measurements of all five sulfur isotopes (^{32}S, ^{33}S, ^{34}S, ^{35}S, and ^{36}S) in the same sulfate aerosol samples, I discovered two distinct mass-independent sulfur isotope effects in the present-day atmosphere, which points to previously unrecognized areas for understanding the fundamental chemical physics of sulfur isotopic mass-independent fractionation and the earliest sulfur cycle on Earth during the appearance and evolution of early life (chapters 9 and 10).

Chapter 1 Introduction

This Chapter is intended to provide a brief overview of the history of radioactive and stable isotopes and their applications in the Earth, atmospheric, and planetary sciences. Because the major focus of this study is the use of radiosulfur measurements in understanding the atmospheric sulfur cycle on Earth, the terrestrial sulfur cycles in both Archean (~4.0 to ~2.5 billion years ago) and present times and their significance in the Earth system will be briefly introduced. The motivation of this study and a brief outline of this dissertation will be presented at the end of this chapter. More detailed and relevant introduction can be found at the beginning of each chapter.

1.1 Isotopes and Applications in Earth, Atmospheric, and Planetary Sciences

1.1.1 Radioactive Isotopes

The chemical properties of elements are determined by the number of electrons. If two or more nuclides contain different numbers of neutron (i.e., different masses) but equal number of protons, their chemical properties would be nearly identical (i.e., the same elements) and these nuclides are referred as isotopes. The stability of a nuclei is determined by the binding energy, which is the net energy between the strong force and the repulsion force among protons and neutrons. Therefore, isotopes can be either stable or unstable, depending on the numbers of protons and neutrons. The existence of isotopes was discovered by Frederick Soddy, after the discovery of spontaneous radioactivity at 1896 by Antoine Henri Becquerel and Pierre Curie and Marie Curie's subsequent works on understanding radioactivity. Radioactive isotopes are unstable isotopes that decay spontaneously to other nuclides at fixed rates. Energy is released in three major forms: alpha or beta particles, or gamma radiation. The decay rate is conventionally measured in half-life ($t_{1/2}$), which is defined as the length of time required for one half of the radioactive nuclides to disintegrate.

In Earth, atmospheric, and planetary sciences, radioactive isotopes can serve as a clock to track varying natural processes. For example, the ages of our galaxy, the solar system, and Earth could be dated by long-lived chronometers such as ^{187}Re-^{187}Os ($t_{1/2}$ = ~41.2 billion years) [*Luck et al.*, 1980], ^{235}U-^{207}Pb ($t_{1/2}$ = ~0.7 billion years) and ^{238}U-^{206}Pb ($t_{1/2}$ = ~4.47 billion years) [*Bouvier and Wadhwa*, 2010] or relatively short-lived (now extinct) chronometers such as ^{26}Al-^{26}Mg ($t_{1/2}$ = ~0.7 million years) [*Lee et al.*, 1977] and ^{182}Hf-^{182}W ($t_{1/2}$ = ~8.9 million years) [*Lee and Halliday*, 1996]. Radiocarbon (^{14}C, $t_{1/2}$ = ~5730 years) is probably the most well-known radioactive isotope because of its broad applications to dating archaeological, geological, hydrological samples [*Longin*, 1971]. Because abundance of radioactive isotopes in different reservoirs vary, radioactive isotopes can be also utilized to source apportionment. For instance, radiocarbon is a unique tracer to identify carbon-bearing compounds emitted from biomass burning (radiocarbon "alive") or from fossil fuel combustion (radiocarbon "dead") [*Gustafsson et al.*, 2009; *Li et al.*, 2016; *Winiger et al.*, 2016]. This is a different approach as it uses the proportion of the radionuclide rather than the activity as a chronometer.

In the dissertation, the focus is on radioactive sulfur isotopes. Cosmogenic ^{35}S is the only radioactive sulfur isotope with an ideal half-life (~87 days) for tracking atmospheric, hydrological, and biogeochemical processes. It is naturally produced by cosmic-ray spallation of ^{40}Ar in the atmosphere and subject to beta decay into ^{35}Cl. Because the physical and chemical properties of radiosulfur are nearly identical to stable sulfur, once ^{35}S produces, it converts to $^{35}SO_2$ in ~1 second and incorporates into the atmospheric sulfur cycle immediately, and may subsequently participate in the sulfur cycles in the hydrosphere, cryosphere, pedosphere, and biosphere after wet/dry deposition. Although ^{35}S may provide unique information for constraining a wide range of biogeochemical processes, it was rarely measured in terrestrial samples because of its low-energy decay (E_{max} = 167 keV), low abundance in nature, and associated analytical difficulties. As pioneers of atmospheric ^{35}S studies, *Tanaka and Turekian* [1991] first measured ^{35}S in gaseous SO_2, aerosol

SO_4^{2-} and precipitation using an internal gas proportional counting technique (sulfur carrier: gaseous SO_2). In later studies, they used solid barium sulfate ($BaSO_4$) as a sulfur carrier to measure ^{35}S using a low-level liquid scintillation counting (LSC) technique [*Tanaka and Turekian*, 1995]. A Geiger-Mullur counter, which was designed for ^{33}P measurements, was also used by *Lee and Thiemens* [2001] to measure ^{35}S in aerosols. These pilot studies, albeit limited, provided a new way to quantify the removal/oxidation rates and source altitudes of atmospheric sulfur [*Lee and Thiemens*, 2001; *Tanaka and Turekian*, 1991; 1995; *Turekian and Tanaka*, 1992]. In 2010, an optimized ultralow-level liquid scintillation counting technique was developed for high-sensitivity measurements of cosmogenic ^{35}S in atmospheric samples [*Brothers et al.*, 2010]. The major development of this method is the use of aqueous sulfate solution as sulfur carrier, which significantly reduced the background activity and increased the counting efficiency, and facilitated high-sensitivity ^{35}S determination of atmospheric samples. This method boosted a growing number of atmospheric ^{35}S measurements in the ensuing years [*Priyadarshi et al.*, 2011a; *Priyadarshi et al.*, 2011b; *Priyadarshi et al.*, 2012a; *Priyadarshi et al.*, 2014; *Priyadarshi et al.*, 2013], but new problems were identified: the cocktail made by the aqueous solution is not stable and easily affected by color quenching, which hampers an accurate determination of ^{35}S. The LSC technique using $BaSO_4$ as a sulfur carrier [*Hong and Kim*, 2005; *Uriostegui et al.*, 2015] has been utilized in hydrologic studies (e.g., quantifying the sources and ages of meltwater runoff [*Cecil et al.*, 1998; *Cooper et al.*, 1991; *Michel et al.*, 2000], groundwater [*Clark et al.*, 2016; *Plummer et al.*, 2001; *Uriostegui et al.*, 2016; *Urióstegui et al.*, 2016], and surface water in watersheds [*Kester et al.*, 2003]). However, this method requires a large amount of water samples (~20 L), restricting comprehensive field-based measurements.

1.1.2 Stable Isotopes, Mass-Dependent and Mass-Independent Fractionation

The application of stable isotopes in the earth, atmospheric, and planetary sciences is predominantly based on the slightly different physical and chemical properties of the isotopically

substitute molecular species. A benchmark work is the discovery of deuterium by *Urey et al.* [1932a; 1932b] based on the different vapor pressures of deuterated and non-deuterated water. A thermodynamic model for the thermal properties of hydrogen and deuterium was subsequently developed [*Scott et al.*, 1934]. With three milestone studies, the year of 1947 is regarded as the "birth-year" of stable isotope geochemistry: *Urey* [1947], *Bigeleisen and Mayer* [1947] provided detailed thermodynamic calculations of the temperature-dependent equilibrium for isotope exchange reactions directly from the small difference in free energy of the isotopically substituted molecules, and *Nier* [1947] developed an isotope ratio mass spectrometry for measuring the small variations of stable isotopes in physical and chemical processes. These significant advancements led to the development of numerous applications. In particular, the temperature dependency of isotope exchange reactions and precise measurements of geological samples enabled stable isotopes served as a paleothermometry [*Mccrea*, 1950].

In equilibrium fractionation, the equilibrium constant K for isotopic exchanges can be described by the partition function of statistical mechanics (q):

$$K = \prod q_n^{\xi}$$

where ξ presents the stoichiometric coefficients for reactants/productions *n*. As electronic and nuclear spin energies are negligible in isotopic fractionations, the partition function can be written as the product of the translational, rotational, and vibrational partition functions ($q_{total}=q_{trans}q_{rot}q_{vib}$). The quantum translational energy of a particle in a cubical box can be determined by a classical mechanical approach. Because translational energy levels are very closely spaced, the total translational partition function in a cubic box can be described by integration (assuming all energy levels are continuous):

$$q_{trans} = \frac{(2\pi mkT)^{3/2}}{h}\mathrm{V}$$

where m is mass of the particle, k is Boltzmann's constant, T is thermodynamic temperature, h is Planck's constant, V is box volume. The quantum rotational energy is determined by the rotational quantum number and the moment of inertia (I). Because the spacing between rotational energy level is also small, and the total rotational partition function can be evaluated by integration as well. The rotational partition function for a diatomic molecule is given by:

$$q_{rot} = \frac{8\pi^2 IkT}{\sigma h^2}$$

where σ is the symmetry number. For diatomic molecules, $I=\mu d^2$, where μ is reduced mass $[m_1m_2/(m_1+m_2)]$ and d is the bond length. Different from translational and rotational energies, the spacing between vibrational energy is relatively large. For diatomic molecules, the summed vibrational partition function is given by:

$$q_{vib} = \frac{e^{-h\nu/2kT}}{1 - e^{-h\nu/kT}}$$

where ν is the vibrational frequency. Because the diatomic molecule is treated as a harmonic oscillator in this calculation, ν can be expressed as $\omega/2\pi$, where ω is the frequency of oscillation is defined as:

$$\omega = \sqrt{\frac{k}{\mu}}$$

In kinetic fractionation (e.g., diffusion and evaporation), because all molecules have the same kinetic energy ($E=1/2\times mv^2$), the ratio of velocities for two isotopologues (v) depends on masses (with an ideal gas assumption). If intermolecular forces and molecular collisions are considered, the mass (m) is replaced by the reduced mass (μ). In addition, molecules containing lighter isotopes have lower dissociation energies (i.e., higher reaction rates) than those bearing heavier isotopes on based on the difiniation of the reaction rate (R):

$$R = Ae^{-E_b/kT}$$

where A is the frequency factor for the reaction and E_b is the barrier energy. Therefore, it is obvious that equilibrium and kinetic fractionation effects for isotopologues are both ultimately associated with isotopic masses (i.e., mass-dependent). In the triple-oxygen-isotope system (^{16}O, ^{17}O, and ^{18}O), mass-dependent fractionation exponents may slightly vary (from ~0.50 to ~0.53) depending on various fractionation processes, but they are all close to ~0.5, which means that a change in the $\delta^{17}O$ of 1‰ (parts per thousand) is accomplished by an approximate 2‰ variation of $\delta^{18}O$ because $\delta^{17}O$ is sensitive to the ^{17}O-^{16}O mass separation (~1 amu) in the fractionation process while $\delta^{18}O$ is sensitive to the ^{18}O-^{16}O mass separation (~2 amu).

The deviation of mass-dependent fractionation law was firstly found by *Hulston and Thode* [1965] in quadruple sulfur isotopic measurement of meteorite samples, and was concluded as a result of nuclear process. Later, triple oxygen isotopic measurements conducted on the calcium aluminum inclusions (CAI) from carbonaceous chondrite Allende (one of the oldest objects formed in the Solar System) showed a result similar to that of *Hulston and Thode* [1965]: the oxygen isotopes did not obey the conventional relation $\delta^{17}O=0.5\delta^{18}O$ as predicted by classic mass-dependent fractionation law [*Clayton et al.*, 1973]. The observed relation of $\delta^{17}O=\delta^{18}O$ was (Figure 1.1) was suggested as a nuclear process based on the earlier work of *Hulston and Thode* [1965] using multiple sulfur isotopes. It was proposed that these objects could be a product of supernova and the deviation of mass-dependent fractionation can be utilized as an effective tracer for distinguished chemistry and nuclear processes. However, the major assumption underlying the entire model, i.e., the only possible way to explain a mass-independent isotopic composition was via a nuclear process, was later proven to be invalid.

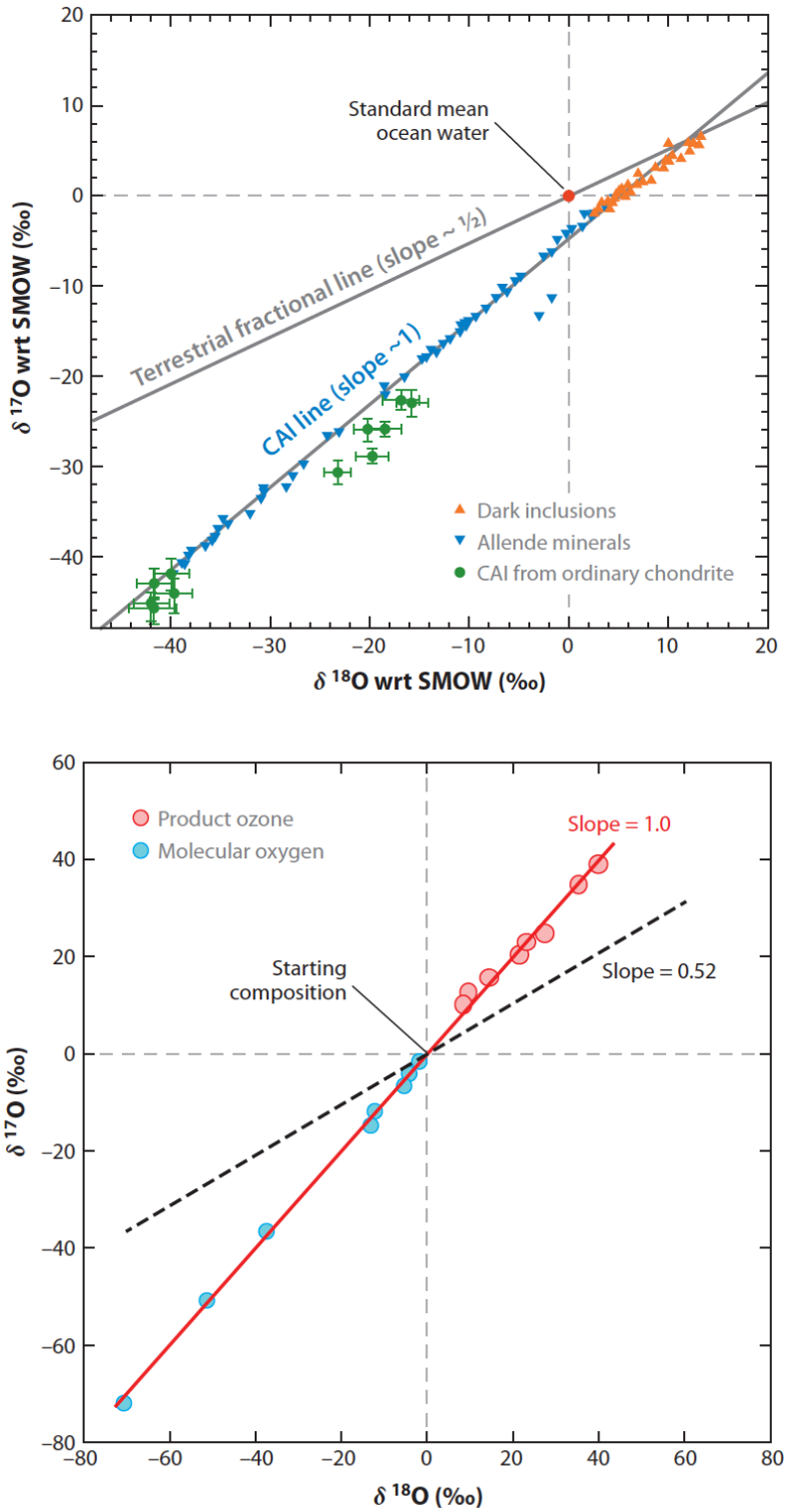

Figure 1.1. The triple oxygen isotopic composition in calcium aluminum inclusion (CAI) (upper) and ozone produced from the Thiemens' 1983 experiment (lower) [*Thiemens et al.*, 2012].

In 1983, a chemically produced mass-independent fractionation (MIF) was demonstrated to be possible by *Thiemens and Heidenreich* [1983], which is a milestone in the study of this unconventional isotope effect. They showed that in the production of ozone from molecular ozone, the product is equally enriched in $\delta^{17}O$ and $\delta^{18}O$, yielding a slope of ~1 nearly identical to the oxygen isotopes distribution found in CAI ten years ago (Figure 1.1). This surprising result raised a question whether the previously observed MIF signature in meteorites derives from a chemical, instead of nuclear, process. In fact, if the MIF signature in CAI was the result of explosive carbon burning in a supernova, associated anomalies in ^{24}Mg and ^{28}Si should be also observed [*Clayton et al.*, 1973]. However, such observations are still absent, leading to the abandonment of the nuclear process hypothesis [*Thiemens et al.*, 2012]. The MIF composition of oxygen isotopes has been observed in many important molecules (e.g., carbon monoxide, carbon dioxide, nitrous oxide, hydrogen peroxide, and water vapor) and oxyanions (e.g., sulfate, nitrate, carbonate, and perchlorate) in nature, and utilized in widely varying research fields in the Earth, atmospheric, and planetary sciences (e.g. atmospheric chemistry, carbon cycle, paleoclimate, and the history of primitive Earth, Mars, and solar system) [*Thiemens*, 2006; *Thiemens et al.*, 2012]. Although it is widely agreed that chemical processes accounted for most of the observed MIF composition of oxygen isotopes in natural samples, our understanding of the underlying physical chemistry, even for ozone molecules, remains incomplete. Early studies pointed to the important role of molecular symmetry, which determines the lifetime of metastable ozone transition state and the stabilization probability [*Heidenreich and Thiemens*, 1986]. In 21st century, Marcus' group developed a modified statistical Rice-Ramsperger-Kassel-Marcus (RRKM) model, with a non-statistical (non-RRKM) factor η included in the partition function, to quantitatively explain the ozone MIF process, although the physical meaning and origin of η remains unclear [*Gao and Marcus*, 2001]. Recently, Babikov and his colleagues are developing quantum-mechanic based approaches to provide quantum level treatment of collisional energy transfer and passage of rotational/vibrational energy to reproduce the ozone MIF process, especially the η effect [*Ivanov and Babikov*, 2013]. For other

molecules such as carbon monoxide, the mechanistic origin of oxygen isotope MIF effect (e.g., self-shielding, wavelength-dependent effect) is highly debated [*Chakraborty et al.*, 2008; 2009; *Federman and Young*, 2009; *Lyons et al.*, 2009; *Yin et al.*, 2009].

With four stable isotopes (^{32}S, ^{33}S, ^{34}S and ^{36}S), sulfur is directly below oxygen in the periodic table. Therefore, it is not surprising that chemically induced MIF can be also observed in the quadruple sulfur isotope system, although the mechanistic origin is more complex and the theoretical understanding is less advanced than triple oxygen isotopes. In early experiments, MIF compositions of sulfur isotopes were observed in the formation of S_2F_{10} [*Bainssahota and Thiemens*, 1989] and photopolymerization of CS_2 [*Colman et al.*, 1996], but might be less relevant to processes occurring in nature. Subsequent photolysis experiments of atmospherically relevant molecule SO_2 [*Farquhar et al.*, 2001; *Farquhar et al.*, 2000b; *Masterson et al.*, 2011; *Ono et al.*, 2013; *Whitehill et al.*, 2015; *Whitehill and Ono*, 2012; *Whitehill et al.*, 2013] highlighted the role of SO_2 photochemistry in producing mass-independent sulfur isotopic composition in nature. In the SO_2 absorption band between ~240 and ~340 nm, SO_2 is excited and may be subject to photooxidation. In the SO_2 absorption band between ~180 and ~220 nm, SO_2 is photolyzed to SO and O. Both processes produce mass-independent sulfur isotopic fractionation effects, which are likely wavelength dependent, but responsible chemical physics remain elusive. Because molecular symmetry effects as proposed in ozone formation may not apply in SO_2 photochemistry reactions, self-shielding is proposed as an alternative mechanism [*Lyons*, 2007; *Ono et al.*, 2013]. It is highly unlikely that such processes can occur in the ambient atmosphere because they require a substantial amount of SO_2 (~0.1 mbar) [*Ono et al.*, 2013]. Other mechanisms such as different reaction rates associated isotopologue-dependent absorption cross sections [*Endo et al.*, 2015], and intersystem crossing via vibronic coupling [*Whitehill and Ono*, 2012] are also proposed. Because of the complex excited-state chemistry of SO_2, the state-state transitions and associated isotopic effects are difficult to model in the current stage. Despite the incomplete knowledge of SO_2 photochemistry,

it is the currently most investigated and accepted reactions accounting for most of MIF compositions of sulfur isotopes observed on the Earth [*Farquhar et al.*, 2000a; *Lyons et al.*, 2014; *Ono*, 2017] and possibly Mars [*Franz et al.*, 2014]. In the next section, I further introduce how quadruple sulfur isotopic measurements were utilized in understanding the Archean and present-day sulfur cycles and discuss limitations of current interpretations that predominantly stem from SO_2 photochemistry.

1.2 Terrestrial Sulfur cycle

1.2.1 Archean sulfur cycle and the origin of life

Sulfur is the 6th most abundance element on the Earth and has been ubiquitous since the formation of Earth (~4.5 billion years ago). Most (~97%) of Earth's sulfur likely presents in the core, and the fractionated sulfur isotopic composition in the terrestrial mantle with respect to chondrites therefore provides information to constrain the core-mantle differentiation during the formation of Earth [*Labidi et al*., 2013]. Sulfur is one of the "CNOPS (carbon, nitrogen, oxygen, phosphorus, and sulfur)" elements and essential in all life on Earth. It likely supported the earliest life and played an important role in the origin of life [*Mandeville*, 2010]. With highly variable valence states (from -2 to +6), sulfur actively participates in a host of biogeochemical processes. In particular, many sulfur microbial metabolic processes (such as sulfate reduction, disproportionation, and sulfide oxidation) are intimately coupled with carbon and oxygen cycles [*Lyons and Gill*, 2010]. Therefore, sulfur is an ideal recorder of the evolution of oxygen and early life on a geological scale. For example, metabolic processes are associated with significant sulfur isotope fractionation, and the variation of $\delta^{34}S$ in Earth's oldest rocks (Figure 1.2) allow time calibration of the evolution of metabolic processes in the primitive Earth and a deep node on the tree of life [*Shen et al*., 2001]. The magnitude of sulfur isotope fractionation also constrains levels of seawater sulfates and atmospheric oxygen [*Canfield et al*., 2000].

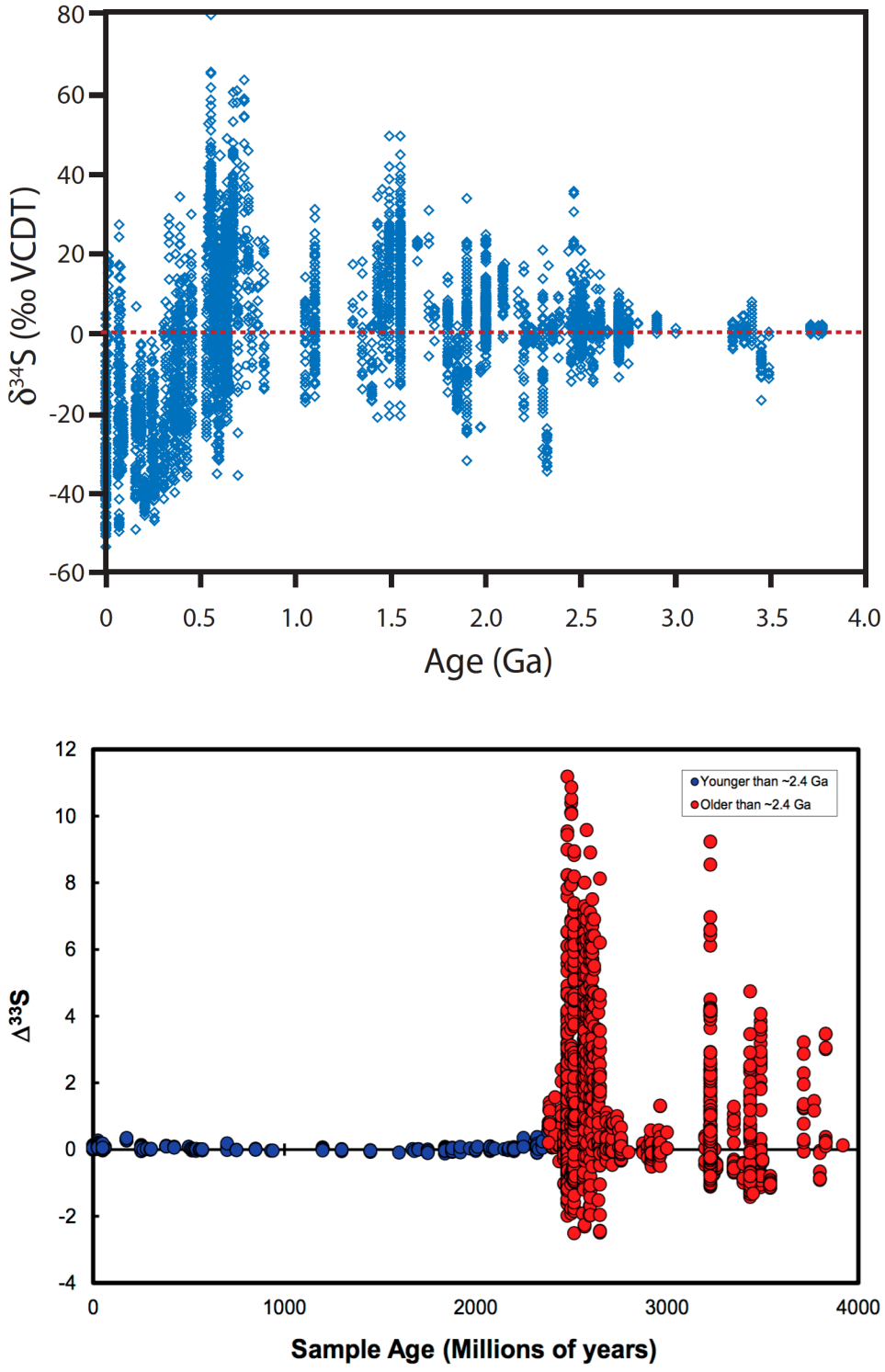

Figure 1.2. Compilation of $\delta^{34}S$ (upper) and $\Delta^{33}S$ (lower) versus age for rock samples. [*Lyons and Gill*, 2010; *Thiemens*, 2013]

Because the atmospheric oxygen level is highly linked to the evolution of life, the rise of oxygen is probably one of the most important events in our Earth's history, and understanding its tempo is a focus of active research. The "smoking gun" for the first Great Oxygenation Event comes from the pronounced signature of sulfur isotope mass-independent fractionation in Archean (~4 to ~2.5 Ga) rocks, which disappears in younger rocks [*Lyons et al.*, 2014] (Figure 1.2). As discussed in the previous section, sulfur isotope mass-independent fractionation is likely originating from the photolysis of SO_2 in the UV region. In the present-day atmosphere, such reactions do not occur in the troposphere as the stratospheric ozone layer shields most of UV light (< ~290 nm). The large sulfur isotopic anomalies observed in the Archean rocks therefore provide a strong evidence that O_2 and O_3 concentrations in the Archean are at a very low level permitting UV light to penetrate into the Earth's surface. Subsequent modeling efforts quantified the atmospheric oxygen concentration to be $<10^{-5}$ times the present atmospheric level [*Pavlov and Kasting*, 2002].

The surprising finding of sulfur isotopic MIF signatures launched a new wave of quadruple sulfur isotopic analysis in Archean rocks to understand the rise of oxygen [*Lyons et al.*, 2014], which reveals discernable temporal structures of $\Delta^{33}S$ and $\Delta^{36}S$ (Figures 1.2 and 1.3) and indicates changing atmospheric sulfur chemistry, volcanoic, continental, and biological activities across the Archean [*Farquhar et al*., 2007; *Halevy et al*., 2010; *Philippot et al*., 2012]. Although it has been widely accepted that the sulfur isotope MIF composition in Archean rocks indicates an anoxic atmosphere allowing SO_2 photolysis, the observation in nature cannot be exactly reproduced by laboratory SO_2 photolysis experiments. Therefore, current research is predominantly focused on modeling efforts incorporating some previously unappreciated atmospheric composition [*Ueno et al.*, 2009] and non-atmospheric mechanisms such as continental crust formation [*Halevy et al.*, 2010] and ocean oxygenation [*Fakhraee et al.*, 2018] that may modify the formation and preservation of MIF signatures. The difficulty of reproducing the Archean sulfur isotope MIF record may be also because (i) chemical physics of MIF processes in SO_2 photolysis is highly

depending on wavelength and the fine structures of the spectral actinic solar flux in the Archean atmosphere is difficult to reproduced, and (ii) additional MIF processes are required but not yet identified. Some studies suggested that thermochemical sulfate reduction might by an alternative mechanism [*Watanabe et al.*, 2009], but this sulfur isotopic MIF process was later attributed to magnetic isotope effects [*Oduro et al.*, 2011], which only lead to ^{33}S anomalies and therefore cannot explain the Archean record.

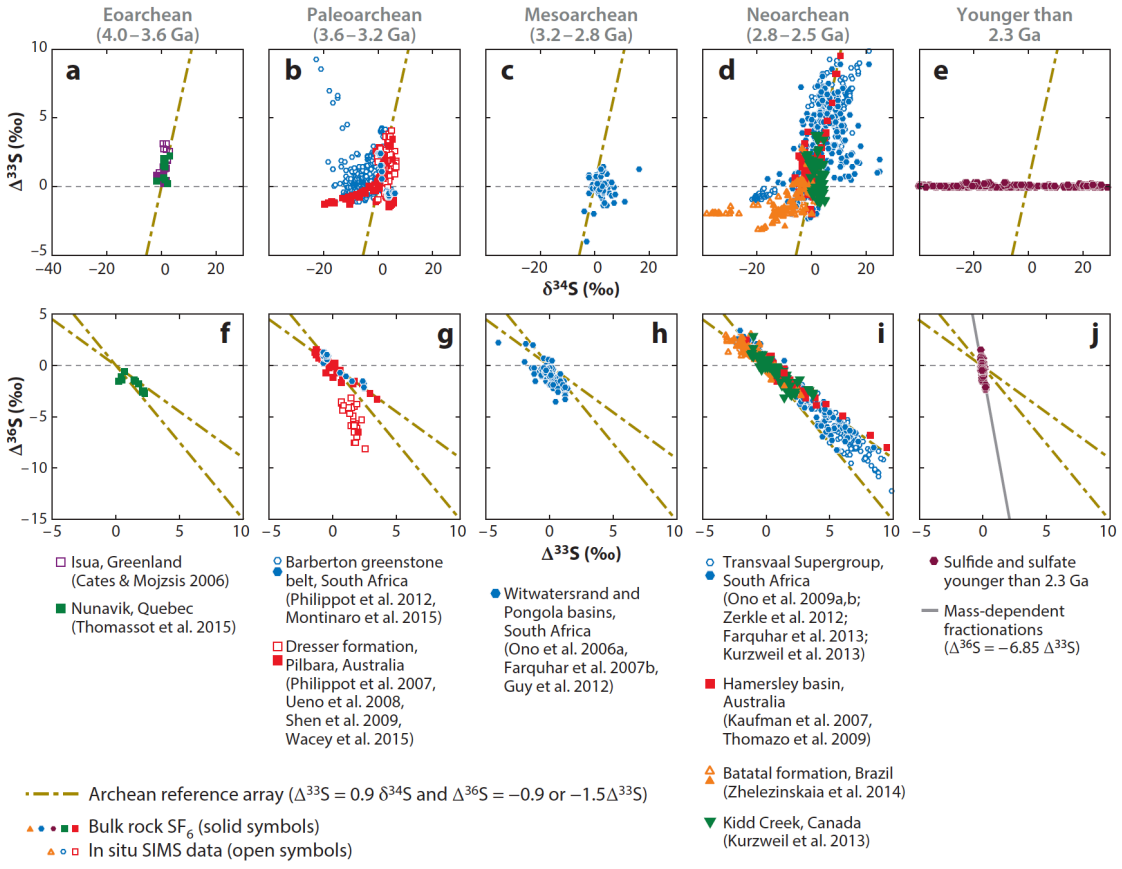

Figure 1.3. Compilation of $\delta^{34}S$, $\Delta^{33}S$ and $\Delta^{36}S$ for samples with different ages [*Ono*, 2017].

The potential role of symmetry effects in sulfur isotopic MIF has been noted since the early chemical physics experiments [*Bainssahota and Thiemens*, 1989]. In SO_2 photolysis, elemental sulfur is one of the products and therefore it is reasonable to suspect that elemental recombination reactions (such as $S + S_2 \rightarrow S_3$) may be important in producing MIF signatures as observed in ozone formation. A recent theoretical study suggested that this reaction can generate significant isotope effects ($\Delta^{33}S$ = -200‰) and a slope (-1.16) similar to the Archean record [*Babikov*, 2017]. However, this MIF effect has not been experimentally verified because it is difficult to separate the effect of recombination reactions from others (such as photolysis) in laboratory investigation.

1.2.2 Present-day sulfur cycle and climate impacts

The present-day sulfur cycle is significantly influenced by anthropogenic activities, especially fossil fuel combustion. In volcanically quiescence periods, anthropogenic SO_2 emission (~50 Tg S $year^{-1}$) accounts for more than 50% of total sulfur source strengths in the troposphere [*Sheng et al.*, 2015]. In particular, emissions in the developing Asia including China, Russia, India, and Middle East account for approximate a half of global SO_2 emission. Once emitted, SO_2 is either removed from the atmosphere via dry or wet deposition, or oxidized to sulfate in the atmosphere via varying oxidation pathways such as gaseous oxidation by OH radical or Criegee intermediates and aqueous oxidation by H_2O_2, O_3, O_2 (catalyzed by transition metal ions) or hypohalous acid (HOX; X = Cl or Br) [*Chen et al.*, 2016a; *Zhang et al.*, 2015]. Recently, heterogeneous oxidation of SO_2 (via O_3, H_2O_2, O_2, and/or NO_2 oxidation), especially in Beijing haze, is receiving increasing attention because conventional SO_2 oxidation pathways cannot fully explain the observed rapid sulfate enrichment [*Cheng et al.*, 2016; *Wang et al.*, 2016].

Sulfate, the oxidized form of sulfur, play a key role in affecting climate [*Lelieveld and Heintzenberg*, 1992] and public health [*Harrison and Yin*, 2000]. However, an accurate and precise quantification of its impacts on aerosol radiative forcing and mortality is currently unavailable because of our incomplete knowledge of the atmospheric sulfate budget as a result of widely

varying emission sources and complicated chemical transformations of sulfur compounds [*Berresheim et al.*, 2014; *Cheng et al.*, 2016; *Huang et al.*, 2015a; *Wang et al.*, 2016; *Wang et al.*, 2010]. Conventional isotopic studies were focused on the most abundant rare stable isotope ^{34}S and ^{18}O for source apportionment, which provided more useful information than sulfate concentration measurements [*Cortecci and Longinel.A*, 1970]. Measurements of other rare stable isotopes (especially ^{17}O) in sulfates became important after the discovery of MIF effects [*Dominguez et al.*, 2008; *Thiemens*, 2006]. For example, the $\Delta^{17}O$ value in sulfate originates from oxidants involved in its formation, and therefore provides an isotopic constraint for the relative importance of sulfate formation pathways [*Lee et al.*, 2001; *Lee and Thiemens*, 2001; *Lyons*, 2001; *Savarino et al.*, 2000; *Savarino and Thiemens*, 1999; *Vicars and Savarino*, 2014]. The unique $\delta^{18}O$ and $\Delta^{17}O$ values in primary sulfate emitted from ship also offers an isotopic fingerprinting for the identification of this previously unappreciated emission source [*Dominguez et al.*, 2008]. Measurements of $\Delta^{17}O$ in sulfates preserved in ice core or snow pits can be utilized as a probe for investigating the perturbation of atmospheric sulfur cycles in the paleo-atmosphere [*Alexander et al.*, 2004; *Shaheen et al.*, 2013].

In the present-day atmosphere, only stratospheric sulfates are presumed to acquire sulfur isotopic MIF signatures because SO_2 photolysis is likely the only mechanism producing sulfur isotopic anomalies and short UV light is shielded by the stratospheric ozone layer. Therefore, the sulfur isotopic MIF signatures in sulfates preserved in ice cores, snow pits, and ash beds are interpreted as deriving from massive volcanic eruptions with stratospheric SO_2 injection, and utilized as a tracer for identifying the possible volcanic perturbations of the stratosphere in the past and understanding their influences on both atmospheric chemistry and climate [*Baroni et al.*, 2007; *Martin and Bindeman*, 2009; *Savarino et al.*, 2003]. Because quadruple sulfur isotopic analysis is relatively time-consuming and it is assumed that all tropospheric sulfates are isotopically normal, such measurements in present-day aerosols are limited [*Guo et al.*, 2010; *Han et al.*, 2017; *Romero*

and Thiemens, 2003]. However, existing analysis [*Guo et al.*, 2010; *Han et al.*, 2017; *Romero and Thiemens*, 2003] showed that nearly all tropospheric sulfates possess non-zero $\Delta^{33}S$ and $\Delta^{36}S$ values, which is not explicable by mass-dependent fractionation [*Harris et al.*, 2013a]. This observation is further confirmed by a recent high-resolution snow pit measurement [*Shaheen et al.*, 2014]. Although previous studies suggest that the observed sulfur isotopic anomalous in tropospheric sulfates are probably originating from the stratosphere [*Guo et al.*, 2010; *Han et al.*, 2017; *Romero and Thiemens*, 2003], an independent stratospheric tracer in the same sulfate samples that support this argument remains absent. Given the notable signature of sulfur isotopic MIF composition in tropospheric sulfate aerosols, even in the highly polluted boundary layer [*Han et al.*, 2017], there may be a previously unknown MIF process occuring in the troposphere. If such a MIF process is identified, the Archean record may yield a deeper insight.

Because of the higher production rate of ^{35}S in the stratosphere (1-2 orders of magnitude greater than in the troposphere) [*Lal and Peters*, 1967], radiosulfur may be an ideal stratospheric tracer to constrain the stratospheric influence. Another advantage of ^{35}S is that it behaves both as a gas (SO_2) and an aerosol, and the radioactivity may serve as an actual clock for quantifying gas-to-particle (SO_2 to SO_4^{2-}) conversion rates. Although ^{35}S measurements made by the recently developed optimized LSC technique [*Brothers et al.*, 2010] have been utlized to study the polar vortex activity [*Priyadarshi et al.*, 2011a], Santa Ana winds and shallow stratosphere-troposphere exchange events in southern California [*Priyadarshi et al.*, 2012a], the reliability of ^{35}S as a stratospheric tracer remains uncertain and debated because the magnitudes of ^{35}S enrichments were relatively small and other stratospheric signatures (e.g. high O_3 level, low humidity) were not observed in suspected stratospheric air masses.

1.3 Motivation and Dissertation Outline

In summary, several missing pieces of the puzzle restrict our understanding of the atmospheric sulfur cycle (for both Archean and present times). The purpose of this dissertation is

to develop new analytical technique for cosmogenic ^{35}S measurements, which are utilized to solve three important scientific questions: (i) Can ^{35}S be an unambiguous tracer to quantify stratospheric air at the Earth's surface and the oxidation lifetime of SO_2? (ii) What new knowledge can be gained if cosmogenic ^{35}S isotope is measured along with other 7 stable isotopes in sulfate aerosols (^{16}O, ^{17}O, ^{18}O, ^{32}S, ^{33}S, ^{34}S, and ^{36}S), especially in the polluted East Asia? (iii) What is the physical chemical mechanism responsible for sulfur mass-independent fractionation and what it may mean for the Archean record?

In Chapters 2 and 3, I present the newly developed analytical methods for determining cosmogenic ^{35}S in atmospheric, cryospheric, and hydrospheric samples. In particular, a first proof-of-concept study for quantifying glacial melting processes over the Tibetan Plateau is presented. In Chapter 4, the ability of ^{35}S for tracing stratospheric air is demonstrated. It is found that the coupling between mid-latitude cyclones and Santa Ana winds could lead to regional O_3 pollution episodes in the coastal southern California, and the ^{35}S measurement may provide additional evidence for excluding such naturally occurring "exceptional pollution events" defined by the US Environmental Protection Agency. In Chapter 5, a theoretical framework for quantifying gas-to-particle conversion rate of sulfur in the terrestrial atmosphere based on high-sensitivity ^{35}S measurements is presented. Implications for possible experimental investigations of atmospheric sulfur chemistry on Earth and extraterrestrial bodies (such as Venus and Europa) in the future are also discussed.

In Chapters 6, 7, and 8, the uses of cosmogenic ^{35}S measurements in understanding atmospheric mixing and sulfur chemistry in East Asia and the Himalayas and Tibetan Plateau are presented. We observed unexpected enrichment of aged stratospheric air in the boundary layer during the monsoon transitional period (mid-autumn) in East Asia, which may have crucial implication for understanding O_3 pollution in this region. We also found that sulfate in the higher atmosphere over East China is produced in a way similar to that occurring at the ground level,

which may result from a combination of large air pollutant emissions and active vertical mixing in the atmosphere over East China. This finding is useful in improving current atmospheric chemistry and climate models to evaluate the extent to which sulfur emissions in East China influence regional and global climates. Measurements of ^{35}S over the Himalayas and Tibetan Plateau reveals that the Himalayas is a gate way of springtime stratospheric intrusions, while the central Tibetan Plateau is mainly affected by aged and mixed air masses of semi-recent stratospheric origin.

In Chapter 9, two distinct mechanistic origins of sulfur isotopic MIF in the present-day's atmosphere are identified with the use of radiosulfur on an observational basis: a positive ^{33}S anomaly likely originating from high-altitude (stratospheric SO_2 photolytic reactions) and a negative ^{36}S anomaly mainly associated with combustion processes. This finding is further confirmed by our quadruple sulfur isotopic measurements from coal (from the Carboniferous, Permian, and Triassic periods) and SO_2 emitted from combustion. In Chapter 10, atmospheric sulfur isotopic anomalies recorded in the Himalayas reveal significant changes in the regional atmospheric sulfur cycle and glacial hydrological system during the second industrial revolution. The data is the first long-term atmospheric sulfur isotopic anomaly record obtained from a non-polar region, and mimics the Archean barite record. The Archean-barite-like sulfur isotopic fingerprinting in an oxygen-rich atmosphere therefore points to the non-photochemical sulfur isotopic MIF process identified in Chapter 9. Because the non-photochemical S-MIF process discovered in Chapters 9 and 10 is previously unrecognized, the identification allows further definition of the sulfur isotopic MIF record in Archean rocks, and may provide new insights into the relative roles of the dynamics, atmospheric chemistry, and microbial metabolisms on the formation and preservation of sulfur isotopic MIF composition on the primitive Earth.

Chapter 2 Accurate quantification of radiosulfur in chemically complex atmospheric samples

2.1 Abstract

An ultra-low-level liquid scintillation counting (LSC) technique has been used in measuring radiosulfur (cosmogenic ^{35}S) in natural samples. The ideal half-life of ^{35}S (~87 d) renders it a new way to examine various biogeochemical problems. A major limit of the technique is that complex chemical compositions in atmospheric samples may lead to color quenching of LSC cocktails, a serious problem prolonging the pretreatment time (>1 week) and hampering the accurate determination of ^{35}S. For application of the technique where many of the most important atmospheric chemical processes are examined, significant interferences arise and accurate analysis in small samples is not possible. In this study, we optimized the LSC method to minimize/eliminate color quenching in high-sensitivity ^{35}S measurements. The analytical performance of this new method was evaluated using control laboratory experiments and natural aerosol samples. Results show that the new method offers comparable accuracy as the traditional method for normal environmental samples (bias: $< \pm 0.03$ disintegrations per minute [DPM]) and significantly shortens the pretreatment time to less than 3 days. For samples that were heavily contaminated by color quenching agents, the accuracy of this new method is notably higher than the traditional method (maximum bias: -0.3 *v.s.* -1.5 DPM). With the growing use of radiosulfur in the field of Earth and planetary sciences, the accurate determination of ^{35}S would provide a reliable field-based constraint for modeling ^{35}S production in the atmosphere and allow a wide range of atmospheric, hydrological, and biogeochemical applications.

2.2 Introduction

Sulfur has been ubiquitous in the global terrestrial atmosphere since the earliest geological record of the primitive Earth and has played an important role in the evolution of life and the ability

to track its origin and evolution [*Fike et al.*, 2015]. Interest in the modern atmospheric sulfur cycle predominantly stems from the key role of sulfate in affecting climate [*Lelieveld and Heintzenberg*, 1992] and public health [*Harrison and Yin*, 2000]. Our knowledge of the sulfate budget in the atmosphere is incomplete due to widely varying emission sources and complicated chemical transformations of sulfur compounds [*Berresheim et al.*, 2014; *Cheng et al.*, 2016; *Huang et al.*, 2015a; *Wang et al.*, 2016; *Wang et al.*, 2010], hampering an accurate and precise quantification of its association with aerosol radiative forcing and mortality. Isotopic analysis of atmospheric sulfate samples has been utilized to provide additional constrains on these processes [*Thiemens*, 2006]. Conventional isotopic studies have been focused on the most abundant rare stable isotope ^{34}S and ^{18}O for source apportionment [*Cortecci and Longinel.A*, 1970]. Measurements of other rare stable isotopes (^{33}S, ^{36}S and ^{17}O) in sulfates became important after the discovery of mass-independent isotopic fractionation effects, which provide essential information on both emission sources and chemical formation pathways that cannot be quantified by conventional sulfate concentration or single isotope ratio measurements [*Dominguez et al.*, 2008; *Thiemens*, 2006].

The radiosulfur nuclide (^{35}S) is naturally produced by bombardment of ^{40}Ar in the atmosphere by high energy cosmic rays. Cosmogenic ^{35}S is the only radioactive sulfur isotope with a half-life (~87 days) of ideal age to track atmospheric and hydrological processes. Unlike stable isotopes, radiosulfur in atmospheric sulfates have been rarely measured because of its low activity in the atmosphere and associated analytical difficulties [*Hong and Kim*, 2005; *Tanaka and Turekian*, 1991; 1995; *Turekian and Tanaka*, 1992]. In 2010, an ultra-low-level liquid scintillation counting (LSC) technique was developed [*Brothers et al.*, 2010] in which sulfate samples were prepared as aqueous sulfate solution for reducing the background activity and enhancing the ^{35}S counting efficiency. Since then, this method has been used in the high-sensitivity determination of ^{35}S in atmospheric samples for quantifing a wide range of atmospheric processes such as neutron leakage at the Fukushima nuclear plant, gas-to-particle (SO_2-to-sulfate) conversion rate determination, and

horizontal/vertical air mass transport (e.g., westerly jet stream, convection, stratospheric intrusion, foehn wind, and polar vortex) [*Lin et al.*, 2017a; *Lin et al.*, 2017c; *Lin et al.*, 2016a; *Priyadarshi et al.*, 2011a; *Priyadarshi et al.*, 2011b]. This LSC method (using aqueous sulfate solution as radiosulfur carrier) was recently extended to radiosulfur measurements in hydrological and cryogenic samples [*Lin et al.*, 2017d], which has broad implications on understanding the interaction between the atmosphere, hydrosphere, and cryopshere (e.g., snow and glacier melting) and serves as an important supplement to existing radiosulfur biogeochemical and hydrologic studies (e.g., microbial sulfate reduction in lake and marine sediments [*Howarth and Jorgensen*, 1984], age and source determination of meltwater runoff [*Cecil et al.*, 1998; *Cooper et al.*, 1991; *Michel et al.*, 2000], groundwater [*Clark et al.*, 2016; *Plummer et al.*, 2001; *Uriostegui et al.*, 2016; *Urióstegui et al.*, 2016], and surface water in watersheds [*Kester et al.*, 2003]) using a different type of LSC technique (using solid $BaSO_4$ as radiosulfur carrier) [*Hong and Kim*, 2005; *Uriostegui et al.*, 2015]. These studies illustrate the wide range of biogeochemical applications to date. This paper presents a technique to allow for measurement to include environments where measurement is not presently feasible.

Presently, standard techniques require a relatively long pretreatment process to purify environmental samples because of their chemically complex nature that hampers an accurate determination of ^{35}S. Color quenching resulting from impurities (e.g., organic compounds and nitric acids) [*Hou et al.*, 2005; *Peng*, 1960] in the atmospheric samples is a major problem. The photons produced from scintillation are absorbed or scattered by the LSC cocktail (sample-gel mixture) and therefore reduce the ^{35}S counting efficiency and sensitivity. To prevent the possible influence of color quenching, one must repeat purification procedures multiple times requiring at least one week for each sample. Occasionally, the prepared LSC cocktail remains influenced by color quenching after multiple purification steps, leading to an underestimated ^{35}S activity in the environmental sample. Hydrogen peroxide (H_2O_2), a strong oxidant, was suggested as an effective bleaching agent

for LSC cocktails in measuring high-radioactivity samples (>10,000 disintegrations per minute [DPM]) [*Mahin and Lofberg*, 1966; *Thomson*, 2001] but it remains unclear if this agent can be used in the high-sensitivity ^{35}S measurements (<3 DPM) because O_2 produced from H_2O_2 decomposition may quench aromatic hydrocarbon triplet states [*Gijzeman et al.*, 1973; *Smith*, 1994] and therefore may reduce the counting efficiency via capturing π electrons associated with the aromatic solvent in LSC cocktails (also known as chemical quenching). In this study, we tested the bleaching ability of H_2O_2 in high-sensitivity ^{35}S measurements and optimized the traditional method with an aim to improve the measurement accuracy and also reduce the pretreatment time.

2.3 Experimental Section

2.3.1 Preparation of Laboratory ^{35}S Standards

A PerkinElmer $H_2{}^{35}SO_4$ standard stored in the Radiation Division of the Environment, Health and Safety Department (EH&S) at the University of California San Diego (UCSD) was used to evaluate the accuracy and precision of the method developed in this study. A set of laboratory standards with varying ^{35}S activities (ranging from 1 to 30,000 DPM) were prepared at the EH&S facility and stored separately in a clean hood in our laboratory. In this study, the focus was mainly on standards with low ^{35}S activities that are comparable to most environmental samples (<3 DPM). Experiments were conducted in a different room to prevent any possible ^{35}S contamination during chemical processing.

2.3.2 Preparation of Environmental Samples

Aerosol samples collected at San Diego (a coastal site; 32.8°N, 117.2°W), Beijing (an urban site; 39.9°N, 116.4°E), Harbin (an industrial site; 45.8°N, 126.5°E), and Mount Wuyi (a forested site; 27.7°N, 117.7°E) using high volume air samplers (flow rates: ~1 m^3 min^{-1}) were used to identify major analytical problems in ^{35}S measurements. Samples were trapped on quartz or glass-fiber filters (Whatman) and each sample was collected for 2-7 days. Because aerosol samples are relatively difficult to collect in remote regions, snow samples collected from a glacier site

(39.5°N, 96.5°W) at the Tibetan Plateau (Laohugou [LHG] Glacier) were used. The volume of melted water for each sample, which was concentrated in a Bio-Rad AG1-X8 anion exchange resin (analytical grade, 100−200 mesh, chloride form), is 2-4 liters. Detailed aerosol and snow sampling description can be found in the literature [*Lin et al.*, 2016a; *Lin et al.*, 2017d; *Lin et al.*, 2016c]. These environmental samples collected from varying locations may represent the chemically complex nature in a wide range of environments. The sample purification procedure followed the protocol described by *Brothers et al.* [2010] and *Lin et al.* [2017d] Filters with aerosol samples were immersed in ~30 mL of Milli-Q deionized water (18 MΩ cm) overnight. Filters and insoluble materials were removed by a disposable vacuum-driven filtration system equipped with a 0.22 μm Millipore Express Plus Membrane. A 5 mL of H_2O_2 (30%, Certified ACS Grade, Fisher Scientific) was added into the filtrate containing sulfate ions, which was subsequently dried in a clean oven (80°C) overnight. Concentrations of reduced sulfur compounds in the condensed phase are negligible relative to sulfates [*Lin et al.*, 2017a], and the use of H_2O_2 in this step therefore would not affect the accurate determination of ^{35}S in sulfate aerosols. Regarding snow samples, sulfate ions were eluted from the anion exchange resin by hydrobromic acid (1 M). H_2O_2 and sodium sulfates containing no ^{35}S were added to the solution, which was subsequently evaporated in a clean hood (80°C) overnight. The dried sulfate-containing solids from aerosol or snow samples were re-dissolved, and further purified by a polyvinylpyrrolidone (PVP) column and a Ag cartridge (Dionex OnGuard II). The collected sample solution was freeze-dried overnight, after which white crystals were formed. If there was any visible impurity, the entire purification procedure described previously was repeated. In most cases, aerosol samples collected from polluted regions required 2-4 purification cycles.

2.3.3 Ultra-Low-level Liquid Scintillation Counting

The purified sulfate samples were prepared as aqueous sulfate solution (instead of solid $BaSO_4$) following *Brothers et al.* [2010] and *Lin et al.* [2017d]. The solution was quantitatively

transferred to a 20-mL plastic scintillation vial (Fisherbrand) (total volume: 5 mL) and mixed with 10 mL of scintillation gel (Insta-Gel Plus, PerkinElmer). This aqueous solution method eliminates the use of barium reagents, which contains a few radionuclides such as ^{133}Ba that may interfere ^{35}S analysis [*Brothers et al.*, 2010; *Uriostegui et al.*, 2015]. This technique is capable of handling <1.5 mmol of sulfates [*Lin et al.*, 2017d], and is therefore suitable for most atmospheric samples. An ultra-low-level LSC spectrometer (Quantulus 1220, PerkinElmer) following the default setting for ^{14}C was used to quantify ^{35}S activity [*Brothers et al.*, 2010]. Because natural samples may contain trace amounts of ^{14}C that affect the ^{35}S measurements, the channels 1-450 was selected to minimize the radiocarbon interference (with peak at the channel ~500) without significantly reducing the counting efficiency of radiosulfur (with peak at the channel ~300).[*Brothers et al.*, 2010] The ^{35}S counting efficiency (the ratio of counts per minute [CPM] to DPM) in this study is determined using ^{35}S standards in the optimized channels (1-450). Each sample or standard was counted for 6-12 times (2-h counting for each cycle) and the average is reported. Potential outliers, if any, were identified by the Dixon's Q-Test (99% confidence level) and rejected. As discussed by *Lin et al.* [2017d], the standard variation of all counting cycles is usually greater than the net counting error estimated by the standard environmental counting statistics method, especially for samples with low ^{35}S activity [*E.W. Rice*, 2012]. In this study, we compared both errors and reported the larger one, which was further propagated in subsequent arithmetic calculations (e.g. corrections for the background activity) [*E.W. Rice*, 2012]. To identify any possible phase separation and/or color quenching during counting, which will affect the ^{35}S counting efficiency, each sample-gel mixture was inspected visually before and after counting.

2.3.4 Development of New Cocktail Preparation Methods

In this study, two sets of experiments were performed to minimize or eliminate the impact of color quenching on analytical accuracy. In set 1, cocktails made by environmental samples that turned dark were used for the development of a H_2O_2 bleaching method. In this set of experiments,

2 mL of H_2O_2 was added to existing cocktails to bleach them. Samples were re-measured again and the results before and after bleaching were compared. To further investigate how the H_2O_2 bleaching method affect the measurements, control experiments with ^{35}S standards were conducted. In set 2, we used H_2O_2 to re-dissolve freeze-dried samples and prepare the LSC cocktail. The aim of this set of experiments is to simplify purification procedures and minimize the effect of color quenching. Ambient aerosol samples were used to test this newly developed method. Details of the experimental parameters and results are described and discussed in the next section.

2.4 Results and Discussion

2.4.1 Set 1: Color quenching of environmental samples and H_2O_2 bleaching

In this study, environmental samples (cocktails) that turned dark or grey were selected and bleached by 2 ml of H_2O_2 as described in the method section. These samples include aerosols samples collected from Beijing, Harbin, and Mt. Wuyi in China and snow samples collected from the LHG Glacier on the Tibetan Plateau. Figure 2.1 shows that these samples were highly affected by color quenching, and the counting rates of three samples (Beijing-1, LHG Glacier-1, and LHG Glacier-2) are even equal to or lower than the background counting rate of scintillation gel (0.9-1.0 CPM; Type A in Table 1) because most photons derived from the fluorescence of scintillation gel (excited by β^- particles emitted from radioactive ^{35}S decay events) were absorbed by the dark LSC cocktails. After H_2O_2 bleaching, colors disappeared and the counting rates increased significantly (Figure 2.1). Recounting of these samples approximate 10-30 days later confirmed that the detected activities were resulted from ^{35}S decay events. The results indicate that more photons can be detected by the photomultiplier tubes after H_2O_2 bleaching and H_2O_2 is of potential application to eliminate or minimize color quenching in the course of measurements. The quenching level might be determined by the Quantulus 1220 based on the change of logarithmic spectrum endpoint of an external standard (^{152}Eu) pneumatically transported to the vicinity of the sample vial, which is reported as a standard quenching parameter (SQP) [*Lin et al.*, 2017d; *Uriostegui et al.*, 2015]. If a

clear relationship between the SQP and ^{35}S counting efficiency is determined, the measured SQP might be utilized to determine the counting efficiency for samples with unknown ^{35}S activity [*Thomson*, 2001]. However, because different quenching agents yield different relationships between SQP and counting efficiency [*Thomson*, 2001], it is difficult to create a reliable quenching curve that can be applied for all environmental samples. Figure 2.2 showed that the quantitative relationship between SQP and the ^{35}S counting efficiency in both laboratory standards and environmental samples cannot be precisely defined by a regression equation. Therefore, control experiments using ^{35}S standards with known activities are required.

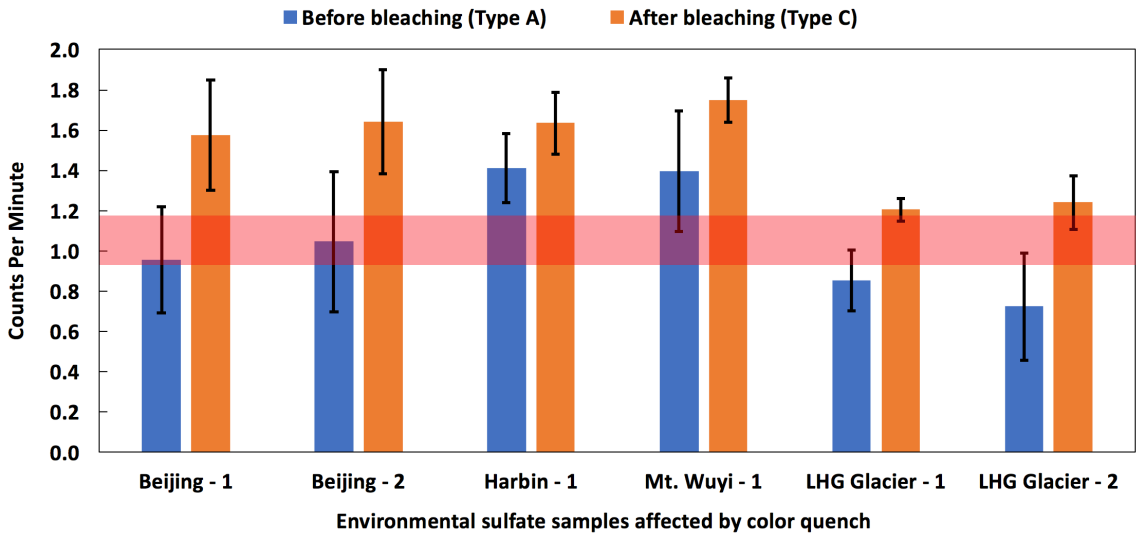

Figure 2.1. Comparison of ^{35}S counting rates for various environmental samples before and after H_2O_2 bleaching. Error bars stand for one standard deviation. The red shaded bar represents the approximate range of background counting rates (Types A and C) shown in Table 2.1. Types A and C are the cocktail preparation methods described in Table 2.1.

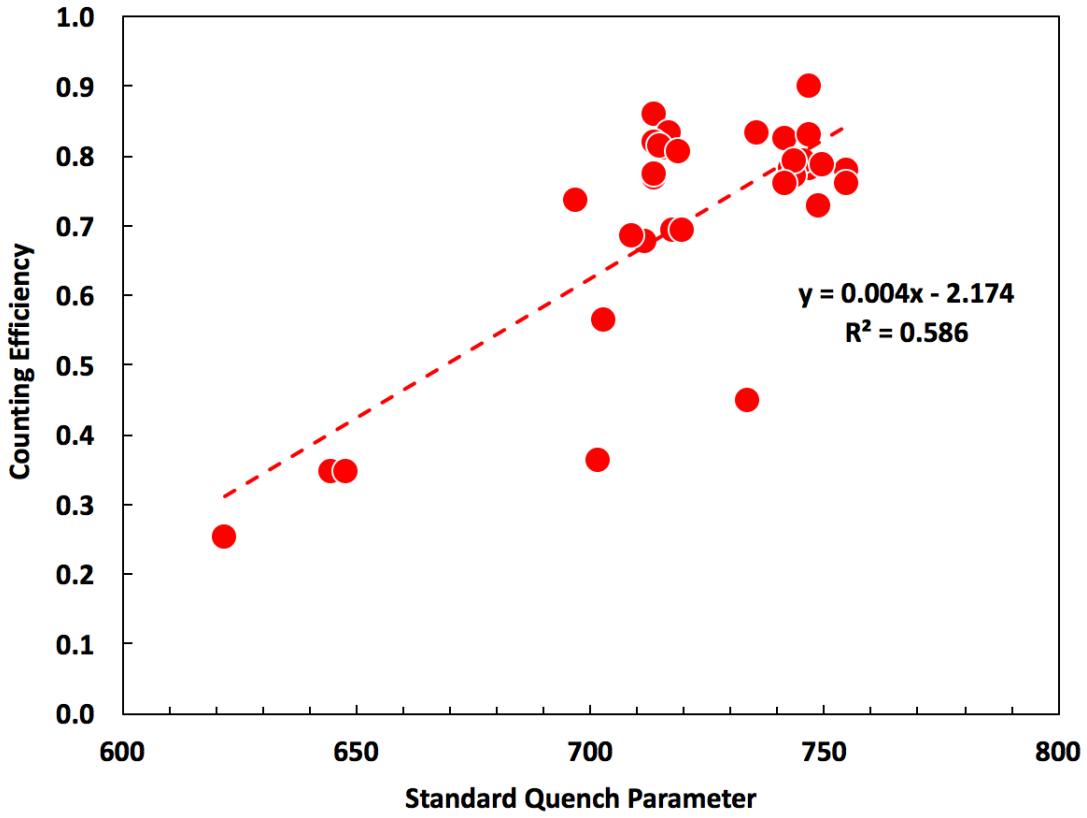

Figure 2.2. Scatter plots of ^{35}S counting efficiencies and measured standard quench parameters for laboratory ^{35}S standards and environmental samples (spiked with ^{35}S standards). All cocktails are prepared in the same volume (5 mL of aqueous solution and 10 mL of scintillation gel). The low coefficient of determination (R^2) indicates that the ^{35}S counting efficiency cannot be accurately calculated by the fitted equation and standard quench parameter.

To investigate the extent to which H_2O_2 bleaching affects the ^{35}S counting efficiency, a series of control experiments were conducted. Because the original cocktail was made by 5 mL of solution and 10 mL of scintillation gel, adding additional H_2O_2 as a bleaching agent would increase the cocktail volume. Although chemical quenching was not observed, we found that the background counting rate increased significantly when the cocktail volume reached or exceeded 17 mL (Table 2.1). In this study, we found that only 1 ml of H_2O_2 could not efficiently bleach our environmental samples, and therefore a higher background counting rate (>1.18 CPM) than the traditional method was inevitable. Using ^{35}S standards (~2.5 DPM), we determined the counting efficiencies for types C and D (Table 2.1) to be 74±6% (n=2) and 69±4% (n=3), respectively, which are lower than the traditional method (type A, 80±5%, n=6). Given the complex chemical matrix in environmental samples, the ^{35}S counting efficiency for environmental samples may be lower than the control experiments. Nevertheless, if a sample significantly affected by color quenching is a precious one and cannot be replicated, this H_2O_2 bleaching method offers a last choice to save the sample and provide relatively accurate analytical results. To further improve the accuracy of ^{35}S measurements in environmental samples, a new method that has a lower background counting rate and a higher ^{35}S counting efficiency than this method is desired.

Table 2.1. Background counting rates (unit: counts per minute, CPM) of scintillation cocktails with varying mixes.

Scintillation Cocktail Mixes					Test #	CPM±σ	Averaged CPM±σ
Type	H_2O	H_2O_2 (30%)	Scintillation Gel	Total Volume			
A	5 mL	0 mL	10 mL	15 mL	1	0.97±0.10	0.97±0.05
					2	0.92±0.05	
					3	1.04±0.11	
					4	0.93±0.11	
B	5 mL	1 mL	10 mL	16 mL	1	1.04±0.19	1.02±0.08
					2	0.99±0.13	
					3	1.04±0.08	
C	5 mL	2 mL	10 mL	17 mL	1	1.11±0.11	1.17±0.07
					2	1.26±0.15	
					3	1.14±0.14	
D	5 mL	3 mL	10 mL	18 mL	1	1.24±0.07	1.21±0.06
					2	1.18±0.09	
					3	1.21±0.14	
E	3 mL	2 mL	10 mL	15 mL	1	0.97±0.11	0.97±0.05
					2	0.91±0.12	
					3	1.03±0.08	
					4	0.99±0.12	

2.4.2 Set 2: New method for preparing scintillation cocktails

With the aim of simplifying the purification procedure and prevent adding H_2O_2 to existing LSC cocktails, we prepared the LSC cocktail using H_2O_2 directly. To test the proposed method, an LSC cocktail containing 3 mL of H_2O, 2 mL of H_2O_2, and 10 mL of scintillation gel (total volume: 15 mL) was prepared (type E in Table 2.1). We found that the background counting rate of this new method is identical to the traditional one (type A in Table 2.1). There are various conventions to estimate the detection limit. In this study, we follow the standard environmental counting statistics method for radiochemistry [*Currie*, 1968; *E.W. Rice*, 2012]. If sample counting rates are close to the background, the detection limit L_D of this new method (defined as the smallest amount of radioactivity that has a 95% probability of being detected) is estimated to be 0.23 DPM (using 4.66σ above the background counting rate [*E.W. Rice*, 2012]), which is also identical to the traditional method. The SQP for the new method (~715) is slightly lower than the traditional method (~745), but as discussed previously (and shown in Figure 2), SQP could not accurately reflect the ^{35}S counting efficiency. We further measured ^{35}S standards with ^{35}S activities ranging from 1 to 30,000 DPM using both methods. For samples with ^{35}S activities less than 3 DPM, the relative standard deviations (RSD) for both methods are less than 20% (Figure 2.3). If the ^{35}S activities are greater than 3 DPM, the RSDs for both methods, especially the newly developed one, are less than 10%. The relationship between RSD and DPM qualitatively follows the expected $1/(N)^{1/2}$ curve, where N represents the number of counts observed in the measurement, though the observed RSD is larger because of the background interference. The ^{35}S activities in most environmental samples in the course of analysis are usually less than 3 DPM. In this range (1-3 DPM), the counting efficiency of our new method (79±4%, n=7) are nearly identical to the traditional method (80±5%, n=6) in this study period. A two-sample *t*-test revealed that the difference between these two methods is statistically insignificant (p=0.71). In addition, we do not see any significant chemical quenching resulting from O_2 in our new method based on the stable counting rate and SQP in the first 40 hours after the cocktail was made (Figure 2.4). *Lin et al.*

[2017d] noted that the counting efficiency of the scintillation cocktail prepared by aqueous sulfate solution started to drop down at ~50 days after the cocktail was made. In this study, we observed a similar trend for the new method and we therefore recommend counting samples as soon as possible after the sample-gel mixture was made. Occasionally (6% of the most recent 500 measurements), the counting rates in the first cycle (2 hours) for both traditional and improved methods (Types A and E) were unusually high, which was identified as an outlier and rejected by the Dixon's Q-Test as mentioned in the experimental section. The reason for the artificially high counting rate may be attributed to chemiluminescence in the LSC cocktail during the formation of a stable gel phase.

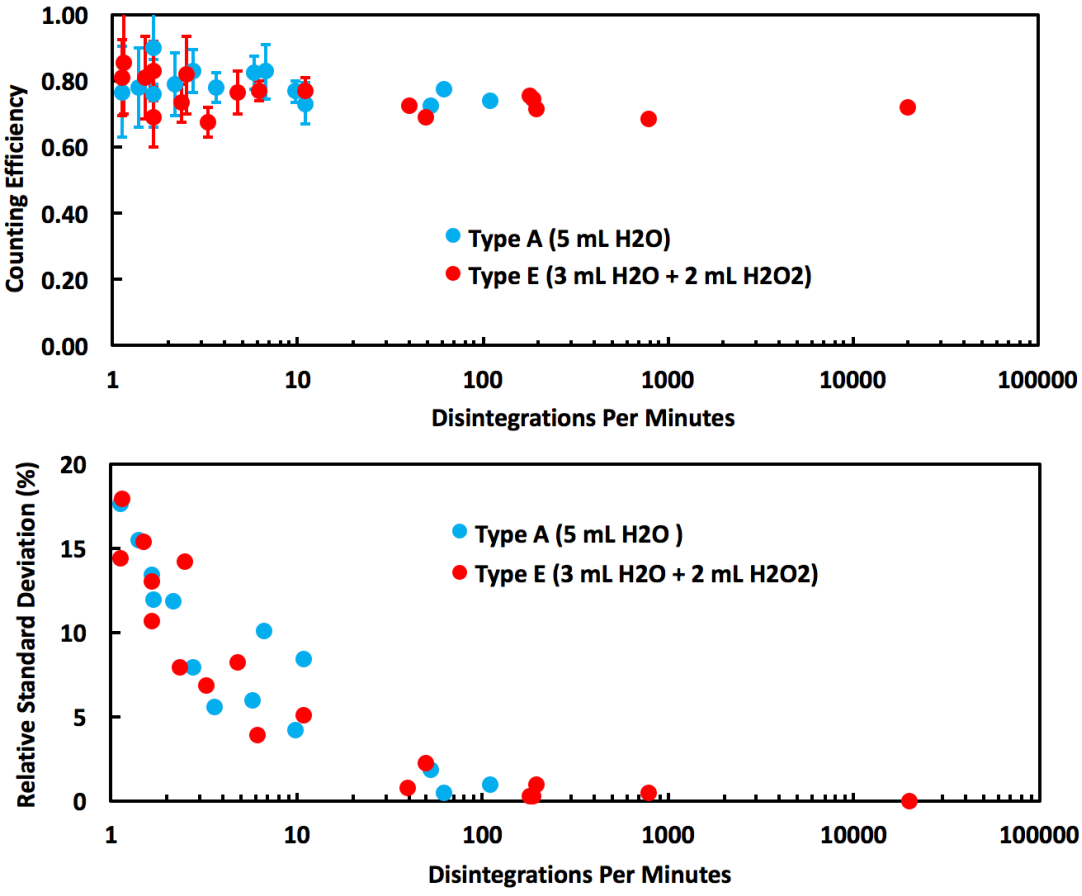

Figure 2.3. Counting efficiency (upper panel) and relative standard deviation (lower panel) as a function of ^{35}S activity.

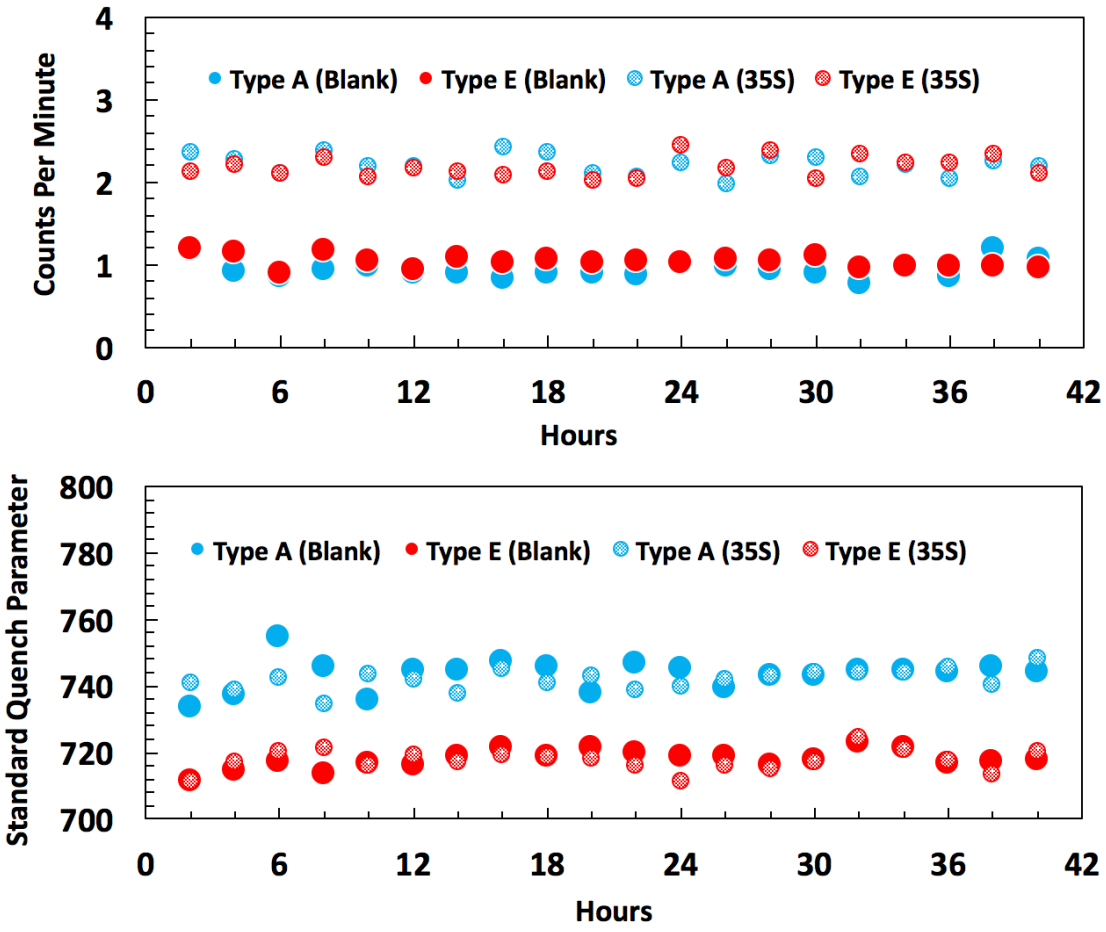

Figure 2.4. Counting efficiency (upper panel) and standard quench parameter (lower panel) for the first 40 hours (20 counting cycles) after the scintillation cocktail was made. Types A and E represent the traditional and new cocktail preparation methods (described in the main text and Table 2.1), respectively.

Ambient aerosol samples free of ^{35}S were used to examine the analytical results of our new method in environmental samples. Soluble sulfates in dissolved environmental samples can be precipitated by adding barium ions, but the produced barium sulfates often contain color quenching agents such as nitrates and organics [*Hou et al.*, 2005; *Peng*, 1960] from the samples [*Xie et al.*, 2016], which may change the chemical matrix of environmental samples. Therefore, we used aerosols that have been stored in a freezer for at least 2.5 years (~10 half-lives) to perform the test. The samples were collected in San Diego as described in the experimental section and the collection

duration time for each sample is 5-6 days. The sampling site is predominately affected by air masses from the polluted marine boundary layer, and therefore the samples are enriched by nitrates and organics and ideal for our test [*Day et al.*, 2010]. The ^{35}S activity in 2/5 of each sample was measured in 2015 while the rest was stored in a freezer. The ^{35}S activity in each of these samples during collection was determined to be less than 10 DPM (Lin et al., manuscript in preparation). Since most ^{35}S atoms (>99.93%) have decayed, the remaining ^{35}S activities are much less than 0.007 DPM through the course of this study and therefore would not influence our experiments. In this study, the sample solution was evenly divided into two aliquots. One aliquot was subject to the traditional chemical processing protocol detailed in the experimental section and prepared as sample-gel mixture using the traditional method (Type A in Table 1). The other aliquot was subject to the same chemical processing protocol, but a 2.0 mL of H_2O_2 was used to re-dissolve the freeze-dried sample and the sample-gel mixture was prepared using the newly developed method (Type E in Table 2.1). The ^{35}S standard (~2.5 DPM) was spiked into the sample when the LSC cocktail was made, and therefore the measured ^{35}S activity directly reflects the ^{35}S counting efficiency instead of any possible loss during the purification process. Figure 2.5 shows that the ^{35}S counting efficiency in the improved method is comparable with, if not slightly higher than, the traditional method.

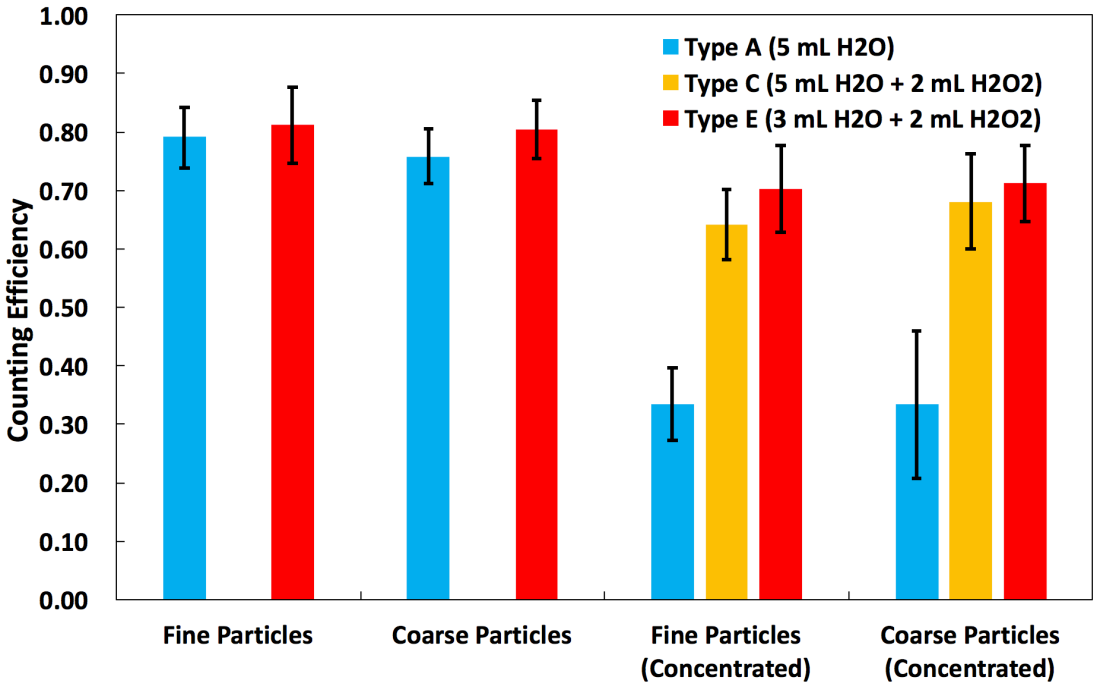

Figure 2.5. Comparison of ^{35}S counting efficiency for atmospheric samples collected at San Diego using various cocktail preparation methods. The use of H_2O_2 for bleaching increases the counting efficiency. "Concentrated" represents samples with concentrated color bleaching agents prepared by combining four samples (see the main text of details). Error bars stand for one standard deviation.

To examine the analytical performance of this new method for samples with concentrated color quenching agents, four samples were combined and subject to the same test. For samples prepared by the traditional method, the cocktails turned dark (even after multiple purification cycles) and the ^{35}S counting efficiencies were ~33%, indicating profound influences of color quenching. An additional 2 mL of H_2O_2 were added to bleach these sample-gel mixtures and the ^{35}S counting efficiencies remained less than 70%. In contrast, samples directly prepared by the new method, the ^{35}S counting efficiencies were greater than 70%. This ^{35}S counting efficiency is at the lower end of the normal range of ^{35}S counting efficiency (70-80%) (Figure 2.3), probably a combined result of inherent-uncertainty of the instrument and color quenching that cannot be visually identified. To determine ^{35}S activities in environmental samples (without spiking ^{35}S standards), the DPM were

corrected from the CPM using a fixed ^{35}S counting efficiency determined from ^{35}S standards. If a ^{35}S counting efficiency of 80% is used, the bias of the new method is determined to be ranging from 0.03 to -0.31 DPM, significantly smaller than the traditional method (ranging from -0.03 to -1.48 DPM).

2.5 Conclusions

In this study, we optimized the LSC method for high-sensitivity determination of ^{35}S. For normal environmental samples, the sample pretreatment time is reduced by several days without changing the accuracy and precision in any noticeable way. For samples significantly affected by color quenching, the new method displays a higher accuracy. In summary, the new method offers a rapid sample pretreatment methodology for high-accuracy quantification of ^{35}S in chemically complex atmospheric samples. Unlike other cosmogenic isotopes (e.g., ^{7}Be, ^{10}Be, ^{14}C, ^{22}Na, and ^{36}Cl), the production rate of ^{35}S in the atmosphere has not been updated for more than 50 years for lack of accurate measurements of atmospheric ^{35}S around the globe [*Poluianov et al.*, 2016]. Recent findings of lightning-produced radioisotopes [*Babich*, 2017; *Enoto et al.*, 2017] make the numerical calculation more complicated and therefore reliable field-based measurements are essential to validate and improve the theoretical calculation. Our new method for high-accuracy determination of ^{35}S provides a novel tool for constraining the ^{35}S production rate in the atmosphere and for developing a three-dimensional global ^{35}S model in the future. Such models are important for understanding atmospheric vertical and horizontal transport, atmospheric chemistry, and the sulfur and oxygen cycles in both modern and paleo-atmosphere on the Earth. In addition, this new method could be readily expanded toward the determination of ^{35}S in water/snow samples with high ^{35}S specific activities (defined as the ratio of ^{35}S activity to stable sulfate concentration) [*Lin et al.*, 2017d]. For samples with low ^{35}S specific activities (e.g. groundwater, seawater, and soils), the use of a different LSC method that converts sulfate to solid $BaSO_4$ is required [*Uriostegui et al.*, 2015]. Our method may has a potential to adapt such analysis though additional tests are required.

Determination of radiosulfur in these non-atmospheric samples would yield new insights into varying natural processes in the hydrosphere, cryosphere, biosphere, and their interaction with the atmosphere.

2.6 Acknowledgements

We thank Dr. Hill-Falkenthal for beneficial scientific discussions at the early stage of this study. Yanhua Fang, Xiemin Huang, Kun Wang, and Dr. Zhisheng Zhang are acknowledged for collecting and providing parts of aerosol and snow samples used in this study. Mang Lin acknowledges a fellowship from Guangzhou Elite Project (JY201303).

This chapter, in full, is a reprint of the material "Accurate quantification of radiosulfur in chemically complex atmospheric samples" as it appears in Analytical Chemistry 2018. Lin, Mang; Thiemens, Mark H., American Chemical Society, 2018. The dissertation author was the primary investigator and author of this paper.

Chapter 3 Simple method for high-sensitivity determination of cosmogenic ^{35}S in snow and water samples collected from remote regions

3.1 Abstract

Cosmogenic ^{35}S is useful in understanding a wide variety of chemical and physical processes in the atmosphere, the hydrosphere and the cryosphere. The 87.4-day half-life and the ubiquity of sulfur in natural environments renders it an ideal tracer of many phenomena. Measurements of ^{35}S in snow and water samples are scarce as existing analytical methods require a large volume of sample (>20 L) due to their high analytical activity background and low counting efficiency. Here, we present a new set of snow/water sample collecting and handling procedures for high-sensitivity determination of cosmogenic ^{35}S using a low-level liquid scintillation spectrometer. Laboratory experiments using diluted ^{35}S standards (with activities of <5 disintegrations per minute) showed a ^{35}S recovery percentage of ~95%, demonstrating a relatively small deviation from the true value. Using this method, we successfully measured ^{35}S in ~1 L of fresh snow sample collected from a glacier on the Tibetan Plateau to be 47±7 mBq/L. Based on ^{35}S activities in 9 natural samples measured in this study, a first proof-of-concept approximation for age determinations and source attributions was presented. This new method will provide a powerful tool in studying ^{35}S in small volumes of snow and water samples, especially those from remote but climatically important regions such as the polar regions and the Tibetan Plateau and Himalayas. The measurements are particularly important as the radioactive sulfur provides an actual clock of glacial melting processes. With the growing rate of glacial loss, the need for measurements from remote locations becomes all the more important.

3.2 Introduction

As a ubiquitous element in the environment, sulfur has multiple valence states (from S^{2-} to S^{6+}) and hence participates in a wide variety of biogeochemical processes. Cosmogenic ^{35}S is a radioactive isotope (half-life = ~87.4 days) naturally produced by the bombardment of ^{40}Ar in the atmosphere by high energy cosmic rays [*Goel*, 1956]. The physical and chemical properties of ^{35}S are nearly identical to stable sulfur [*Tanaka and Turekian*, 1991]. After production, cosmogenic ^{35}S becomes $^{35}SO_2$ in ~1 second, and is further oxidized to $^{35}SO_4^{2-}$ before wet and dry deposition [*Black et al.*, 1982; *Junkermann and Roedel*, 1983; *Tanaka and Turekian*, 1991]. Similar to stable SO_4^{2-}, radioactive $^{35}SO_4^{2-}$ can actively incorporate into various physical, chemical and even biological processes in the atmosphere, the hydrosphere and the cryosphere. The suitable half-life and the unique production pathway of ^{35}S provide chronology and source information additional to and independent of other isotopes such as ^{35}Cl. However, measurements of ^{35}S in natural samples are challenging because of its low-energy decay (E_{Max} = 167 keV). As pioneers of atmospheric ^{35}S studies, *Tanaka and Turekian* [1991] first measured ^{35}S in gaseous SO_2, aerosol SO_4^{2-} and precipitation using an internal gas proportional counting technique. In a later study, they developed a method to convert atmospheric sulfur to barium sulfate ($BaSO_4$) and measure ^{35}S using a low-level liquid scintillation counting technique [*Tanaka and Turekian*, 1995]. These pilot studies provided a new tool to quantify the removal and oxidation rates of atmospheric sulfur [*Tanaka and Turekian*, 1991; 1995; *Turekian and Tanaka*, 1992]. This analytical method has been further developed[*Hong and Kim*, 2005; *Uriostegui et al.*, 2015] and utilized in hydrologic studies to quantify the sources and ages of meltwater runoff [*Cecil et al.*, 1998; *Cooper et al.*, 1991; *Michel et al.*, 2000], groundwater [*Clark et al.*, 2016; *Plummer et al.*, 2001; *Uriostegui et al.*, 2016; *Urióstegui et al.*, 2016], and surface water in watersheds [*Kester et al.*, 2003].

However, the limitation of counting solid $BaSO_4$ is the low counting efficiency (~20-60%) and high background activity (~1-5 counts per minute, cpm) [*Hong and Kim*, 2005; *Tanaka and Turekian*, 1995; *Uriostegui et al.*, 2015], and therefore a large volume of samples (>20 L) is

required. Such large volumes of water are difficult to obtain in the field, especially in the remote but climatically important region such as the polar regions and the Tibetean Plateau and Himalayas. For example, the Tibetean Plateau and Himalayas region, which is also widely known as the third pole because it contains the largest ice store outside the polar regions, provides fresh water supply to nearly 40% of the world's populution [*Immerzeel et al.*, 2010; *Xu et al.*, 2008]. The glacier retreat and snow melting in this region play an crucial role in the hydrological cycle in Asia but are not well understood because the harsh environment restricts comprehensive field-based measurements. Therefore, a high-sensitive analytical method for measuring ^{35}S in small volumes of water sample is required to assist in such quantification.

Recently, *Brothers et al.* [2010] modified the sample preparation method for the low-level liquid scintillation counting technique and suggested to convert sulfur samples to aqueous Na_2SO_4/H_2SO_4. It was shown that counting aqueous Na_2SO_4/H_2SO_4 generated a high counting efficiency (up to ~95%) and a low background activity (~0.9 counts per minute, cpm). This optimizition made ^{35}S measurements in small sizes of samples possible. Even though this method has led to a growing number of ^{35}S measurements in aerosol samples, which provide new insights into the vertical and horizontal transport processes in the atmosphere [*Lin et al.*, 2016a; *Lin et al.*, 2016c; *Priyadarshi et al.*, 2011a; *Priyadarshi et al.*, 2011b; *Priyadarshi et al.*, 2012b], the utility of ^{35}S in hydrologic studies remains limited, mainly due to a lack of sample collection and preparation method for natural water. Although our previous studies successfully measured ^{35}S in small volumes (~3 L) of glacier snow and runoff samples collected from the Tibetan Plateau and Himalayas using ion exchange resins,[*Lin et al.*, 2016b; *Priyadarshi et al.*, 2014] the reliability of the sample handling method was not unambigously demonstrated and reported in detail, which resulted in uncertainties in data interpretation and restricted further comprehensive studies. In this study, a series of control experiments were conducted to evaluate the accuracy of previous measurements [*Lin et al.*, 2016b; *Priyadarshi et al.*, 2014] and develop a new, simple and

economical method for collections of snow, ice and meltwater samples and the highly sensitive and accurate analysis of comosgenic ^{35}S activity. The ^{35}S activities in natural samples collected from a glacier on the Tibetan Plateau were determined using our newly developed method.

3.3 Experimental Sections

3.3.1 Ultra-Low-Level Liquid Scintillation Spectrometer and Counting Efficiency

In this study, an ultra-low-level liquid scintillation spectrometer (Quantulus 1220, PerkinElmer) was used to quantify cosmogenic ^{35}S activity. The setting of two software selectable parameters (the Pulse Shape Analyzer and the Pulse Amplitude Comparator) on the Quantulus 1220 followed the default setting for ^{14}C because of the significant overlap between the energy spectra of the β^- decay of ^{35}S (E_{Max} = 167 keV) and ^{14}C (E_{Max} = 156 keV) [*Brothers et al.*, 2010; *Tanaka and Turekian*, 1995]. The ^{35}S counting window was set as channel 1-450 to minimize the possible influence of ^{14}C (with peak at channel ~485). Each sample was counted for 12 times (2-h counting for each cycle) and the average was reported. Potential outliers, if any, were identified by the Dixon's Q-Test (99% confidence level) and rejected. In all measurements made in this study, no outlier was identified. Using the propagation-of-error method of the standard environmental counting statistics [*E.W. Rice*, 2012], the net counting error (95% confidence level) can be calculated as follows:

$$error = 1.96 \times \sqrt{\left(\frac{S}{t_S} + \frac{B}{t_B}\right)}$$

where S and B represent sample and background counting rates, respectively, and t_S and t_B represent elapsed counting times at which sample and background counting rates were measured, respectively. In this study, the long elapsed counting time (24-h = 2-h × 12) yields a small error (e.g., 0.09 cpm for a sample with a counting rate of 2.0 cpm). Given the standard environmental counting statistics also recommends to divide the total counting time into several equal cycles to

check variability of counting rates [*E.W. Rice*, 2012], we carefully checked results for 12 counting cycles (see examples in Figure 3.1) and found that the standard variation of 12 counting rates (e.g., 0.16 cpm for a sample with an average counting rate of 2.0 cpm) was greater than the net counting error estimated previously. Therefore, the larger error (i.e., one standard deviation for 12 counting cycles) was reported in this study. This error was further propagated in subsequent arithmetic calculations (e.g. corrections for the background activity and the decay time) [*E.W. Rice*, 2012; *Skoog et al.*, 2007].

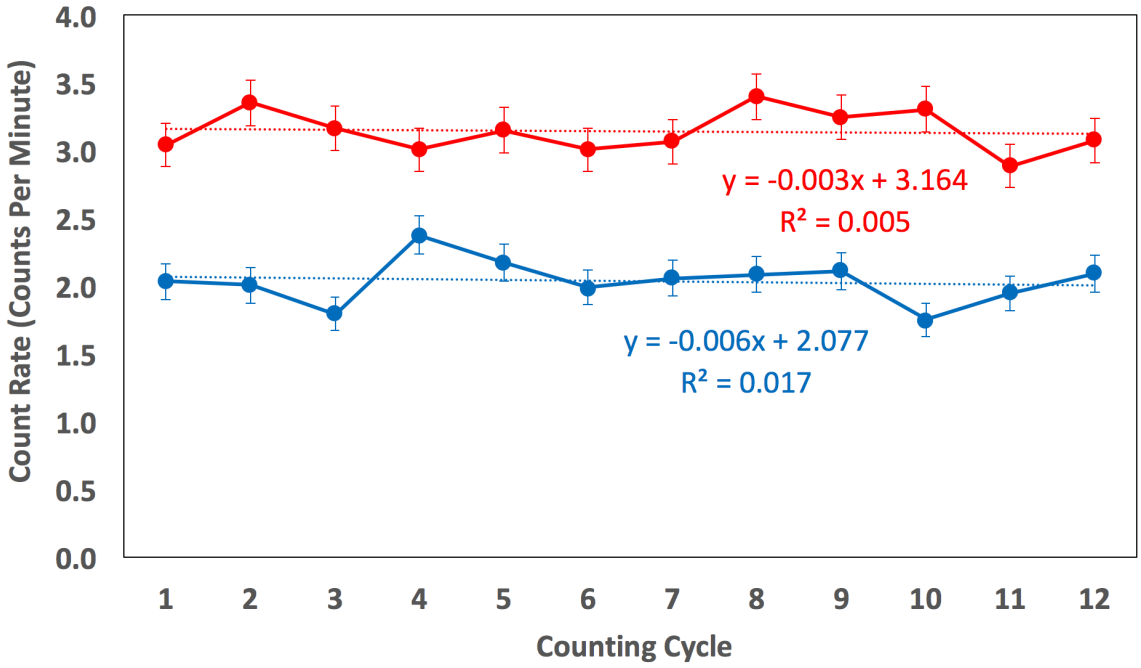

Figure 3.1. Count rates for 12 counting cycles for a ^{35}S standard (set 2 experiment; red) and a natural sample (fresh snow; blue). The error bar represents counting error for each cycle. The regression equations and regression coefficients (R^2) are shown.

Standard or sample was prepared in aqueous form (Na_2SO_4/H_2SO_4) instead of solid form ($BaSO_4$) to eliminate the potential contamination of other radionuclides (e.g. ^{133}Ba, ^{226}Ra, ^{228}Ra and their daughter products) in $BaCl_2$ reagents [*Brothers et al.*, 2010; *Uriostegui et al.*, 2015]. The pure

Na_2SO_4/H_2SO_4 solution was quantitatively transfer to a 20-mL plastic scintillation vial (Fisherbrand) and mixed with 10 mL of scintillation gel (Insta-Gel Plus, PerkinElmer). Plastic scintillation vials had a lower background activity (~0.15 cpm) than traditional glass vials which contain ^{40}K (~0.45 cpm) [*Brothers et al.*, 2010]. The mixed cocktail was shaken and vibrated vigorously prior to loading into the ultra-low-level liquid scintillation spectrometer.

The background and counting efficiency for various volumes of Na_2SO_4/H_2SO_4 samples are summarized in Table 3.1. Similar to our previous study [*Brothers et al.*, 2010], the counting efficiency of this method was greater than 90% if 1 mL of aqueous solution was used. However, such small volume of solution was potentially problematic in natural sample analysis because as little as ~0.1 M of SO_4^{2-} can impede the formation of a stable microemulsion and cause phase instability due to the divalent charge and relative size of divalent anions [*PerkinElmer*, 2014; *Uriostegui et al.*, 2015]. In addition, if the aqueous solution was not completely clean, trace amount of organics from natural samples may also lead to color quench problems in such a small volume of solution [*PerkinElmer*, 2014]. Table 3.1 shows that the counting efficiency dropped down to 79.0±0.4% when 2 mL of aqueous solution were used, but the further losses of counting efficiency due to using larger sample volume (5 mL) were marginal. Therefore, we diluted the solution to a larger volume (5 mL) to eliminate the potential problems of phase instability and color quench. It should be noted that the sample should be counted as soon as possible after the sample-gel mixture was made, because we found that the counting efficiency for 5 mL of aqueous solution dropped down to <70% at ~100 days after the first measurement (Figure 3.2a). The decreasing counting efficiency was likely derived from the phase of sample-gel mixture (microemulsion) becoming unstable during a long-term storage.

Table 3.1. Comparison of counting efficiencies using various sample-gel mixtures in our method and results from previous methods for natural water ^{35}S measurements

Instrument	Types of Sample and Scintillation Vial	Background (cpm)	Efficiency (%)	Reference
Quantulus 1220	1 mL of SO_4^{2-} solution in a plastic vial	0.9±0.1	91.0±0.8	This study
	2 mL of SO_4^{2-} solution in a plastic vial	1.0±0.1	79.0±0.4	This study
	5 mL of SO_4^{2-} solution in a plastic vial	0.9±0.1	77.5±0.4	This study
Quantulus 1220	$BaSO_4$ in a plastic vial	0.8	53.0±0.1	[Uriostegui et al., 2015]
	$BaSO_4$ in a glass vial	1.3	56.5±0.1	[Uriostegui et al., 2015]
TriCarb 3100	$BaSO_4$ in a plastic vial	1.6	57.0±0.1	[Uriostegui et al., 2015]
	$BaSO_4$ in a glass vial	1.6	60.3±0.2	[Uriostegui et al., 2015]
TriCarb 3170	$BaSO_4$ in a plastic vial	1.9	25.2±1.2	[Hong et al., 2005]
	$BaSO_4$ in a glass vial	2.2	21.9±1.2	[Hong et al., 2005]
TriCarb 1050	$BaSO_4$ [a]	2.4±0.1	37.0	[Tanaka and Turekian, 1995]

a. The material of scintillation vial was not mentioned in the literature.

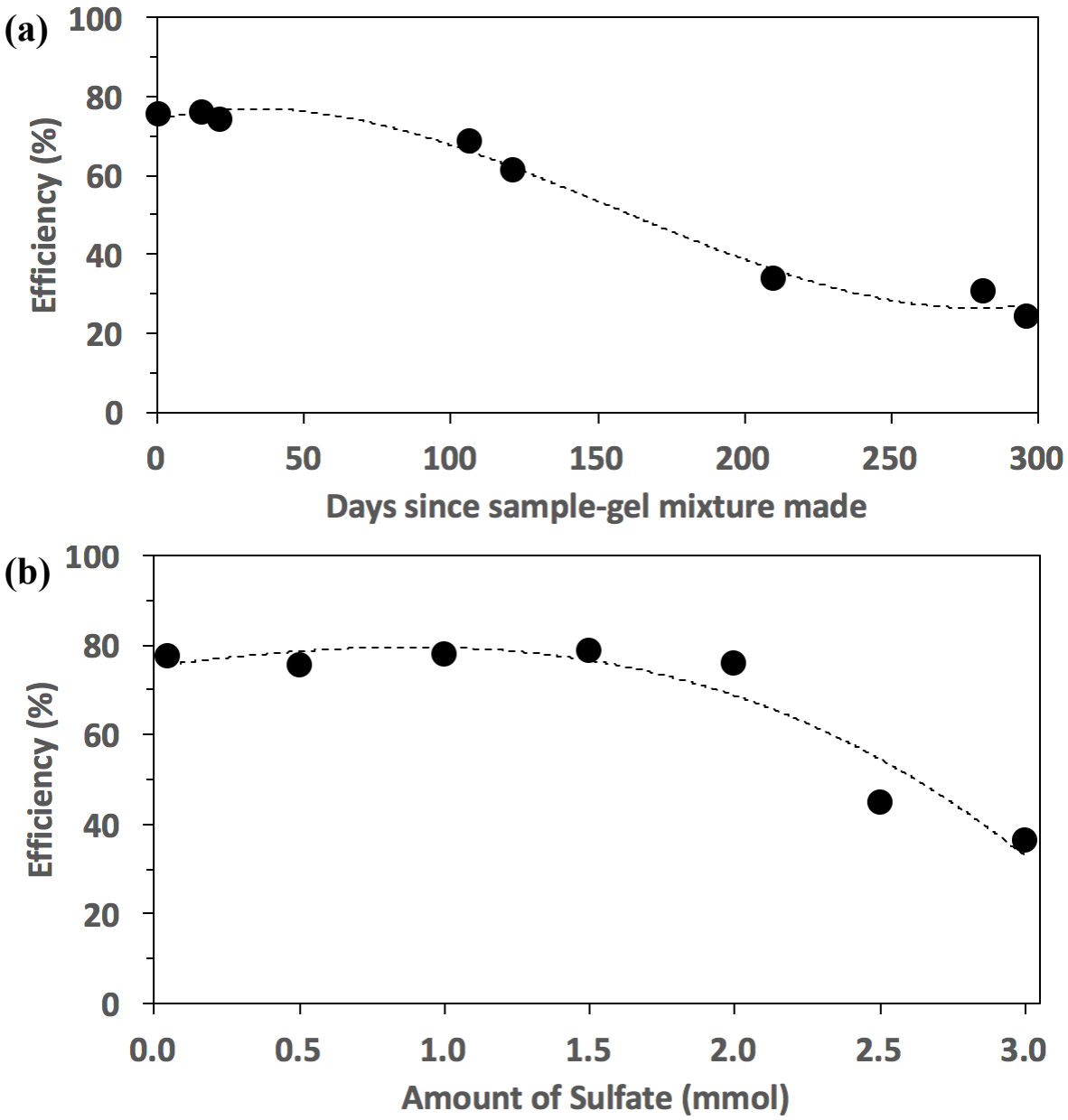

Figure 3.2. Counting efficiency for ^{35}S as a function of (a) days since sample-gel mixture made and (b) sulfate amount. The error bar is smaller than the symbol used. The dashed lines represent the fitted third-order polynomial curves.

To prevent any possible phase separation and color quench during counting, each sample-gel mixture was inspected visually after counting. Quantitatively, the constancy of 12 counting cycles was checked and we did not find any drop in counting rates during 12 counting cycles for all measurements made in this study (see examples in Figure 3.1). In addition, the standard quench parameter (SQP) reported by the Quantulus 1220, a parameter analogous to the transform Spectral Index of the External Standard on the Tri-Carb family (different low-level liquid scintillation counters used in other studies [*Hong and Kim*, 2005]), can quantify levels of quenching [*Uriostegui et al.*, 2015]. The stability of the phase of sample-gel mixture (and counting efficiency) in 12 counting cycles for counting 5 mL of aqueous solution was further supported by constant SQP values (748±2).

In this study, the counting efficiency (77.5±0.4%) determined from 5 mL of aqueous solution was significantly greater than previous methods using $BaSO_4$ for measuring ^{35}S in natural water sample (Table 3.1), indicating a higher sensitivity in ^{35}S measurements. Brothers et al.[*Brothers et al.*, 2010] suggested that the minimum detectable activity (MDA) of this method is 0.2 disintegrations per minute (dpm) (2σ above the background counting rate). In this study, we estimate the MDA to be 0.4 dpm using 4.66σ above the background counting rate [*E.W. Rice*, 2012]. It is noted that our study focused on snow, melted water and rainwater samples, which possess relatively high ^{35}S specific activities (SA, defined as ^{35}S activity over total sulfate amount) due to a large contribution of atmospheric sulfate and a relatively small fraction of non-radioactive crustal sulfate. Figure 3.2b shows that phase separation occurred (at 17°C, the temperature in the measuring chamber) and counting efficiency dropped down significantly if >2 mmol of sulfate was added to cocktail. Based on the fitted polynomial curve (Figure 3.2b), an upper limit of 1.5 mmol of sulfate is recommended for this method. If the analytical goal is to measure samples with low ^{35}S SA, e.g. groundwater and seawater, converting sulfate to $BaSO_4$ is required and a method recently developed by *Uriostegui et al.* [2015], is recommended.

3.3.2 Standard Preparation.

The ^{35}S activities in environmental samples, which depend on the sample size and storage time, are usually less than 5 dpm. A $H_2{}^{35}SO_4$ standard (PerkinElmer), which was stored separately in a locker at the Radiation Division of the Environment, Health and Safety Department (EH&S) at the University of California San Diego (UCSD), was diluted to laboratory sub-standards with comparable activities (< 5 dpm) in the EH&S. These sub-standards were used to develop the sample extraction and purification method for ^{35}S analysis in a sensitive, accurate and economical way. To prevent any possible cross-contamination in experiments, these sub-standards were stored in a different laboratory (instead of our wet chemistry laboratory).

3.3.3 Concentrating SO_4^{2-} in the Field Using Anion Exchange Resins

Previous methods using Amberlite IRA 400 anion exchange resins for large volumes of samples (>20 L) require the acidification of samples using concentrated hydrochloric acid (HCl) and the exchange efficiency enhancement using a pump or an industrial spinner [*Hong and Kim*, 2005; *Uriostegui et al.*, 2015]. Such complicated concentration processes are conventionally performed in the laboratory. In this study, because the aqueous Na_2SO_4/H_2SO_4 method has a lower background activity and higher counting efficiency (Table 3.1), only ~3 L of water is required. We utilized a Bio-Rad AG1-X8 anion exchange resin (analytical grade, 100-200 mesh, chloride form) to concentration sulfate, which adsorption efficiency and recovery percentage for anions in fresh water samples is greater than 98% [*Silva et al.*, 2000]. In this study, the focus is on the recovery percentage of ^{35}S. This concentration method is relatively simple and straight forward and easily done in the field. It eliminates transporting large volumes of water (~3 L per sample) from the field to the laboratory. This method is especially convenient and economical for collecting samples from remote regions. Before using, the resin (3-4 mL) was filled into a plastic column (Bio-Rad; i.d. 0.8 cm, length 4 cm) and rinsed by 5 mL deionized (DI) water (18 MΩ·cm) for three times. Sulfate was collected by gravity dripping samples (or laboratory sub-standards with known ^{35}S activities)

through the resin column. The exchange capacity of the AG1-X8 anion exchange resin is 1.2 meq/mL, and therefore 3-4 mL of resin can handle most snow and melted water samples.

3.3.4 Elution of SO_4^{2-} from Anion Exchange Resins

Sulfate trapped in resins was eluted by gravity dripping 15 mL of 1 M hydrobromic acid (HBr) through the column in 5 mL increments. To quantitatively collect all samples trapped in resins, 15 mL of DI water was dripped through the column in 5 mL increments and collected after elution with HBr. Positive air pressure was applied to inject residual eluent/water using a clean 60-mL syringe. The 30 mL of eluent containing SO_4^{2-}, NO_3^-, Cl^- and Br^- was collected by a 50-mL plastic centrifuge tube. After stripping, excess Br^-/Cl^- (~15 mmol) must be removed because such high concentrations of ions cannot be handled by the scintillation gel.

3.3.5 Purification Using Ag_2O and Preparation of Aqueous SO_4^2 for Counting

Two sets of experiments were performed to remove excess Br^-/Cl^- ions in two different ways. In this set of experiments (set 1), excess Br^-/Cl^- were precipitated as AgBr/AgCl by slowly adding Ag_2O (~2 grams) in successive increments of ~0.4 grams. The pH of the solution was tested by pH paper to ensure that Br^-/Cl^- completed precipitation and the solution turned neutral (pH≈7). The AgBr/AgCl slurry was removed by a disposable vacuum-driven filtration system (with 0.22 um Millipore Express Plus Membrane, Steriflip, Millipore) and the filtrate was collected by another clean 50-mL centrifuge tube. An additional ~10 mL of DI water was used to wash any trace amount of sample left in the original 50-mL centrifuge tube and the filter membrane into the new 50-mL centrifuge tube in successive increments of ~5 mL, bringing the sample volume to ~40 mL. This large volume of solution must be concentrated for further processing. It is noted that H_2SO_4 reacts with Ag_2O to form Ag_2SO_4,[*Savarino et al.*, 2001] which is minimally soluble in water (0.83 g / 100 mL at 25°C). To minimize the possible losses of ^{35}S during handling small volume (~1 mL) of sample, 5 mL of 1000 ppm Na_2SO_4 solution containing no ^{35}S was added to the solution. The solution was evaporated and dried in a clean oven (80°C) overnight. After drying, the sample was

re-dissolved by adding 2 mL of DI water to the 50-mL centrifuge tube and was subjected to sonication for 1 hour.

The subsequent cleaning procedure followed the protocol developed by *Brothers et al.* [2010]: the 2 mL of solution was passed through a polyvinylpyrrolidone (PVP) column and a Ag-cartridge (Dionex OnGuard II) to remove organics and any remaining Cl^- (or Br^-), respectively, and was collected by a 15-mL centrifuge tube. An additional ~8 mL of DI water was used to wash trace amount of sample left in the 50-mL centrifuge tube, the PVP column and the Ag-cartridge into the 15-mL centrifuge tube in successive increments of ~2 mL. The 15-mL centrifuge tube containing ~10 mL solution was put in a freeze-dryer overnight. After freeze-drying, the sulfate sample (white crystalline solid) was re-dissolved again by added 1 mL of DI water and was sonicated for 1 hour. If any remaining dirty residue was observed in this step, ~2 mL of hydrogen peroxide (H_2O_2) was added to remove organics and PVP-cleaning and freeze-drying should be repeated. Following this cleaning procedure, the sample was ready to transfer to a plastic scintillation vial for preparing the sample-gel mixture. To quantitatively transfer, the "empty" 15-mL centrifuge tube was washed with 1 mL DI water and transferred into the scintillation vial and this procedure was repeated for four times. The sample-gel mixture was prepared and sent to the Quantulus 1220 following the procedure described in the previous section (*Ultra-Low-Level Liquid Scintillation Spectrometer and Counting Efficiency*).

Our results show that the recovery percentage of ^{35}S was ~90% in this set of experiments (Table 3.2). It is noted that the sulfur carrier (Na_2SO_4) is important because without adding Na_2SO_4 the recovery percentage was less than 50% (i.e., the measured ^{35}S was more than -50% deviation from the true value) (set 0) (Table 3.2). Since our previous pilot study [*Priyadarshi et al.*, 2014] did not notice the importance of the sulfur carrier, the measured ^{35}S activities (without the sulfur carrier during processing) may be underestimated. Another concern is the cost of Ag_2O (Fisher Scientific, current price: ~900 US$ for 100 grams). Previous studies used 15 mL of 3 M HCl as

eluent to strip NO_3^- and SO_4^{2-} samples from AG1-X8 resins, which required ~6.5 grams of Ag_2O (~60 US$) to remove excess Cl^- for each sample [*Silva et al.*, 2000]. Even though 15 mL of 1 M HBr was used as the eluent in this study, which can significantly cut down the required amount of Ag_2O without reducing the recovery percentage of anion because the relative selectivity of Br^- for AG1-X8 resin is more than 2 times greater than Cl^- (AG1, AG MP-1 and AG2 Strong Anion Exchange Resin Instruction Manual: http://www.bio-rad.com/webroot/web/pdf/lsr/literature/9114_AG_1.pdf), the cost for each sample remained high (~18 US$). Therefore, we developed another set of experiments to remove Br^-/Cl^- without using Ag_2O.

Table 3.2. Recovery percentages of ^{35}S in various experiments with different procedures

Experiment	Resin Adsorption and Elution	Method for Removing Br^-/Cl^-	Addition of 1000 ppm Na_2SO_4 (mL)	Evaporation at 80°C	Pass through PVP + Ag-Cartridge and Freeze-Dry	^{35}S Recovery Percentage (%)
Set 0	✓	Ag_2O	0	Oven	✓	42
Set 0 (duplicated)	✓	Ag_2O	0	Oven	✓	44
Set 1	✓	Ag_2O	1	Oven	✓	60
Set 1	✓	Ag_2O	5	Oven	✓	88
Set 1 (duplicated)	✓	Ag_2O	5	Oven	✓	91
Set 2	✓	H_2O_2	5	Hood[a]	✓	95
Set 2 (duplicated)	✓	H_2O_2	5	Hood	✓	95
Control	✗	n.a.[b]	5	Oven	✓	94
Control (duplicated)	✗	n.a.	5	Oven	✓	100
Control (triplicated)	✗	n.a.	5	Oven	✓	99

a. Heating tape was used for heating; b. “n.a.” stands for “not applicable”

3.3.6 Improved Purification Method Using H_2O_2

In this set of experiments (set 2), 5 mL of 30% H_2O_2 was added to eluent to oxidize HBr/HCl to Br_2/Cl_2. The color of solution immediately changing from colorless to yellow characterizes the formation of Br_2. The H_2O_2 can also help to remove organics in the solution. Following adding H_2O_2, 5 mL of 1000 ppm Na_2SO_4 containing no ^{35}S was added to the sample. Although H_2SO_4 is a nonvolatile acid (boiling point: ~330°C; vapor pressure: <0.0001 kPa at 20°C), the sulfur carrier can further minimize the possible losses of H_2SO_4 during processing and transferring sample. After completely mixing, the 50-mL centrifuge tube containing sample was wrapped by a heating tape and heated at 80°C in a clean fume hood overnight. Because Br_2 can catalyze the decomposition of H_2O_2, when ~5-10 mL of solution was left, at least 5 mL of 30% H_2O_2 was added to ensure that most Br^-/Cl^- was removed. This H_2O_2 oxidation procedure should be repeated until no dirty residue can be found in the centrifuge tube. After drying, the Na_2SO_4/H_2SO_4 was re-dissolved by adding 2 mL of DI water and the following procedure was followed exactly as described in set 1. The results showed that the recovery percentage of this method was 95% (Table 3.2), slightly higher than set 1 (purification using Ag_2O), indicating a higher accuracy in measurements.

We suspected that the higher recovery percentage was because of the elimination of AgBr/AgCl precipitation and filtration procedures. Ag_2SO_4 produced from the $Ag_2O+H_2SO_4$ reaction may be easy to lose during filtrating AgBr/AgCl slurry. To test this hypothesis, a control experiment was performed, in which we added 5 mL of 1000 ppm Na_2SO_4 in $H_2{}^{35}SO_4$ sub-standards and put it in a clean oven as what we did in set 1 of experiments. The following procedure was followed exactly as described in set 1. The recovery percentage of ^{35}S in these control experiments were 94-100% (Table 3.2), higher than set 1 in which AgBr/AgCl slurry was present. The recovery percentage in set 2 of experiments was comparable to these values, supporting that the improved accuracy in set 2 of experiments was likely because of the elimination of AgBr/AgCl slurry. This

improved method was benefited from the use of 1M HBr as eluent because the oxidation of HBr by H_2O_2 is more effective than the $HCl+H_2O_2$ reaction due to a lower standard reduction potential of $Br_2(l)/Br^-$ (+1.066 V) than for $Cl_2(g)/Cl^-$ (+1.36 V).

The SQP values (732±3) for set 2 of experiments were slightly smaller than 748±2 (^{35}S standards without any chemical processing), which might indicate slight decreases of counting efficiency related to wet chemical processing and explain the non-100% recovery percentage in this set of experiments. The non-100% recovery percentage can be also explained by the sample losses incurred from several cleaning procedures, which was inevitable.

3.3.7 Natural Sample Collection and Analysis

To test our new method, natural samples (fresh snow, snowpit, firn, ice and river runoff) were collected at a glacier [Laohugou Glacier No.12; 39°05'-40'N, 96°07'-97°04'E; 4260–5481 m a.s.l. (above sea level)] on the northeastern Tibetan Plateau at the end of August 2015. A snowpit (120 cm) was dug in the accumulation zone of the glacier (5050 m a.s.l.) and three samples with a vertical resolution of 40 cm were collected. Two fresh snow samples which deposited on the glacier less than 1 day were collected at 4800 and 4400 m a.s.l. Surface (depth: ~5 cm) firn and ice samples were also collected at 4900 and 4800 m a.s.l., respectively. All snow, firn and ice samples were stored in 5-L Whirl-Pak bags and melted at room temperature. Two river runoff samples were collected at the glacier terminal (4200 m a.s.l.) and stored in pre-cleaned polycarbonate bottles (Nalgene). If water samples appeared to be murky, insoluble particles in samples were removed using quartz microfiber filters (Whatman, 2.2 μm). A small aliquot of solution (~20 mL) was taken and stored in a small pre-cleaned polycarbonate bottle (Nalgene) for ion analysis, and the rest was gravity dripped through the anion exchange resins prepared at UCSD. Ion analysis was performed in the State Key Laboratory of Cryosphere Sciences, Chinese Academy of Sciences using an ion chromatography (Dionex ICS-2500). Anion exchange resins were sent to UCSD for ^{35}S analysis following the new methodology developed in this study. The raw ^{35}S counting data were corrected

for the background activity and the decay time. It is noted that after elution only an aliquot of sample (ranging from 40% to 90%) was used for ^{35}S measurements while the rest was stored in a freezer for other studies (stable isotope measurements in sulfate and nitrate). The overall procedures for sampling, preparation and analysis are summarized in Figure 3.3.

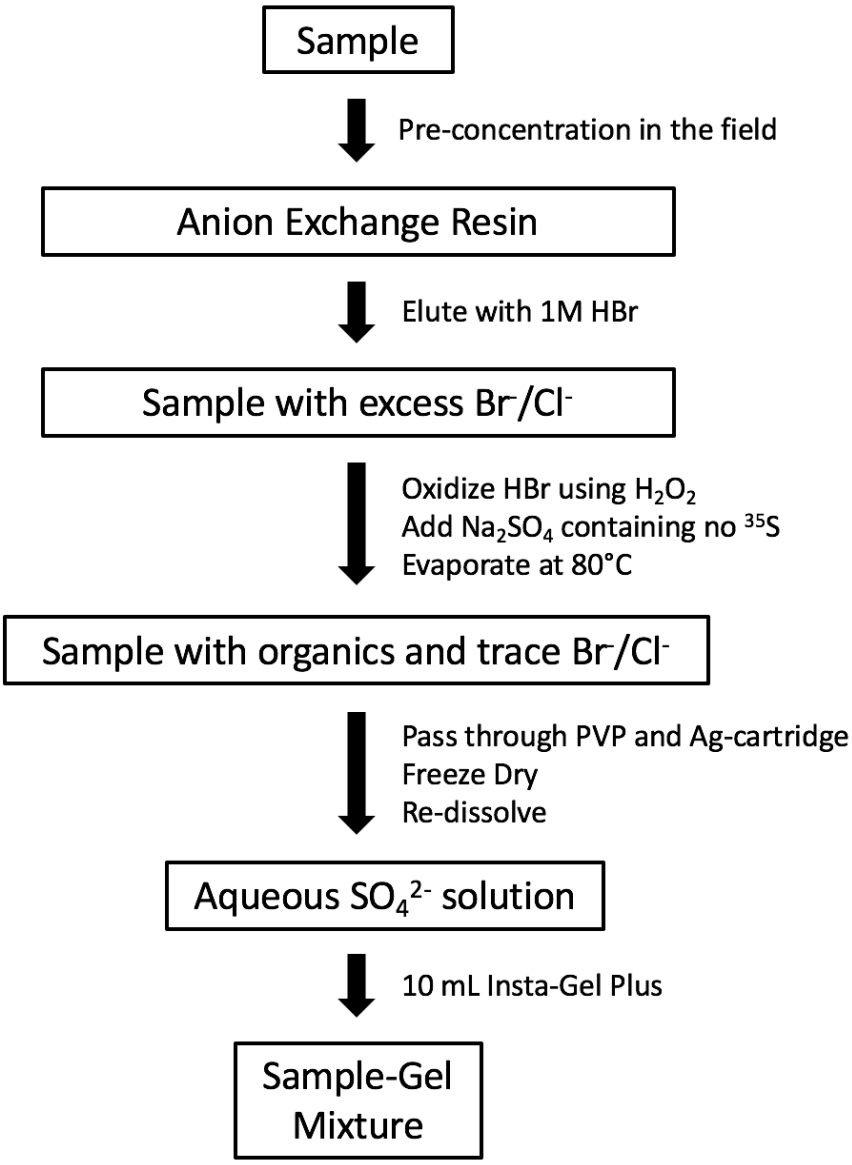

Figure 3.3. Schematic illustration of collecting and handling snow/water samples for ^{35}S measurements

3.4 Results and discussions

The ^{35}S activities in natural samples measured by the new analytical method developed in this study are summarized in Table 3.3. The new method effectively measured most snow and water samples in small volumes (1.1-3.2 L). Even though the volumes of samples are ~1/10 of that required by conventional methods, the errors in our measurements are only slightly larger than, if not comparable with, previous studies (usually <3 mBq/L). Since our samples were counted 4-5 months after collection (i.e., 62-70% of ^{35}S atoms decayed), if samples may be shipped and measured earlier, the error would be significantly lower. In addition, the anion exchange resins used in this study can handle at least 3.6 meq of anions, and the highest concentrations of anion (sulfate and nitrate only) in samples collected at Laohugou Glacier No.2 was only 0.06 μeq/L (river samples). If possible, collecting larger volumes of samples can also improve the measurement precision.

To provide proper context to relate our ^{35}S measurements to age determinations and source attributions of snow and water, we presented a first proof-of-concept approximation as followed. As expected, the highest ^{35}S activity was found in fresh snow samples. The near-zero (but generally above the background counting rate) ^{35}S activities in snowpit samples suggested that the snow had been accumulated over months and ^{35}S atoms depleted due to snow melting [*Johannessen and Henriksen*, 1978] and radioactive decay. Both ^{35}S activities and sulfate concentrations in fresh snows were highly variable, suggesting the current estimation may possess large uncertainties because of lack of long-term ^{35}S data in fresh snow. If we simply assume the lower limit of ^{35}S activity in fresh snow as 23 (=29-6) mBq/L (Table 3.3) and the ^{35}S activities in snowpit samples were only affected by radioactive decay, the average ages of two snowpit samples at upper layers (0-40, 40-80 cm) can be estimated to be as young as ~150 and ~260 days, respectively. The ^{35}S activities in the deepest snowpit (80-120 cm), firn and ice samples were not detected, suggesting that their ages were likely longer than ~260 days. It is noted that these values may be overestimated

because aged snow melting, which can reduce ^{35}S activity in a snowpit [*Johannessen and Henriksen*, 1978], was not considered in this first approximation. In the future, comparison with dating results using high-resolution water stable isotope measurements, which were less affected by snow melting, can assist in evaluating the snow melting rate.

Table 3.3. ^{35}S activities measured in natural samples collected at Laohugou Glacier No.12

Sample	Altitude (m a.s.l.)	Volume (L)[a]	^{35}S activity (mBq / L)[b]	^{35}S concentration[c] (10^3 atoms / L)	Sulfate (nmol/L)	^{35}S SA (atoms/nmol)
Fresh Snow	4800	1.6	29±6	310±70	1390	230±50
Fresh Snow	4400	1.1	47±7	520±80	3370	150±20
Snowpit (0-40 cm)	5050	3.2	7±3	70±40	661	110±60
Snowpit (40-80 cm)	5050	2.4	3±3	40±40	981	40±40
Snowpit (80-120 cm)	5050	2.4	2±3	20±30	1600	10±20
Firn	4900	4.0	0±3	0±30	199	10±150
Ice	4800	4.0	1±2	10±20	408	20±50
River Runoff[d]	4200	2.7	11±4	120±40	26700	5±2
River Runoff[e]	4200	2.7	7±3	80±30	23000	3±1

a. volume of samples used for ^{35}S analysis; b. all errors reported here are the standard deviation of 12 counting cycles (see Experimental Sections for details); c. the $^{35}SO_4^{2-}$ concentration was determined using the relationship: $[^{35}SO_4^{2-}] = (^{35}S\text{-activity} \times 0.06\ dpm/mBq \times t_{1/2} / \ln(2)) / V_{water}$, where ^{35}S-activity, $t_{1/2}$ and V_{water} represent the total activity of ^{35}S in the unit of mBq, the radioactive-decay half-life of ^{35}S in the unit of minute, and total volume in the unit of liter in each sample, respectively; d. this sample was collected at dawn; e. this sample was collected at dusk.

The ^{35}S concentrations (in the unit of atoms/L, see Table 3.3 for unit conversion) in river runoff samples were 80×10^3 - 120×10^3 atoms/L (Table 3.3). Because melted water from ice, aged and fresh snow contained different ^{35}S concentrations (Table 3.3), the maximum contributions from these sources can be estimated. As discussed previously, aged snow melting can reduce ^{35}S

concentrations in aged snow. Therefore, the ^{35}S concentrations in melted aged snow could be higher than 70×10^3 atoms/L and cannot be determined in this study. In this case, the maximum contribution from melted aged snow can be as high as 100%. Given melted ice did not contain any ^{35}S (0 atom/L), by assuming no contribution from melted aged snow (i.e., all ^{35}S atoms in runoff derived from melted fresh snow), we can estimate the maximum contribution from melted fresh snow and melted ice ($f_{\text{melted-fresh-snow, max}}$ and $f_{\text{melted-ice, max}}$, respectively):

$$f_{\text{melted-fresh-snow, max}} = {}^{35}S_{\text{runoff}} / {}^{35}S_{\text{melted-fresh-snow}}$$

$$f_{\text{melted-ice, max}} = 1 - f_{\text{melted-fresh-snow, max}}$$

where $^{35}S_{\text{runoff}}$ and $^{35}S_{\text{melted-fresh-snow}}$ represents ^{35}S concentrations in runoff (80×10^3 - 120×10^3 atoms/L) and fresh snow (310×10^3 - 520×10^3 atoms/L), respectively. It yielded $f_{\text{melted-fresh-snow, max}}$ and $f_{\text{melted-ice, max}}$ with ranges of 23-39% and 61-76%, respectively.

Stable sulfate concentrations in runoff samples were significantly greater than snow/ice samples (Table 3.3), indicating large influences from weathering of continental rocks. The signature of anomalous ^{17}O enrichments in atmospheric nitrate was used to quantify the contribution of atmospheric nitrate to river water [*Liu et al.*, 2013]. Because the magnitude of anomalous ^{17}O enrichments in atmospheric sulfate was usually ~20 times smaller than nitrate [*Patris et al.*, 2007], this tracing method might be not sensitive enough to identify atmospheric sulfate in river water that contained a large fraction of non-atmospheric sulfate. Because non-atmospheric sulfates are non-radioactive (with ^{35}S SA of 0 atoms/nmol), our ability to measure ^{35}S concentrations in atom levels may provide a more sensitive and accurate assessment of atmospheric sulfate in river water. With an assumption that ^{35}S SA of atmospheric sulfate was identical to fresh snow, the mass balance of ^{35}S SA suggested that atmospheric sulfate accounted for 1-3% of the total sulfate in river runoff.

3.5 Conclusions

We have presented a new method to collect snow and water samples from remote regions and analyze ^{35}S activities with high sensitivity in a simple and economical way. The counting background and efficiency were ~0.9 cpm and 78%, respectively, and therefore we can easily analyze water samples as small as ~2 L, ~10 times smaller than previous methods. The use of anion exchange resins is simple and easily done in the field, eliminating the need of transporting large volumes of water from the field to the laboratory. Excess Br^-/Cl^- ions in eluent during sample extraction can be removed by the H_2O_2 method detailed in this study, which costs for each sample were approximately 60 US$ lesser than the conventional Ag_2O method. The deviation from true values in this new method was -5%, significantly smaller than the early stage of this method (-55%). This new method represents an advance in ^{35}S analysis in small volumes of water samples, although it is not applicable to natural water samples that contain a large amount of sulfate (> 1.5 mmol).

Using this new method, we successfully tested ~1 L of fresh snow collected from a glacier on the Tibetan Plateau and the measured ^{35}S activity was 47±7 mBq/L. We point out that the precision can be easily improved by collecting relatively larger amounts of samples (e.g. ~3 L) and measuring samples as soon as possible. Based on our ^{35}S measurements in snow, ice and water samples collected from the Tibetan Plateau, we presented a first proof-of-concept approximation showing how this method can assist in age determinations and source attributions. Although no definitive statement might be made from 9 samples in this study, our result does suggest that it is worthwhile to design a more strategic and comprehensive study to understand the snow and glacier melting in this climatically important region. The ^{35}S measurement in snow and water may also be used for assessing the chemical exchange (such as other cosmogenic radionuclides) between the atmosphere (especially upper atmosphere) and the hydrosphere/cryosphere. For instance, with proper understanding of several post-production and fallout processes such as stratosphere-

troposphere exchange and dry/wet deposition in the polar regions, which can be constrained by ^{35}S measurements, cosmogenic ^{10}Be (half-life = 14 Myr) records in ice cores can be used to probe past changes in the cosmic ray intensity, the geomagnetic field intensity and the solar activity [*Aldahan et al.*, 2008].

In summary, the method developed in this study opens new frontiers in studying ^{35}S in snow and water, an important cosmogenic isotope in tracing chemical and physical processes in the hydrosphere and the cryosphere, and even their interaction with other earth systems such as the atmosphere.

3.6 Acknowledgements

We thank Drs. Hill-Falkenthal and Priyadarshi for beneficial scientific discussions at the early stage of this study. Two anonymous reviewers are thanked for their valuable suggestions that improved the manuscript. This work was supported, in part, by National Natural Science Foundation of China (41421061). Mang Lin acknowledges a fellowship from Guangzhou Elite Project (JY201303).

This chapter, in full, is a reprint of the material "Simple method for high-sensitivity determination of cosmogenic ^{35}S in snow and water samples collected from remote regions" as it appears in Analytical Chemistry 2017. Lin, Mang; Wang, Kun; Kang, Shichang; Thiemens, Mark H., American Chemical Society, 2017. The dissertation author was the primary investigator and author of this paper.

Chapter 4 Detection of deep stratospheric intrusions by cosmogenic ^{35}S

4.1 Abstract

The extent to which stratospheric intrusions on synoptic scales influence the tropospheric ozone (O_3) levels remains poorly understood because quantitative detection of stratospheric air has been challenging. Cosmogenic ^{35}S mainly produced in the stratosphere has the potential to identify stratospheric air masses at ground level, but this has not yet been unambiguously demonstrated. Here, we report unusually high ^{35}S concentrations (7390 atoms m^{-3}, ~16 times greater than annual average) in fine sulfate aerosols (aerodynamic diameter less than 0.95 μm) collected at a coastal site in southern California on May 3, 2014, when ground level O_3 mixing ratios at air quality monitoring stations across southern California (43 out of 85) exceeded the recently revised United States National Ambient Air Quality Standard (daily maximum 8-h average: 70 ppbv). The stratospheric origin of the significantly enhanced ^{35}S level is supported by *in situ* measurements of air pollutants and meteorological variables, satellite observations, meteorological analysis and box model calculations. The deep stratospheric intrusion event was driven by the coupling between mid-latitude cyclones and Santa Ana winds, and was responsible for the regional O_3 pollution episode. These results provide direct field-based evidence that ^{35}S is an additional, sensitive and unambiguous tracer in detecting stratospheric air in the boundary layer, and offers the potential for resolving the stratospheric influences on the tropospheric O_3 level.

4.2 Introduction

High ground level ozone (O_3) mixing ratios exert adverse impacts on human health, vegetation and materials [*Arneth et al.*, 2010; *McGrath et al.*, 2015]. In the free troposphere, O_3 is an important greenhouse gas contributing to global warming. It also controls the lifetime of other reactive greenhouse gases through oxidation processes [*Verstraeten et al.*, 2015], and serves as the dominant precursor of the hydroxyl radical (OH) and enhances the oxidizing capacity of the

troposphere [*Skerlak et al.*, 2014]. Tropospheric O_3 formation involves a series of photochemical reactions related to anthropogenic emissions of O_3 precursors (e.g., nitrogen oxides (NO_x), carbon monoxide (CO) and volatile organic compounds (VOCs)), biomass burning and lightning [*Huang et al.*, 2015b]. In addition, elevated levels of tropospheric O_3 may be due to the intrusion of O_3-rich stratospheric air masses [*Langford et al.*, 2012; *Lin et al.*, 2012b; *Lin et al.*, 2015; *Skerlak et al.*, 2014]. Detection of such stratospheric intrusion events by field-based measurements has been a major scientific concern since the 1970s [*Stohl et al.*, 2003]. Concurrent measurements of ground level O_3, CO and humidity are the most common method [*Cristofanelli et al.*, 2010; *Langford et al.*, 2015b], but it is ambiguous and only useful in extreme events and in background sites. Ozonesondes, lidar and aircraft measurements provide high resolution information on vertical O_3 distributions [*Chan et al.*, 2004; *Cooper et al.*, 2005; *Kuang et al.*, 2012], but they are relatively expensive and not widely available. Therefore, it is crucial to find an additional and unambiguous stratospheric tracer at ground level to assist in such investigations.

^{35}S (half-life = 87 days) is a cosmogenic isotope, naturally produced by the interaction of high energy cosmic rays with ^{40}Ar in the atmosphere. The flux of cosmic rays and the production rate of ^{35}S depends on both latitude and altitude, with higher values at the polar region and in the stratosphere (and lower at the equatorial region and in the boundary layer) [*Lal and Peters*, 1967]. Cosmogenic ^{35}S quickly oxidizes to $^{35}SO_2$ in ~1 second after production, and is further oxidized to $^{35}SO_4^{2-}$ before wet and dry removal. Therefore, the variation of $^{35}SO_4^{2-}$ concentrations at ground level is controled by the SO_2 oxidation and sulfate removal rates as well as air masses originating from the higher atmosphere. Because of the higher production rate of ^{35}S in the stratosphere (1-2 orders of magnitude greater than in the troposphere) [*Lal and Peters*, 1967], significant enhancement of $^{35}SO_4^{2-}$ concentration at ground level may offer a new tool to quantify the impact of deep stratospheric intrusions on tropospheric O_3. A unique advantage of ^{35}S is that it behaves both as a gas (SO_2) and an aerosol and has an ideal half-life (87 days) for studying atmospheric processes on synoptic scales, providing additional information on potential impacts of stratospheric

intrusions on gas-to-particle (SO_2 to SO_4^{2-}) conversion rates. The development of optimized low-level liquid scintillation counting technique [*Brothers et al.*, 2010] gave rise to a growing number of aerosol $^{35}SO_4^{2-}$ measurements in recent years. Based on simple and unconstrained 1-D box model calculations, slightly elevated $^{35}SO_4^{2-}$ concentrations in early studies were linked to the polar vortex activity [*Priyadarshi et al.*, 2011a], Santa Ana winds and shallow stratosphere-troposphere exchange events in southern California [*Priyadarshi et al.*, 2012a]. Recent studies applied mesoscale meteorology models to investigate the possible downward transport processes of aged stratospheric air [*Lin et al.*, 2016b; *Lin et al.*, 2016c]. However, the reliability of ^{35}S as a stratospheric tracer remains uncertain and debated because the magnitudes of $^{35}SO_4^{2-}$ enhancements were relatively small and other stratospheric signatures (e.g. high O_3 level, low humidity) were not observed in suspected aged stratospheric air masses [*Lin et al.*, 2016b; *Priyadarshi et al.*, 2012a]. Measurements of $^{35}SO_4^{2-}$ during deep stratospheric intrusions which directly entrain fresh stratospheric air to the boundary layer have never been made.

Climatological studies showed that the western United States (U.S.) is one of the global hotspots for deep stratospheric intrusions, which is likely because of the east Pacific storm track and the high-altitude orography [*Skerlak et al.*, 2014; *Sprenger and Wernli*, 2003]. Such deep stratospheric intrusion events compromise high-altitude regions of the western U.S. in attaining U.S. National Ambient Air Quality Standards (NAAQS) for O_3 [*Lin et al.*, 2012b]. Further field-based observation studies indicated that these O_3-rich stratospheric air can even be transported to low altitude regions such as Los Angelas at the southern California coast [*Baylon et al.*, 2016; *Langford et al.*, 2012; *Langford et al.*, 2015a]. Consequently, this region is a natural laboratory for studying the potential of ^{35}S as a tracer for stratospheric intrusions. In October 2015, the NAAQS for O_3 was revised to 70 ppbv (daily maximum 8-h average, MDA8) from the previous standard of 75 ppbv by the U.S. Environmental Proctection Agency (EPA). This new standard has been effective since December 28, 2015, and hence, identifying and excluding such naturally occurring "exceptional events" become increasingly important [*Cooper et al.*, 2015]. The EPA recommends

identifying "exceptional events" with supporting evidence, emphasizing the urgent need to find a new and sensitive stratospheric tracer such as ^{35}S to offer an unambigeous diagnostic for stratospheric intrusions. In this study, we measure ^{35}S concentrations during deep stratospheric intrusions for the first time to demonstate the sensitivity of ^{35}S to stratospheric air in the boundary layer.

4.3 Field-based ^{35}S measurements

Table 4.1 summarizes ^{35}S concentrations in size-segregated sulfate aerosol ($^{35}SO_4^{2-}$) collected at the rooftop of Pacific Hall on the campus of the University of California San Diego (32.876°N, 117.242°W, 120 m above sea level [a.s.l.]) in spring 2014. Most of ^{35}S concentrations agree well with our previous measurements at the Scripps Pier (10 m a.s.l. and 1.7 km from the sampling site in this study) [*Priyadarshi et al.*, 2012a], but an unusually high $^{35}SO_4^{2-}$ concentration of 7390 atoms m^{-3} was found in the fine aerosol sample (with aerodynamic diameter less than 0.95 μm) collected on May 3, 2014, ~16 times greater than the annual mean of 460 atoms m^{-3} [*Priyadarshi et al.*, 2011b; *Priyadarshi et al.*, 2012a] (Figure 4.1). In fact, this is the highest $^{35}SO_4^{2-}$ concentration ever reported for natural aerosol samples in the literature, which may be explained by stratospheric influence. It is noted that comparably high ^{35}S levels were measured in two rainwater samples collected at Korea in spring and winter (200 and 400 mBq L^{-1}, respectively), two seasons with frequent stratospheric intrusions in East Asia [*Oltmans et al.*, 2004], which were significantly greater (> factor of ~6) than other rainwater samples (4-60 mBq L^{-1}) [*Cho et al.*, 2011]. Using the $^{35}SO_4^{2-}$ scavenging ratio obtained at Japan [*Priyadarshi et al.*, 2013], the atmospheric $^{35}SO_4^{2-}$ concentrations in Korea were calculated to be 150-2200 atoms m^{-3} in most cases and 7500 and 15000 atoms m^{-3} in two episodes. While this estimation is subject to large uncertainties (~60% relative standard deviation) [*Priyadarshi et al.*, 2013], it matches the most recent $^{35}SO_4^{2-}$ measurement directly made on aerosol samples collected in East Asia (90-1130 atoms m^{-3} in most samples and an increased $^{35}SO_4^{2-}$ concentration of 3150 atoms m^{-3} in a sample affected aged

stratospheric air from the free troposphere) [*Lin et al.*, 2016c]. The aforementioned high rainwater ^{35}S activities [*Cho et al.*, 2011] were likely affected by stratospheric intrusions but were not considered. In this study, the stratospheric origin of our unusually high $^{35}SO_4^{2-}$ concentration directly measured on sulfate aerosol is examined.

Table 4.1. $^{35}SO_4^{2-}$ concentrations in size-segregated aerosol samples collected in University of California San Diego in spring 2014

Date	Total air flow (m^3)	$^{35}SO_4^{2-}$ (atoms m^{-3})		
		>7.2 μm	0.95-7.2 μm	<0.95 μm
Mar 27 – Apr 4	11647	12 ± 7	33 ± 5	90 ± 4
Apr 6-7	1543	n.d. [a]	n.d.	170 ± 40
Apr 12-18	9503	15 ± 8	77 ± 6	230 ± 10
May 3-7	7176	4 ± 6	75 ± 8	7390 ± 50
May 10-14	7571	n.d.	50 ± 10	370 ± 20
May 19-23	7727	3 ± 7	51 ± 7	130 ± 10

a. "n.d." stands for "not detectable".

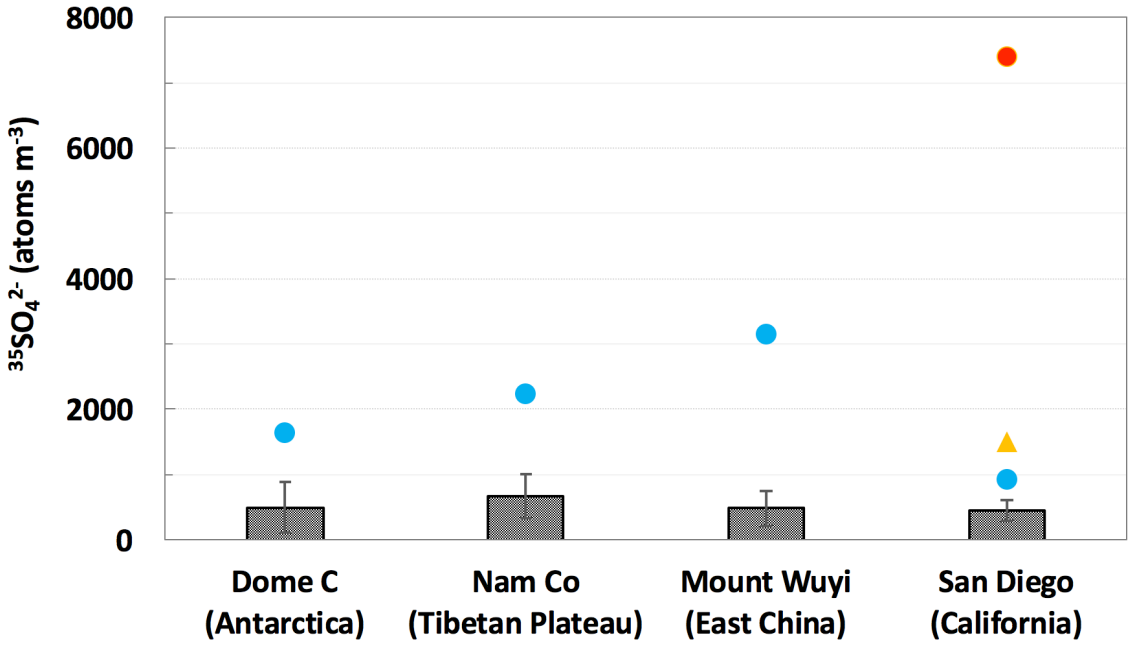

Figure 4.1. The $^{35}SO_4^{2-}$ concentration in the fine aerosol sample collected on May 3, 2014 (red dot), and the comparison with annual means (grey bars; error bars stand for one standard deviation) and the highest values (blue dots) measured at different sampling sites in previous studies. Orange triangle represents the sample affected by the trans-Pacific transport of ^{35}S produced from the $^{35}Cl[n,p]^{35}S$ reaction in Fukushima.

Prior to discussing the impacts of stratospheric intrusions, other potential factors should be carefully evaluated. Apart from natural cosmogenic production, the $^{35}Cl[n,p]^{35}S$ reaction between neutrons escaping from the Fukushima and ^{35}Cl in the coolant seawater is the only identified anthropogenic source of ^{35}S [*Priyadarshi et al.*, 2011b; *Priyadarshi et al.*, 2013]. It is worthwhile to note that core elements reactors do not emit ^{35}S. It is the addition of ^{35}Cl from seawater that allows the neutron as reactant and ^{35}S productions. Given the highly specific reaction condition, there is no evidence showing that the observed $^{35}SO_4^{2-}$ spike in this study is due to the $^{35}Cl[n,p]^{35}S$ reaction in the Fukushima, or any, nuclear plant. In addition, it was proposed that atmospheric $^{35}SO_4^{2-}$ removed by precipitation or dry deposition processes might re-enter the boundary layer through the atmosphere and land-surface interaction (biomass burning or wind-blown terrestrial dust) within ~66 days and elevate $^{35}SO_4^{2-}$ concentrations in the boundary layer [*Cho et al.*, 2011].

Even though this hypothesis remains to be proven, we carefully screen out this potential scenario. Large wildfires (>300 acres, defined by the California Department of Forestry and Fire Protection) were not recorded during the sampling period (http://cdfdata.fire.ca.gov/pub/cdf/images/incidentstatsevents_253.pdf). The absence of large wildfires is also supported by the satellite observations (Figure 4.2). Therefore, any significant contribution of ^{35}S from biomass burning is implausible in this study period. The low $^{35}SO_4^{2-}$ concentration in coarse particle observed in the same set of aerosol samples (Table 4.1) also suggests that $^{35}SO_4^{2-}$ in re-suspended terrestrial soil or dust cannot account for the notable enhancement of $^{35}SO_4^{2-}$ in this study. To date, there is no evidence or theory showing that other sources/processes can lead to significant variations or productions of ^{35}S. After considering all potential factors, the impact of air masses from the stratosphere, where the natural cosmogenic production rate of ^{35}S is ~2 order of magnitude greater than the Earth's surface [*Lal and Peters*, 1967], is the most likely candidate to explain the elevated ^{35}S concentration.

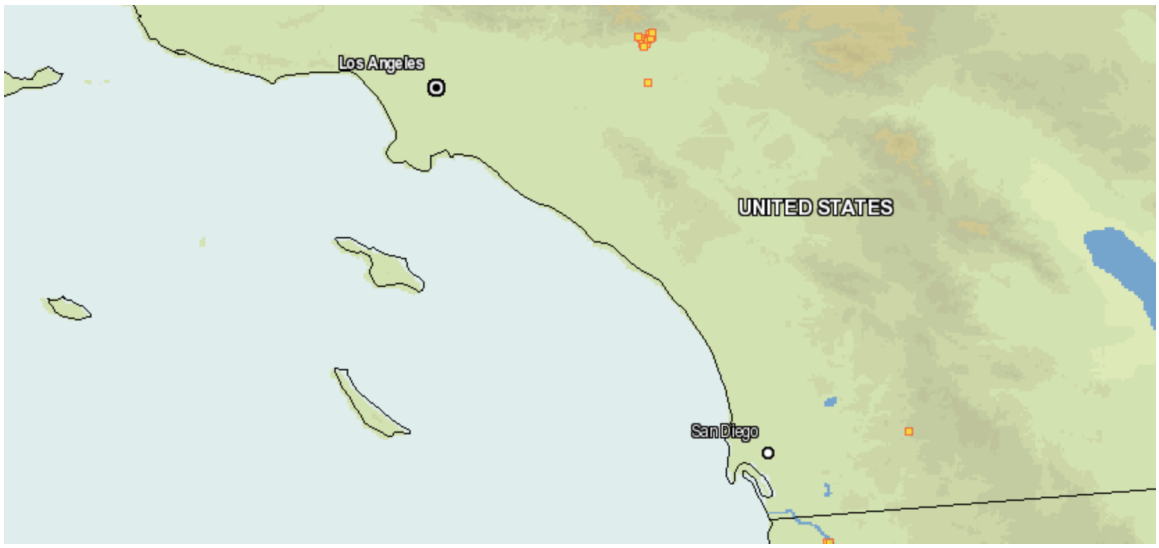

Figure 4.2. Fire counts observed by the MODIS during the periods of April 27 to May 3 2014 (Santa Ana period).

4.4 An exceptional event of O_3 enrichment

On May 3, 2014, when the ^{35}S-rich aerosol sample was collected, a regional O_3 pollution event was observed over Southern California (Figure 4.3). Two stations in Los Angeles were in the category of "Unhealthy" (Air Quality Index, AQI: 151-200; or MDA8: 86-105 ppbv), and 80% stations in Southern California (68 out of 85) were in the categories of "unhealthy for sensitive groups" (AQI: 101-150; or MDA8: 71-85 ppbv) or "moderate" (AQI: 51-100; or MDA8: 55-70 ppbv). Although other 15 stations were in the category of "good" (AQI: 0-50; or MDA8: 0-54 ppbv) on this day, the O_3 mixing ratios in 14 stations were still higher than annual means and 5 of them were significantly greater (>80th percentile) than normal days. The relatively low O_3 mixing ratios (compared with other stations) are because of substantial NO emissions from vehicles in surrounding areas that lower ambient O_3 mixing ratios via the "titration effect" ($NO+O_3 \rightarrow NO_2+O_2$) [*Chan et al.*, 1998]. For example, the MDA8 of 54 ppbv in the Otay Mesa station (located at the U.S.-Mexico border and affected by busy crossing Heavy-Duty trucks) on May 3, 2014 was the annual highest value.

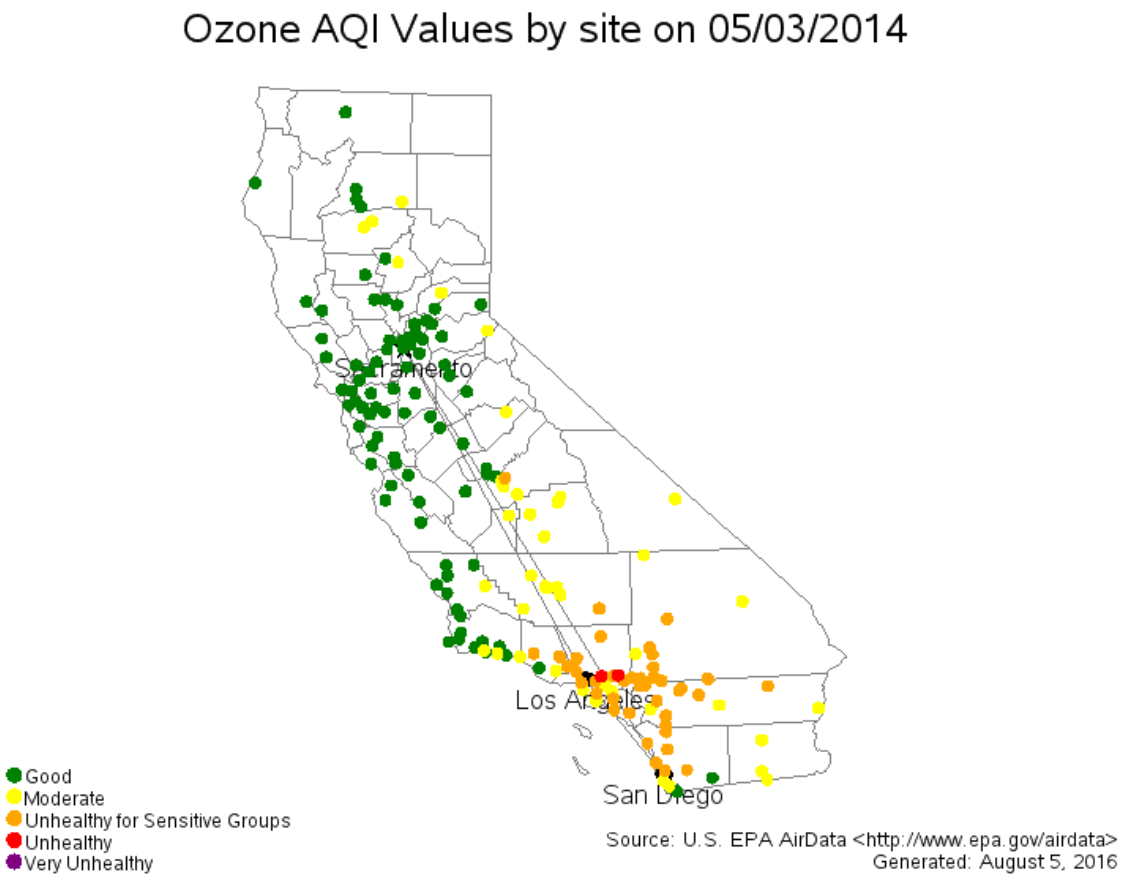

Figure 4.3. Distribution of ozone air quality index (AQI) and levels of health concern in California recorded by the U.S. EPA on May 3, 2014 (http://www.epa.gov/airdata).

Figures 4.4a and 4.4b show the time series of relative humidity (RH), temperature and wind speed recorded at San Diego from April 27 to May 8, 2014. RH dramatically dropped down from 67% at 2100 Pacific Standard Time (PST) on April 28 to 7% at 1500 PST on April 29, accompanied with enhanced temperature (~30°C) and wind speed (>15 m/s). The wind speed reached a maximum of 28 m s^{-1} on April 30, with wind direction shift from variable to northwesterly (Figure 4.4b). These are typical signatures of Santa Ana winds, which are highly dry, hot and strong winds that descend from inland desert regions to the Pacific coastal region at southern California [*Bytnerowicz et al.*, 2010; *Cao and Fovell*, 2016; *Langford et al.*, 2015a; *Priyadarshi et al.*, 2012a; *Sommers*, 1978]. These foehn-like katabatic winds result from a strong pressure gradient between a high pressure over the Great Basin and an offshore low pressure. The high pressure can compress sinked air, force the air temperature to rise and reduce its RH. Although the wind speed returned back to normal on May 2, 2014, low RH and high temperature persisted till May 4, suggesting that the Santa Ana wind event lasted for 5 days (April 29 – May 3, 2014).

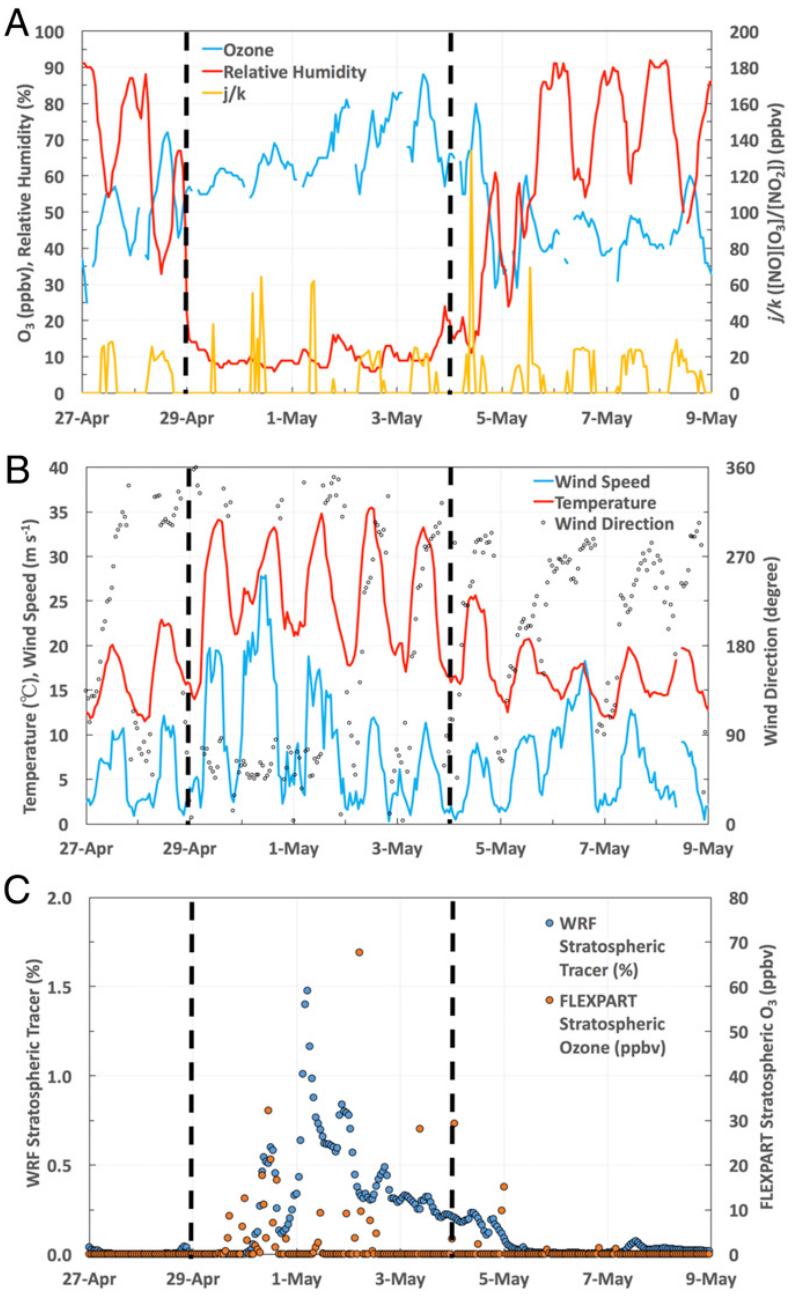

Figure 4.4. Time serials of hourly (a) O_3, relative humidity and *j/k* measured at San Diego (the Alpine monitoring station) (b) temperature, wind speed and direction measured at San Diego (the Kearny Mesa station) and (c) Simulated WRF stratospheric tracer and FLEXPART stratospheric O_3 at the boundary layer of San Diego. The vertical black dashed lines define the period of Santa Ana event (April 29 – May 3, 2014) based on abnormal relative humidity and temperature.

Santa Ana wind events are often behind a cold front associated with an upper level trough [*Sommers*, 1978], which can not only exacerbate the katabatic winds but also lead to the formation

of deep tropopause folds and stratospheric intrusions [*Langford et al.*, 2015a]. A recent study suggested that the coupling between Santa Ana winds and stratospheric intrusions might pose serious O_3 pollution threats across the coast of Southern California [*Langford et al.*, 2015a]. In this study, ground level O_3 mixing ratios during the Santa Ana event increased significantly (Figure 4.4a). The annual highest MDA8 in the Apline station at San Diego (81 ppbv) was recorded on May 3, with a maximum 1-h O_3 mixing ratio of 88 ppbv at 1200 PST. Solar radiation and temperature were stronger during the Santa Ana episodes, but the ratio of NO_2 photolysis to $NO+O_3$ reaction rates (j/k=[NO][O_3]/[NO_2], with the photostationary state assumption) [*Clapp and Jenkin*, 2001]showed only slight enhancement during April 29 to May 1, suggesting that photochemical production of O_3 in the O_3-NO-NO_2 cycle was not a major factor leading to the elevated O_3 levels during the entire Santa Ana period. Although wildfires occur commonly during Santa Ana wind events, which can significant increase ground level O_3 mixing ratios [*Bytnerowicz et al.*, 2010; *Langford et al.*, 2015a], no significant wildfire occurred in our study period (Figure 4.2), suggesting that emissions from wildfires were not a major contributor either. A closer look into the O_3 diurnal variations reveals significant enhancements of nighttime O_3 mixing ratios during the Santa Ana period, which were 20-29 ppbv greater than normal days (Figure 4.5). Because photochemical O_3 production ceases at nighttime, this result suggests a larger contribution of long range transports (including stratospheric intrusions) to the enhanced O_3 mixing ratios in the Santa Ana period. A negative correlation between O_3 and CO (a tracer of anthropogenic emission) may suggest O_3 originating from the stratosphere, where CO is depleted and O_3 is rich [*Jiang et al.*, 2015; *Parrish et al.*, 1998]. To rule out the potential impact of night-time titration effect which can also lead to negative O_3-CO correlation [*Mao and Talbot*, 2004; *Voulgarakis et al.*, 2011], only daytime data (0700-1800) were considered in this study. A significant negative correlation between O_3 and CO in the Santa Ana event ($r = -0.60$, confidence level > 99.9%) compared with normal days ($r = -0.04$, confidence level = 40.9%) implies that the elevated O_3 levels during the Santa Ana event was likely related to the vertical transport of O_3 from high altitudes.

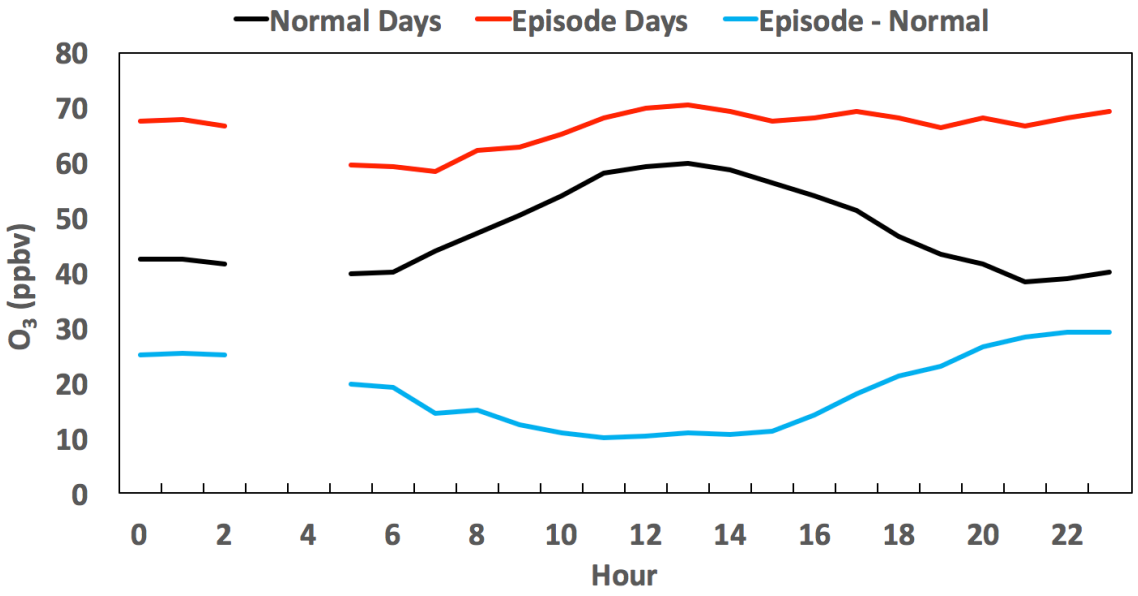

Figure 4.5. Diurnal patterns of O3 mixing ratios in normal days (April 27-28 and May 4-9 2014, black), episode days (April 29 – May 3 2014, red) and their differences (blue).

In summary, the concurrently enhanced ground level $^{35}SO_4^{2-}$ and O_3 concentrations and negative O_3-CO correlation indicate that the O_3 episode on May 3, 2014 was likely affected by a deep stratospheric intrusion event, a natural occurring "exceptional event". Since most Santa Ana winds only entrain air masses from the free troposphere to the boundary layer and would not lead to a significant enhancement of ground level O_3 mixing ratios [*Bytnerowicz et al.*, 2010; *Priyadarshi et al.*, 2012a], a stratospheric intrusion event that transports O_3-rich stratospheric air to the free troposphere prior to or during the Santa Ana event is required to result in the observed ground level $^{35}SO_4^{2-}$ and O_3 concentrations. The vertical ozone profile retrieved from Global Ozone Monitoring Experiment-2 (GOME-2) satellite observation at April 30, 2014 revealed significant enhancements of the tropopause O_3 levels and total O_3 columns at the upstream region of southern California during the Santa Ana event, indicating stratospheric air masses mixing into the

troposphere (Figure 4.6). Under the influences of Santa Ana winds, such O_3-rich stratospheric air may be transported downward to the boundary layer and westerly to coastal southern California.

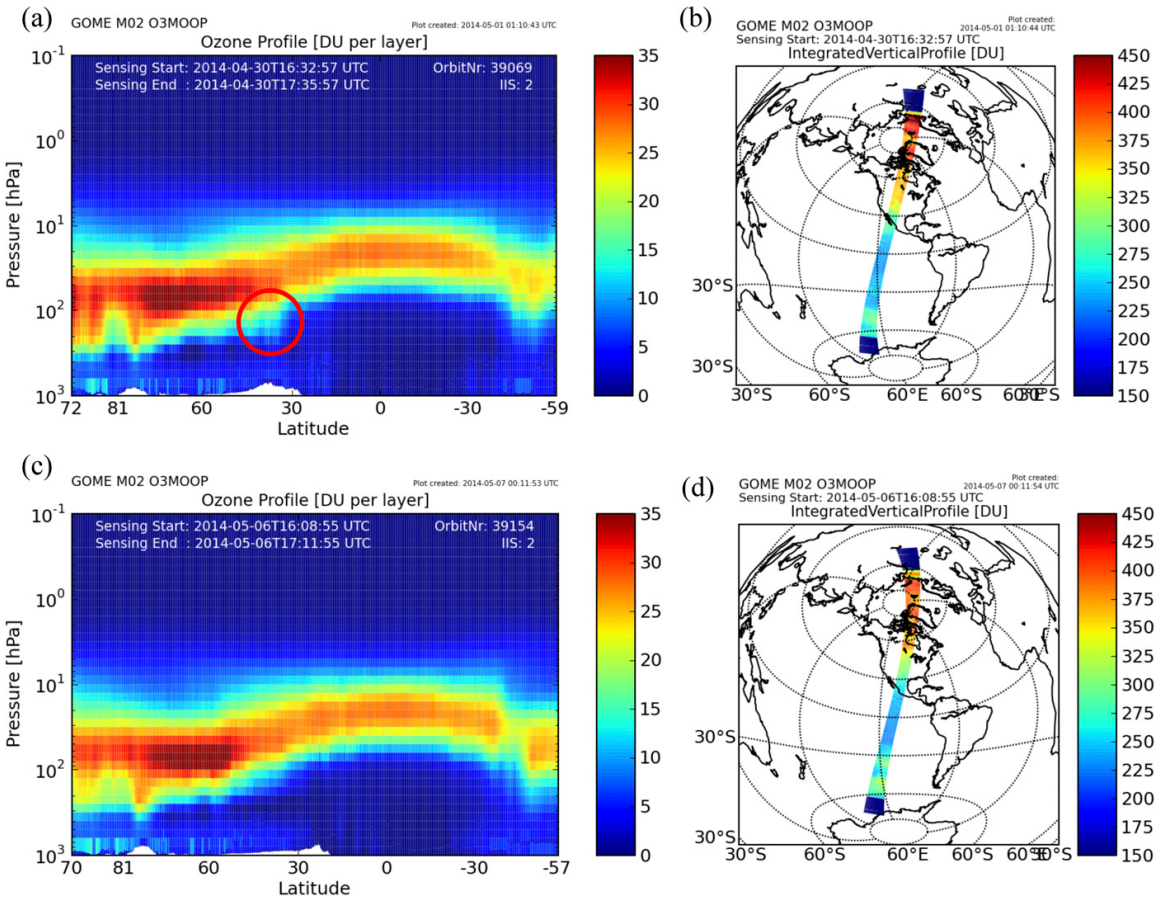

Figure 4.6. (A) The GOME-2 vertical ozone profiles and (B) the location of the GOME-2 orbit on April 30, 2014. (C and D) The same as in A and B but on May 6, 2014. The red circle in A highlights the enhanced O_3 levels induced by stratospheric intrusions. DU, Dobson unit.

4.5 Meteorological Model Analysis

To quantitatively estimate the probability that air masses sampled in this Santa Ana wind event partly originating from the stratosphere, an inert stratospheric tracer was simulated by a mesoscale meteorology model (Weather Research and Forecasting Model, WRF) [*Lin et al.*, 2016c]. The time series of the WRF-simulated stratospheric tracer at the boundary layer show a small peak

(0.6%) at 1200 PST on April 30, 2014, one day after the onset of the Santa Ana wind event, and the highest peak (1.5%) at 0500 PST on May 1, 2014 (Figure 4.4c). The WRF-simulated stratospheric tracer gradually decreased from the highest peak to baseline (~0%) during May 1-5, 2014 (Figure 4.4c). Stratospheric O_3 mixing ratios at the boundary layer simulated by an independent Lagrangian particle dispersion model (FLEXPART, driven by the WRF output) [*Lin et al.*, 2016b] show a consistent trend (Figure 2c), further supporting the stratospheric origins of ^{35}S and O_3.

The process how this plume intruded to the troposphere and reached coastal southern California is investigated by the horizontal distributions of the WRF-simulated stratospheric tracers and weather systems at various altitudes. As clearly shown in Figure 4.7a, the stratospheric intrusion episode leading to the elevation of WRF-simulated stratospheric tracer was directly triggered by a cutoff low-pressure system, which is accompanied by strong convective motions and tropopause folding and is a typical synoptic condition resulting in active stratosphere-to-troposphere exchange over western U.S. [*Langford et al.*, 2015a; *Langford et al.*, 2015b]. The development of this synoptic situation is shown in Figure 4.8. At the beginning, a strong mid-level short-wave trough developed into a closed low-pressure area as the system occluded over the central high plains since April 27, 2014. An associated mid- to low-level cyclone then reached its peak intensity while a trailing cold front move eastward across eastern Kansas, eastern Oklahoma and northern Texas on April 29, 2014. Meanwhile, the strong northeasterly flow on the southwest flank of the cyclone swept through southwest U.S. and caused a significant late-season Santa Ana event. Later on, the low-pressure system started to abate and stretched southward from Canada to New Mexico and from northern California to Gulf of Mexico on April 30, and eventually dissipated after May 2, 2014.

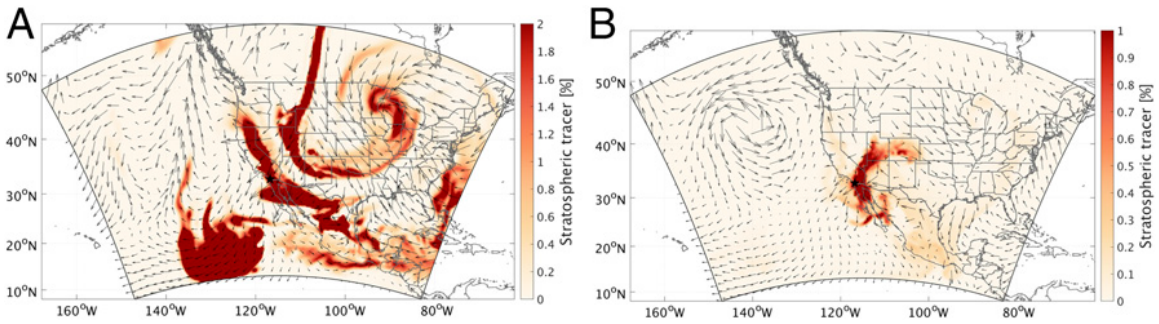

Figure 4.7. Spatial distribution of the WRF stratospheric tracer at (A) 500 hPa at 0000 hours PST on April 30 and (B) 390 m above ground level at 0500 hours PST on May 1. The black star indicates the location of San Diego.

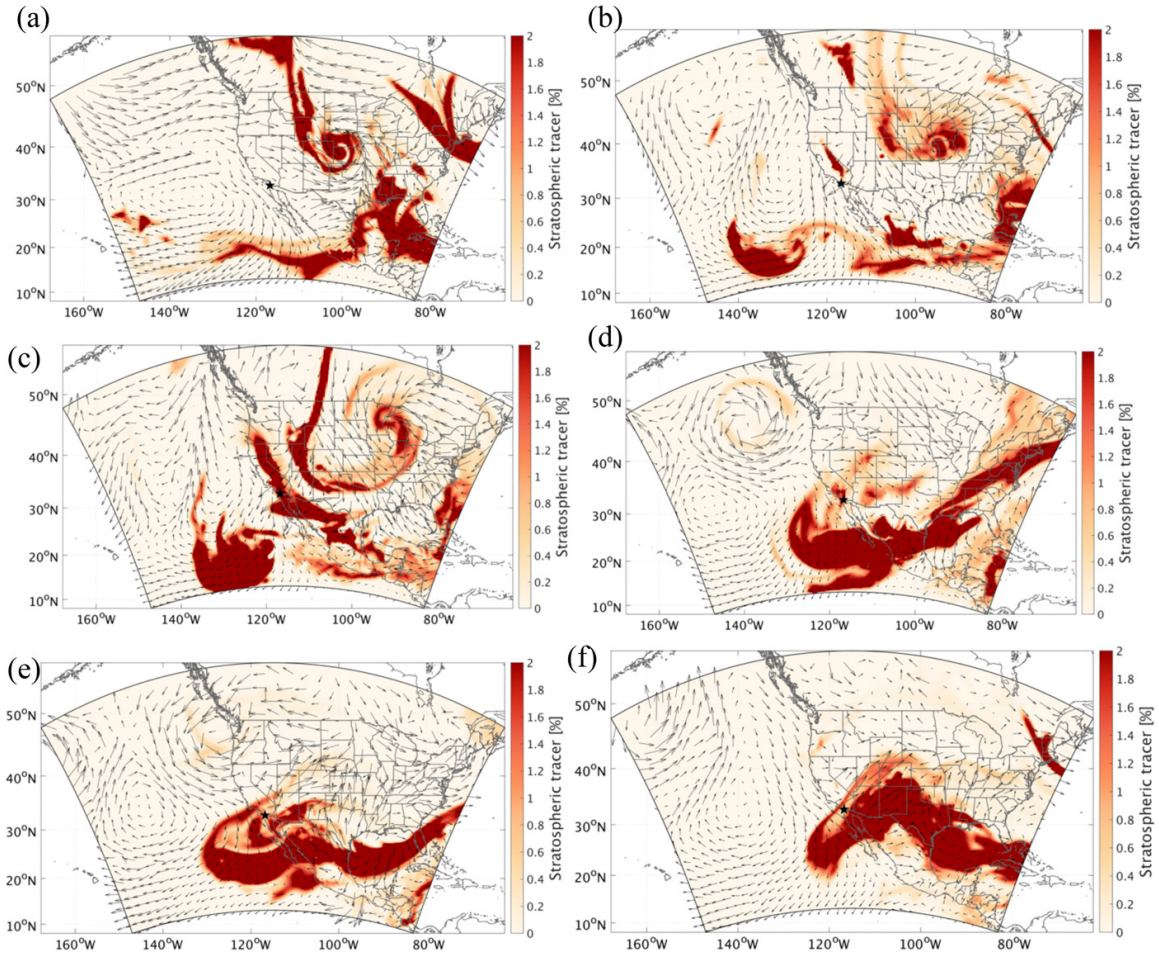

Figure 4.8. Spatial distribution of the WRF stratospheric tracer at 500 hPa at (A) 1200 hours PST on April 27, (B) 0000 hours PST on April 29, (C) 0000 hours PST on April 30, (D) 1600 hours PST on May 2, (E) 0000 hours PST on May 4, and (F) 1400 hours PST on May 5 (all 2014). The black stars indicate the location of San Diego.

Exchange processes between the free troposphere and the boundary layer are vital to bring ^{35}S and O_3 rich stratospheric air to the sampling site. Figure 4.7 shows that the impacts of stratospheric air on the boundary layer were mostly confined in the regions affected by the Santa Ana wind. Stratospheric air masses in the free troposphere started to penetrate into the boundary layer at Utah at 1000 PST on April 30, 2014 behind the trough line, and were subsequently transported to southern California via the northeast Santa Ana wind on May 1 (Figure 4.9). Zonal cross-sections of potential vorticity (PV) and WRF-simulated stratospheric tracer clearly show the distinctive tropopause folding associated with the cutoff low between ~105°W and ~115°W and a tongue of stratospheric air sloping downward at ~115°W (Figure 4.10), highlighting the pathway of the stratospheric air into the boundary layer. The MDA8 O_3 mixing ratios recorded at Las Vegas (35.786°N, 115.357°W, 924 m a.s.l.), the upstream region of southern California, were 59, 69 and 56 ppbv on April 30, May 1 and 2, 2014, respectively (http://airquality.clarkcountynv.gov). The increases of MDA8 on May 1 in part support our model results. As the stratospheric air masses were continuously entrained into the free troposphere by the occluded low-pressure system, these southwestward-transported air masses might slope downward to the boundary layer at southern California as well (Figure 4.8 and Supporting Information text).

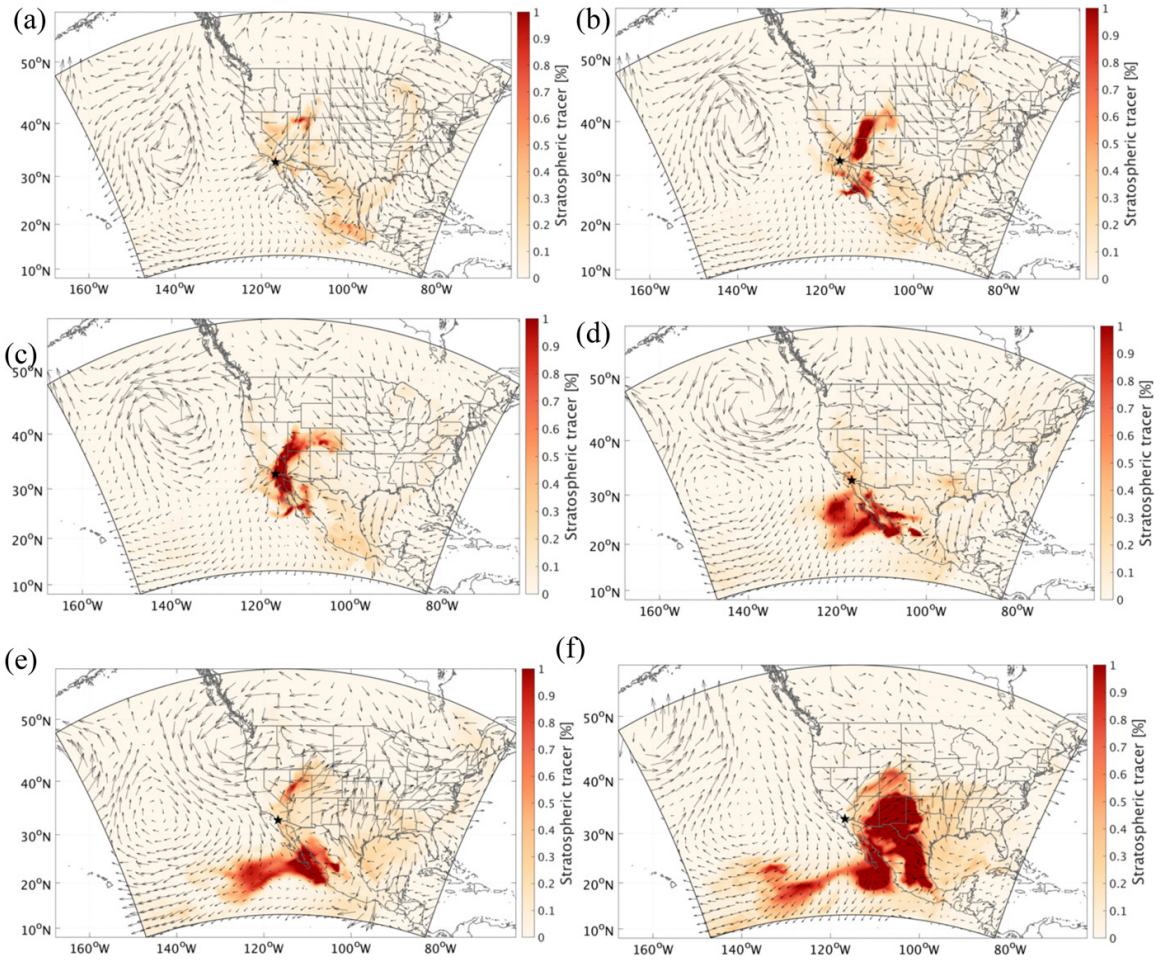

Figure 4.9. Spatial distribution of the WRF stratospheric tracer at 390mabove ground level at (A) 1000 hours PST on April 30, (B) 0000 hours PST on May 1, (C) 0500 hours PST onMay 1, (D) 1600 hours PST on May 2, (E) 0000 hours PST onMay 4, and (F) 1400 hours PST on May 5 (all 2014). The black stars indicate the location of San Diego.

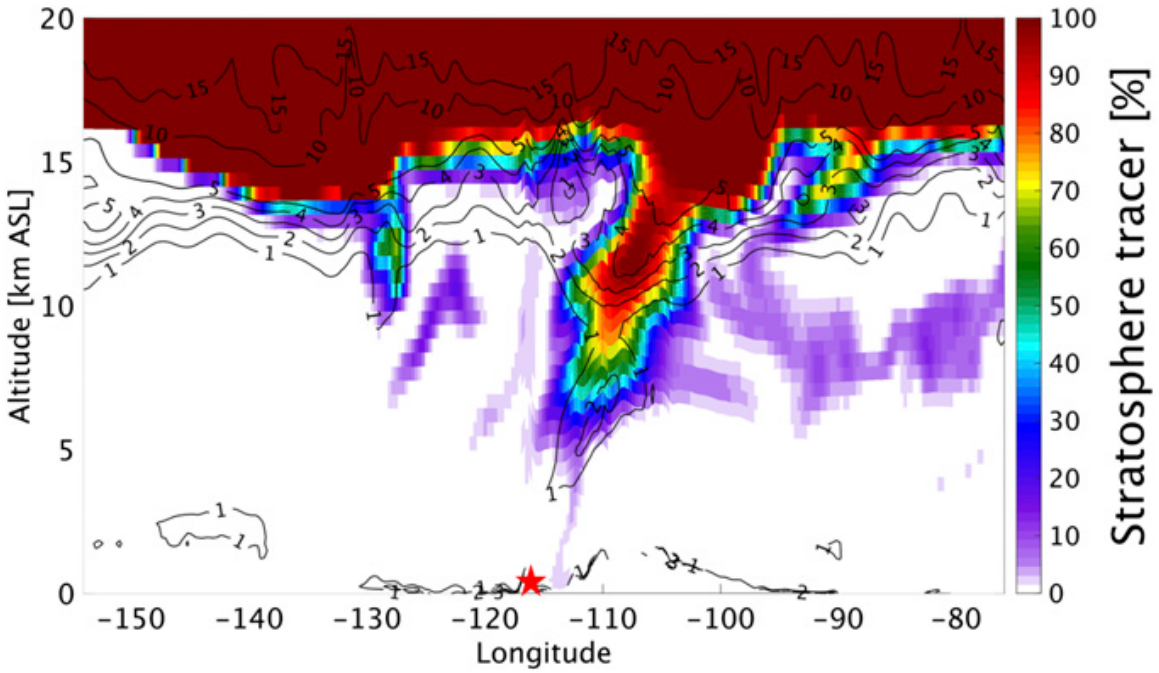

Figure 4.10. Zonal cross-section of the WRF stratospheric tracer with PV (unit: PV unit) contours superimposed at 0000 hours PST on May 1, 2014. The red star indicates the location of San Diego.

4.6 ^{35}S Box Model Calculation

[*Priyadarshi et al.*, 2012a] used a 1-D 4-box model, which was developed to calculate the $^{35}SO_4^{2-}$ concentration in fine aerosol collected at the Scripps Pier, to quantify air mixing during the Santa Ana wind events and shallow stratosphere-troposphere exchange events. The model parameters (Table 4.1) and uncertainties were thoroughly described by [*Priyadarshi et al.*, 2011b; *Priyadarshi et al.*, 2012a]. Specifically, it was suggested that in a shallow stratosphere-troposphere exchange event, ~7% of the total air masses in the free troposphere was originated in the low stratosphere per day, while during the Santa Ana wind event, ~41% of air mass sampled in the marine boundary layer recently originated from the free troposphere per day [*Priyadarshi et al.*, 2012a]. Here, we utilize the same box model and combine the mixing effects of stratospheric intrusions and Santa Ana winds (i.e., 7% × 41% = ~3% of total air sampled in the boundary layer originated from the stratosphere in one day) to simulate the coupling between Santa Ana winds and

stratospheric intrusions in this study. The averaged $^{35}SO_4^{2-}$ concentration during May 3-7 2014 calculated by the model was 7100 atoms m^{-3}, reasonably agreeing with our measurement (7390 atoms m^{-3}). The model predicts that the averaged $^{35}SO_2$ and $^{35}SO_4^{2-}$ concentrations during the episode period (April 29 – May 3) were 2100 and 11000 atoms m^{-3}, respectively, which however cannot be verified in this stage because samples were not collected during April 29 – May 2 2014 due to operational issues. To date, the highest $^{35}SO_2$ concentration (1800 atoms m^{-3}) was measured at New Haven by [*Tanaka and Turekian*, 1995] in April 1992. The highest atmospheric $^{35}SO_4^{2-}$ concentration was estimated to be 15000 atoms m^{-3} from rainwater samples as discussed previously [*Cho et al.*, 2011]. These field-based measurements suggest that our model-estimated ^{35}S concentrations during deep stratospheric intrusions are plausible. If only the mixing of stratospheric intrusion (or the Santa Ana wind) was considered, the estimated averaged $^{35}SO_4^{2-}$ concentration during May 3-7 2014 was 3400 (or 742) atoms m^{-3}, significantly lower than our field-based data and previous calculations, implying that the coupling between stratospheric intrusions and Santa Ana winds is crucial to lead to the observed high ^{35}S, and probably O_3, levels.

Table 4.2. Parameters of ^{35}S box model for calculating $^{35}SO_4^{2-}$ at San Diego, California[a]

Parameter	Value
A. Height, km	
Planetary Boundary Layer (Box 1)	0.6
Buffer Layer (Box 2)	1.0
Free Troposphere (Box 3)	8.0
Lower Stratosphere (Box 4)	16.0
B. Cosmic ray production rate of ^{35}S (atoms cm^{-3} d^{-1})	
P_1	2.8×10^{-6}
P_2	2.8×10^{-6}
P_3	6.5×10^{-5}
P_4	1.1×10^{-4}
C. $^{35}SO_2$ lifetime (days)	
$\tau_{ox-1} = \tau_{ox-2}$	4(8)[b]
$\tau_{ox-3} = \tau_{ox-4}$	8
τ_d	1.5
$\tau_{c1} = \tau_{c2}$	5(∞)[b]
$\tau_{c3} = \tau_{c4}$	143
τ_λ	126
D. $^{35}SO_4^{2-}$ removal lifetime (days)	
$\tau_{r1} = \tau_{r2}$	12(3)[b]
τ_{r3}	24
τ_{r4}	365

Table 4.2. Parameters of ^{35}S box model for calculating $^{35}SO_4^{2-}$ at San Diego, California[a] (Countinued)

Parameter	Value
E. Air mass mixing time (days)	
$\tau_{12} = \tau_{21}$	$1(\tau_{12}=\infty)$[b]
$\tau_{23} = \tau_{32}$	$14(\tau_{12}=\infty)$[b]
$\tau_{34} = \tau_{43}$	290
τ_H	30
τ_{HS}	1

a. The San Diego ^{35}S box model and input parameters are adopted from [*Priyadarshi et al.*, 2012a; *Priyadarshi et al.*, 2013]

b. Values in bracket represent those during the Santa Ana period (April 29 – May 3 2014) as used in [*Priyadarshi et al.*, 2012a]

Previous studies suspected that the mixing between O_3-rich stratospheric air masses and polluted plumes might accelerate the oxidation of SO_2 [*Lin et al.*, 2016c]. In this study, significant enhancement of *j/k* are observed during the post Santa Ana period (May 4-5) (Figure 4.4a), indicating stronger photochemical production of O_3. This phenomenon may be because the downward transported stratospheric O_3 actively participated in the O_3-NO_x-VOCs chemistry (39, 40) when the O_3-rich air masses were mixed with polluted low-altitude air masses (41). The decreased O_3 mixing ratio (Figure 4.4a) suggested that the photochemically produced O_3 might rapidly participate in other reactions (e.g., the formation of secondary aerosols including heterogeneous productions of sulfate) as a sink. If the oxidation lifetime of SO_2 in the boundary layer during the post Santa Ana period (May 4-5) is reduced from 4 to 0.5 days, an averaged $^{35}SO_4^{2-}$ concentration during May 3-7 of 7400 atoms m^{-3} is obtained, perfectly matching the observational data (7390 atoms m^{-3}). Although this hypothesis has yet to be tested by high temporal resolution $^{35}SO_2/^{35}SO_4^{2-}$ measurement and proper chemistry modeling, the suspected enhanced aerosol formation rate is partly supported by higher $PM_{2.5}$ concentrations (mean±σ) during the post Santa Ana period (10.8±3.3 μg m^{-3}) than the Santa Ana period (6.3±2.4 μg m^{-3}) (2014 annual mean: 8.1±3.6 μg m^{-3}). This potential influence is particularly important in the regions heavily impacted by SO_2 emissions and stratospheric intrusions such as East Asia [*Lin et al.*, 2016c; *Lu et al.*, 2010; *Shao et al.*, 2006; *Verstraeten et al.*, 2015].

4.7 Conclusions and Implications

In summary, our result is encouraging because it demonstrates the high sensitivity of ^{35}S to stratospheric intrusions and reveals the crucial role of coupling between Santa Ana wind and stratospheric intrusions in bringing fresh stratospheric air to southern California coast. The absolute amount of radiation (or activity) in the ^{35}S-rich sample is small (0.68 mBq m^{-3}) and not a concern for human health, but our highly sensitive measurement technique renders ^{35}S a sensitive tracer of stratospheric intrusions, an important process in nature for which there are gaps in understanding.

There is an urgent need to identify and screen the "exceptional events" for ground level O_3 caused by stratospheric intrusions. Our study reveals that field-based measurement of cosmogenic ^{35}S at ground level can serve as an additional valuable diagnostic for the occurrence of deep stratospheric intrusions. This method has three advantages: 1) The optimized aerosol sample handling procedures and low-level liquid scintillation spectroscopy method enable measuring low ^{35}S activities (0.2 disintegration per minute) in a simple, economical, effective, and highly sensitive way [*Brothers et al.*, 2010]; 2) The half-life of ^{35}S (87 days) is ideal for studying atmospheric processes on synoptic time scales, and it also permits a relatively long storage time of aerosol samples, which are routinely collected by the EPA, until the sampling period is suspected; 3) Radiogenic ^{35}S is of potential in providing additional information on the impacts of stratospheric intrusions on gas-to-particle conversion rates and thereafter possible PM pollution events.

While the present box model shows the ability to reproduce the observed $^{35}SO_4^{2-}$ concentration, we should mention that the box model result still possesses uncertainties because most parameters in the model are not constrained by field-based measurements [*Priyadarshi et al.*, 2012a]. The low temporal resolution of ^{35}S measurements in this study limits the use of field-based ^{35}S measurement in evaluating the model result and improving the model. In the future, a more strategic and comprehensive study can be designed to fully resolve the impacts of deep stratospheric intrusions on the tropospheric sulfur cycle and ground level O_3 concentrations. The Realtime Air Quality Modeling System (RAQMS) model has been widely used in predicting and analyzing the stratospheric intrusion events [*Baylon et al.*, 2016; *Langford et al.*, 2015a; *Sullivan et al.*, 2015]. Although the RAQMS model underestimated the ground level O_3 concentration in this episode (May 3, 2014), it showed capability to forecast the east Pacific storm track and stratospheric O_3 intrusions in the higher atmosphere (http://raqms-ops.ssec.wisc.edu/previous_products/). The forecast result of RAQMS can be used to design intensive aerosol and SO_2 sampling for ^{35}S measurements ~2 days prior to the occurrences of

stratospheric intrusion events. With high temporal resolution (0.5-1 day), the evolution of ^{35}S during deep stratospheric intrusions can be resolved.

Aircraft field missions showed that concentrations of cosmogenic beryllium isotopes (^{7}Be and ^{10}Be, half-life = 53 days and 1.38 My, respectively) in the lower stratosphere can be ~40-110 times greater than the boundary layer [*Aldahan et al.*, 2008; *Jordan et al.*, 2003]. Similar measurements for ^{35}S are crucial to constrain box model results. More efforts on modeling works (e.g. updating ^{35}S production rate and incorporating ^{35}S into a 3-D chemistry transport model with O_3 and sulfur chemistry) can advance quantifying the impacts of stratospheric intrusions on ground level ^{35}S and O_3 at high temporal and spatial resolutions. The extent to which stratospheric intrusions may affect the gas-to-particle conversion rate can also be quantified by coupled measurements of ^{7}Be and ^{35}S and proper modeling [*Tanaka and Turekian*, 1995].

Climatological studies revealed the western U.S. and the Himalayas are two global hotspots for deep stratospheric intrusions [*Skerlak et al.*, 2014]. In particular, a global chemistry-climate model showed strong contributions of stratospheric intrusions to MDA8 ground level O_3 in Nevada [*Langford et al.*, 2015b; *Lin et al.*, 2012b; *Lin et al.*, 2015]. Our previous measurements showed high ^{35}S concentrations in San Fernando Valley at California (a sampling site close to Nevada) [*Brothers et al.*, 2010] and Mount Everest at Himalayas [*Lin et al.*, 2016b], supporting the model results. These measurements imply that the spatial distribution of ^{35}S may provide invaluable information on regional variabilities of stratospheric intrusion strength and frequency to constrain model results. The high sensitivity of ^{35}S also allows for precise quantification of the contribution of aged stratospheric air to the background troposphere, which is crucial in understanding the O_3 budget [*Lin et al.*, 2015; *Verstraeten et al.*, 2015], the carbon cycle [*Liang et al.*, 2008; *Thiemens et al.*, 2014] and the variations of other cosmogenic radionuclides such as ^{10}Be, a primary proxy archive of past changes in solar activity, cosmic rays and geomagnetic field intensity [*Aldahan et al.*, 2008].

4.8 Materials and Methods

Size-segregated aerosol samples were collected by a high-volume flow aerosol sampler (HVP-4300AFC, Hi-Q, U.S.) operated at a flow rate of ~1.13 m^3 min^{-1}. Soluble sulfate extracted from glass-fiber filter papers was subject to ^{35}S analysis using an ultra-low level liquid scintillation counting spectrometer (Wallac 1220 Quantulus) technique [*Brothers et al.*, 2010]. Data of air pollutants (O_3, NO_2, NO, CO and $PM_{2.5}$) and meteorological variables (temperature, RH, solar radiation, wind speed and direction) were provided by the Air Pollution Control District County of San Diego (www.sdapcd.org). Field-based measurements were supported by a mesoscale meteorology model (WRF), which permitted investigations of stratospheric intrusion processes [*Lin et al.*, 2016c]. Detailed sampling, chemical processing, quality assurance and control procedures, as well as modeling approach can be found in Supporting Information.

4.9 Supporting Information

4.9.1 Aerosol Sampling, ^{35}S Measurements, Quality Assurance and Control

The high-volume flow aerosol sampler (HVP-4300AFC, Hi-Q, U.S.) was equipped with a cascade impactor (TE-234, Tisch, U.S.) and glass-fiber filters (Slotted: Tisch, U.S.; 8"×10" backup: Whatman, U.K.) were used as filtration substrates to collect airborne particulate matters with aerodynamic diameters larger than 7.2 μm, between 7.2 and 0.95 μm, and less than 0.95 μm, respectively. Each set of samples was collected continuously for 23-172 hours. The time gap between sets of samples varies from 2-15 days because of operational issues. A static field blank was created by loading a fresh filter on the sampler for 5–10 min without turning on the pump.

Soluble sulfate extracted from filter papers was converted to aqueous Na_2SO_4 solution and mixed with Insta Gel Plus cocktail in a scintillation vial to determine ^{35}S radionuclide concentrations using an ultra-low level liquid scintillation counting spectrometer (Wallac 1220 Quantulus) technique [*Brothers et al.*, 2010]. To improve the ratio of signal to noise, organic contaminants and chlorine salts were removed by a PVP (polyvinylpyrrolidone) resin and a Dionex

Ag cartridge (OnGuard II), respectively. Each sample was counted for 6 times (2-hour counting for each cycle). Averages and standard deviations were reported. To determine the background activity, the static field blank was subjected to the same chemical analysis procedure. The raw ^{35}S counting data was corrected for the background activity and for the decay time. Given the low activity of ^{35}S in natural aerosol samples, the measured ^{35}S activity (unit: disintegrations per minute, *dpm*) was reported as the $^{35}SO_4^{2-}$ concentration (unit: atoms m^{-3}) following previous studies [*Brothers et al.*, 2010]. The $^{35}SO_4^{2-}$ concentration was determined using the relationship: $[^{35}SO_4^{2-}] = (DPM \times t_{1/2} / \ln(2)) / V_{air}$, where DPM, $t_{1/2}$ and V_{air} represent the total activity of ^{35}S in the unit of *dpm*, the radioactive-decay half-life of ^{35}S in the unit of minute, and total air flow in the unit of m^{-3} in each sample, respectively.

Given the huge deviation of ^{35}S activity in the sample collected during May 3-7 2014 from the background activity, additional quality assurance and quality control (QA/QC) were conducted. The energy spectra of the sample were checked and compared with $^{35}SO_4^{2-}$ standard, showing that the signal was clean and the measured high activity was unlikely contaminated by other radionuclides (e.g.,^{3}H, ^{14}C or ^{36}Cl) (Figure 4.11). Standard and blank were counted right after the counting of this sample and compared with previous measured results. The differences were within measurement error and no significant drift was observed. The sample was recounted one month after the first measurement and recounted again once the naturally present ^{35}S had fully decayed, which further supported that the measured activity was the decay event of ^{35}S rather than the interference from other radionuclides. Database from Radiation Division of the Environment, Health & Safety department in UCSD showed no ^{35}S use or inventory at the sampling building (Pacific Hall) during this period, suggesting the sample was not contaminated during collection. Cross-contamination in chemical processing is highly unlikely because the ^{35}S activity of our laboratory standard, which was stored separately in another room, was only ~1/4 of measured activity in this sample. In summary, these procedures allowed us to assure the measured activity

was not an experimental artifact and there was no experimental reason or scientific evidence showing that we should exclude this data point from the dataset.

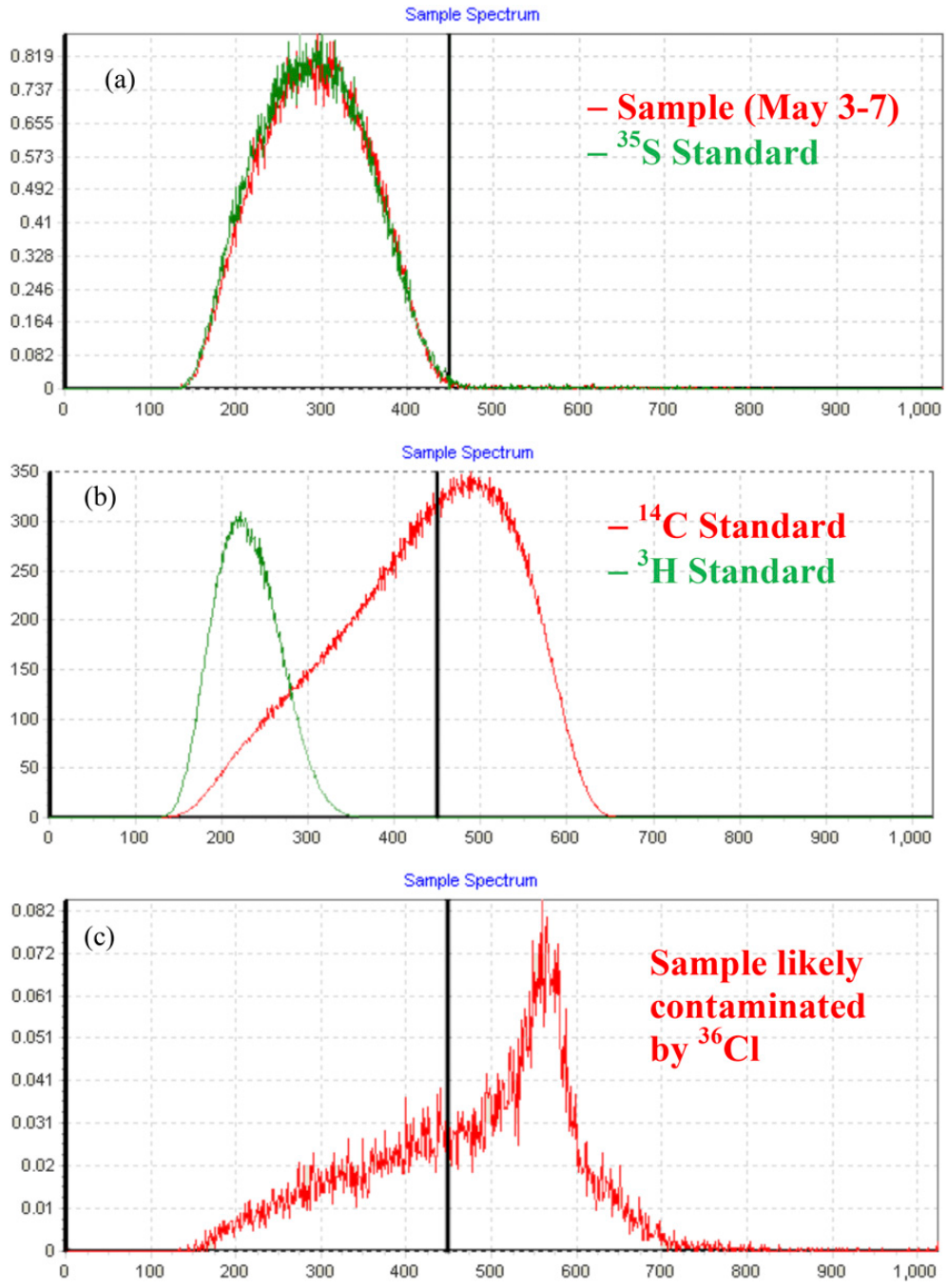

Figure 4.11. Energy spectrums of (A) the aerosol sample collected during May 3–7, 2014 and ^{35}S standard with comparable activity, (B) ^{14}C and ^{3}H standards, and (C) an aerosol sample (not reported in this study) likely contaminated by ^{36}Cl (or other unknown nuclides) because of the incomplete removal of chlorine.

4.9.2 Air Pollutants and Meteorological Data

The Air Pollution Control District County of San Diego (SDAPCD) monitoring network follows the guidelines of U.S. EPA and all data provided have been subject to strict QA/QC procedure required by the U.S. EPA (SDAPCD Ambient Air Quality Monitoring Quality Management Plan, available at: http://www.sdapcd.org/content/dam/sdc/apcd/PDF/Misc/APCD_SDAPCD_QMP.pdf). The Alpine station (32.836°N, 116.777°W, 516 m a.s.l), the easternmost station in the San Diego county, was selected because it is the O_3 design value site. In most of days, this station monitors the air downwind of the San Diego county's major metropolitan areas, while in the Santa Ana days, it is located at the upwind region monitoring the air entrained to the San Diego county. Compared to other stations in the San Diego county, this station is less influenced by the "titration effect" ($NO+O_3 \rightarrow NO_2+O_2$), which lowers ambient O_3 concentrations in an urban environment by means of substantial NO emissions and NO_x scavenging [*Chan et al.*, 1998].

4.9.3 Satellite Observations

Wildfire events over the southern California during the sampling period were detected by the Moderate-Resolution Imaging Spectroradiometer (MODIS) mounted on NASA's Terra and Aqua satellite. The spatial resolution is 1×1 km^2 and the dataset was obtained on NASA's website (http://earthdata.nasa.gov/data/near-real-time-data/firms). The vertical O_3 profiles obtained from the Global Ozone Monitoring Experiment 2 (GOME-2) instrument were used to study the structure of the upper troposphere. The data and imageries are provided by the Royal Netherlands Meteorological Institute in the framework of the European Organization for the Exploitation of Meteorological Satellites' Satellite Application Facility on Ozone and Atmospheric Chemistry Monitoring, and are available from the Tropospheric Emission Monitoring Internet Service website (http://www.temis.nl/profiles/).

4.9.4 Mesoscale Meteorological Simulation and Further discussion

The evolution of stratospheric air masses in the atmosphere during the study period was simulated and quantified by the Weather Research and Forecast model coupled with Chemistry module (WRF-Chem). WRF-Chem is an advanced atmospheric modeling system with capability of simulating complicated dynamical, physical and chemical processes in the atmosphere. In this study, the chemistry module was activated only to provide the initial condition of a stratospheric tracer, which was treated as an inert gas without reacting with other species. Therefore, only advection, convection and turbulence diffusion during the tracer transport were considered in the simulation. The Final (FNL) reanalysis data from the National Center of Environmental Prediction (NCEP) were used to provide the initial and boundary meteorological conditions for the simulation, with the fraction of stratospheric air mass above the tropopause being initialized as 100% at the beginning. The domain setting for the simulation is shown in Figure 4.12. The horizontal resolutions of the outer domains are 27 km and 9 km, respectively, both with 50 vertical layers and the top layer at 50 hPa. The simulation was started on April 19, 2014 - 8 days ahead of the investigated period - and lasted for 20 days till May 8, 2014. The 8 days ahead were considered as the spin-up time for the simulation to allow the stratospheric tracer to accumulate in the troposphere to a reasonable level comparable to realistic conditions at the beginning of the investigated period. The simulation was conducted for the investigated period continuously without re-initialization, enabling stratospheric air masses to accumulate and transport in the troposphere [*Lin et al.*, 2016c]. In order to prevent the simulations from drifting away from the realistic conditions, Four-dimensional data assimilation (FDDA) was conducted every 6 hours using temperature, wind and humidity fields from FNL reanalysis data.

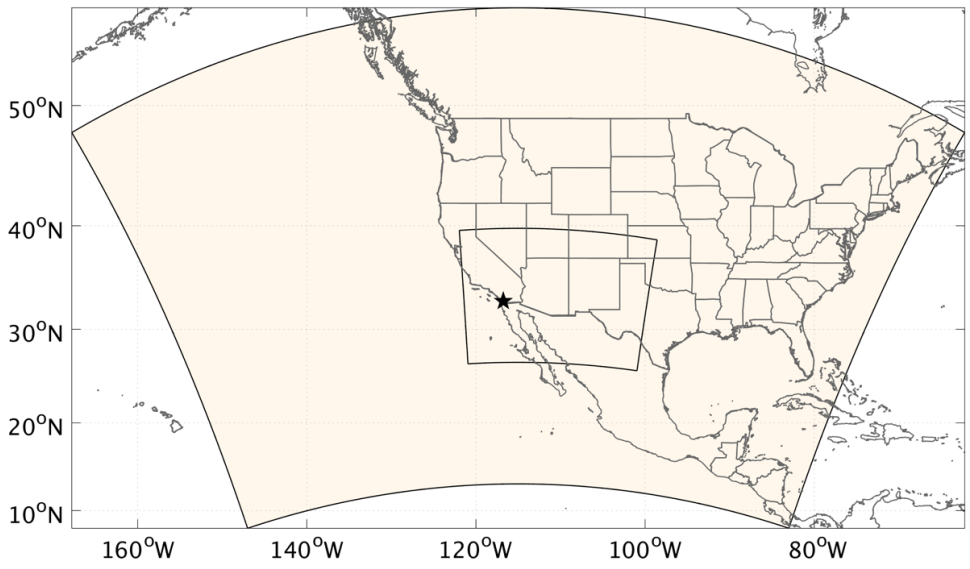

Figure 4.12. The domain setting for the WRF simulation. The black star indicates the location of San Diego.

A relatively simple (compared to chemical transport models) but quantitative Lagrangian particle dispersion model [*Stohl et al.*, 1998] was utilized to quantify the contribution of stratospheric O_3. Specifically, the FLEXPART-WRF version 3.2 driven by WRF output data was utilized, with horizontal resolution of 0.1 degree and 50 vertical layers from surface to 9000 m above ground level. Whether a particle is stratospheric or not is determined using the dynamical definition of the tropopause based on a threshold value for PV of 2.0 PVU. In the calculation, stratospheric particles were assigned a mass according to the equation $M_{O3}=M_{air}\times PV\times C\times 48/29$, where $C=60\times10^{-9}$ PVU^{-1} is the average ratio between the O_3 mixing ratio and PV in the lower stratosphere in spring based on the ozonesonde data and factor 48/29 converts from a volume to mass mixing ratio [*Cooper et al.*, 2005]. Detailed description of the FLEXPART stratospheric O_3 tracer modeling is given by [*Cooper et al.*, 2005].

The process how the stratospheric air masses intruded to the troposphere and reached coastal southern California during the Santa Ana event is discussed in the main text. In addition, it is noted that the stratospheric air masses were piled up in the free troposphere above the Pacific Ocean near Baja California by the convergent wind flow behind the trough line during May 2-4, 2014 (Figure 4.8), which descended to the boundary layer slowly. These aged stratospheric air were transported to Arizona and New Mexico by strong southwestly flow and penetrated downward dramatically on May 5, 2014 (Figure 4.9). Although *in situ* ground level O_3 measurement show minimal influences at San Diego region on May 5, 2014 (Figure 4.3a), such synoptic situation may contribute in part to the observed high $^{35}SO_4^{2-}$ concentration during May 3-7 2014 because $^{35}SO_4^{2-}$ is able to detect aged stratospheric air while the stratospheric signature in O_3 is erased rapidly by tropospheric processes [*Lin et al.*, 2016b; *Lin et al.*, 2016c; *Priyadarshi et al.*, 2012a]. However, due to the low temporal resolution of ^{35}S measurement in this study, it is difficult to verify this hypothesis.

4.10 Acknowledgement

This study was supported in part by the National Science Foundation - Atmospheric Chemistry Division (Grant No. AGS1258305). We thank Dr. J. Hill-Falkenthal for helpful discussion on ^{35}S data, T. Jackson and R. Thomas for helping in sampler setups. Two anonymous reviewers are acknowledged for their valuable comments that helped to improve the manuscript. M.L. acknowledges a fellowship from the Guangzhou Elite Project (JY201303).

This chapter, in full, is a reprint of the material "Detection of deep stratospheric intrusions by cosmogenic ^{35}S" as it appears in Proceedings of the National Academy of Sciences of the United States of America 2016. Lin, Mang; Su, Lin; Shaheen, Robina; Fung; Jimmy C.H.; Thiemens, Mark H., National Academy of Sciences of the United States of America 2016. The dissertation author was the primary investigator and author of this paper.

Chapter 5 Quantification of gas-to-particle conversion rates of sulfur in the terrestrial atmosphere using high-sensitivity measurements of cosmogenic ^{35}S

5.1 Abstract

The productions of sulfuric acid and sulfate aerosol (SO_4^{2-}) from the oxidation of sulfur dioxide (SO_2) are fundamental chemical processes in nature and play important roles in the sulfur cycles and climates of Earth and extraterrestrial bodies such as Venus and Europa. Numerous experimental and theoretical efforts have been made to understand kinetics and mechanisms of SO_2 oxidation, but quantifying SO_2-to-SO_4^{2-} conversion rates in the terrestrial atmosphere remains a challenge due to varying sources for both SO_2 and SO_4^{2-}. Here we use high-sensitivity measurements of cosmogenic ^{35}S (half-life = 87 days), a radiogenic isotope exclusively produced by cosmic rays in the atmosphere, in both SO_2 and SO_4^{2-} collected from the ambient atmosphere to assist in such quantification. The monthly SO_2-to-SO_4^{2-} conversion rates in the boundary layer over coastal California and the Tibetan Plateau are calculated using a steady-state ^{35}S box model. A distinct seasonal variation of SO_2-to-SO_4^{2-} conversion rates with maximum in summer and minimum in winter is found in both regions. The rapid SO_2-to-SO_4^{2-} conversion rates in summer (ranging from ~1 to ~2 d^{-1}) not only provide an additional field-based constraint for reducing uncertainties in current chemistry transport and climate models, but also highlight the need for a better understanding of SO_2 oxidation pathways in the chemically complex terrestrial atmosphere. Implications for future field missions, modeling and experimental investigations are discussed.

5.2 Introduction

Airborne particles (or aerosols) in the terrestrial atmosphere have substantial influences on public health [*Lelieveld et al.*, 2015], visibility [*Tao et al.*, 2014b], ecosystem [*Longo et al.*, 2016], weather [*Creamean et al.*, 2013], and climate [*Haywood and Boucher*, 2000]. They are emitted to the atmosphere directly (primary aerosols) or produced in the atmosphere via gas-to-particle

conversion (secondary aerosols). Because secondary aerosols contribute significantly to the total aerosol burden [*Huang et al.*, 2014a], an accurate quantification of gas-to-particle conversion rate is crucial to estimate the budget of aerosols and evaluate their impacts [*Liu et al.*, 2016b]. As a major component of aerosols, SO_4^{2-} (including condensed-phase sulfuric acid and sulfate aerosol) is mainly oxidized from SO_2 and closely associated with mortality [*Fang et al.*, 2017] and radiative forcing [*Haywood and Ramaswamy*, 1998]. Sulfur is an ubiquitous element in the Universe, and therefore SO_2 and SO_4^{2-} are also important components in some other planets (e.g., Venus and Mars) and moons of Jupiter (e.g., Europa and Io) that profoundly influence climates and geological structures [*Carlson et al.*, 1999; *Franz et al.*, 2014; *Pearl et al.*, 1979; *Zhang et al.*, 2010]. A complete understanding of sulfur chemistry in the present-day terrestrial atmosphere can shed light on similar processes that occur in the Earth's paleo-atmosphere and in the atmospheres of extraterrestrial bodies.

In the terrestrial atmosphere, secondary SO_4^{2-} is synthesized via a number of SO_2 oxidation pathways, such as gaseous oxidation by OH radical or Criegee intermediates and aqueous oxidation by H_2O_2, O_3, O_2 (catalyzed by transition metal ions) or hypohalous acid (HOX; X = Cl or Br) [*Chen et al.*, 2016a; *Zhang et al.*, 2015]. Because of the complicated SO_4^{2-} formation chemistry, laboratory kinetic experiments cannot accurately simulate processes occurring in nature. Models using laboratory data fail to fully explain observations in the ambient atmosphere, especially in the boundary layer [*Berresheim et al.*, 2014; *van Donkelaar et al.*, 2008; *Zheng et al.*, 2015a]. Early studies estimated the ambient SO_2-to-SO_4^{2-} conversion rate using in-situ measurements of SO_2 and SO_4^{2-} concentrations [*Alkezweeny and Powell*, 1977; *Luria et al.*, 2001; *Meagher et al.*, 1983; *Zak*, 1981]. There is a fundamental assumption in their calculations that atmospheric SO_4^{2-} is exclusively produced from SO_2 oxidation and not affected by other sources such as primary SO_4^{2-} from crustal minerals and fossil fuel combustion. Unfortunately, this assumption is not valid for most environments because of varying sources for both SO_2 and SO_4^{2-} (Figure 5.1a). To accurately

quantify the ambient SO_2-to-SO_4^{2-} conversion rate using SO_2 and SO_4^{2-} concentrations, one has to consider the production/emission rates of all other sources, which is difficult to achieve.

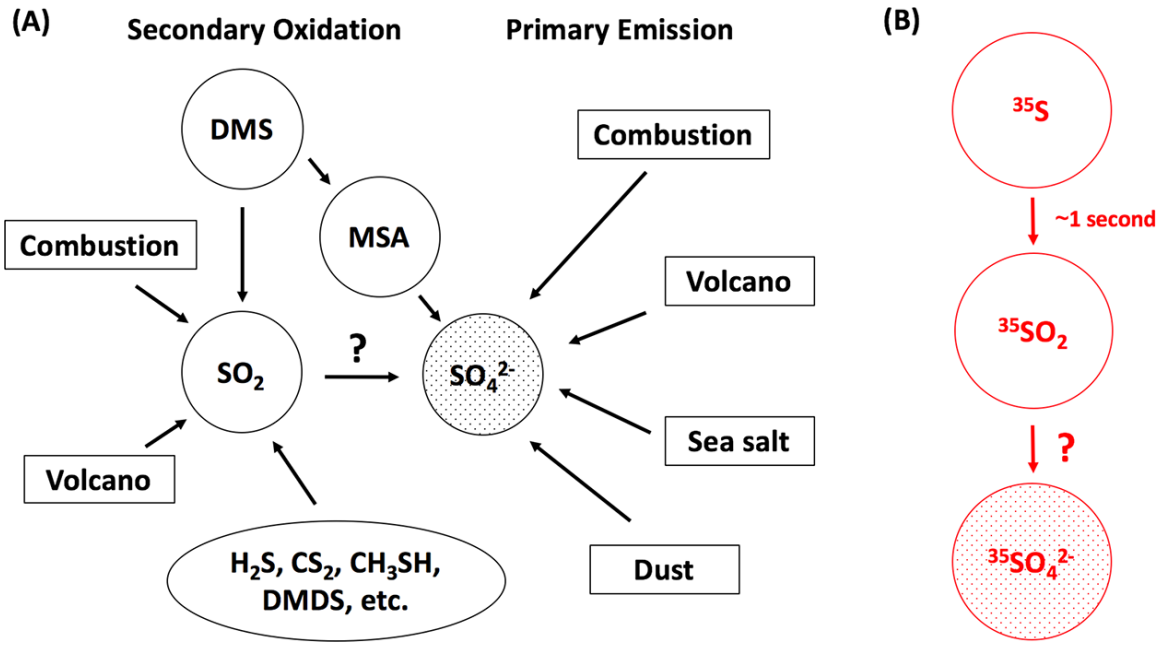

Figure 5.1. Schematic graph showing main sources of (A) stable and (B) cosmogenic sulfate in the troposphere. DMS, MSA, and DMDS stand for dimethyl sulfide (CH_3SCH_3), methanesulfonic acid (CH_3SO_3H), and dimethyl disulfide (CH_3SSCH_3), respectively. The shaded circles are particlephase, while others are gas-phase.

Cosmic ray spallation, in which a nucleus impacted by a high-energy particle shatters into many nuclei, is responsible for the production of some elements and isotopes. This process not only occur in deep space but also in the terrestrial atmosphere. Cosmogenic ^{35}S and ^{38}S are radiogenic isotopes spallogenically produced in the terrestrial atmosphere by the bombardment of ^{40}Ar with high energy cosmic rays. Because cosmogenic sulfur behaves nearly identically to stable sulfur [*Junkermann and Roedel*, 1985; *Turekian and Tanaka*, 1992], it exists in gas (SO_2) and particulate (SO_4^{2-}) phases simultaneously. Subsequently, the radiogenic sulfur may offer an actual clock to quantify the sulfur gas-to-particle conversion rate. A unique character of cosmogenic sulfur is that

it is exclusively produced in the higher atmosphere and convert to radiogenic SO_2 in ~1 s after production [*Junkermann and Roedel*, 1985; *Turekian and Tanaka*, 1992]. Given their short half-life (^{35}S: ~87 d; ^{38}S: ~2.8 h), concentrations of cosmogenic sulfur in primary SO_4^{2-} sources (e.g. fossil fuel) and other sulfur-containing trace gases (e.g. biogenic dimethyl sulfide [DMS]) are negligible, which means that radiogenic SO_4^{2-} is exclusively produced by the conversion of radiogenic SO_2 in the atmosphere (Figure 5.1b). The single source of radiogenic SO_2 and SO_4^{2-} notably simplifies the quantification of SO_2 and SO_4^{2-} lifetimes.

A pilot study measured ^{38}S in SO_2 to estimate the lifetime of SO_2 [*Junkermann and Roedel*, 1983]. The result implied that SO_2 oxidation rates in the ambient atmosphere might be much faster than previously thought. Because of the short half-life of ^{38}S (~2.8 h) and large uncertainty in measurements, this method has not been further developed. The radionuclide ^{35}S is the only radiogenic sulfur isotope that possesses a half-life longer than 3 hours, and its half-life (~87 d) is of a proper time scale for understanding a variety of physical and chemical processes in nature, especially for quantifying the lifetime of SO_2 and SO_4^{2-} in the atmosphere. Turekian and Tanaka, the pioneers in such studies, first measured $^{35}SO_2$ and $^{35}SO_4^{2-}$ in aerosols and rain water to determine the deposition rate of SO_2, with an assumption that the SO_2-to-SO_4^{2-} conversion rate is constant [*Tanaka and Turekian*, 1991; *Turekian and Tanaka*, 1992]. In a later study, with additional measurements of another cosmogenic isotope ^{7}Be (half-life = ~53 d), the seasonal variation of SO_2-to-SO_4^{2-} conversion rate was determine [*Tanaka and Turekian*, 1995], but the obtained values possess large uncertainties as a result of conventional low-sensitivity ^{35}S measurements. Due to the difficulty of ^{35}S measurements, similar studies had been scarce until 2010, when *Brothers et al.* [2010] developed an optimized ^{35}S analytical method for atmospheric samples. Using the high-sensitivity method [*Brothers et al.*, 2010], combined measurements of $^{35}SO_2$ and $^{35}SO_4^{2-}$ were conducted at coastal California and the Tibetan Plateau to understand atmospheric vertical mixing [*Brothers et al.*, 2010; *Priyadarshi et al.*, 2012b; *Priyadarshi et al.*, 2014]. However, the SO_2-to-

SO_4^{2-} conversion rate was assumed to be constant in previous data interpretation, and chemical information recorded by cosmogenic ^{35}S was not explored. In this study, we present a new and comprehensive analysis to quantify ambient SO_2-to-SO_4^{2-} conversion rates at coastal California and the Tibetan Plateau using yearlong high-sensitivity ^{35}S measurements.

5.3 Experimental Methods

5.3.1 Sample Collection and Cosmogenic ^{35}S Analysis

High-sensitivity measurements of cosmogenic ^{35}S from two sampling sites (Figure 5.2a and Figure 5.3) are used for quantifying SO_2-to-SO_4^{2-} conversion rates. Scripps Pier Shore Station (32.85°N, 117.28°W, 10 m above sea level) (hereafter referred to as Scripps) is located at the Scripps Institution of Oceanography in coastal southern California, which is affected by anthropogenic emissions from the highly-populated Los Angeles area and busy ship-traffic in the polluted marine boundary layer [*Ault et al.*, 2010; *Dominguez et al.*, 2008]. Samples at this site were collected from June 2009 to July 2010. Nam Co Monitoring and Research Station for Multisphere Interactions (30.77°N, 90.98°E, 4730 m above sea level) (hereafter referred to as Nam Co) is a relatively pristine background site located at the central Tibetan Plateau and influenced mainly by long-range transport of air pollutants from South Asia [*Cong et al.*, 2013; *Li et al.*, 2016]. Samples at this site were collected from November 2010 to December 2011 (except for January 2011 and the period of July-November 2011 due to operational issues). Total suspended particle (TSP) samples were collected on filter papers by high-volume aerosol samplers at an operation flow rate of ~1 m^3 min^{-1}, while ambient SO_2 was trapped by KOH-impregnated backup filters installed in the same samplers. Glass-fiber and quartz filters (Whatman) were used in Scripps and Nam Co, respectively [*Priyadarshi et al.*, 2012b; *Priyadarshi et al.*, 2014]. Fractions of SO_2 adsorbed on filters that collect TSP were estimated as ~3% for both substrates [*Forrest and Newman*, 1973]. All samples were converted to aqueous SO_4^{2-} in the University California San Diego and subjected to cosmogenic ^{35}S analysis using an ultra-low-level liquid scintillation

counting spectrometer (Wallac 1220 Quantulus) technique developed by [*Brothers et al.*, 2010]. The reported ^{35}S concentrations are corrected for blank and decay time. Detailed chemical analysis procedure can be found in the literature [*Brothers et al.*, 2010; *Priyadarshi et al.*, 2012b; *Priyadarshi et al.*, 2014].

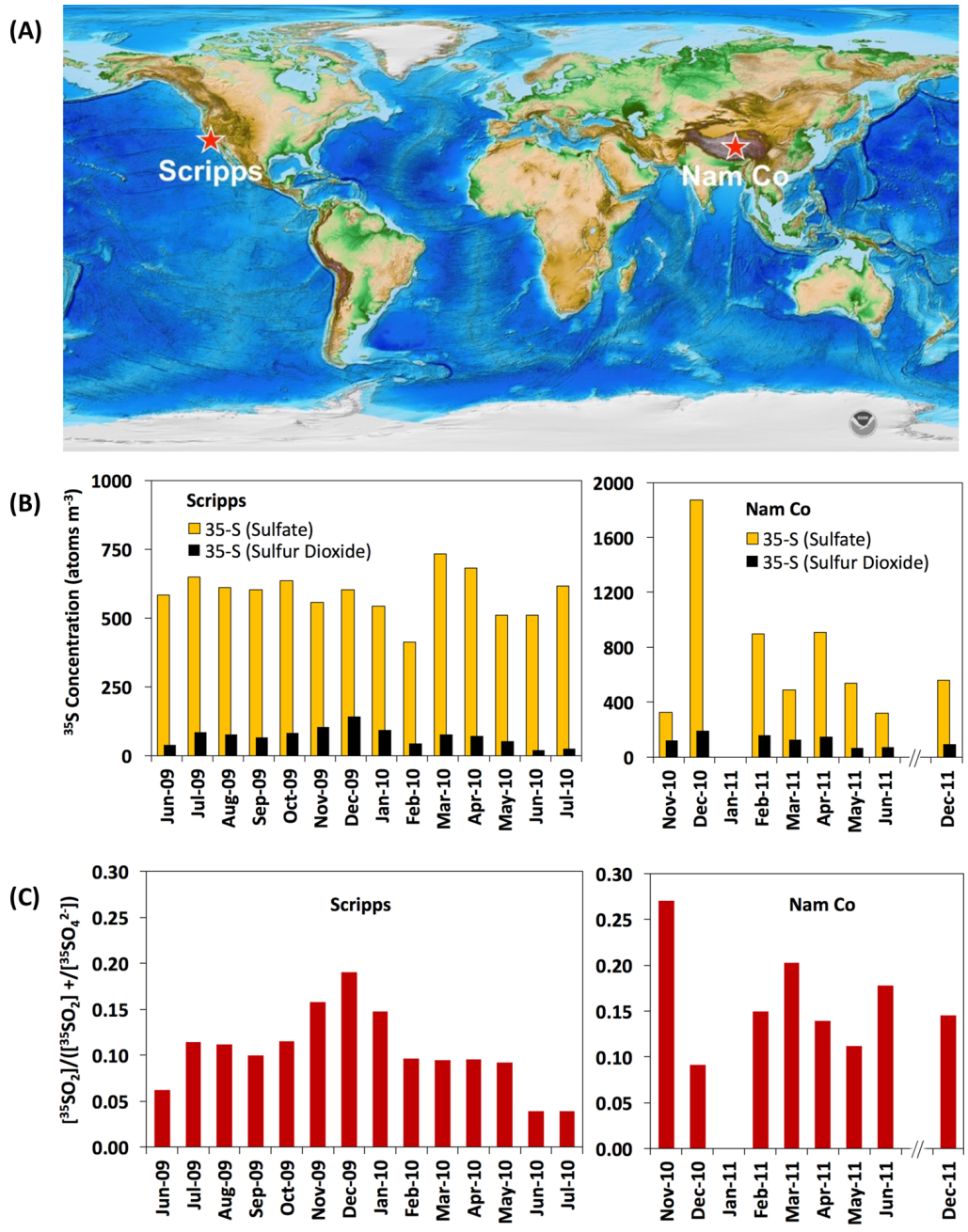

Figure 5.2. (a) Map showing locations of Scripps and Nam Co. The topographic base map is obtained from the National Centers for Environmental Information of the National Oceanic and Atmospheric Administration (https://www.ngdc.noaa.gov/mgg/global/). (b) Monthly averaged concentrations of $^{35}SO_2$ (black) and $^{35}SO_4^{2-}$ in TSP (orange) and (c) ratios of $[^{35}SO_2]/([^{35}SO_2]+[^{35}SO_4^{2-}])$ measured in Scripps and Nam Co.

Figure 5.3. Pictures of sampling sites: (a) Scripps; (b) Nam Co.

5.3.2 Quantification of SO_2-to-Sulfate Conversion Rate

Figure 1b illustrates the sources of $^{35}SO_2$ and $^{35}SO_4^{2-}$ in the atmosphere. Because both $^{35}SO_2$ and $^{35}SO_4^{2-}$ are subject to dry and wet removal, the time-dependent variation of $^{35}SO_2$ and $^{35}SO_4^{2-}$ in the boundary layer can be expressed as follows:

$$\frac{d[^{35}SO_2]}{dt} = P_{\mathrm{CR}} + \frac{F}{H} - \frac{[^{35}SO_2]}{\tau_{ox}} - \frac{[^{35}SO_2]}{\tau_{SO2-w}} - \frac{[^{35}SO_2]}{\tau_{SO2-d}} - \frac{[^{35}SO_2]}{\tau_{\lambda}}$$

$$\frac{d[^{35}SO_4^{2-}]}{dt} = n\times\frac{F}{H} + \frac{[^{35}SO_2]}{\tau_{ox}} - \frac{[^{35}SO_4^{2-}]}{\tau_{SO4-w}} - \frac{[^{35}SO_4^{2-}]}{\tau_{SO4-d}} - \frac{[^{35}SO_4^{2-}]}{\tau_{\lambda}}$$

where [$^{35}SO_2$] and [$^{35}SO_4^{2-}$] represent ^{35}S concentrations measured in SO_2 and SO_4^{2-} (unit: atoms m^{-3}), respectively; P_{CR} is the cosmogenic production rate of ^{35}S in the boundary layer (unit: atoms m^{-3} d^{-1}); F is the downward vertical flux of $^{35}SO_2$ from the free troposphere outside the boundary layer (unit: atoms m^{-2} d^{-1}) and H is the height of the boundary layer (unit: m); the coefficient n is the [$^{35}SO_4^{2-}$]/[$^{35}SO_2$] ratio in the free troposphere; τ_{ox} is the oxidation lifetime of SO_2 (unit: d); $\tau_{SO2\text{-}w}$, $\tau_{SO2\text{-}d}$ are the wet and dry removal lifetimes of SO_2, respectively, whereas $\tau_{SO2\text{-}w}$, $\tau_{SO2\text{-}d}$ represent the wet and dry removal lifetimes of SO_4^{2-}, respectively (unit: d); τ_λ is the decay lifetime of ^{35}S (half-life / ln(2) = 126 d). In this equation system, it is assumed that 1) the boundary layer is well mixed and $^{35}SO_2$ and $^{35}SO_4^{2-}$ concentrations are vertically uniform in the boundary layer; 2) horizontal mixing of $^{35}SO_2$ and $^{35}SO_4^{2-}$ is neglected. Because the conversion of cosmic-ray-produced ^{35}S to $^{35}SO_2$ is of the order of ~1 s, the production rate of $^{35}SO_2$ in the boundary layer is limited by the production of ^{35}S (P_{CR}), while the production rate of $^{35}SO_4^{2-}$ is controlled by the SO_2-to-SO_4^{2-} conversion ([$^{35}SO_4^{2-}$]/τ_{ox}).

To solve τ_{ox} in the equation system, we utilize the measured monthly $^{35}SO_2$ and $^{35}SO_4^{2-}$ concentrations. The SO_2 and SO_4^{2-} removal lifetime is adopted from the corresponding monthly values at the sampling sites simulated by the National Center for Atmospheric Research-Community Atmospheric Model (NCAR-CAM) in the Atmospheric Chemistry and Climate Model Intercomparison Project (ACCMIP) [*Lamarque et al.*, 2013b]. To evaluate the uncertainties, two versions (5.1 and 3.5) and multiple-year data in the 21st century are used. A total of 10-year data (2000-2009) from the version 5.1 is used, while the version 3.5 provides 8-year data (2002-2009). It is noted that the removal lifetime depends on the height of the boundary layer (H), which is not directly measured in this study. The average height during summer measured by 9 sounding stations along the coastal California is ~800 m [*Dorman et al.*, 2000], while the annual average is reported to be ~500 m on the basis of radiosonde observations, meteorological reanalysis and climate models [*Seidel et al.*, 2012]. The H value at the Tibetan Plateau is more variable, which is typically 1-2 km

and can be developed to ~4 km or several hundred meters in some extreme cases [*Chen et al.*, 2016b]. At Nam Co, the 5-year average is reported to be ~1 km based on gridded meteorological data [*Yin et al.*, 2017]. Because H was not measured in this study, an arbitrarily imposed seasonal variation of H may introduce more uncertainties. Therefore, seasonal variability of H is not included in calculations but will be qualitatively discussed. We use 2 values for each station (Scripps: 500 and 800 m; Nam Co: 1000 and 3000 m) to evaluate the uncertainty of calculated results. The average production rate of ^{35}S in the box depends on the location of sampling site and the height of the boundary layer. The P_{CR} for Scripps (H = 500 m: 1.6 atoms m^{-3} d^{-1}; H = 800 m: 1.9 atoms m^{-3} d^{-1}) and Nam Co (H = 1000 m: 42.3 atoms m^{-3} d^{-1}; H = 3000 m: 52.9 atoms m^{-3} d^{-1}) are adopted from the calculation of [*Lal and Peters*, 1967]. The value of n is difficult to determine because $^{35}SO_2$ and $^{35}SO_4^{2-}$ concentrations in the free troposphere have never been measured. In a ^{35}S one-dimensional four-box model (consisting of the boundary layer, buffer layer, free troposphere and lower stratosphere) the $[^{35}SO_4^{2-}]/[^{35}SO_2]$ ratio in the free troposphere is estimated to be 2.3 in California and 3.0 in East China [*Lin et al.*, 2016c; *Priyadarshi et al.*, 2012a]. Because of the relatively short chemical lifetime of SO_2 in the boundary layer (compared to the free troposphere), the $[^{35}SO_4^{2-}]/[^{35}SO_2]$ ratio in the boundary layer is usually larger (>3) than the free troposphere [*Lin et al.*, 2016c; *Priyadarshi et al.*, 2011a; *Priyadarshi et al.*, 2012a; *Priyadarshi et al.*, 2014]. However, relatively small values of $[^{35}SO_4^{2-}]/[^{35}SO_2]$ ratios in the boundary layer (<2.3) were occasionally observed in an early study conduct in New England [*Tanaka and Turekian*, 1995], suggesting that the value of n may be even smaller. Although large uncertainties may exist in those early measurements, we designate a value of 2.0 as the lower limit of n. Accordingly, three values of n (2.0, 2.3 and 3.0) are used to evaluate how the uncertainty of n affects the quantification of τ_{ox}. If we assume the concentrations of $^{35}SO_2$ and $^{35}SO_4^{2-}$ remain the same in a duration of a certain month (i.e., applying a steady-state approximation), the degrees of freedom decrease to two and the values of F and τ_{ox} can be uniquely determined. The steady-state approximation is reasonable as

the lifetimes of SO_2 and SO_4^{2-} in the boundary layer (hours to days) is significantly shorter than 1 month.

In this study, we assume that SO_2 oxidation reactions in the boundary layer are pseudo first order, and the SO_2-to-SO_4^{2-} conversion rate k can be therefore expressed as $1/\tau_{ox}$ (unit: d^{-1}). Since 6 different combinations of H and n values (Table 5.1) are used, the SO_2-to-SO_4^{2-} conversion rate in each month will be calculated for 60 (=6×10) and 48 (=6×8) times using multiple-year (10 and 8) deposition data obtained from CAM 5.1 and 3.5, respectively. The average and one standard deviation of all runs are reported. Because the value of τ_{ox} must be physically meaningful (> 0), solutions with $\tau_{ox} < 0$ are excluded. The total numbers of valid solutions for each month and station are summarized in Table 5.2. The calculated results using deposition data obtained from CAM 5.1 and 3.5 will be hereinafter simply referred to as CAM 5.1 and 3.5, respectively. One should keep in mind that only deposition data from CAM is used for calculations and the SO_2-to-SO_4^{2-} conversion rate reported in this study is not simulated by CAM. It is noted that a small fraction of $^{35}SO_4^{2-}$ may be in vapor phase (radiogenic sulfuric acid) and collected by KOH-impregnated backup filters. Because of the low volatility of sulfuric acid (boiling point: ~330 °C; vapor pressure: <0.0001 kPa at 20 °C), the typical concentrations of sulfuric acid vapor in the terrestrial atmosphere are of the order of 10^6-10^7 cm^{-3}, ~3 orders of magnitude smaller than SO_2 concentrations at remote sites (10^9-10^{10} cm^{-3}) [*Kulmala et al.*, 2014; *Meng et al.*, 2010]. Therefore, treating such minuscule amounts of radiogenic sulfuric acid vapor as $^{35}SO_2$ in calculations would not affect our quantification.

Table 5.1. Different combinations of parameters used in calculations

	Scripps			Nam Co		
	H (m)	*P* (atoms m^{-3} d^{-1})	*n*	*H* (m)	*P* (atoms m^{-3} d^{-1})	*n*
Series 1	500	1.6	2.3	1000	42.3	2.3
Series 2	500	1.6	3	1000	42.3	3
Series 3	500	1.6	2	1000	42.3	2
Series 4	800	1.9	2.3	3000	52.9	2.3
Series 5	800	1.9	3	3000	52.9	3
Series 6	800	1.9	2	3000	52.9	2

Table 5.2. Total number of valid solutions for each month and station

Month	Scripps		Month	Nam Co	
	CAM 5.1	CAM 3.5		CAM 5.1	CAM 3.5
Jun 2009	60	48	Nov 2010	60	48
Jul 2009	60	45	Dec 2010	60	48
Aug 2009	60	47	Jan 2011	n.a.	n.a.
Sep 2009	60	48	Feb 2011	60	48
Oct 2009	60	48	Mar 2011	60	48
Nov 2009	42	28	Apr 2011	60	48
Dec 2009	12	24	May 2011	60	48
Jan 2010	48	44	Jun 2011	60	48
Feb 2010	60	47	Jul 2011	n.a.	n.a.
Mar 2010	60	48	Aug 2011	n.a.	n.a.
Apr 2010	60	48	Sep 2011	n.a.	n.a.
May 2010	60	48	Oct 2011	n.a.	n.a.
Jun 2010	60	48	Nov 2011	n.a.	n.a.
Jul 2010	60	48	Dec 2011	60	48

n.a.: not applicable because of the lack of combined measurements $^{35}SO_2$ and $^{35}SO_4^{2-}$.

5.4 Results and Discussion

5.4.1 Coastal California

The annual averages (±σ) of $^{35}SO_2$ and $^{35}SO_4^{2-}$ (in TSP) concentrations in Scripps are 70±30 and 590±80 atoms m^{-3}, respectively (Figure 5.2b). A clear seasonal pattern for $^{35}SO_4^{2-}$ concentrations is not found, while $^{35}SO_2$ concentrations appear higher in the period of November

2009 to January 2010 (late-autumn to mid-winter) (110±30 atoms m^{-3}) than the rest period (60±20 atoms m^{-3}). The seasonal pattern of $^{35}SO_2$ concentrations may be because of (*i*) a higher downward flux of high-altitude air masses, and/or (*ii*) a slower SO_2-to-SO_4^{2-} conversion rate in the late-autumn to mid-winter period.

The ratio of $[SO_2]/([SO_2]+[SO_4^{2-}])$ or $[SO_4^{2-}]/([SO_2]+[SO_4^{2-}])$, where $[SO_2]$ and $[SO_4^{2-}]$ represent concentrations of stable SO_2 and SO_4^{2-} respectively, is traditionally used as a qualitative indicator for secondary SO_4^{2-} formation rate [*Lin et al.*, 2012a; *Squizzato et al.*, 2013]. In this study, the ratio of $[^{35}SO_2]/([^{35}SO_2]+[^{35}SO_4^{2-}])$ is reported. The seasonal pattern of $[^{35}SO_2]/([^{35}SO_2]+[^{35}SO_4^{2-}])$ ratio is more distinct (0.17±0.02 in the late-autumn to mid-winter period and 0.09±0.03 in the rest period) (Figure 5.2c), qualitatively implying a slower SO_2-to-SO_4^{2-} conversion rate in the late-autumn to mid-winter period.

The calculated monthly SO_2-to-SO_4^{2-} conversion rates are shown in Figure 3, with an annual mean of 0.45 and 0.35 d^{-1} (CAM 5.1 and 3.5, respectively). The seasonal pattern matches the variation of $[^{35}SO_2]/([^{35}SO_2]+[^{35}SO_4^{2-}])$ ratio, showing a fast SO_2-to-SO_4^{2-} conversion rate in summer and a slower rate in the period of mid-autumn to mid-winter (October 2009 to January 2010). Specifically, the highest SO_2-to-SO_4^{2-} conversion rate is found in July 2010 (2.0±1.1 and 1.4±0.7 d^{-1} for CAM 5.1 and 3.5, respectively), close to the summertime SO_2 removal rates in United States estimated from a global chemistry transport model (1.8 d^{-1}) and satellite measurements (1.3±0.5 d^{-1}).[*Lee et al.*, 2011] The relative standard deviation (RSD) for CAM 5.1 and 3.5 ranges from 33% (June 2009) to 380% (October 2009) and from 36% (July 2010) to 380% (November 2009), respectively (Table 5.2). Generally, higher RSDs are found in autumn and winter, suggesting a large uncertainty in estimating the SO_2-to-SO_4^{2-} conversion rate at these seasons in this study.

5.4.2 Tibetan Plateau

In the study period (November 2010 to December 2011), large variations exist in the $^{35}SO_4^{2-}$ concentration (ranging from 320 to 1870 atoms m^{-3}). The annual average of $^{35}SO_2$ and $^{35}SO_4^{2-}$ concentrations are 120±40 and 740±510 atoms m^{-3}, respectively, both of which are slightly higher than Scripps at sea level (Figure 5.2b). The difference is the result of an altitude effect. As shown earlier, the production rate of ^{35}S at Nam Co is ~27 times greater than Scripps. Nam Co is also more affected by the downward transport of air masses from a higher altitude than Scripps. At present, it is difficult to determine if there is any clear seasonal variation of $^{35}SO_2$ or $^{35}SO_4^{2-}$ at Nam Co because samples were not collected during summer and autumn due to operational issues at the remote station.

The ratio of $[^{35}SO_2]/([^{35}SO_2]+[^{35}SO_4^{2-}])$ at Nam Co is 0.16±0.05, close to the value observed at Scripps during November 2009 to January 2010. The calculated monthly SO_2-to-SO_4^{2-} conversion rates show averages of 0.69 and 0.84 d^{-1} (CAM 5.1 and 3.5, respectively) in the study period, almost twice the rates calculated in Scripps. The faster SO_2-to-SO_4^{2-} conversion rate is likely associated with the intense solar ultraviolet radiation over the Tibetan Plateau (~1.5 times stronger than coastal California) [*Ren et al.*, 1999; *Ren et al.*, 1997]. It is noted that the seasonal variation of SO_2-to-SO_4^{2-} conversion rates differ from the concentrations of $^{35}SO_2$ and $^{35}SO_4^{2-}$ and the ratios of $[^{35}SO_2]/([^{35}SO_2]+[^{35}SO_4^{2-}])$. The clearer seasonal pattern found in SO_2-to-SO_4^{2-} conversion rates imply that this gas-to-particle conversion information cannot be obtained without the quantification method shown in this study. The highest values observed in May (1.0±0.3 and 1.3±0.5 d^{-1} for CAM 5.1 and 3.5, respectively) and June (1.2±0.5 and 1.2±0.4 d^{-1} for CAM 5.1 and 3.5, respectively) suggest a faster SO_2-to-SO_4^{2-} conversion rate in this season (late-summer and early autumn), a pattern similar to Scripps. The RSDs of monthly SO_2-to-SO_4^{2-} conversion rates in Nam Co range from 17% (February 2011) to 54% (May 2011) and from 27% (December 2011) to 48% (April 2011) for CAM 5.1 and 3.5, respectively, notably lower than Scripps.

5.4.3 Uncertainties in Quantifying SO_2-to-SO_4^{2-} Conversion Rates

Prior to discussing the implications of our results, the uncertainties of our calculations are examined. The sensitivity of this model to the SO_2/SO_4^{2-} deposition lifetime is tested by using different versions and years of modeled data, as described previously. The uncertainties (RSD) in most results are generally less than ~50%, but large uncertainties (RSD > 100%) exist in results from Scripps in winter (Figure 5.4). Because wet precipitation become more frequent in winter in coastal California [*Pierce et al.*, 2013], the uncertainties may be derived from a potential misrepresentation of SO_2 and SO_4^{2-} wet deposition rates in CAM models at this region. A thorough discussion of the CAM-modeled SO_2 and SO_4^{2-} deposition data is beyond the scope of this study, but a previous study showed significant overestimations in ACCMIP-modeled SO_4^{2-} wet deposition rates (more than twice than observed values) in coastal California [*Lamarque et al.*, 2013a], in part supporting our interpretation. Results using CAM 3.5 deposition data are ~24% lower than CAM 3.5 in Scripps but ~18% lower than CAM 5.1 in Nam Co (Figures 5.4 and 5.5). The discrepancy may be because CAM 5.1 considers size-resolved deposition processes while CAM 3.5 does not [*Lamarque et al.*, 2013b].

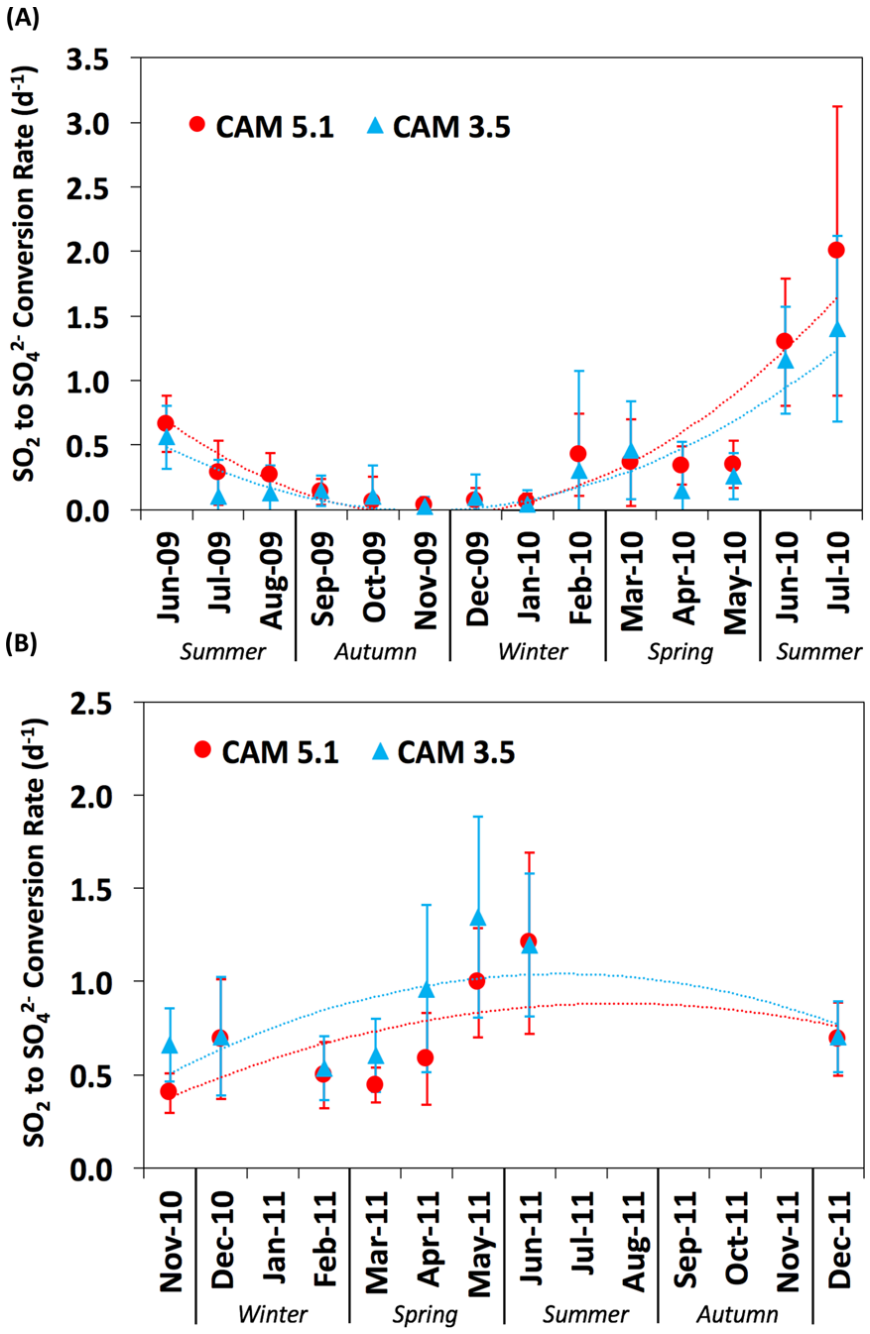

Figure 5.4. Time series of monthly SO_2-to-SO_4^{2-} conversion rates in (A) Scripps and (B) Nam Co calculated using deposition data from CAM 5.1 (red) and 3.5 (blue). The error bar represents one standard deviation. The dotted curves represent the fitted second-order polynomial regression trendlines.

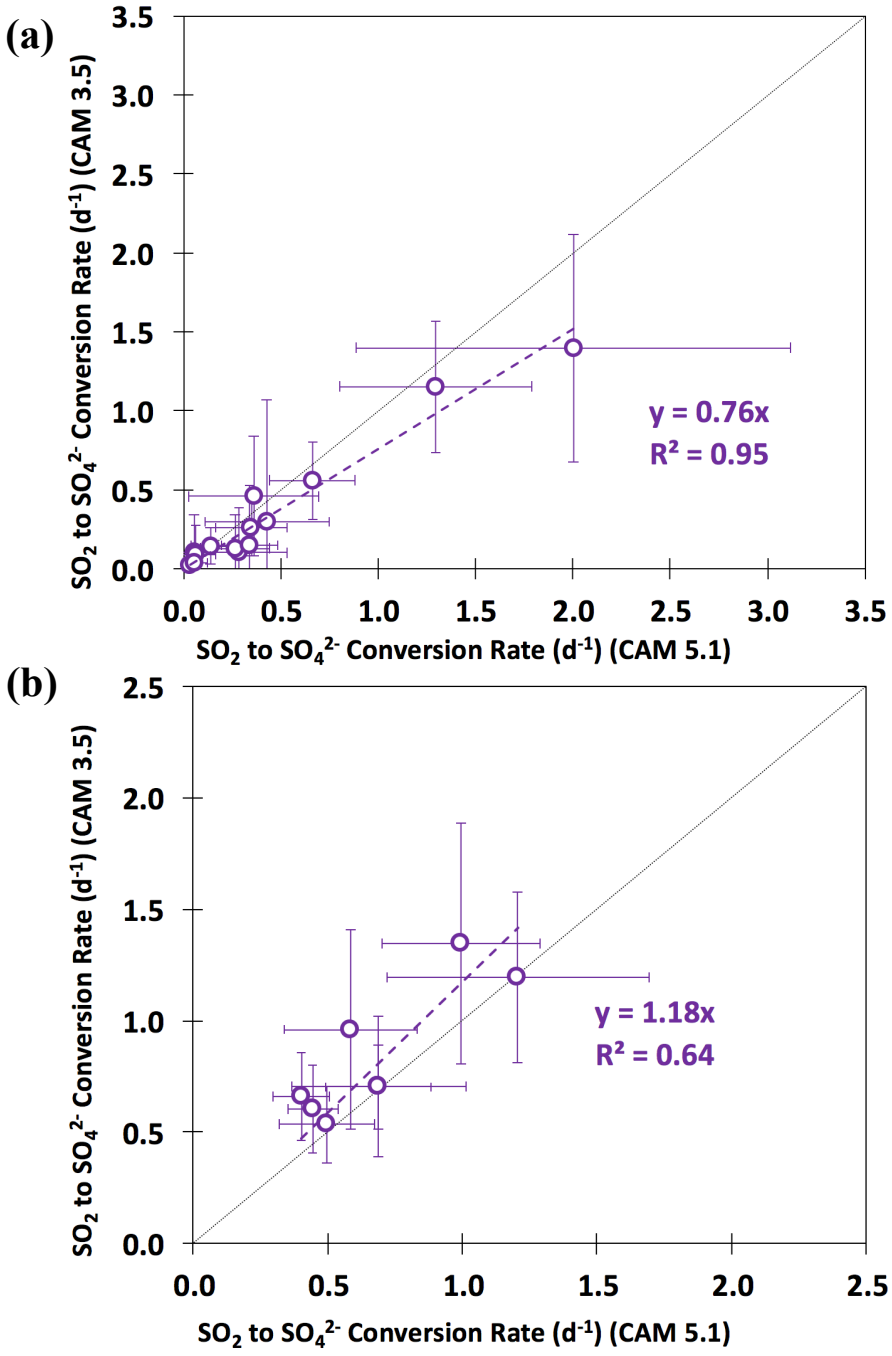

Figure 5.5. Scatter plots of monthly SO_2-to-SO_4^{2-} conversion rates in (a) Scripps and (b) Nam Co calculated using deposition data from CAM 5.1 and 3.5. The error bar represents one standard deviation. The dotted lines represent the 1:1 line.

The calculated SO_2-to-SO_4^{2-} conversion rates using different combinations of *H* and *n* values are summarized in Figures 5.6 and 5.7. Increases of *H* from 500 to 800 m (+60%) at Scripps lead to 26±11% and 30±28% decreases of SO_2-to-SO_4^{2-} conversion rates for CAM 5.1 and 3.5, respectively. Increases of *n* from 2 to 3 (+50%) at Scripps result in 55±19% and 62±21% decreases of SO_2-to-SO_4^{2-} conversion rates for CAM 5.1 and 3.5, respectively. The results show that the selection of ratio *n* significantly influences the quantification. Although no combined measurement of $^{35}SO_2$ and $^{35}SO_4^{2-}$ has been made in the free troposphere, the range of ratio *n* simulated by previous box-models (2.3 - 3) [*Lin et al.*, 2016c; *Priyadarshi et al.*, 2012a] suggest that the uncertainties derived from this value would not be larger than 50%. For Nam Co, increases of *H* from 1000 to 3000 m (+300%) only lead to 32±12% and 42±7% decreases of SO_2-to-SO_4^{2-} conversion rates for CAM 5.1 and 3.5, respectively. Increases of *n* from 2 to 3 (+50%) at Nam Co only result in 13±5% and 12±3% decreases of SO_2-to-SO_4^{2-} conversion rates for CAM 5.1 and 3.5, respectively. The results suggest that our estimation is more reliable in Tibetan Plateau. Because *H* is usually higher in summer than winter, if the seasonal variation of *H* was measured and considered in calculations, the accuracy of our results may be improved, but the ability to acquire *H* accurately was not available in this study. Nevertheless, the seasonal pattern of SO_2-to-SO_4^{2-} conversion rates revealed in this study is unlikely to be altered as our previous sensitivity tests show that enormous changes of *H* (>1500%) are required to explain the observed winter-summer differences (Figure 5.4), which is dynamically unlikely.

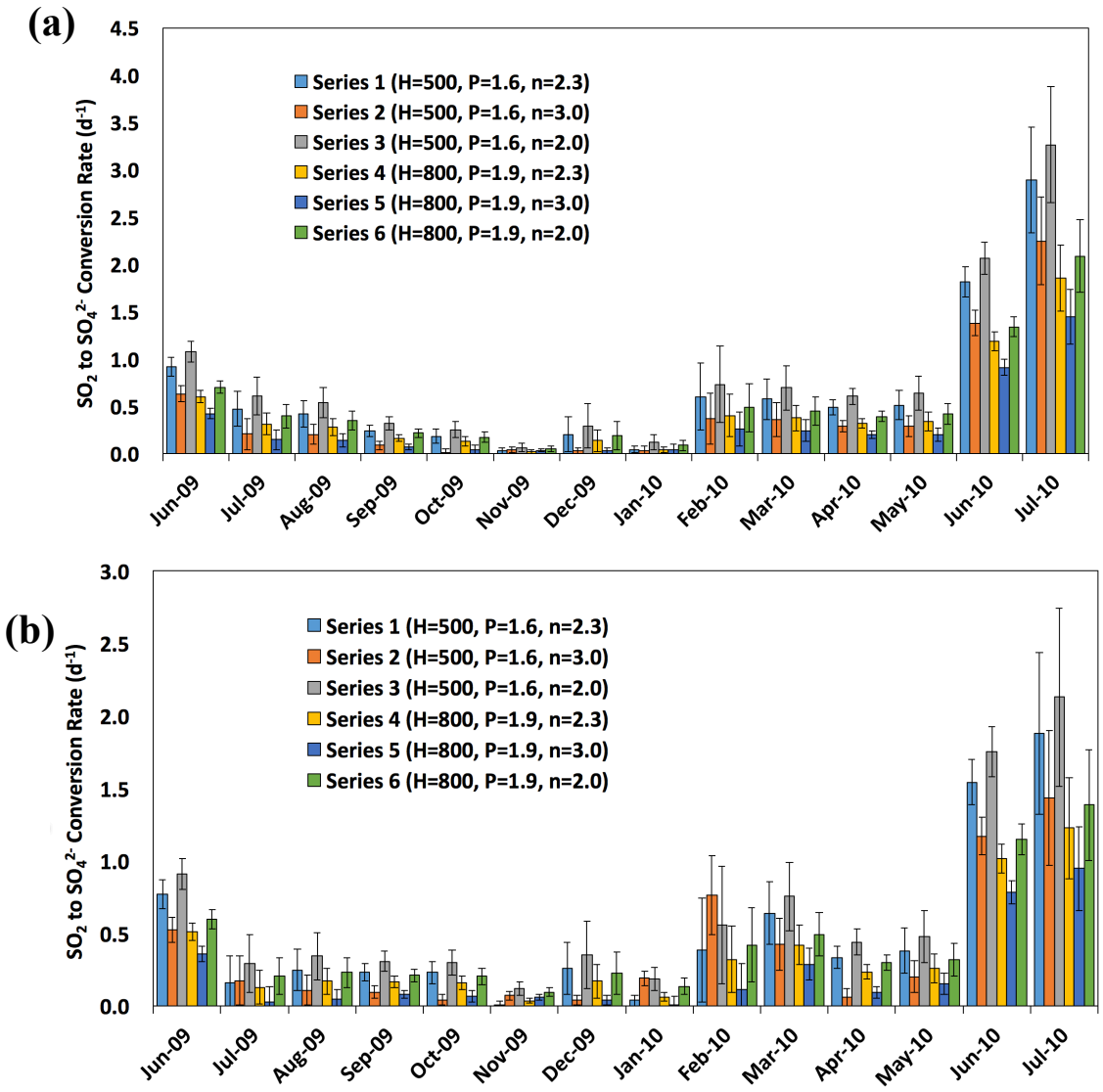

Figure 5.6. Time series of monthly SO_2-to-SO_4^{2-} conversion rates in Scripps calculated using different combination of *H* and *n* values (see Table 5.2) and deposition data from (a) CAM 5.1 and (b) 3.5. The error bar represents one standard deviation.

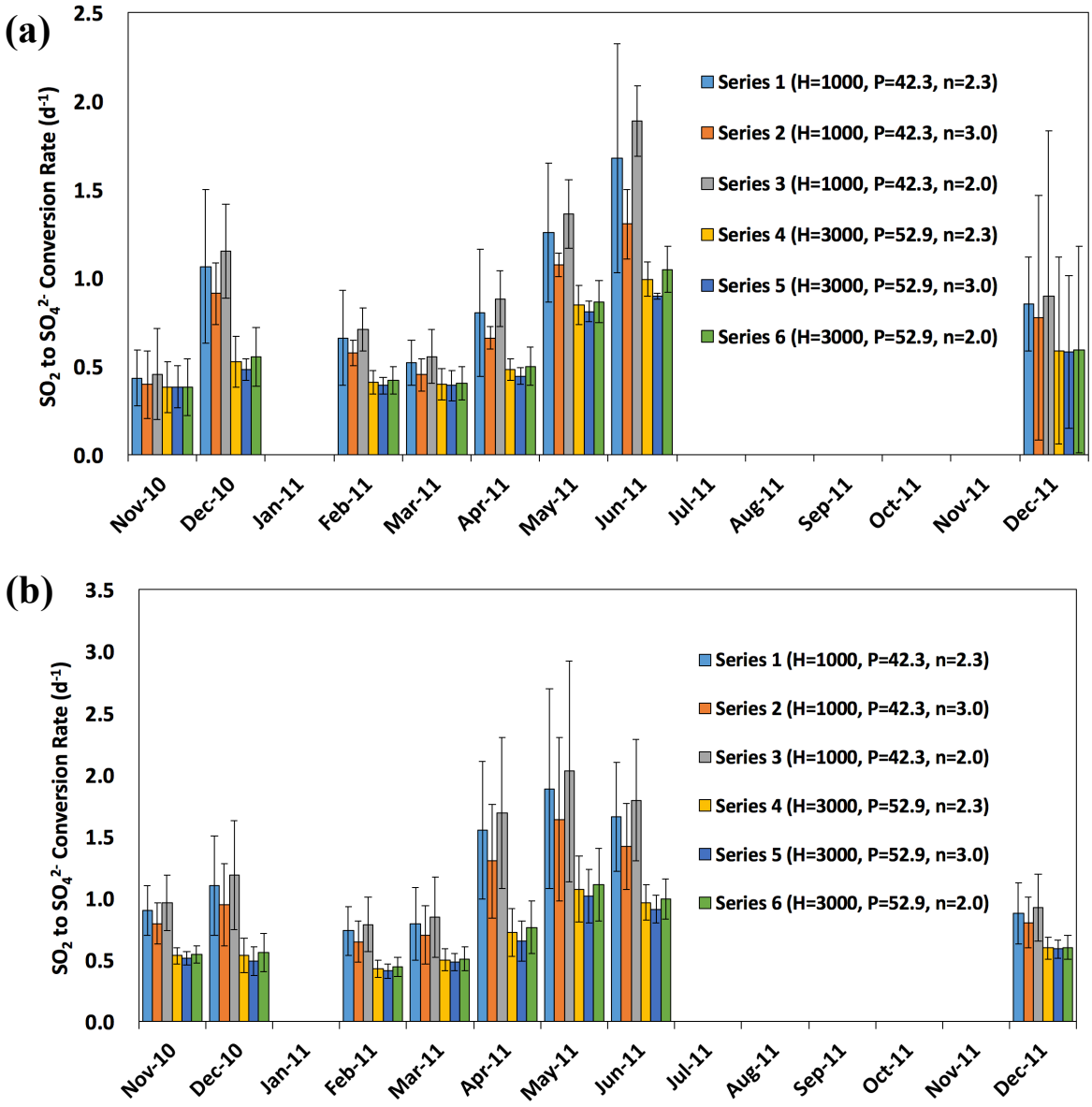

Figure 5.7. Time series of monthly SO_2-to-SO_4^{2-} conversion rates in Nam Co calculated using different combination of *H* and *n* values (see Table 5.2 for units) and deposition data from (a) CAM 5.1 and (b) 3.5. The error bar represents one standard deviation.

The last potential source of uncertainty is the production rate of ^{35}S, which was calculated by Lal and Peters half a century ago using direct field-based observations and empirical parameterizations [*Lal and Peters*, 1967]. The vertical production profiles of other cosmogenic isotopes (e.g., ^{7}Be, ^{10}Be, ^{14}C and ^{36}Cl) have been updated basing on more comprehensive calculations of the atmospheric cascade and yield functions [*Masarik and Beer*, 1999; 2009; *Poluianov et al.*, 2016], but a new state-of-the-art estimation of ^{35}S production rates remains absent. Given the similarity of ^{35}S and ^{36}Cl production pathways (cosmic ray spallation of argon in the atmosphere), we investigate the sensitivity of calculated SO_2-to-SO_4^{2-} conversion rates to the ^{35}S production rate on the basis of ^{36}Cl results. The recently calculated global average production rate of ^{36}Cl is twice the early estimation by Lal and Peters, with an uncertainty of 15% [*Masarik and Beer*, 1999; 2009; *Poluianov et al.*, 2016]. We assume the production ratio of ^{36}Cl to ^{35}S is a constant (0.8) [*Lal and Peters*, 1967], and find that doubling the ^{35}S production rate in our calculations only lead to 8±17% and 29±12% increases in the SO_2-to-SO_4^{2-} conversion rates at Scripps and Nam Co, respectively. Because the ^{35}S production rate at the top of the boundary layer is approximately twice the value used in this study, this sensitivity test also indicates that ignoring the vertical variation of ^{35}S production rates in the boundary layer would not significantly affect the quantification results.

5.4.4 Possible Factors Responsible for Fast SO_2-to-SO_4^{2-} Conversion Rates in Summer

The SO_2-to-SO_4^{2-} conversion rates in the chemically active boundary layer can be controlled by a number of factors (e.g., temperature, solar radiation, concentrations of oxidants). A seasonal pattern with summer maximum and winter minimum found in both northern mid-latitude sites suggest that temperature and solar radiation may be important factors affecting the SO_2-to-SO_4^{2-} conversion rates at the seasonal scale. It is noted that this seasonal variation is similar to the result from the pioneering study conducted by Turekian and Tanaka in New England, but their value in summer seems unrealistically large (7 d^{-1}), probably due to large uncertainties in early ^{35}S

measurements and several unconstrained parameters in their calculations [*Tanaka and Turekian*, 1995].

It is well known that the production rate of OH radical is directly linked to solar radiation, especially in our sampling sites that possess relatively high O_3 levels and humidity in most time [*Lin et al.*, 2016a; *Lin et al.*, 2008b; *Yin et al.*, 2017]. It is possible that the enhanced SO_2-to-SO_4^{2-} conversion rates observed in summer are due to a more important role of OH oxidation in SO_4^{2-} production. This interpretation is supported by the measurement of the ^{17}O anomaly in SO_4^{2-} (an isotopic signature for quantifying the relative contribution of oxidation pathways involved in SO_4^{2-} formation processes) made in coastal California [*Lee and Thiemens*, 2001]. The $^{17}O(SO_4^{2-})$ in the Tibetan Plateau is only measured in spring and subsequently cannot provide oxidation pathway information for summer [*Lin et al.*, 2016b]. It is noted that at typical atmospheric OH levels at northern mid-latitudes in summer (2.5×10^6 radicals cm^{-3}) the lifetime of SO_2 with respect to OH oxidation is ~1 week, which cannot fully explain the fast SO_2-to-SO_4^{2-} conversion rates observed in summer (~1 d^{-1}). This result is consistent with a previous field measurement at Mace Head showing that at least one gas phase oxidation process (apart from OH oxidation) is apparently missing in the marine boundary layer, which contributes ~5 times more than the OH oxidation [*Berresheim et al.*, 2014]. The study suggested that the halogen oxide oxidations are kinetically unlikely because of their slow reaction rates (at least 35 times slower) [*Berresheim et al.*, 2014]. An oxidation by Criegee intermediates is possible but may be unlikely at present understanding because of the low concentrations of precursors in the marine boundary layer (compared to forested environments) [*Assaf et al.*, 2017; *Berresheim et al.*, 2014; *Newland et al.*, 2015]. Our results highlight again the importance of laboratory efforts to find out an oxidation mechanism accounting for the fast SO_2-to-SO_4^{2-} conversion rate observed in the terrestrial atmosphere.

Since the ambient SO_2-to-SO_4^{2-} conversion rate incorporates both gas- and aqueous-phase oxidations in a chemically active environment, a potentially enhanced aqueous-phase oxidation

pathway in summer should be considered. The seasonal variations of the ^{17}O anomaly in the coastal California do not support an enhanced role of aqueous H_2O_2/O_3 oxidation in summer [*Lee and Thiemens*, 2001]. Transition-metal-ion-catalyzed oxidation by O_2 is also unlikely due to its slow reaction rate in summer [*Alexander et al.*, 2009]. A recent study showed that 33-50% of SO_4^{2-} in the marine boundary layer is produced through the HOX oxidation [*Chen et al.*, 2016a]. The concentration of HOX is linked to photochemistry as a clear diurnal (with maximum at noon and undetectable amount at night) is observed [*Liao et al.*, 2012]. Because the SO_2 and SO_4^{2-} samples from Scripps were collected at the marine boundary layer (Figure 5.2), the HOX oxidation may contribute, in part, to the enhanced SO_2-to-SO_4^{2-} conversion rates during summer. It is noted that the reaction may occur predominantly on sea spray aerosols in Scripps due to the cloudless sky through most of summer in coastal southern Califonia [*Bailey*, 1966]. Given the fast HOX oxidation ($k = \sim 2\times10^9$ M^{-1} s^{-1}; $[HOX]aq = \sim 9\times10^{-13}$ M) [*Chen et al.*, 2016a], the SO_2-to-SO_4^{2-} conversion rate should be limited by the SO_2 uptake rate. The net uptake coefficient γ (unitless) at Scripps in summer is therefore estimated to be of the order of 10^{-2}, consistent with the value measured in laboratory using synthetic sea salt [*Gebel et al.*, 2000]. The higher aerosol loading in summer (Figure 5.8) may provide more available surface areas for facilitating this reaction and the condensation of vapor-phase H_2SO_4 [*Dominguez et al.*, 2008]. Our results thus provide additional isotopic evidences for the important role of the HOX oxidation in the marine boundary layer. Reactive halogen species have been observed at Great Salt Lake in Utah, which mixing ratios are comparable to the marine boundary layer [*Saiz-Lopez and von Glasow*, 2012; *Stutz et al.*, 2002]. Given that Nam Co Lake is the second largest salt lake at the Tibetan Plateau (surface area: ~1900 km^2) and our SO_2 and SO_4^{2-} samples were collected at the shore of this lake, it is possible that the HOX oxidation also plays an important role at Nam Co, especially a higher aerosol loading is also observed in this region in summer [*Liu et al.*, 2017]. In the future, a proper modeling of the chemical interaction between SO_2 and all possible oxidants can validate our interpretation.

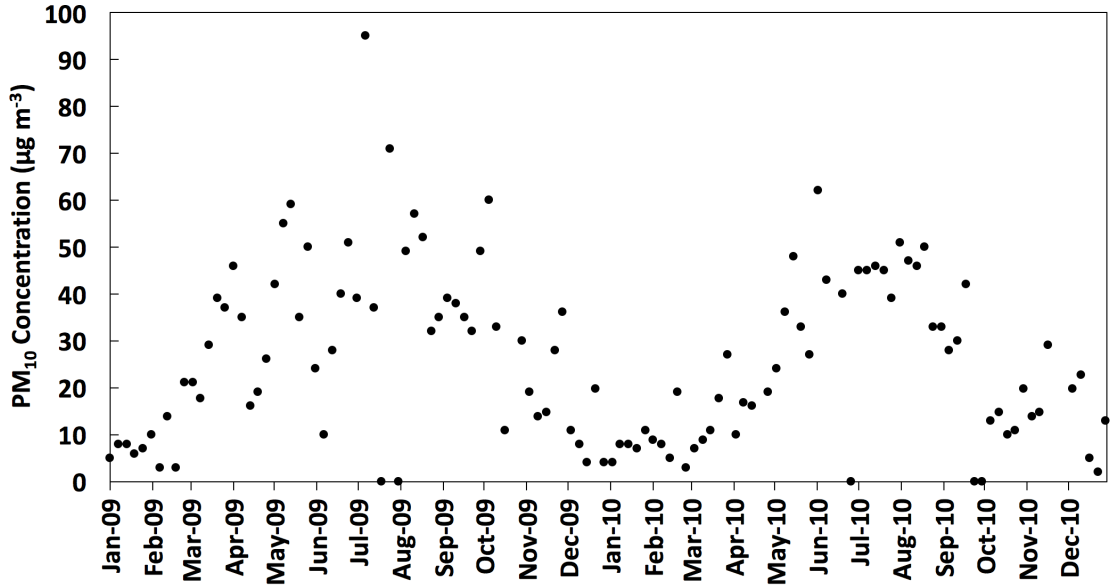

Figure 5.8. Daily mean PM_{10} concentrations measured in San Diego during 2009-2010 (Station ID: 06-063-0077). Data is obtained from the United States Environmental Protection Agency (https://www.epa.gov/air-data).

5.5 Summary and Outlook

In this study, we use the combined measurement of ambient $^{35}SO_2$ and $^{35}SO_4^{2-}$ to quantify the SO_2-to-SO_4^{2-} conversion rate (and even the uptake coefficient of SO_2) in the terrestrial atmosphere. The unique advantage of this method is its simplicity as it eliminates requirements of accurately quantifying emission/production rates from numerous sulfur sources (Figure 5.1) and measuring ^{35}S in precipitation samples and other cosmogenic isotopes (e.g. ^{7}Be and ^{210}Pb) in aerosol samples [*Tanaka and Turekian*, 1995]. Interestingly, results from two sampling sites (coastal California and the Tibetan Plateau) reveal rapid SO_2-to-SO_4^{2-} conversion rates in summer, suggesting that some unconventional oxidation pathways (e.g. the HOX oxidation) might be more important than previously thought. Further combined efforts in field missions, modeling and laboratory studies should be encouraged in the future to understand the rapid gas-to-particle conversion rate of sulfur in the chemically complex terrestrial atmosphere.

Comprehensive field works can significantly reduce uncertainties in estimations. Measurements of $^{35}SO_2$ and $^{35}SO_4^{2-}$ in the free troposphere are particularly crucial because their concentrations greatly influence the budget of ^{35}S in the boundary layer, especially at low-altitude regions due to the extremely low in-situ production rate of cosmogenic ^{35}S. Field-based observations of the boundary layer height and deposition rates can also improve the accuracy of quantification. A recent study underlines the importance of incorporating ^{35}S in global chemical transport models to understand the stratosphere-troposphere exchange [*Lin et al.*, 2016a]. Such simulations have been done using cosmogenic ^{7}Be, which are found to be technically simple and computational low-cost [*Liu et al.*, 2016a]. The additional advantage of ^{35}S is its ability to quantify the SO_2-to-SO_4^{2-} conversion rate as demonstrated in this study. Due to the single source of $^{35}SO_4^{2-}$, a comparison of simulated and observed ^{35}S concentrations is a more reasonable and unambiguous way to constrain the SO_2 oxidation rate in models. Since the physical and chemical properties of ^{35}S are nearly identical to stable S, such model development should be straightforward if the quantification of 3-dimensional ^{35}S production rates is improved.

Cosmogenic ^{35}S is of high potential in laboratory studies. Although the ^{35}S-labeled technique has been used in laboratory experiments to understand a wide variety of biochemical and biogeochemical processes for decades [*Haase et al.*, 1985; *Hwang et al.*, 1992; *Thodeandersen and Jorgensen*, 1989], it is not applied to investigate kinetics and photochemical processes of sulfur compounds in the terrestrial and extraterrestrial atmospheres. Due to the low-energy decay of ^{35}S (E_{Max} = 167 keV), an accurate counting of ^{35}S requires at least 2 h and a high-temporal-resolution *in-situ* measurement is therefore impossible at present [*Brothers et al.*, 2010; *Lin et al.*, 2017d]. Nevertheless, the advantage of ^{35}S-labeled technique is its extremely low quantification limit (~2×10^6 molecules; 10σ above the background counting rate) [*Brothers et al.*, 2010; *Lin et al.*, 2017d]. A pilot study highlights that this feature is particularly crucial to accurately quantify the slow uptake of SO_2 onto some minerals such as SiO_2 [*Hill-Falkenthal*, 2014]. The ^{35}S-labeled

technique will also allow comprehensive understanding the mechanistic nature of complicated reactions in a system containing various sulfur-containing compounds such as the Criegee intermediate reactions with H_2O, SO_2 and DMS [*Newland et al.*, 2015], and formation of organosulfates (an important component in secondary organic aerosol in the terrestrial atmosphere) [*Froyd et al.*, 2010; *Riva et al.*, 2015; *Surratt et al.*, 2008] and elemental sulfur aerosols (a dominant constituent in the atmospheres of Venus, early Earth and Mars) [*Kumar and Francisco*, 2017].

5.6 Additional Discussion

Cosmogenic ^{35}S is a direct measure of downward mixing of high altitude air masses [*Lin et al.*, 2016a]. Here we briefly report and discuss downward fluxes of $^{35}SO_2$ (F) calculated by the model in this study. A bimodal seasonal cycle is observed in Scripps (Figure S2a), showing stronger downward transport of high altitude air masses during summer and winter. However, a seasonal pattern for Nam Co is not apparent due to limited data (8 months) and large uncertainties (RSD>100%) (Figure 5.9). The average $^{35}SO_2$ flux in Nam Co (222 and 251 atoms m^{-2} d^{-1} for CAM 5.1 and 3.5, respectively) is ~6 times greater than Scripps (38 and 37 atoms m^{-2} d^{-1}), which is reasonable because of the altitude effect discussed in the main text. In Scripps, the winter peak is likely due to the high frequency of Santa Ana wind events during this season [*Guzman-Morales et al.*, 2016], which enhance downward mixing of air masses from the free troposphere [*Hill-Falkenthal et al.*, 2012a; *Lin et al.*, 2016a; *Priyadarshi et al.*, 2012a]. The summer peak may result from the uncertainty in the height of the boundary layer (H) because increases of H in the calculation lead to decreases of F. It is possible that the true value of F should have been smaller because the mixing layer during warm summer may be deeper, especially during daytime [*Seidel et al.*, 2012]. With constraints from radiosonde observations, this hypothesis can be tested in the future.

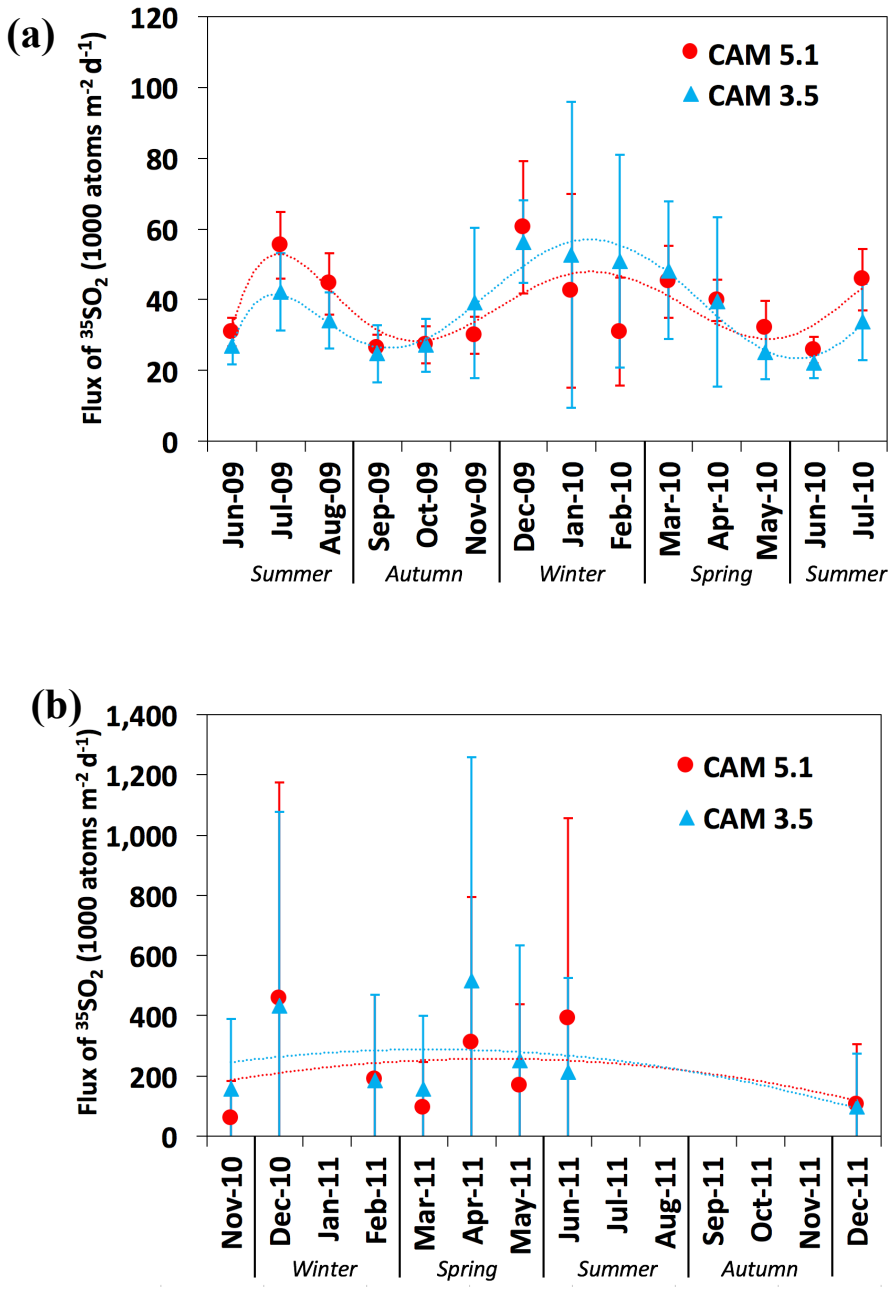

Figure 5.9. Time series of monthly $^{35}SO_2$ fluxes (F) in (a) Scripps and (b) Nam Co calculated using deposition data from CAM 5.1 (red) and 3.5 (blue). The error bar represents one standard deviation. The dotted curves in (a) and (b) represent the fitted sixth-order and second-order polynomial regression trendlines, respectively.

5.7 Acknowledgements

This paper is dedicated to the late Karl K. Turekian for his pioneering work and friendship. We thank Lin Su for her guidance in obtaining CAM data, and Jiayue Huang for beneficial scientific discussions on interpreting deposition data. Mang Lin acknowledges a fellowship from the Guangzhou Elite Project (JY201303).

This chapter, in full, is a reprint of the material "Quantification of gas-to-particle conversion rates of sulfur in the terrestrial atmosphere using high-sensitivity measurements of cosmogenic ^{35}S" as it appears in ACS Earth and Space Chemistry 2017. Lin, Mang; Biglari, Saman; Thiemens, Mark H., American Chemical Society, 2017. The dissertation author was the primary investigator and author of this paper.

Chapter 6 Unexpected high ^{35}S concentration revealing strong downward transport of stratospheric air during the monsoon transitional period in East Asia

6.1 Abstract

October is the monsoon transitional period in East Asia (EA) involving a series of synoptic activities that may enhance the downward transport of stratospheric air to the planetary boundary layer (PBL). Here, we use cosmogenic ^{35}S in sulfate aerosols ($^{35}SO_4^{2-}$) as a tracer for air masses originating from the stratosphere and transported downward to quantify these mixing processes. From one-year $^{35}SO_4^{2-}$ measurements (March 2014 - February 2015) at a background station in EA we find remarkably enhanced $^{35}SO_4^{2-}$ concentration (3150 atoms m^{-3}) in October, the highest value ever reported for natural sulfate aerosols. A 4-Box 1D model and meteorological analysis reveal that strong downward transport from the free troposphere (FT) is a vital process entraining aged stratospheric air masses to the PBL. The aged stratospheric masses are accumulated in the PBL, accelerating the SO_2 transformation to SO_4^{2-}. Implications for the tropospheric O_3 budget and the CO_2 biogeochemical cycle are discussed.

6.2 Introduction

Downward transport of stratospheric air on synoptic scales plays a vital role in the tropospheric O_3 budget [*Dufour et al.*, 2015; *Lin et al.*, 2015; *Oltmans et al.*, 2004] and the CO_2 biogeochemical cycle [*Hoag et al.*, 2005; *Liang and Mahata*, 2015; *Liang et al.*, 2008]. In East Asia (EA), frequent stratospheric intrusions in spring significantly influencing O_3 concentrations in the upper and middle troposphere have been widely investigated by ozonesonde measurements and are closely tied to the location of subtropical jet stream [*Chan et al.*, 2003; *Huang et al.*, 2015b; *Liu et al.*, 2002; *Oltmans et al.*, 2004; *Zhang et al.*, 2012]. The signature of stratospheric air in the planetary boundary layer (PBL) is not readily identifiable. This is in part due to deep stratospheric intrusions which directly admit a large amount of fresh stratospheric air to the PBL at infrequent

times [*Chan et al.*, 2003; *Huang et al.*, 2015b], and/or the difficulty of identifying the subtle signal in the PBL in O_3 measurements and meteorological data [*Lin et al.*, 2016b]. Recently, *Liang et al*. [2015] utilized oxygen isotope anomaly in CO_2 originating in the stratosphere and with a lifetime of several weeks to months in the troposphere [*Thiemens et al.*, 2014] to document enhanced downward transport of stratospheric air to sea level in mid-autumn (October) at the subtropical EA. This result raises the question of how stratospheric air was transported to the PBL in this season. *Liang et al*. [2015] suggested that it is potentially linked to the position of subtropical jet stream and the changing meteorology in October, but the precise mixing process remains elusive.

October is the monsoon transitional period from EA summer to winter monsoon involving a series of synoptic activities that are active and accompanied by strong and deep convections. These synoptic patterns include the establishment of the EA major trough and the monsoon jet stream, the southeastward retreat of the western Pacific subtropical high, and the tropical cyclones over the western Pacific Ocean with decreasing frequency, all of which significantly influence the vertical distributions of air pollutant levels [*Zheng et al.*, 2015b]. Here we propose that the interaction of these synoptic patterns can enhance the mixing between the free troposphere (FT) and the PBL and facilitate the downward transport of aged stratospheric air masses from the FT. Since the monsoon transition is rapid, a chemical tracer originating in the stratosphere and with a relatively short lifetime is needed to support this hypothesis and to resolve the processes.

Cosmogenic ^{35}S (half-life: 87 days) is a naturally produced radionuclide generated by high-energy cosmic ray spallation of atmospheric ^{40}Ar. Following production, ^{35}S is rapidly oxidized to $^{35}SO_2$ in ~1 s, and is further oxidized to $^{35}SO_4^{2-}$ before wet and dry removal. Since the production rate of ^{35}S in the stratosphere is 1-2 orders of magnitude greater than in the troposphere [*Lal and Peters*, 1967], enhanced $^{35}SO_4^{2-}$ concentration in the troposphere (especially the PBL) is due to the downward transport of stratospheric air masses containing higher concentrations of $^{35}SO_2$ and $^{35}SO_4^{2-}$. The relatively short lifetime of tropospheric $^{35}SO_4^{2-}$ (several days) also renders it a useful

and sensitive tracer to identify air masses that recently spent time in the stratosphere and may quantify the mixing processes on synoptic scales [*Lin et al.*, 2016b; *Priyadarshi et al.*, 2011a; *Priyadarshi et al.*, 2012a]. A unique advantage of ^{35}S is that it behaves both as a gas (SO_2) and an aerosol and therefore offers additional information on the extent to which enhanced O_3 levels in aged stratospheric air may affect the SO_2 oxidation rate [*Lin et al.*, 2016b], which is not captured by other short-lived cosmogenic radionuclides (e.g., ^{7}Be, half-life 53 days). In this letter, we report one-year $^{35}SO_4^{2-}$ measurements made at a background station in East Asia that provides an observational evidence of a seasonal cycle for the strength of downward transport of stratospheric air to the PBL in this region and support for the hypothesis that strong mixing between the FT and the PBL is a vital process entraining significant amounts of stratospheric air to the PBL during the monsoon transitional period in mid-autumn.

6.3 Experimental Methods

Weekly fine aerosol (with aerodynamic diameter smaller than 2.5 μm) samples were collected from March 2014 to February 2015 at a regional background station in eastern China (Mount Wuyi, 27.72°N, 117.68°E, 1139 m above sea level, Figure 6.1) using a high volume air sampler (TE-6070DV-BLX, Tisch Environmental Inc., USA). The sampler was operated at a flow rate of ~1.13 m^3 min^{-1} and quartz filters (Whatman, UK) were used as filtration substrates. After sampling, half of the filter was sent to the University of California San Diego for ^{35}S analysis using an ultra-low level liquid scintillation counting spectrometer (Wallac 1220 Quantulus) technique [*Brothers et al.*, 2010]. Detailed chemical processing, quality assurance and control procedures can be found in Supporting Information (SI) Text.

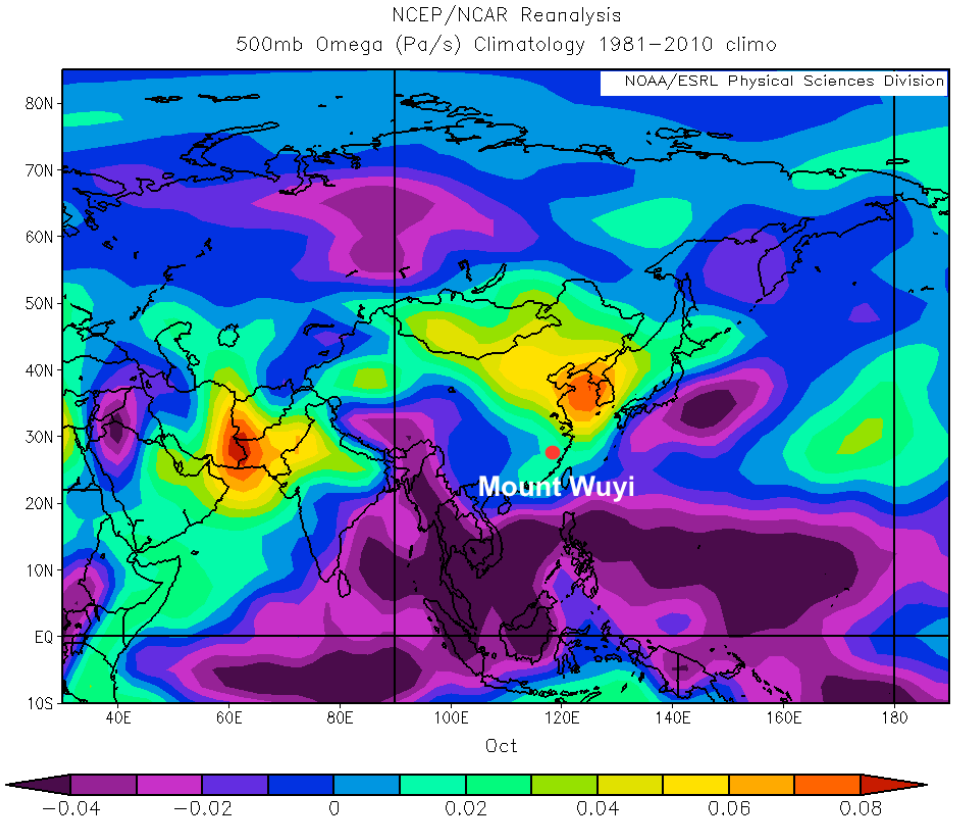

Figure 6.1. Map showing the location of Mount Wuyi. The base map shows typical vertical pressure velocity (omega) at 500 hPa during October for 1981-2010 using the NCEP reanalysis data.

6.4 Results and Discussion

6.4.1 Seasonal Pattern of ^{35}S and Unexpected Peak in October

The $^{35}SO_4^{2-}$ concentrations in fine particles vary from 80 (2014/08/13-2014/08/19) to 3150 atoms m^{-3} (2014/10/22-2014/10/29), with an annual average of 530±470 atoms m^{-3}. The large standard deviation observed here is due to the extraordinarily high $^{35}SO_4^{2-}$ concentration in the sample collected during 2014/10/22-2014/10/29, which is related to the downward transport of a large parcel of stratospheric air and will be discussed. If this sample was excluded, the annual mean concentration of 480±270 atoms m^{-3} was close to the Scripps Pier at the coastal California (460±160

atoms m^{-3}) and Dome C at the Antarctica Plateau (500±300 atoms m^{-3}) [*Hill-Falkenthal et al.*, 2013], but lower than Nam Co at the southern Tibetan Plateau (660±340 atoms m^{-3}) [*Priyadarshi et al.*, 2014].

In spring and early summer (March – June), the time series of $^{35}SO_4^{2-}$ concentrations show an obvious sawtooth pattern (Figure 6.2). Three distinct peaks are found in this period, among which the highest $^{35}SO_4^{2-}$ concentration is 1130 atoms m^{-3} (2014/4/2-2014/4/9), comparable to those observed in aged and mixed air masses with semi-recent stratospheric origin in the PBLs at the Tibetan Plateau (1100-1250 atoms m^{-3}) [*Lin et al.*, 2016b] and coastal California (1100 atoms m^{-3}) [*Priyadarshi et al.*, 2012a]. It suggests that cross-tropopause irreversible exchange is frequent in this period, which mainly influences the chemical components in the FT but its contribution to the surface air in the PBL is minor. This result agrees well with previous ozonesonde measurements and modeling results [*Chan et al.*, 2003; *Huang et al.*, 2015b]. From mid-summer to early autumn (July - September), when summer monsoon prevails, the $^{35}SO_4^{2-}$ concentrations are lower than 500 atoms m^{-3} (with an exception of 560 atoms m^{-3} during 2014/7/16-2014/7/23), suggesting that the sampling site is generally affected by low altitude air masses in this season. Other contributing factors to these low concentrations may be the higher rainfall abundance in this wet season and better dispersion capacity of the PBL due to solar thermal heating.

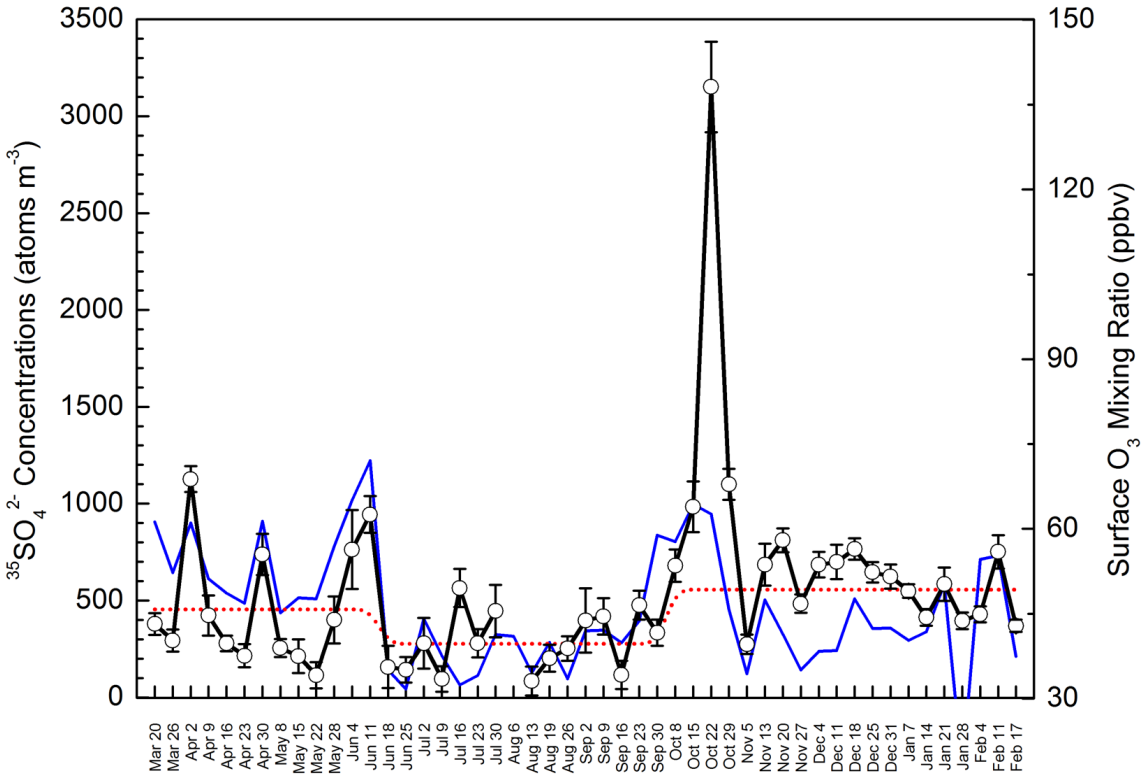

Figure 6.2. Time series of $^{35}SO_4^{2-}$ concentrations measured in Mount Wuyi from March 2014 to February 2015. Error bars stand for one standard deviation in ^{35}S measurement. Red dot line shows seasonal variation of steady-state $^{35}SO_4^{2-}$ concentrations calculated by a 4-Box 1D model. Surface O_3 mixing ratio (blue line) is also presented to highlight the potential contribution of downward transport of stratospheric air on surface O_3 levels (see text for discussion). $^{35}SO_4^{2-}$ sample likely contaminated by ^{36}Cl (2014/8/6-2014/8/13) and exceptionally low O_3 mixing ratio (17.4 ppbv, 2015/1/28-2015/2/4) are not shown.

The most interesting and striking finding in this study is the dramatic enhancement of $^{35}SO_4^{2-}$ concentrations in October. Figure 6.2 shows that $^{35}SO_4^{2-}$ concentrations steadily and continuously increased from 330 at early October to 980 atoms m^{-3} at mid-October, followed by steep increases to 3150 atoms m^{-3} during 2014/10/22-2014/10/29, which is the annual maximum and the highest $^{35}SO_4^{2-}$concentration measured in any natural aerosol samples to date. At late October and early November, $^{35}SO_4^{2-}$ concentrations decreased to 1100 atoms m^{-3} and subsequently returned to the annual average level. The high ^{35}S levels in mid-autumn persisting over 3 weeks (>980 atoms m^{-3}) are likely due to a continuous mixing of stratospheric air instead of a single deep

intrusion episode. In late autumn and winter (November-February), most samples contain higher $^{35}SO_4^{2-}$ concentrations (>500 atoms m^{-3}) than those in spring and summer. It suggests the overall contribution of stratospheric air masses to surface air is enhanced in winter, consistent with previous measurements of other stratospheric tracers (^{7}Be on particle and oxygen isotope anomaly in CO_2) conducted in this region [*Liang and Mahata*, 2015; *Lin et al.*, 2014b]. However, the absence of a significant $^{35}SO_4^{2-}$ peak (~1000 atoms m^{-3}) in winter suggests that strong stratospheric intrusion event that occurred in ~1 day as observed in springtime may be a rare occurrence.

Prior to further discussing how downward transport of stratospheric air leads to a notable deviation of $^{35}SO_4^{2-}$ activity from the background to the elevated levels in October, it is necessary to carefully evaluate the possible impact of the ^{35}Cl[*n*,*p*]^{35}S reaction between neutrons escaping from the Fukushima, or any nuclear plant, and ^{35}Cl in the coolant seawater, which is the only identified anthropogenic source of ^{35}S [*Priyadarshi et al.*, 2011b]. The prevailing wind is transiting from southwest to northeast in October, with the sampling site located downwind of Japan. If a significant amount of ^{35}S had been consistently produced from the Fukushima region and entrained to the sampling site by winter monsoon, comparably high $^{35}SO_4^{2-}$ concentrations as those in 10/15/2014-11/5/2014 (>980 atoms m^{-3}) should be observed in the entire winter when northeasterly wind prevails. However, this is not the case. Alternatively, if the sudden spike in ^{35}S was due to an episodic nuclear reactor accident, similar spikes of ^{35}S and other radionuclides should be observed in the Fukushima region and probably around the globe [*Hsu et al.*, 2012; *Priyadarshi et al.*, 2011b]. However, distinct peaks of ^{134}Cs, ^{137}Cs, gross beta and ^{3}H in the Fukushima nuclear plant were not found during October 2014 (Tokyo Electric Power Company: http://www.tepco.co.jp/en/nu/fukushima-np/roadmap/conference-e.html). Relatively low ^{35}S concentrations in southern California during 10/17/2014-11/15/2014 (160±30 atoms m^{-3}, 3 samples) [*Lin et al*, manuscript in preparation] further suggest dramatic ^{35}Cl[*n*,*p*]^{35}S reactions as observed in the Fukushima disaster during 3/13/2011-3/26/2011 (when a huge amount of seawater was used as

coolant) [*Priyadarshi et al.*, 2011b] is implausible. In fact, the conditions of $^{35}Cl[n,\gamma]^{35}S$ reaction are highly specific. It is the reaction of neutrons with high levels of chloride in seawater that produce ^{35}S. Core elements of nuclear reactor do not emit ^{35}S and the $^{35}Cl[n,p]^{35}S$ reaction does not occur in freshwater cooled reactor [*Priyadarshi et al.*, 2011b]. Therefore, impact of fresh or aged stratospheric air is the only candidate that can explain this enhancement.

The strong impact of stratospheric air on the PBL is unexpected because most previous studies showed that in this region stratospheric intrusions only play an important role in spring/winter instead of autumn [*Liu et al.*, 2002; *Oltmans et al.*, 2004]. Presently, it is difficult to determine whether this dramatic enhancement of $^{35}SO_4^{2-}$ concentration is an abnormality in 2014 or yearly occurrence. Recently, [*Lin et al.*, 2014b] estimated higher contributions of stratospheric air to surface O_3 levels in stratospheric intrusion episodes in autumn than in spring/winter during 2011-2012, although the episode frequency in autumn is significantly lower than in winter. [*Liang and Mahata*, 2015] also observed an increasing trend of the oxygen isotope anomaly in CO_2 in October 2013. These results reasonably suggest a strong downward transport of stratospheric air in this monsoon transitional period. In the ensuing section, we interpret our observation data with a 4-box 1D model and meteorological analysis to quantify the contributions of stratospheric air transporting downward to the PBL and to investigate the mixing processes.

6.4.2 Box Model Simulation and Meteorological Analysis

A 4-box 1D model is utilized in this study following the treatment of [*Priyadarshi et al.*, 2011a] (see SI Text), which is useful for quantifying vertical mixing in atmospheric regimes such as the polar vortex [*Priyadarshi et al.*, 2011a] and during Santa Ana wind events [*Priyadarshi et al.*, 2012a]. With the parameters shown in Table 6.1, our model results generally agree with the observed seasonal pattern (Figure 6.2). In spring, some cases with $^{35}SO_4^{2-}$ concentrations significantly lower than the steady-state concentration were affected by strong wet removal. As for the cases with high $^{35}SO_4^{2-}$ concentrations, pulses of stratospheric intrusion to the FT are required

to reproduce these peaks. With no change in the mixing between the FT and the PBL, the model shows that stratosphere-to-troposphere transport events which last for 1-2 days and a contribution of 5-9% stratospheric air masses to the FT would lead to the three springtime peaks as described previously (see SI Text). To increase the $^{35}SO_4^{2-}$ concentration to 3150 atoms m^{-3} as observed during Oct 22-29, the model predicts that at least 50% of air masses in the FT are required to be originating from the lower stratosphere, which is dynamically highly unlikely. Since the $^{35}SO_4^{2-}$ concentrations built up steadily from early October (Figure 6.2), the downward transport of stratospheric air masses to the PBL is likely linked to the development of jet stream which leads to the enhancement of cross-tropopause exchange [*Liang and Mahata*, 2015], and a series of synoptic activities that facilitates the mixing between the FT and the PBL. As shown in Figure 6.1, the vertical pressure velocity (omega) at 500 hPa during October over the East China coast (> 0.02 Pa/s) is larger than surrounding areas, suggesting strong and uniform descending motion is prevalent in this region during October as noted by [*Zheng et al.*, 2015b]. It is highly possible that stratospheric air masses were mixed into and accumulated in the FT first, and the strong descending motion subsequently entrained these aged stratospheric air masses to the PBL.

Table 6.1. Parameters of 4-Box 1D model for calculating the steady-state concentrations of $^{35}SO_2$ and $^{35}SO_4^{2-}$ at Mount Wuyi, China

Parameter	Value
A. Height, km	
Planetary Boundary Layer (Box 1)	0.5
Buffer Layer (Box 2)	1
Free Ttroposphere (Box 3)	8
Lower Stratosphere (Box 4)	16
B. Cosmic ray production rate of ^{35}S (atoms cm^{-3} d^{-1})	
P_1	2.8×10^{-6}
P_2	2.8×10^{-6}
P_3	6.5×10^{-5}
P_4	1.1×10^{-4}
C. $^{35}SO_2$ lifetime (days)	
$\tau_{ox-1} = \tau_{ox-2}$	3
τ_{ox-3}	6
τ_{ox-4}	8
τ_d	1.6
$\tau_{c1} = \tau_{c2}$	5[a]
$\tau_{c3} = \tau_{c4}$	143
τ_λ	126

Table 6.1. Parameters of 4-Box 1D model for calculating the steady-state concentrations of $^{35}SO_2$ and $^{35}SO_4^{2-}$ at Mount Wuyi, China (Continued)

Parameter	Value
D. $^{35}SO_4^{2-}$ removal lifetime (days)	
$\tau_{r1} = \tau_{r2}$	3[b]
τ_{r3}	24
τ_{r4}	365
E. Air mass mixing time (days)	
$\tau_{12} = \tau_{21}$	1
$\tau_{23} = \tau_{32}$	14
$\tau_{34} = \tau_{43}$	290[c]
τ_H	30
τ_{HS}	1

a. Set to 2.5 during JUN-SEP due to frequent precipitation

b. Set to 1.5 during JUN-SEP due to frequent precipitation

c. τ_{43} is set to 145 during OCT-FEB due to the strengthened subtropical jet system and increased stratosphere-to-troposphere mixing

To better clarify the process, an inert stratospheric tracer was simulated by a mesoscale meteorology model (Weather Research and Forecasting Model, WRF) to estimate the contribution of aged stratospheric air masses to the PBL during October (see SI Text for details). In comparison to ^{35}S measurements, the model shows the capability in reproducing the increasing trend of downward transport of stratospheric air masses at the sampling site from October 10 (Figure 6.3), which is likely related to a strong tropical cyclone (Typhoon Vongfong) in the western Pacific Ocean (Figure 6.4a-b). The frequency of tropical cyclones over the western Pacific Ocean is decreasing in October, but its occurrence is an important mechanism entraining stratospheric air downward [*De Bellevue et al.*, 2007; *Jiang et al.*, 2015]. The strong subsidence of air masses at the outer rim of the cyclone not only facilitates the downward transport of stratospheric air masses from the lower stratosphere to the FT, but also greatly enhances the downward penetration from the FT to the PBL. The largest peak of WRF-simulated stratospheric tracer, which accounts for 0.8% of total air masses in the PBL, is observed on October 18 (Figure 6.3), when a subtropical anticyclone was located at the Taiwan Strait (Figure 6.4c-d). This weather pattern is typical in this monsoon transitional period when the western extent of the western Pacific subtropical high starts to retreat eastward from the inner continent to the ocean. It is accompanied by strong subsiding motions in the lower troposphere and piling-up of air masses in the PBL [*Huang et al.*, 2006], facilitating the entrainment of aged stratospheric air masses from the FT to the PBL.

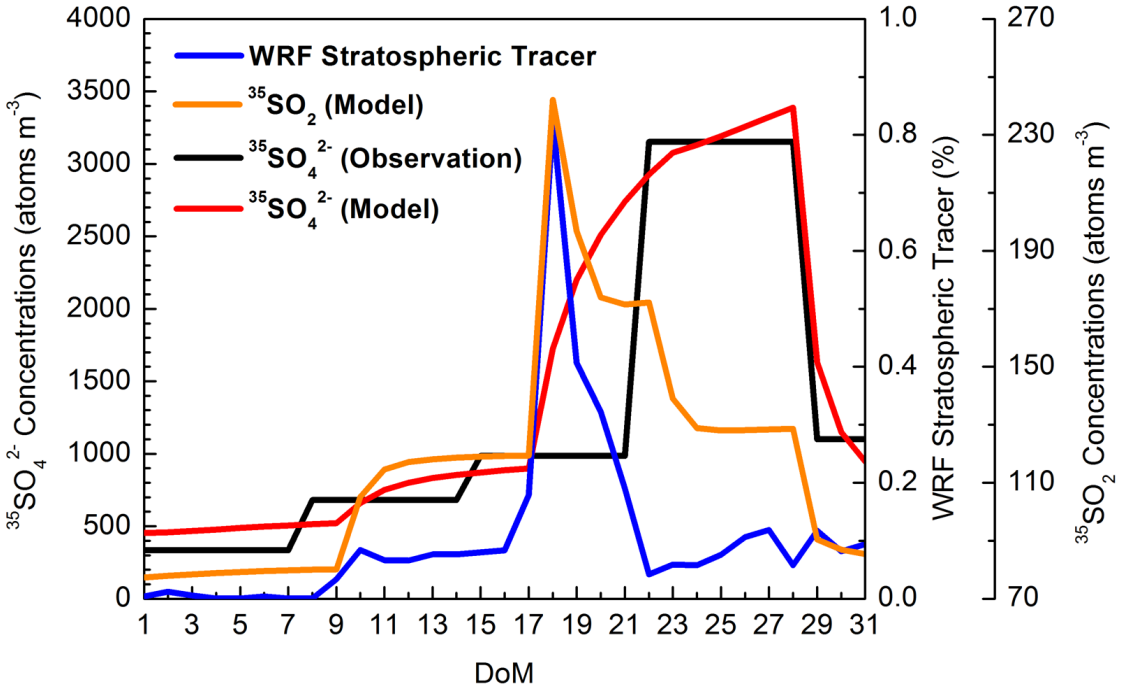

Figure 6.3. Time series of observed $^{35}SO_4^{2-}$ concentrations, the WRF-simulated stratospheric tracer, and $^{35}SO_2$ and $^{35}SO_4^{2-}$ concentrations simulated by a 4-box 1D model from October 1 to October 31 at 2014.

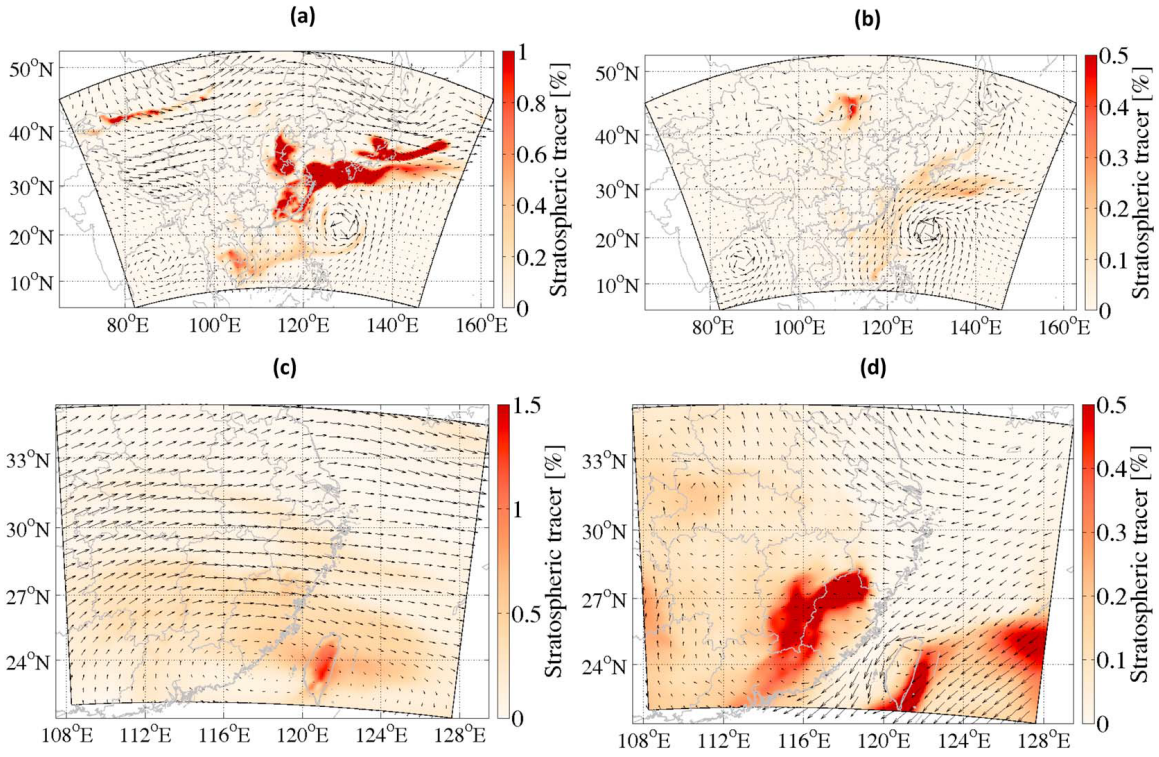

Figure 6.4. Spatial distribution of WRF stratospheric tracer (%) at (a) 500 hPa and (b) 390 m above ground level at 2014/10/10 0000; (c) and (d) As in Figure 4a-b but at 2014/10/18 0800. Note the different domain and scale. The tropical cyclone (2014/10/10) and subtropical anticyclone (2014/10/18) as shown by the wind fields are two major synoptic activities that entrain aged stratospheric air masses in the FT to the PBL in this monsoon transition period (October).

It is noted that the largest peak of $^{35}SO_4^{2-}$ is observed during 10/22/2014-10/29/2014, a trend reproduced by the WRF-simulated stratospheric tracer but with a much smaller magnitude. This underestimation might be attributed to two aspects. Firstly, the chemical processes (i.e., the transformation from $^{35}SO_2$ to $^{35}SO_4^{2-}$ within the aged stratospheric air masses) were not considered in the WRF simulation for the stratospheric tracer in this study, which may contribute to the observed $^{35}SO_4^{2-}$ peak significantly during this period. [*Lin et al.*, 2016b] showed that the mixing of anthropogenic pollution with stratospheric O_3 in aged stratospheric air masses may shorten the oxidative lifetime of SO_2. Taking the enhanced vertical mixing processes mentioned above and the atmospheric SO_2 to SO_4^{2-} conversion into account, our 4-box 1D model was able to reproduce a

$^{35}SO_2$ peak on October 18 and a $^{35}SO_4^{2-}$ peak during 2014/10/22-2014/10/29, which generally match with the WRF-simulated trend and $^{35}SO_4^{2-}$ observation, respectively (Figure 6.3). The 4-box 1D model predicts that aged stratospheric air masses are constantly mixed from the FT and accumulated in the PBL during the $^{35}SO_4^{2-}$ enhancing period, and the oxidative lifetime of SO_2 in the PBL is shortened to 1.5 days under the influences of aged stratospheric air masses (see SI Text and Table 6.2). Our results suggest that $^{35}SO_4^{2-}$ measurement (without $^{35}SO_2$) may not be able to constrain the exact timing of stratospheric intrusion, but it is a highly sensitive tracer to determine the residence time of aged stratospheric air and its impact on the gas-to-particle transformation rate. Secondly, because of the limited computational power, relatively coarse spatial resolutions were used for the simulation, so that the WRF model might not be able to accurately capture some local-scale intrusions or mixing processes, especially those occurred at the outer domain. The cross-tropopause exchange over the upstream areas could be important, because without appropriately considering the mixing and transport of aged stratospheric air masses within the troposphere, the contribution of WRF-simulated stratospheric tracer is at least one order of magnitude smaller at the sampling site (see SI Text and Figure 6.5).

Table 6.2 Input parameters used to simulate the unexpected high $^{35}SO_4^{2-}$ concentrations observed at October 2014. Strong downward transport of aged stratospheric air masses from the FT to the PBL occur in this season. See text for details.

	OCT 10-17	OCT 18	OCT 19-22	OCT 23-27
f_{LS-FT}	0.1%	0.5%	0.5%	0.5%
f_{FT-BuL}	9%	33%	23%	17%
$f_{BuL-PBL}$	9%	33%	23%	17%
$\tau_{ox-1} = \tau_{ox-2}$	3	3	1.5	1.5
τ_{HS}	1	2	3	3

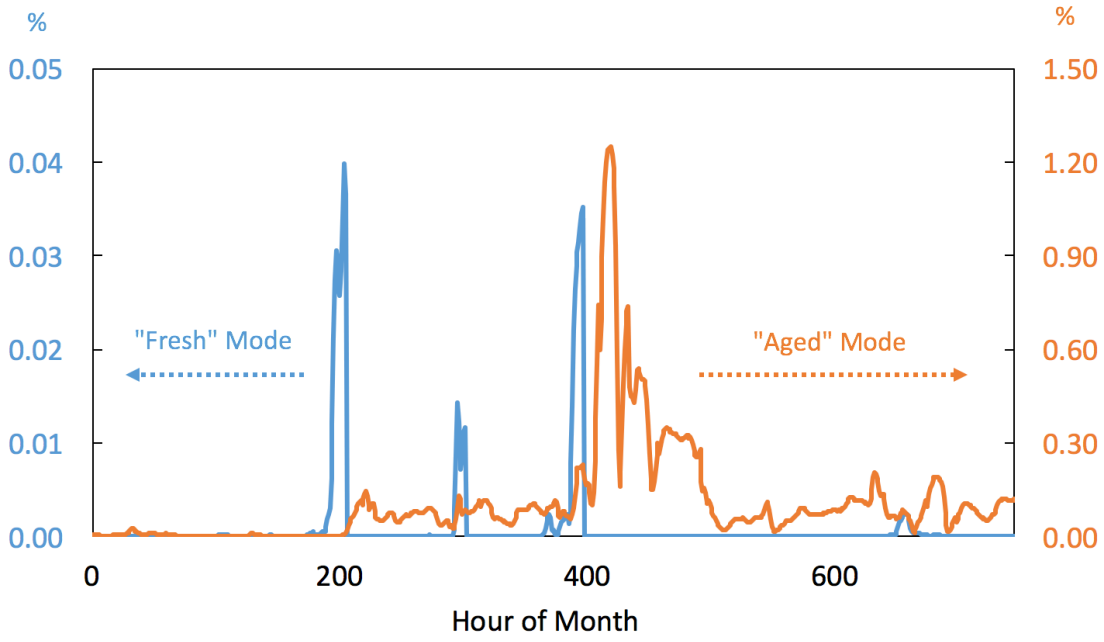

Figure 6.5. Time series of hourly WRF-simulated stratospheric tracer at October 2014

Since our measurements were carried out on a weekly basis and $^{35}SO_2$ concentrations were not measured, we are not able to verify the model results at a high temporal resolution at this stage. Nevertheless, this first attempt unambiguously and reasonably highlights the strong downward transport of stratospheric air masses during this monsoon transitional period, when a series of synoptic activities (i.e., the establishment of the EA major trough and the monsoon jet stream, the southeastward retreat of the western Pacific subtropical high and the tropical cyclones over the western Pacific Ocean) facilitate mixing between the FT and the PBL, entraining aged stratospheric air masses downward and accumulating them in the PBL. In the future, simultaneous measurements of $^{35}SO_2$/ $^{35}SO_4^{2-}$ and other unconstrained parameters at a higher temporal resolution can not only help further resolving the mixing and oxidation processes but also provide a strong basis for model verifications.

6.4.3 Implications for Tropospheric O_3 Budget and CO_2 Biogeochemical Cycle

Based upon the ^{35}S measurements and model simulations, the present study explains why the contributions of stratospheric air masses to the FT in autumn are less than those in spring and winter but more distinct signatures of stratospheric air can be found at the PBL in this season. Our results have broad implications for various research fields such as the tropospheric O_3 budget and the CO_2 biogeochemical cycle.

Tropospheric O_3 plays a crucial role in radiative forcing, troposphere chemistry and air pollution. In EA, surface O_3 maximum is observed in spring, early summer, and autumn, which was traditionally explained by tropospheric photochemical production [*Ding et al.*, 2013; *Ding et al.*, 2008]. Our study shows that the variation of surface O_3 levels (see SI Text for experimental details) is in tandem with $^{35}SO_4^{2-}$ concentration at weekly resolution during these seasons (Figure 6.2). The exception in 10/22/2014-10/29/2014 is likely because the chemical fates of O_3 and $^{35}SO_4^{2-}$ differ in the PBL. Involving a number of physical and chemical scavenging processes, the sinks of O_3 in the PBL are complicated, while $^{35}SO_4^{2-}$ is exclusively removed from the atmosphere by dry

and wet deposition. Furthermore, our model result presented in Section 3.2 shows that the enhanced $^{35}SO_4^{2-}$ is partly due to the oxidation of $^{35}SO_2$ injected into the PBL, which could be a sink of O_3. It highlights that $^{35}SO_4^{2-}$ is useful for tracing the signal and impact of aged stratospheric air, even though most signals are quickly erased in the lower troposphere [*Lin et al.*, 2016b]. Since the mean lifetime of O_3 in the FT is sufficiently long (~30 days) [*Liu et al.*, 1987], our results imply that stratospheric O_3 in aged stratospheric air masses accumulated in the FT may contribute to the surface O_3 concentration and alters the atmospheric chemistry significantly during the mixing between the FT and the PBL in October. Quantifying the amounts of stratospheric O_3 that mix into the PBL is crucial for air quality control and is necessary for establishing reasonable ambient air quality standard [*Lin et al.*, 2015]. A recent study showed that the increases in stratospheric intrusions accounted for ~44% of total increasing trend of O_3 in the FT in China during 2005-2010 [*Verstraeten et al.*, 2015]. Simultaneous measurements of $^{35}SO_2$ and $^{35}SO_4^{2-}$ as shown by [*Lin et al.*, 2016b] can assist in estimating the contributions of stratospheric O_3 to the surface O_3 concentration. In the future, incorporating ^{35}S into a 3D chemistry transport model with O_3 and sulfur chemistry can further advance the quantifications of ^{35}S and stratospheric O_3 at high temporal and spatial resolutions, but more efforts on field-based ^{35}S measurement are required to evaluate the model.

The oxygen isotope anomaly in tropospheric CO_2 due to downwelling flux of CO_2 from the stratosphere may be a probe of estimating gross carbon flux in the troposphere [*Hoag et al.*, 2005; *Liang and Mahata*, 2015; *Thiemens et al.*, 2014]. [*Thiemens et al.*, 2014] showed that this signal could be removed by enhanced atmospheric-biospheric gas exchanges, especially in certain extreme climatic conditions. Considering different lifetimes and removal processes, simultaneous measurements of ^{35}S and oxygen isotope anomaly in CO_2 may provide an additional method to constrain the stratospheric CO_2 influx and illustrate the biogeochemical cycle of CO_2. This work also advances the understanding of ^{14}C (another cosmogenic nuclide, half-life ~5730 years)

injection into the troposphere, which is useful in constraining carbon residence times [*Randerson et al.*, 2002].

6.5 Summary

Our year-long ^{35}S measurements at a background station in EA provided an observational evidence of the seasonal cycle for the strength of downward transport of stratospheric air to the PBL in this region. Our result also reveals strong downward transport of stratospheric air in October, which is tied to a series of synoptic activities facilitating the entrainment of aged stratospheric air masses from the FT to the PBL. This is the first attempt to monitor and resolve the vertical mixing in this period using a chemical tracer mainly originating in the stratosphere with a relatively short lifetime. Our study highlights that further dynamic and meteorological studies to understand the downward transport of aged stratospheric air in EA monsoon transitional period is imperative. In the future, this work can be extended to simultaneous measurements of $^{35}SO_2$, $^{35}SO_4^{2-}$ and other stratospheric tracers (e.g., O_3, ^{7}Be, oxygen isotope anomaly in CO_2) at high temporal resolution to further quantify the mixing process and its effect on the tropospheric sulfur, O_3 and CO_2 budgets.

6.6 Supporting Information

6.6.1 Sample handling and ^{35}S counting procedures

All samples were processed to determine ^{35}S radionuclide concentrations at the University of California San Diego using an ultra-low level liquid scintillation counting spectrometer (Wallac 1220 Quantulus) technique [*Brothers et al.*, 2010]. Soluble sulfate extracted from filter paper was converted to aqueous Na_2SO_4 solution and mixed with Insta Gel Plus cocktail in a scintillation vial before counting. To improve the ratio of signal to noise, organic contaminants and chlorine salts were removed by a PVP (polyvinylpyrrolidone) resin and a Dionex Ag cartridge, respectively. Each sample was counted for 12 times (2-hour counting for each cycle), and any outlier identified by the Dixon's Q-Test ($p<0.01$) was rejected. The energy spectrum of each measurement, especially for the samples with high ^{35}S activity, was checked manually to assure abnormal peaks due to other

radionuclides (e.g., ^{14}C and ^{36}Cl) are absent. The value reported in this paper is the average of 12 individual measurements and was rounded to the nearest ten because measurement errors in most samples (one standard deviation of 12 cycles) are greater than 10 atoms m^{-3}. To determine the background activity, a static field blank created by loading a fresh filter on the sampler for 5–10 min without turning on the pump was subjected to the same chemical analysis procedure. The raw ^{35}S counting data was corrected for the background activity and for the decay time.

6.6.2 Surface ozone measurement

Surface ozone concentrations were measured by a photometric ozone analyzer (Model 49i, Thermo Fisher Scientific, USA). Calibration were performed every month, while zero and span checks were performed every day in order to achieve data with high confidence. The zero drifts were less than 1 ppbv (24 h) and the span drifts were less than 9 ppbv (30 d). The ozone data collected during the sampling period for each ^{35}S sample was averaged for temporal consistency with ^{35}S measurements.

6.6.3 Description of 4-box 1D model

A 4-box 1D model as described by [*Priyadarshi et al.*, 2011a; *Priyadarshi et al.*, 2011b; *Priyadarshi et al.*, 2012a] was utilized to calculate the steady-state concentration of $^{35}SO_4^{2-}$ at Mount Wuyi. The input parameters are listed in Table 6.1. Most values were adopted from the same 4-box 1D model for La Jolla at mid-latitudes [*Priyadarshi et al.*, 2011b; *Priyadarshi et al.*, 2012a] with some exceptions: the height of planetary boundary layer (PBL) was set as 0.5 km above ground level [*Pearson et al.*, 2010]; dry depositional lifetime of SO_2 and removal lifetime of SO_4^{2-} were localized as 1.6 and 3 days, respectively [*Barth and Church*, 1999; *Xu and Carmichael*, 1998]; oxidative lifetimes of SO_2 in the PBL, the buffer layer (BuL) and the free troposphere (FT) were shortened by a factor of ¼ because of higher SO_2 oxidative rate in East Asia than in California [*Lu et al.*, 2010]. As shown by [*Priyadarshi et al.*, 2011b], this model is sensitive to the inputs of the PBL height (H_1) and surface horizontal mixing flux lifetime (τ_{HS}), in which a variation by 10%

varies the model output by 8-10%. Constraining these parameters by field-based measurement in the future can help to improve the model.

The model was run for 400 days to yield the steady-state concentrations of $^{35}SO_4^{2-}$($^{35}SO_2$) in the PBL, the BuL, the FT and the lower stratosphere (LS) of 77 (453), 242 (1035), 310 (929), 774 (7017) atoms m^{-3}, respectively. After the 400-day spin-up, the model was run for another 365 days with some parameters varied depending on season (Table 6.1) to calculate the seasonal steady-state concentrations, which generally agree with the observed seasonal pattern (Figure 6.2). To reproduce the peaks observed at 2014/4/2-2014/4/9, 2014/4/30-2014/5/7 and 2014/6/11-2014/6/18, we applied a factor "f" on both $^{35}SO_2$ and $^{35}SO_4^{2-}$ concentrations to consider the stratospheric intrusion from the LS to the FT [*Priyadarshi et al.*, 2011a]:

$$[^{35}S]_{FT(Spiked)} = [^{35}S]_{FT} + f_{LS\text{-}FT}[^{35}S]_{LS}$$

On April 2, 30 and June 11-12, $f_{LS\text{-}FT}$ was set as 7%, 5% and 9%, respectively, yielding $^{35}SO_4^{2-}$ concentration peaks of 1019, 758 and 953 atoms m^{-3} during 2014/4/2-2014/4/9, 2014/4/30-2014/5/7 and 2014/6/11-2014/6/18, respectively, agreeing with observational data (1127±66, 738±106, 948±95 atoms m^{-3}, respectively). Apart from $f_{LS\text{-}FT}$, we considered downward transports from the FT to the BuL and from the BuL to the PBL with factors $f_{FT\text{-}BuL}$ and $f_{Bul\text{-}FT}$, respectively, during the episode in October. The variations of SO_2 oxidative lifetime (τ_{ox}) and surface horizontal mixing lifetime (τ_{HS}) were also considered in this period because of the favorable conditions for photochemistry (high temperature, clear sky with bright sunshine and strong solar radiation, outflow of polluted air masses) and air pollutant accumulation (weak surface wind) in October [*Zheng et al.*, 2015b]. The parameters used to calculate the variations of $^{35}SO_2$ and $^{35}SO_4^{2-}$ in October are shown in Table 6.2.

6.6.4 WRF stratospheric tracer simulation

The evolution of stratospheric air masses in the atmosphere during October was simulated and quantified by the Weather Research and Forecast model coupled with Chemistry module (WRF-Chem). WRF-Chem is an advanced atmospheric modeling system with capability of simulating complicated dynamical, physical and chemical processes in the atmosphere. In this study, the chemistry module was activated to provide the initial condition of a stratospheric tracer, which was treated as an inert gas without reaction with other species. Therefore, only advection, convection and turbulence diffusion during the tracer transport were considered in the simulation. The Final (FNL) reanalysis data from the National Center of Environmental Prediction (NCEP) were used to provide the initial and boundary meteorological conditions for the simulation, with the fraction of stratospheric tracer above the tropopause being initialized as 100% at the beginning. The domain setting for the simulation is shown in Figure 6.6. The horizontal resolutions of the outer and inner domains are 27 km and 9 km, respectively, both with 50 vertical layers and the top layer at 50 hPa. The simulation was started on September 23, 2014 - 7 days ahead of the investigated period (October) - and lasted for 40 days till November 01, 2014.

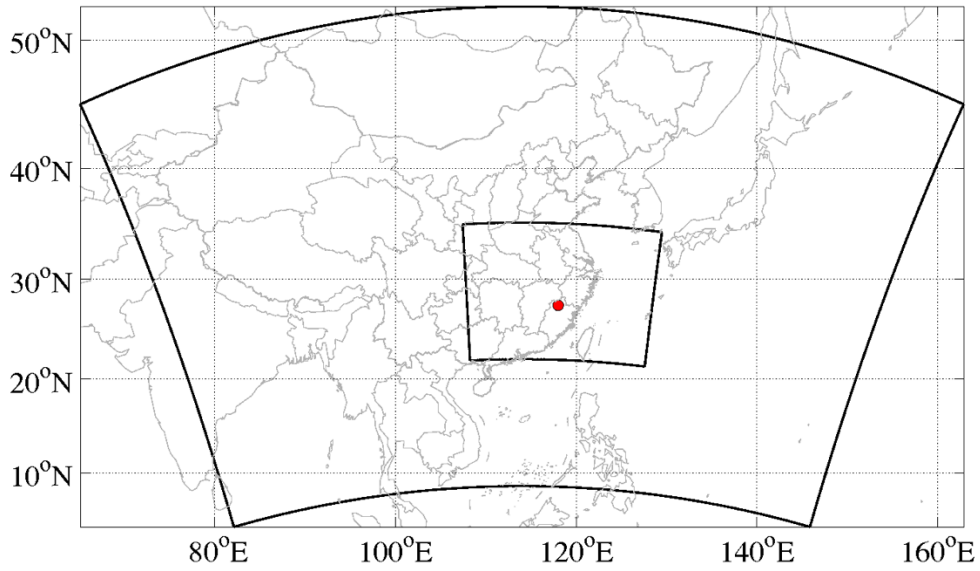

Figure 6.6. The domain setting for WRF simulation. Red dot stands for Mount Wuyi.

In order to evaluate the sensitivity of WRF to aged stratospheric air masses in estimating stratospheric tracer concentration at the sampling site, we conducted two simulations: 1) "Fresh" Mode. The simulation was reinitialized every five days, and the first day of each run was considered as the spin-up time to allow the stratospheric tracer to accumulate in the troposphere. In this case, only the results for the last four days of each run were used for analysis. 2) "Aged" Mode. The 7 days ahead of October were considered as the spin-up time for the simulations to allow the stratospheric tracer to accumulate in the troposphere to a reasonable level comparable to realistic conditions at the beginning of October. The simulation was conducted for the investigated period continuously without re-initialization, enabling stratospheric air masses to accumulate and transport in the troposphere. For both cases, four-dimensional data assimilation (FDDA) was conducted every 6 hours using temperature, wind and humidity fields from FNL reanalysis data to prevent the simulations from drifting away from the realistic conditions. The results show that the

trend of WRF-simulated stratospheric tracer at the sampling site can be captured by both simulations, however, with significantly different magnitudes (Figure 6.5). The magnitude from the first simulation ("fresh" mode) is at least one order smaller than the second one ("aged" mode), indicating that apart from the direct stratospheric intrusion, the aged stratospheric air masses within the FT over the upstream areas play an important role in contributing to the enhancement of WRF-simulated stratospheric tracer at the sampling site. Therefore, the mixing and accumulation of aged stratospheric air masses in the troposphere should be well considered in estimating the contribution of stratospheric intrusion to surface air. In this study, results from "aged" mode were used to compare with $^{35}SO_4^{2-}$ observation.

6.7 Acknowledgement

This study was supported in part by National Natural Science Foundation of China (Grant No. 41475119). Mang Lin acknowledges a fellowship from the Guangzhou Elite Project (JY201303). Reviewers of the manuscript are acknowledged for their careful review and significant contribution to revising the manuscript.

This chapter, in full, is a reprint of the material "Unexpected high ^{35}S concentration revealing strong downward transport of stratospheric air during the monsoon transitional period in East Asia" as it appears in Geophysical Research Letters 2016. Lin, Mang; Zhang, Zhisheng; Su, Lin; Su, Binbin; Liu, Lanzhong; Tao, Jun; Fung; Jimmy C.H.; Thiemens, Mark H., American Geophysical Union, 2016. The dissertation author was the primary investigator and author of this paper.

Chapter 7 Vertically uniform formation pathways of tropospheric sulfate aerosols in East China detected from triple stable oxygen and radiogenic sulfur isotopes

7.1 Abstract

Sulfate aerosols (SO_4^{2-}) in the continental outflow from East China significantly alters the atmospheric sulfur budget across the Pacific Rim, but its formation pathways, especially in the free troposphere (FT), remain poorly understood. Here we analyze stable oxygen ($\delta^{17}O$ and $\delta^{18}O$) and radiogenic sulfur (^{35}S) isotopes in SO_4^{2-} collected at a mountain site in East China to investigate SO_4^{2-} formation pathways at varying altitudes. We find that $\Delta^{17}O$ ($=\delta^{17}O-0.52\times\delta^{18}O$) in SO_4^{2-} is not correlated with ^{35}S (a direct measure of high-altitude air masses). This pattern notably differs from the currently known ^{35}S-$\Delta^{17}O$ relation. The result implies that the formation pathway of tropospheric SO_4^{2-} in East China is vertically uniform, likely due to large emissions and active convection in this region. Our measurements provide unambiguous isotopic constraints for reducing uncertainties in modeling SO_4^{2-} in the FT over East China, which greatly affects regional climate but current models fail to accurately estimate.

7.2 Introduction

As one of the major components of atmospheric aerosols, sulfate (SO_4^{2-}) not only influences the radiative balance of the Earth's climate system but also exerts adverse effects on public health [*Harris et al.*, 2013b; *Wang et al.*, 2016]. Most SO_4^{2-} is produced through the oxidation of sulfur dioxide (SO_2), an air pollutant largely emitted from fossil fuel combustion [*Lu et al.*, 2010; *McLinden et al.*, 2016]. The SO_4^{2-} formation pathways are mainly dominated by gas- or aqueous-phase oxidation of SO_2 by OH radical or H_2O_2/O_3, respectively [*Ishino et al.*, 2017; *Lee et al.*, 2001; *Lee and Thiemens*, 2001; *Savarino et al.*, 2000; *Savarino and Thiemens*, 1999; *Vicars and Savarino*, 2014]. Other oxidants such as O_2 (catalyzed by transition metals) can also contribute to SO_2

oxidation in the aqueous phase [*Alexander et al.*, 2009; *Harris et al.*, 2013b; *Huang et al.*, 2014b; *Li et al.*, 2017a; *McCabe et al.*, 2006; *Wang et al.*, 2016].

Due to rapid economic development, anthropogenic SO_2 emissions in China account for ~1/4 of total global emissions [*Lu et al., 2010*]. The polluted outflow from East China can alter the chemical composition of the atmosphere over the northwestern Pacific and downwind continents [*Goto et al.*, 2015; *Lin et al.*, 2010; *Priyadarshi et al.*, 2011b; *Verstraeten et al.*, 2015]. The global transport GEOS-Chem model shows that up to 24% of SO_4^{2-} over the western United States is contributed by trans-Pacific transport [*Lin et al.*, 2014a]. Given acidic SO_4^{2-} in the polluted outflow can increase the iron solubility in aerosols [*Li et al.*, 2017b], the deposition of aerosols during trans-Pacific transport [*Zhao et al.*, 2006] may enhance the supply of bioavailable iron (a key micronutrient regulating biological productivity in the ocean) to the Pacific Ocean.

Because SO_4^{2-} in the free troposphere (FT) possesses a longer lifetime (~1 week) than the planetary boundary layer (PBL) and can be rapidly entrained offshore by the strong mid-latitude westerly jet (Figure 1), an accurate prediction of sulfur vertical distribution in East China is critically important to evaluate the extent to which sulfur emissions in this region affect regional and global climate. Large uncertainties (up to ~500% relative differences) exist in current model calculations of SO_2/SO_4^{2-} concentrations in the FT over East China due to inadequate understanding of SO_4^{2-} formation and vertical transport [*Goto et al.*, 2015; *He et al.*, 2012]. This gap of understanding derives from difficulty in measuring or sampling SO_4^{2-} in the FT and quantifying its formation pathways by field-based measurements. Aircraft equipped with an aerosol mass spectrometer can assist, in part, in such investigations [*van Donkelaar et al.*, 2008], but measurements are expensive and not widely available.

Here we present multiple isotopic measurements of SO_4^{2-} collected at the Earth's surface to identify SO_4^{2-} originating from the FT and constrain its formation pathway. The oxygen-17 anomaly ($\Delta^{17}O=\delta^{17}O-0.52\times\delta^{18}O$) in SO_4^{2-} is derived from the oxidants involved in its formation,

providing an isotopic constraint for the relative importance of SO_4^{2-} formation pathways [*Lee et al.*, 2001; *Lee and Thiemens*, 2001; *Lyons*, 2001; *Savarino et al.*, 2000; *Savarino and Thiemens*, 1999; *Vicars and Savarino*, 2014] [see Supporting Information (SI) Text S1 and Table S1 for details]. The radiogenic ^{35}S (half-life = 87 days) is exclusively produced in the higher atmosphere by high-energy cosmic rays [*Lal and Peters*, 1967], and therefore an enrichment of ^{35}S in the PBL is a direct measure of downward mixing of SO_2/SO_4^{2-} from the FT (or the stratosphere) [*Lin et al.*, 2016a; *Priyadarshi et al.*, 2011a; *Priyadarshi et al.*, 2012a]. Consequently, the coupled analysis of $\Delta^{17}O$ and ^{35}S in the same SO_4^{2-} samples is a novel, unique and powerful tool to gain formation chemistry ($\Delta^{17}O$) and source altitude (^{35}S) information of SO_4^{2-} from field-based measurements [*Hill-Falkenthal et al.*, 2013; *Hill-Falkenthal et al.*, 2012a].

7.3 Materials and Methods

7.3.1 Aerosol Sampling

The sampling site is located at Mount Wuyi (27.72°N, 117.68°E, 1139 m above sea level), which is a national atmospheric background monitoring station operated by the Ministry of Environmental Protection of People's Republic of China (Figure 7.1). This station has negligible local emissions and was established to investigate regional atmospheric compositions in East China. The isotopic compositions reported in this study represent regional characteristics at this location. During Mar 2014 – Feb 2015, fine aerosol (with aerodynamic diameter < 2.5 μm) samples were collected on quartz filters (Whatman, UK) using a high-volume air sampler (TE-6070DV-BLX, Tisch Environmental Inc., USA) with a $PM_{2.5}$ impactor at a flow rate of ~1.13 m^3 min^{-1}. Each sample was collected for 1 week. After sampling, half of the filter was sent to the South China Institute of Environmental Sciences for soluble inorganic ion measurements, and the other half was sent to the Stable Isotope Laboratory at the University of California San Diego for isotopic analysis. A static field blank was created by loading a fresh filter on the sampler for 30-60 min without turning the pump on, and was subjected to the same chemical analysis procedure.

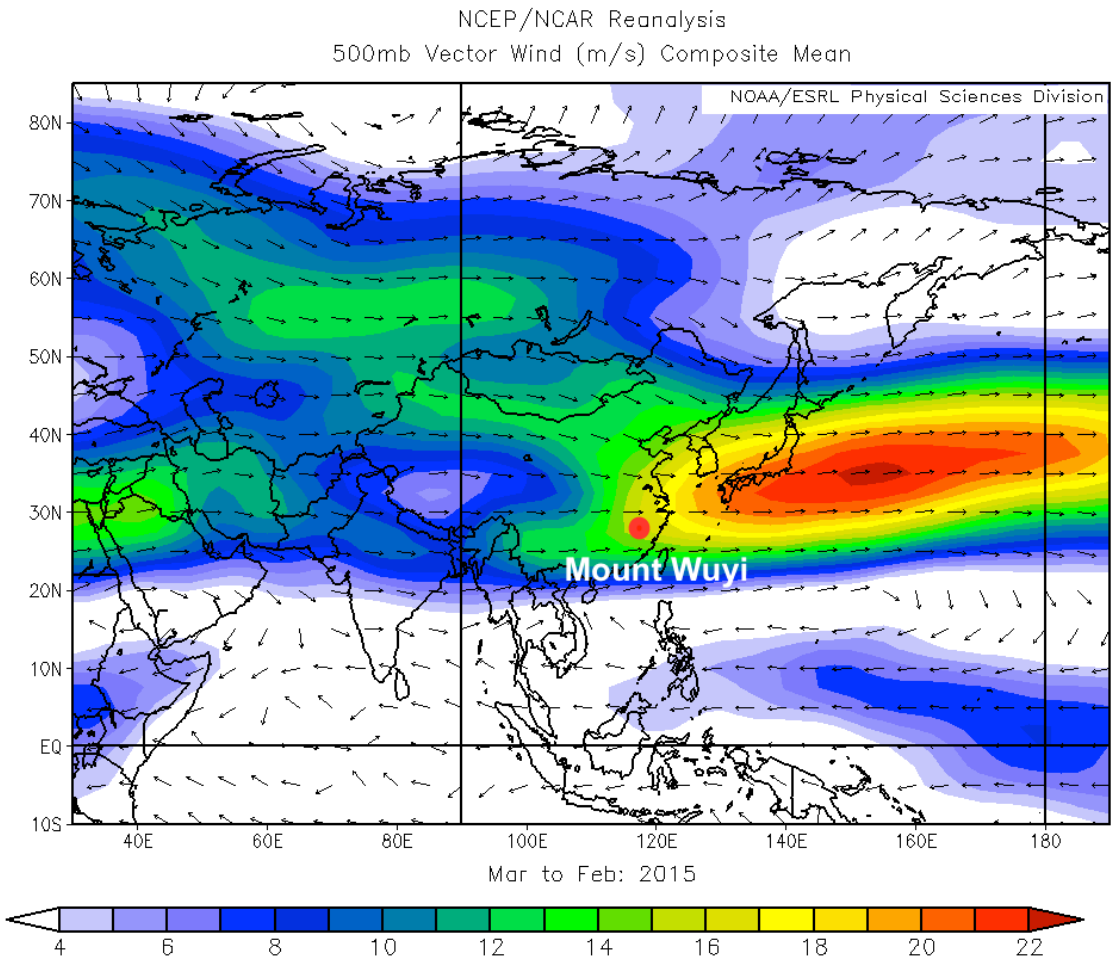

Figure 7.1. Map showing the location of the atmospheric background station in this study (Mount Wuyi). The base map shows vector wind at 500 hPa during the sampling period (Mar 2014 to Feb 2015) using the National Centers for Environmental Prediction (NECP) reanalysis data, highlighting the rapid trans-Pacific transport of the polluted outflow in the free troposphere.

7.3.2 Isotopic Analysis

Water-soluble SO_4^{2-} was extracted from the filter papers using deionized water. An aliquot of solution was taken for stable isotope measurements, while the rest was processed to determine concentrations of radiogenic ^{35}S. For the ^{35}S counting, pre-cleaned aqueous SO_4^{2-} solution was mixed with 10 mL of scintillation gel (Insta-Gel Plus, PerkinElmer) in a plastic scintillation vial (Fisherbrand), and the ^{35}S activity was measured by an ultra-low level liquid scintillation spectrometer (Wallac 1220 Quantulus). The raw ^{35}S counting data were corrected for background

activity and for the decay time. A detailed description of ^{35}S measurements and quality assurance and control can be found in the literature [*Brothers et al.*, 2010; *Lin et al.*, 2016c]. The triple oxygen isotopic analysis was performed by separating SO_4^{2-} using an ion chromatography and converting to Ag_2SO_4 for pyrolysis. The O_2 gas obtained from the pyrolysis of Ag_2SO_4 in a quartz tube at a temperature of 1030°C was purified through a gas chromatography, and its triple oxygen isotopic composition was measured by an isotope ratio mass spectrometry (MAT253). A total of 20 samples covering all seasons in the sampling period (Mar 2014 – Feb 2015) and the full range of ^{35}S variation were used for triple oxygen isotopic analysis (Figure 2). The obtained values of $\delta^{18}O$ and $\Delta^{17}O$ were corrected for the constant isotopic shift associated with this pyrolysis method [*Savarino et al.*, 2001; *Schauer et al.*, 2012]. Replicate analysis of laboratory standards showed that the uncertainties (1 standard deviation) of $\delta^{18}O$ and $\Delta^{17}O$ measurements were 0.8‰ and 0.06‰, respectively. Given that the sea-salt content in each fine aerosol sample (using sodium as a sea salt tracer with an assumption that the molar ratio of SO_4^{2-} to sodium be 0.0604 in sea-salt spray) is less than 1.5% (with an average of 0.9±0.3%), the oxygen isotopic compositions are not corrected for non-sea-salt SO_4^{2-}.

7.3.3 Measurements of Water-Soluble Inorganic Ions

A small portion (2.66 cm^2) from each quartz filter was dissolved in 5.0 mL of deionized water in a glass bottle under ultrasonic agitation for 60 minutes. After removing insoluble materials, the filter extracts were used to determine concentrations of water-soluble inorganic ions. The cations (Na^+, NH_4^+, K^+, Ca^{2+} and Mg^{2+}) were quantified on an ion chromatography (Dionex ICS-1600) using Ionpac CS12 analytical column with 20 mM methanesulfouic acid as the eluent, while the anions (Cl^-, NO_3^- and SO_4^{2-}) were detected on another ion chromatography (Dionex ICS-2100) using Ionpac AG19 analytical column with 20 mM KOH as the eluent. The concentrations of measured ions reported in this study are all corrected by the field blank.

7.4 Results and Discussion

7.4.1 Coupled Measurements of $\Delta^{17}O$ and ^{35}S in the Same SO_4^{2-} Samples

Our yearlong $\Delta^{17}O(SO_4^{2-})$ measurements show an average of 1.24‰, with a small standard deviation (±0.15‰, n = 20) and no clear seasonal variation (Figure 7.2; SI Text and Table 7.1). Figure 7.3 shows that SO_4^{2-} formation in this region is likely dominated by the aqueous S(IV)+H_2O_2 oxidation. Given prevailing acidic conditions in the background atmosphere of East China revealed by previous measurements [*Guo et al.*, 2012] and thermodynamic equilibrium model calculation [*Bougiatioti et al.*, 2016; *Fountoukis and Nenes*, 2007; *Guo et al.*, 2015] (see SI Text and Table 7.2 for detailed discussion and calculation), the S(IV)+H_2O_2 reaction should dominate because the S(IV)+O_3 reaction proceeds very slowly at pH<5.5 [*Lee and Thiemens*, 2001]. Quantitatively, the average upper limit of contribution fractions from the S(IV)+H_2O_2 reaction is estimated to be 92±3% (1σ; SI Table 7.3; see SI Text for calculations). It is noted that the pattern of $\Delta^{17}O$ versus $\delta^{18}O$ found in this study (Figure 7.4) is similar to carbonates extracted from terrestrial aerosols and Martian meteorites (see [*Shaheen et al.*, 2010]). The general trend of $\Delta^{17}O$ indicates that a full understanding of $\Delta^{17}O(SO_4^{2-})$ in this region may also provide new insights into other atmospheric and planetary processes [*Thiemens et al.*, 2012]. More accurate quantification can be obtained by using global chemistry transport models (e.g. GEOS-Chem) [*Alexander et al.*, 2012; *Alexander et al.*, 2009; *Chen et al.*, 2016a; *Sofen et al.*, 2011], but that is beyond the scope of this study.

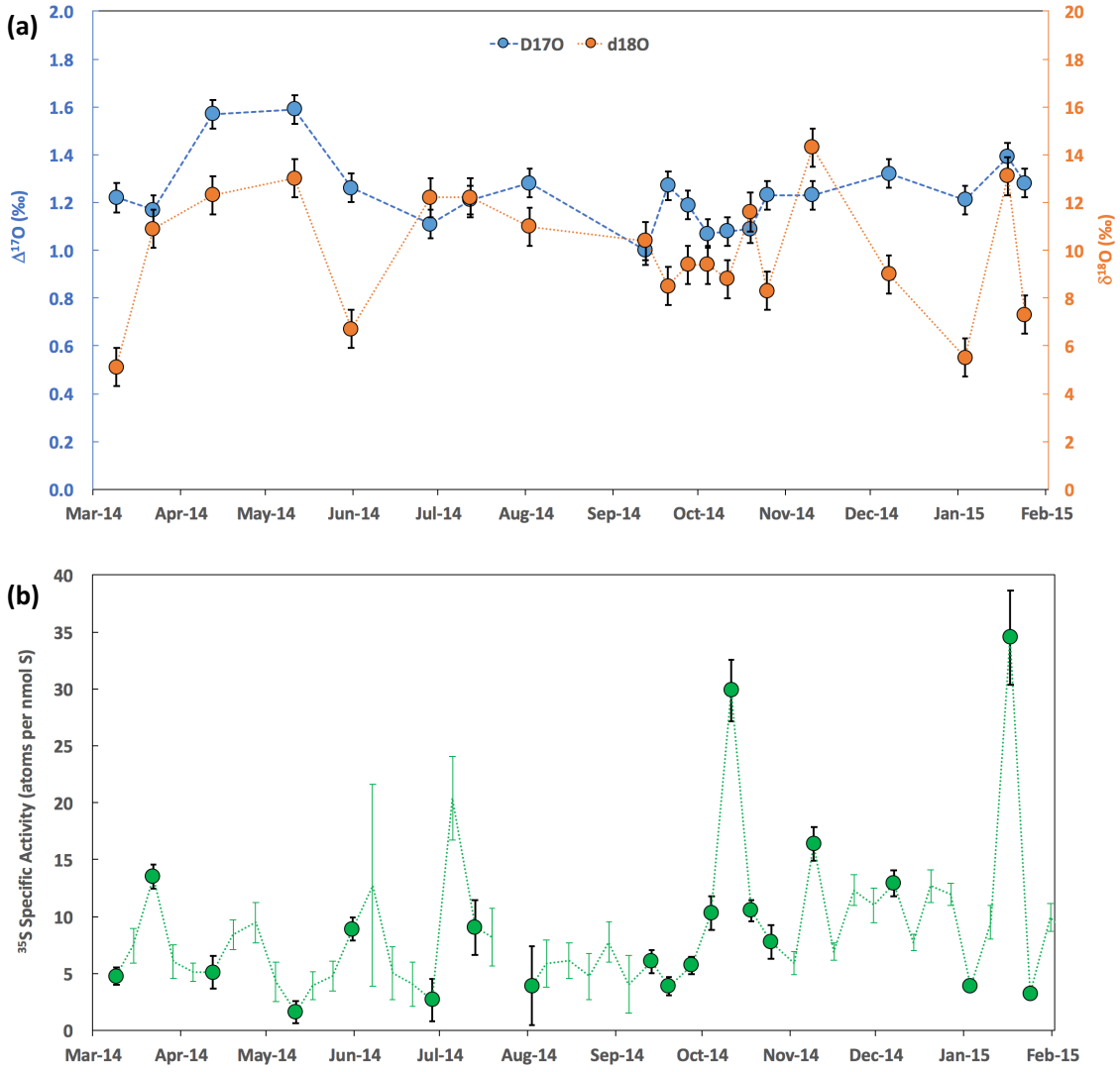

Figure 7.2. Time series of (a) $\Delta^{17}O$ and $\delta^{18}O$ and (b) ^{35}S specific activity for sulfate aerosols collected at Mount Wuyi in the period of 2014-2015. Error bars stand for one standard deviation. In Figure 7.2b, green circles represent samples used for triple oxygen isotopic analysis in this study.

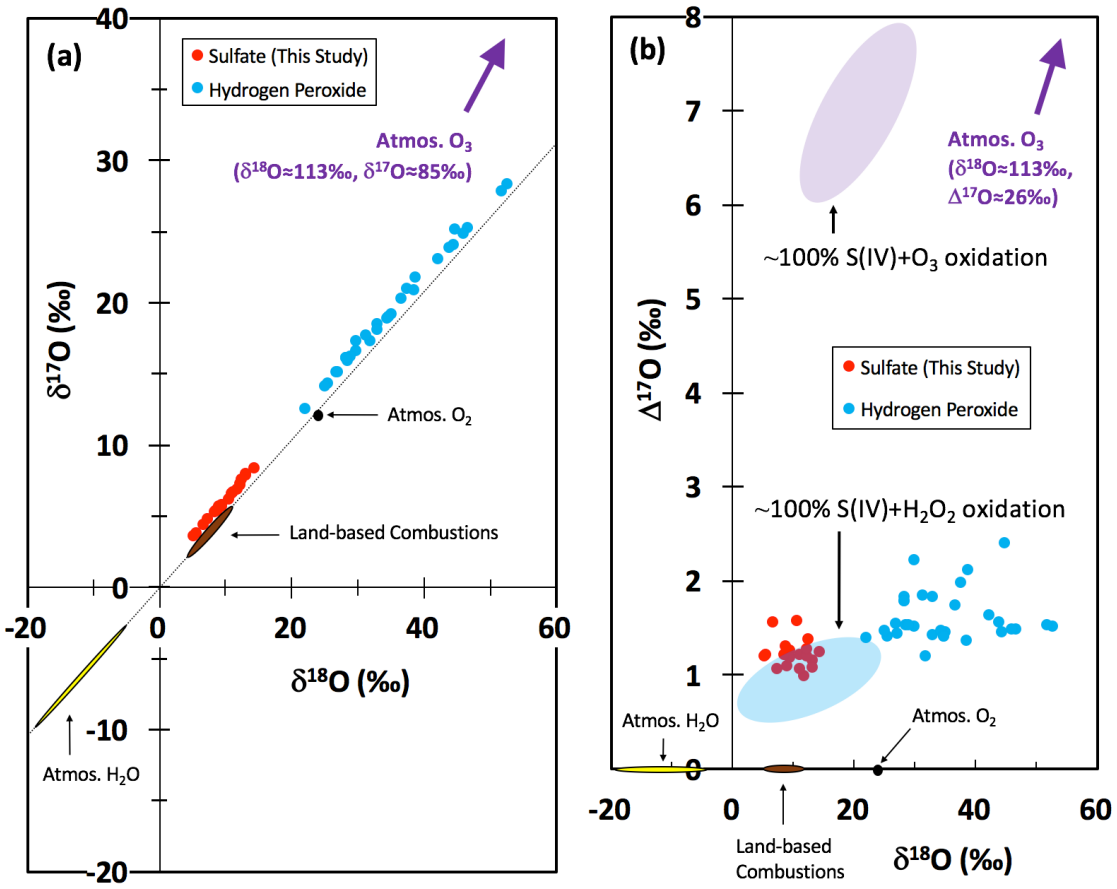

Figure 7.3. Triple oxygen isotopes of sulfate aerosols measured in this study (red circles): (a) $\delta^{17}O$ versus $\delta^{18}O$, the dot line represents mass dependent fractionation line (slope = 0.52); (b) $\Delta^{17}O$ versus $\delta^{18}O$. For comparison, the measurements of hydrogen peroxide in rain water (blue circles), and the ranges of other potential sources of oxygen in sulfate aerosols are also shown. Oxygen compositions of H_2O_2, O_3, O_2, land-based combustions and H_2O (in the study region) are obtained from Savarino and Thiemens [1999], Vicars and Savarino [2014], Luz and Barkan [2005], Lee et al. [2002], and Bowen et al. [2005], respectively. The light blue (or purple) oval represents the estimated oxygen isotopic signature of sulfate aerosols ~100% produced from H_2O_2 (or O_3) oxidation.

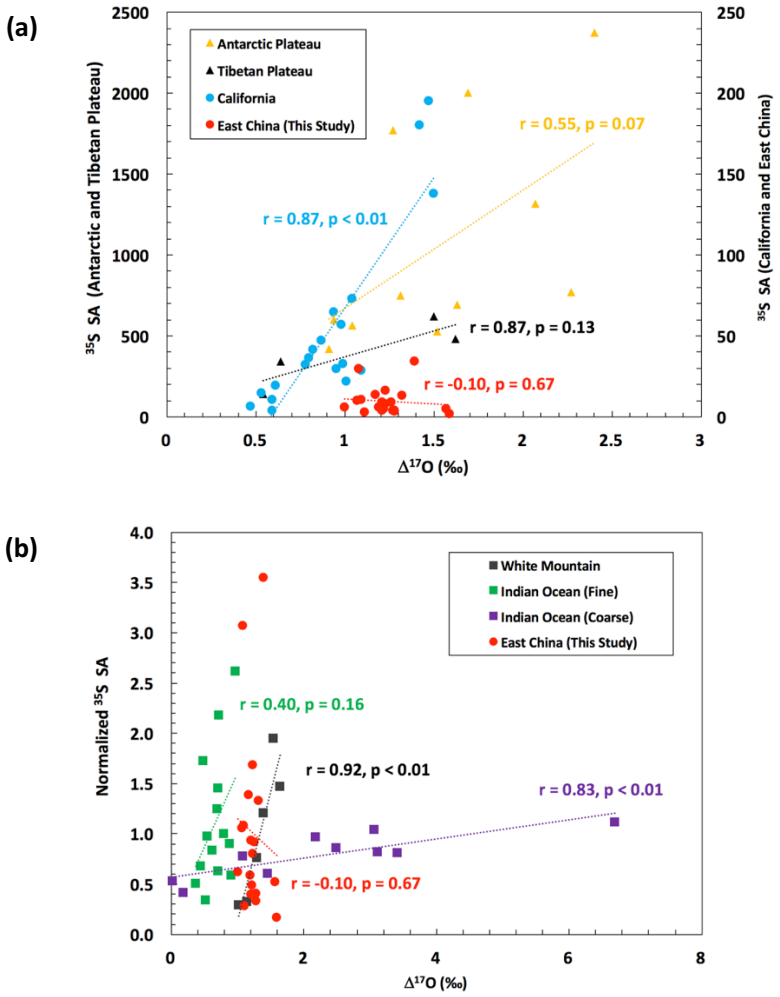

Figure 7.4. (a) Correlation plot between $\Delta^{17}O(SO_4^{2-})$ and ^{35}S specific activities (SA; unit: atoms / nmol SO_4^{2-}) in this study, along with results from previous studies [*Hill-Falkenthal et al.*, 2013; *Hill-Falkenthal et al.*, 2012a; *Lin et al.*, 2016b]. (b) Same as Figure 7.4a. ^{35}S SA for White Mountain and Indian Ocean were reported as normalized ^{35}S SA (dividing individual SA by the average SA) to minimize errors due to the low accuracy and precision of the Geiger-Muller counter technique used in those early studies [*Lee*, 2000; *Lee and Thiemens*, 2001]. The letters "r" and "p" represent the Pearson Correlation Coefficient and the statistically significant level, respectively.

Table 7.1. $\Delta^{17}O$ values of sulfates produced via various major oxidation pathways in the troposphere.

Oxidation Pathway	Phase	$\Delta^{17}O$ (Oxidant)	$\Delta^{17}O(SO_4^{2-})$	References
$SO_2 + OH$	Gaseous	0‰	0‰	[*Lyons*, 2001]
$S(IV) + H_2O_2$	Aqueous	1.6‰	0.8‰	[*Savarino and Thiemens*, 1999]
$S(IV) + O_3$	Aqueous	26‰	6.5‰	[*Vicars and Savarino*, 2014]
$S(IV) + O_2$	Aqueous	-0.34‰	-0.09‰	[*Luz and Barkan*, 2005]

Table 7.2. Soluble inorganic ion concentrations (unit: μg m^{-3}), relative humidity (RH, unit: %), temperature (Temp, unit: K), and ISORROPIA-II-model-calculated aerosol pH values for $PM_{2.5}$ collected at Mount Wuyi.

Sample	Na^+	SO_4^{2-}	NH_4^+	NO_3^-	Cl^-	Ca^{2+}	K^+	Mg^{2+}	RH	Temp	pH
Mar 20-26 2014	0.2	7.6	2.3	0.4	0.0	0.1	0.4	0.0	57.2	281.4	0.4
Apr 2-9 2014	0.1	8.0	2.2	0.0	0.0	0.1	0.2	0.0	75.5	286.5	-0.1
Apr 23-30 2014	0.0	4.1	1.1	0.0	0.0	0.1	0.1	0.0	83.0	288.1	0.2
May 22-28 2014	0.1	6.9	1.8	0.0	0.0	0.1	0.2	0.0	86.7	292.4	0.3
Jun 11-18 2014	0.1	10.2	3.0	0.1	0.0	0.1	0.4	0.0	66.8	295.8	0.1
Jul 9-16 2014	0.1	3.4	1.0	0.0	0.0	0.0	0.1	0.0	78.6	297.3	0.0
Jul 23-30 2014	0.1	3.0	0.9	0.0	0.0	0.0	0.1	0.0	78.3	296.6	0.0
Aug 13-19 2014	0.0	2.1	0.6	0.0	0.0	0.0	0.0	0.0	87.4	295.0	0.2
Sep 23-30 2014	0.1	7.6	2.0	0.0	0.0	0.1	0.2	0.0	80.7	295.2	0.1
Sep30-Oct8 2014	0.1	8.3	2.6	0.1	0.0	0.1	0.3	0.0	62.5	291.7	1.4
Oct 8-15 2014	0.2	11.4	3.4	0.0	0.0	0.1	0.3	0.0	65.2	289.7	0.2
Oct 15-22 2014	0.2	9.2	2.7	0.0	0.0	0.1	0.5	0.0	59.9	290.6	0.2
Oct 22-29 2014	0.2	10.1	3.3	0.2	0.0	0.1	0.5	0.0	68.7	289.7	1.4
Oct29-Nov5 2014	0.2	10.0	3.4	0.4	0.0	0.1	0.5	0.0	77.3	288.0	1.5
Nov 5-12 2014	0.1	3.4	1.0	0.0	0.0	0.0	0.1	0.0	92.4	284.1	0.7
Nov 20-27 2014	0.1	4.8	1.5	0.1	0.0	0.1	0.2	0.0	80.8	286.6	1.6
Dec 18-25 2014	0.2	5.7	2.0	1.8	0.0	0.2	0.5	0.0	43.4	278.9	1.5
Jan 14-21 2015	0.1	10.3	3.6	1.3	0.0	0.1	0.4	0.0	61.3	279.1	1.4
Jan18-Feb4 2015	0.0	1.1	0.4	0.1	0.0	0.0	0.1	0.0	96.4	276.1	2.0
Feb 4-11 2015	0.1	12.7	5.1	4.2	0.0	0.1	0.6	0.0	53.5	276.4	1.7

Table 7.3. $\delta^{18}O$, $\Delta^{17}O$, ^{35}S specific activity (SA) values for sulfate aerosols collected at Mount Wuyi. Errors for $\delta^{18}O$ and $\Delta^{17}O$ are 0.8‰ and 0.06‰, respectively.

Sample	$\delta^{18}O$ (‰)	$\Delta^{17}O$ (‰)	^{35}S SA (atoms / nmol S)	$f_{O3,\ max}$ (%)	$f_{O3,\ min}$ (%)	$f_{O2,\ max}$ (%)	$f_{H2O2,\ max}$ (%)
Mar 20-26 2014	5.1	1.22	5±1	20	7	80	93
Apr 2-9 2014	10.9	1.17	14±1	19	6	81	94
Apr 23-30 2014	12.3	1.57	5±1	25	14	75	86
May 22-28 2014	13.0	1.59	2±1	25	14	75	86
Jun 11-18 2014	6.7	1.26	9±1	20	8	80	92
Jul 9-16 2014	12.2	1.11	3±2	18	5	82	95
Jul 23-30 2014	12.2	1.21	9±2	20	7	80	93
Aug 13-19 2014	11.0	1.28	4±3	21	8	79	92
Sep 23-30 2014	10.4	1.00	6±1	17	4	83	96
Sep 30 - Oct 8 2014	8.5	1.27	4±1	21	8	79	92
Oct 8-15 2014	9.4	1.19	6±1	19	7	81	93
Oct 15-22 2014	9.4	1.07	10±1	18	5	82	95
Oct 22-29 2014	8.8	1.08	30±3	18	5	82	95
Oct 29 – Nov 5 2014	11.6	1.09	11±1	18	5	82	95
Nov 5-12 2014	8.3	1.23	8±1	20	8	80	92
Nov 20-27 2014	14.3	1.23	16±1	20	8	80	92
Dec 18-25 2014	9.0	1.32	13±1	21	9	79	91
Jan 14-21 2015	5.5	1.21	4±0	20	7	80	93
Jan 18 – Feb 4 2015	13.1	1.39	35±4	22	10	78	90
Feb 4-11 2015	7.3	1.28	3±0	21	8	79	92

Our previous study revealed a large variation of absolute $^{35}SO_4^{2-}$ concentrations in these samples (80-3150 atoms m^{-3}) [*Lin et al.*, 2016c], indicating frequent impacts of air masses from varying altitudes at our sampling site. The variation of ^{35}S activity offers an opportunity to identify samples collected in air masses originating from the FT and investigate how $\Delta^{17}O(SO_4^{2-})$ varies depending on altitude. In this study, we report ^{35}S specific activities (SA; unit: ^{35}S atoms / nmol SO_4^{2-}) to compare with $\Delta^{17}O(SO_4^{2-})$ because SA accounts for non-radiogenic sulfur ($[^{35}S] = 0$ atoms m^{-3}) emitted from the PBL, while $^{35}SO_4^{2-}$ concentrations only incorporate radiogenic sulfur from the higher atmosphere [*Brothers et al.*, 2010; *Hill-Falkenthal et al.*, 2013; *Hill-Falkenthal et al.*, 2012a]. The ^{35}S SA in this study ranges from 2 to 35 atoms / nmol SO_4^{2-}, close to most samples collected in California [*Hill-Falkenthal et al.*, 2012a] but significantly lower than the pristine Antarctic and Tibetan Plateau [*Hill-Falkenthal et al.*, 2013; *Lin et al.*, 2016b], which are less affected by emissions of non-radiogenic sulfur and much closer to the higher atmosphere (^{35}S source) (Figure 7.4).

7.4.2 Vertically Uniform Formation Pathway of SO_4^{2-} Revealed by ^{35}S-$\Delta^{17}O$ Relationship

The most striking and salient result from this study is the absence of correlation between ^{35}S SA and $\Delta^{17}O(SO_4^{2-})$ ($r = -0.10$, $p = 0.67$), which notably differs from the currently known ^{35}S-$\Delta^{17}O$ relation [*Hill-Falkenthal et al.*, 2013; *Hill-Falkenthal et al.*, 2012a; *Lee*, 2000; *Lee and Thiemens*, 2001; *Lin et al.*, 2016b] (Figure 7.4). Previous measurements show positive correlations between ^{35}S SA and $\Delta^{17}O(SO_4^{2-})$ in the western United States, Indian Ocean, Antarctic and Tibetan Plateau [*Hill-Falkenthal et al.*, 2013; *Hill-Falkenthal et al.*, 2012a; *Lee*, 2000; *Lee and Thiemens*, 2001; *Lin et al.*, 2016b] [i.e., higher $\Delta^{17}O(SO_4^{2-})$ in the FT than the PBL at regional scales] (Figure 7.4), which was interpreted as results of increased oxidation of SO_2 by high altitude (or stratospheric) O_3 and/or smaller fractions of mass dependent SO_4^{2-} (i.e., $\Delta^{17}O = 0$) [*Lee et al.*, 2002] entrained from the PBL [*Hill-Falkenthal et al.*, 2013; *Hill-Falkenthal et al.*, 2012a; *Lee*, 2000; *Lee and Thiemens*, 2001; *Lin et al.*, 2016b]. As the elapsed time of aerosol sampling in previous studies

[*Hill-Falkenthal et al.*, 2013; *Hill-Falkenthal et al.*, 2012a; *Lee*, 2000; *Lee and Thiemens*, 2001; *Lin et al.*, 2016b] ranges from 2 days to 1 month, the lack of correlation between ^{35}S SA and $\Delta^{17}O(SO_4^{2-})$ in this study cannot be explained by the low temporal resolution of our samples (1 week).

To further understand the variation of $\Delta^{17}O(SO_4^{2-})$ at varying altitudes in East China, the combined $\Delta^{17}O$ and ^{35}S measurements are examined. Because of the active mixing in the atmosphere, it is difficult to collect aerosol 100% originating from the FT. Given that our samples were collected at ~1000 m a.s.l. (the top of the PBL [*Lin et al.*, 2008a]), it is reasonable to suggest that two SO_4^{2-} samples with exceptionally high ^{35}S SA (30 and 35 atoms / nmol SO_4^{2-}, ~6σ greater than the average of other samples) represent SO_4^{2-} mainly originating from the FT (Figure 7.2; see SI Text for detailed discussion and meteorological analysis). Our measurements show that $\Delta^{17}O(SO_4^{2-})$ in the FT (1.23±0.22‰) is identical to others (SO_4^{2-} in the PBL: 1.24±0.15‰). Two samples with the highest $\Delta^{17}O$ (1.57‰ and 1.59‰, ~4σ greater than the average of other samples) possess relatively low ^{35}S SA (2 and 5 atoms / nmol SO_4^{2-}), indicating that the shift of SO_4^{2-} formation pathway is altitude-independent. Elimination of these four samples as outliers, the correlation between ^{35}S SA and $\Delta^{17}O(SO_4^{2-})$ is even weaker ($r = -0.01$, $p = 0.96$), further suggesting that the formation pathway of SO_4^{2-} in our study region does not vary with altitude. Because the samples used for oxygen isotopic analysis cover all seasons in the sampling period (Mar 2014 – Feb 2015) and the full range of ^{35}S SA variation (2-35 atoms / nmol SO_4^{2-}) (Figure 7.2), measuring oxygen isotopic compositions in more weekly samples collected in this sampling period will not change our finding (i.e., insignificant correlation between $\Delta^{17}O$ and ^{35}S SA in SO_4^{2-}).

The vertically uniform $\Delta^{17}O$ values of tropospheric SO_4^{2-} (FT: 1.23±0.22‰; PBL: 1.24±0.15‰) could result from a combination of large pollutant emissions and strong convection in East China. Previous studies highlighted the important role of uplifting air pollutants over East

Asia in modifying the chemical composition of the FT [*Lin et al.*, 2010]. It is shown that air pollutants in the PBL are frequently transported to the FT (every 3-4 days), at time scales of the lofting processes as short as a few hours [*Lin et al.*, 2010]. Because of high concentrations of SO_4^{2-} in the PBL over East China, such frequent upward mixing becomes more important as a small fraction of SO_4^{2-} from the polluted PBL could significantly change oxygen isotopic compositions of SO_4^{2-} in the FT. It is noted that the weakest correlation between ^{35}S SA and $\Delta^{17}O(SO_4^{2-})$ in previous studies is found in fine aerosol samples collected over the Indian Ocean at the Inter Tropical Convergence Zone (characterized by frequent and strong convective activities) ($r = 0.40$, $p = 0.16$; Figure 4) [*Lee*, 2000], further supporting our interpretations.

The upward motion of convective clouds is an efficient way to transport chemical species (including trace gases and aerosols) from the PBL to the FT [*Ervens*, 2015]. Under polluted conditions, a positive feedback cycle (more aerosols – less precipitation – more aerosols) is created [*Rosenfeld et al.*, 2014], and a substantial amount of SO_4^{2-} may be transported to higher altitudes due to SO_4^{2-} resuspension from evaporated cloud droplets. An inter-comparison of global climate models shows that large uncertainties of calculated SO_4^{2-}concentrations in the FT over East China mainly result from uncertainties in simulating SO_4^{2-} formation in clouds and vertical transport patterns [*Goto et al.*, 2015]. Because the aqueous $S(IV)+H_2O_2$ reaction is the dominant SO_4^{2-} production pathway in clouds over East China [*Shen et al.*, 2012], persistent in-cloud productions of SO_4^{2-} via $S(IV)+H_2O_2$ oxidation during upward transport of convective clouds is consistent with the uniform formation pathway of tropospheric SO_4^{2-} revealed by our isotopic measurements.

7.4.3 Implications for Model Improvement and Future Scope

The findings from this study are important because 1) sources and formation pathways of tropospheric SO_4^{2-} (especially in clouds and in the FT) are not well understood, and 2) current models possess significant uncertainties in vertical exchange values between the PBL and the FT. Our study offers unambiguous isotopic evidence to constrain these parameters. For example,

previous studies highlighted the important role of transition-metal-catalyzed O_2 oxidation in SO_4^{2-} formation in East China [*Huang et al.*, 2014b; *Li et al.*, 2017a; *Li et al.*, 2013], which can lead to a small $\Delta^{17}O(SO_4^{2-})$ because of the slightly negative $\Delta^{17}O$ in O_2 [*Luz and Barkan*, 2005] (SI Text S1 and Table S1). However, our observed surface $\Delta^{17}O(SO_4^{2-})$ is greater than the prediction in the GEOS-Chem (<1‰) [*Sofen et al.*, 2011]. This discrepancy suggests that an optimized model parameterization to improve the agreement with our $\Delta^{17}O(SO_4^{2-})$ measurements in East China is needed. The $\Delta^{17}O(SO_4^{2-})$ originating from different regions differ as each region is affected by its own unique atmospheric condition along with varying emission sources and atmospheric composition [*Hill-Falkenthal et al.*, 2013; *Sofen et al.*, 2011]. The spatial distribution of triple oxygen isotopic signature in SO_4^{2-} may be applied to quantify horizontal mixing using isoscape models [*Bowen*, 2010; *Bowen et al.*, 2005]. If ^{35}S can be incorporated in such models, additional isotopic constraints on vertical mixing of SO_4^{2-} will be provided, and a three-dimensional mixing can be quantitatively resolved by coupled measurements of $\Delta^{17}O$ and ^{35}S shown in this study. Although such complicated modeling work is beyond the scope of this study, we use a simple isotope mass balance mixing model to gain a first order insight.

The atmospheric components in the FT in this region are mainly influenced by local regional emissions and long range transport from upwind regions via the westerly jet. Because $\Delta^{17}O(SO_4^{2-})$ and ^{35}S SA are not affected by deposition processes, we assume that the measured $\Delta^{17}O(SO_4^{2-})$ and ^{35}S SA in the FT are represented as a linear combination of fractions of SO_4^{2-} that transported from three end-members: the upwind region (f_{UW}), the upper troposphere (f_{UT}), and the PBL of East China (f_{BL}). The isotope mass balance model can be expressed as follows:

$$SA_{FT} = SA_{UW} \times f_{UW} + SA_{UT} \times f_{UT} + SA_{BL} \times f_{BL}$$

$$\Delta^{17}O(SO_4^{2-})_{FT} = \Delta^{17}O(SO_4^{2-})_{UW} \times f_{UW} + \Delta^{17}O(SO_4^{2-})_{UT} \times f_{UT} + \Delta^{17}O(SO_4^{2-})_{BL} \times f_{BL}$$

$$1 = f_{UW} + f_{UT} + f_{BL}$$

The isotopic signature (^{35}S SA and $\Delta^{17}O$) of three end-members is summarized in the SI Text S3. Our first proof-of-concept approximation shows that the fractions of SO_4^{2-} transported from the upwind region (i.e., Tibetan Plateau), upper troposphere, and PBL of East China are ~3%, ~3% and ~94% respectively (Figure 7.5). This estimation generally supports previous model results, which showed a weak influence (<3%) from the upwind European on O_3 mixing ratio in central China during regionally polluted days [*Lin et al.*, 2010]. It is important to highlight that uncertainties exist in this first proof-of-concept approximation due to limited measurements and relatively broad ranges of $\Delta^{17}O(SO_4^{2-})$ and ^{35}S SA for each endmember (SI Text). At present, it is difficult to estimate the uncertainties without three-dimensional isoscapes of $\Delta^{17}O(SO_4^{2-})$ and ^{35}S SA over the Eurasian continent. In the future, more measurements in different sites (e.g., urban sites in the polluted boundary layer, background sites at the Tibetan and Loess Plateau) should be made. With a Bayesian Markov-Chain Monte Carlo model, which accounts for uncertainties in end-members and has been widely used in carbon-isotope-based source apportionment of carbonaceous aerosols [*Li et al.*, 2016; *Winiger et al.*, 2016], the contributions of regional sulfur emissions to SO_4^{2-} in the FT can be estimated more accurately. Because there are eight isotopes (stable or half-life longer than 3 hours) in natural sulfate molecules (^{16}O, ^{17}O, ^{18}O, ^{32}S, ^{33}S, ^{34}S, ^{35}S and ^{36}S), more variables may be included in the equation system if quadruple stable sulfur isotopes are measured along with $\delta^{18}O$, $\Delta^{17}O$ and ^{35}S. Such measurements at a high temporal resolution can further assist in resolving atmospheric mixing and chemical processes that occur at short time scales (several hours).

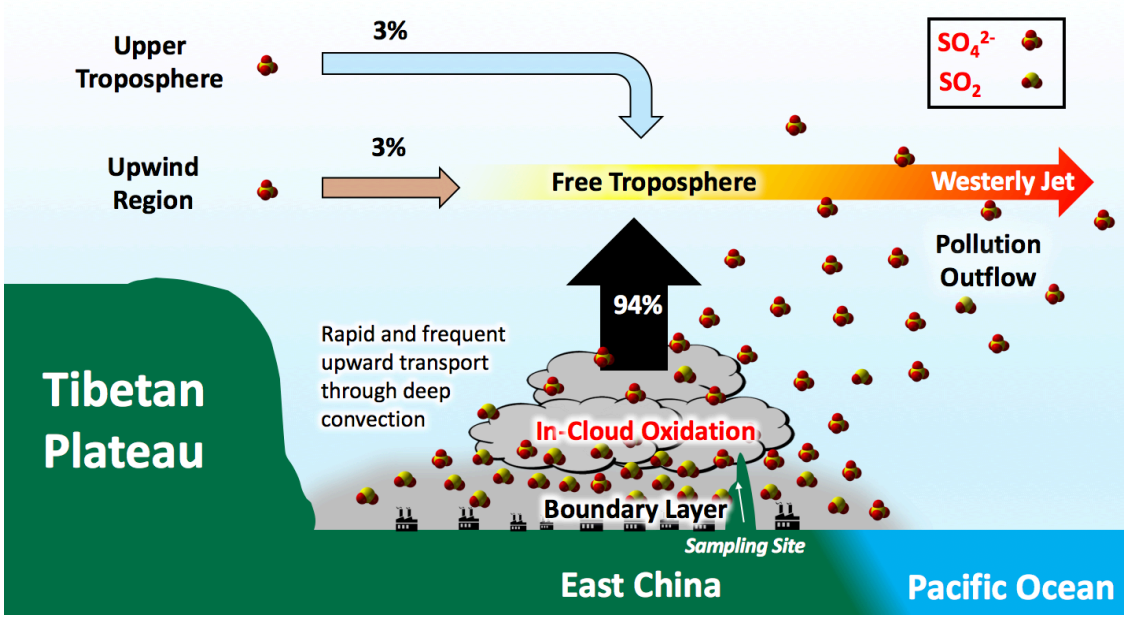

Figure 7.5. Concept model summarizing contributions of three source regions (upwind region, the upper troposphere and the boundary layer) to sulfate aerosols in the free troposphere over East China, which can be rapidly entrained across the Pacific Ocean by the westerly jet and profoundly influence ecosystems and climate.

7.5 Summary

The combined measurement of $\Delta^{17}O$ and radiogenic ^{35}S in the same SO_4^{2-} samples collected at the Earth's surface allow us to determine the formation pathways of SO_4^{2-} for varying altitudes in a unique and effective way. This novel approach provides the most direct and quantitative evidence so far that the formations pathways of SO_4^{2-} in the FT and the PBL over East China are similar (dominated by H_2O_2 oxidation), and SO_4^{2-} in the FT is strongly contributed by large emissions from the PBL. This isotopic constraint can assist in reducing uncertainties in calculating vertical distribution of tropospheric SO_4^{2-} in current models. With proper modeling, more precise contributions from different oxidation pathways and source regions can be quantified. The coupled $\Delta^{17}O$ and ^{35}S measurements in a high temporal resolution and in other regions of East Asia can provide a more complete and clear 3-dimensional picture of tropospheric SO_4^{2-} formation pathways and further validate our results. Such fieldwork and isotopic measurements are currently underway.

7.6 Supporting Information

7.6.1 Oxygen-17 Anomaly in Sulfate

The isotope ratios of ^{17}O and ^{18}O are defined as:

$$\delta^{17}O=[(^{17}O/^{16}O)_{sample}/(^{17}S/^{16}S)_{SMOW}-1] *1000$$

$$\delta^{18}O=[(^{18}O/^{16}O)_{sample}/(^{18}S/^{16}S)_{SMOW}-1] *1000$$

where SMOW stands for Standard Mean Oceanic Water and units of $\delta^{18}O$ and $\delta^{17}O$ are parts per thousand or "per mil" (‰). Most physical and chemical processes in the atmosphere follow a mass-dependent fractionation rule as $\delta^{18}O$ and $\delta^{17}O$ vary in relative proportion to their reduced masses, yielding the following relation: $\delta^{17}O \approx 0.52 \times \delta^{18}O$. Any process that deviates from this relation is termed as mass-independent fractionation and is quantified as oxygen-17 anomaly ($\Delta^{17}O=\delta^{17}O-0.52\times\delta^{18}O$). Because atmospheric SO_2 quickly exchanges its oxygen atoms with water vapor [$\Delta^{17}O(H_2O)=0‰$], the $\Delta^{17}O$ value of SO_4^{2-} [($\Delta^{17}O(SO_4^{2-})$) is dependent only on the $\Delta^{17}O$ of oxidants involved in oxidizing SO_2 to SO_4^{2-}, and therefore provides an observational constraint for the relative importance of SO_4^{2-} formation pathways [*Luz and Barkan*, 2005; *Lyons*, 2001; *Savarino et al.*, 2000; *Savarino and Thiemens*, 1999; *Vicars and Savarino*, 2014]. The $\Delta^{17}O$ of sulfates produced via various major oxidation pathways are summarized in Table S1. Other potential reactions such as NO_2 [*Wang et al.*, 2016], HOBr/HOCl [*Chen et al.*, 2016] and Criegee intermediates oxidations are assumed to be minor in this study.

The time series of $\Delta^{17}O(SO_4^{2-})$ is plotted in Figure 7.2 in the main text along with $\delta^{18}O$ values of SO_4^{2-} [$\delta^{18}O(SO_4^{2-})$]. The narrow range of $\Delta^{17}O$ variation observed in this study is comparable with previous $\Delta^{17}O(SO_4^{2-})$ measurements made in rainwater collected at an urban site located in Central China (0.53±0.19‰) [*Li et al.*, 2013], but the mean $\Delta^{17}O$ value in this study is significantly greater than those measurements. This discrepancy is likely because our study only considers fine aerosol samples in a background site and therefore the fractions of mass-dependent

($\Delta^{17}O$=0‰) sulfate (e.g., dust, primary sulfate from emission sources) are much less than bulk aerosols scavenged by precipitation in an urban site. The $\Delta^{17}O(SO_4^{2-})$ in spring (March, April and May), summer (June, July and August), fall (September, October and November) and winter (December, January and February) are 1.39±0.22‰ (n = 4), 1.22±0.08‰ (n = 4), 1.15±0.10‰ (n = 8) and 1.30±0.08‰ (n = 4), respectively. Although the average of $\Delta^{17}O(SO_4^{2-})$ in the period of winter-spring is slightly higher than summer and fall, the difference (~0.15‰) is notably lower than the seasonal variability of $\Delta^{17}O(SO_4^{2-})$ observed in polar regions (~1‰) [*Hill-Falkenthal et al.*, 2013; *Ishino et al.*, 2017; *McCabe et al.*, 2006]. Given the standard deviation and limited data, it is difficult to conclude if there is any significant seasonality of $\Delta^{17}O(SO_4^{2-})$ in this study. The unclear seasonal variation in this study matches previous $\Delta^{17}O(SO_4^{2-})$ measurements made in mid-latitudes (including Wuhan in central China) [*Li et al.*, 2013].

Table 7.1 shows that the O_3 oxidation can lead to the highest $\Delta^{17}O(SO_4^{2-})$ (6.5‰) while the metal-catalyzed O_2 oxidation can lead to a negative $\Delta^{17}O(SO_4^{2-})$ (-0.09‰). If we treat these two oxidation pathways as two end-members, we can now estimate the maximum contribution from the S(IV)+O_3 reaction ($f_{O3,max}$) for each sulfate sample by assuming no contribution from other oxidation pathways (e.g., H_2O_2 and OH):

$$f_{O3,max} = \frac{\Delta^{17}O(SO_4^{2-})_{obs} - \Delta^{17}O(SO_4^{2-})_{O2}}{\Delta^{17}O(SO_4^{2-})_{O3} - \Delta^{17}O(SO_4^{2-})_{O2}}$$

where $\Delta^{17}O(SO_4^{2-})_{obs}$ is the observed $\Delta^{17}O$ value for each sample and $\Delta^{17}O(SO_4^{2-})_{O3}$ and $\Delta^{17}O(SO_4^{2-})_{O2}$ equal to 6.5‰ and -0.09‰, respectively (Table S1). Because all samples in this study possess $\Delta^{17}O(SO_4^{2-})$ greater than 0.7‰, the minimum contribution from the S(IV)+O_3 reaction ($f_{O3,min}$) for each sulfate sample can be calculated by assuming the S(IV)+H_2O_2 reaction is the only other oxidation pathway:

$$f_{O3,min} = \frac{\Delta^{17}O(SO_4^{2-})_{obs} - \Delta^{17}O(SO_4^{2-})_{H2O2}}{\Delta^{17}O(SO_4^{2-})_{O3} - \Delta^{17}O(SO_4^{2-})_{H2O2}}$$

where $\Delta^{17}O(SO_4^{2-})_{H2O2}$ is 0.8‰ (Table S1). A summary of $f_{O3,max}$ and $f_{O3,min}$ are shown in Table S2. Our calculations yield $f_{O3,max}$ ($f_{O3,min}$) ranging from 16% (4%) to 26% (14%) with an average of 20±2% (8±3%) (1σ) for all samples (Table S2). The maximum contribution from S(IV)+H_2O_2 reaction and metal-catalyzed O_2 oxidation can therefore be estimated by the equations $f_{H2O2,max} = 1 - f_{O3,min}$ and $f_{O2,max} = 1 - f_{O3,max}$, yielding a range of 86-96% (average±σ: 92±3%) and 75-83% (average±σ: 80±3%) for all samples, respectively (Table S2).

A large fraction of S(IV) aqueous oxidation occurs in cloud droplets. Although cloud samples were not collected in this study, it is reasonable to assume that most cloud droplets are acidic (pH<5.5) based on previous measurements at other mountain sites in East China [*Guo et al.*, 2012]. To test this assumption, a thermodynamic equilibrium model ISORROPIA-II is applied to compute the pH value of each aerosol sample [*Fountoukis and Nenes*, 2007]. The inputs to the model are the concentrations of inorganic ions measured using an ion chromatography (Method in the main text), and average relative humidity and temperature during the sampling period recorded at Mount Wuyi (Table S3). The model is run in the forward mode assuming a metastable aerosol state. Since the gaseous ammonia is not measured in this study, the sum of ammonia and ammonium is assumed to be equal to ammonium, which may lead to an underestimation of pH by one unit [*Bougiatioti et al.*, 2016; *Guo et al.*, 2015]. We obtain pH of aerosol ranging from -0.1 to 2.0 with an average of 0.8±0.7 for all samples (Table S3), which in part support our previous assumption. Because the S(IV)+O_3 reaction proceeds slowly at pH<5.5, this oxidation pathway is unlikely dominated under such acidic conditions. Consequently, the contribution of S(IV)+H_2O_2 reaction should be close to $f_{H2O2,max}$ while metal-catalyzed O_2 oxidation should be much smaller than $f_{O2,max}$ on the basis of the isotopic balance.

7.6.2 Samples with High ^{35}S Specific Activities

The ^{35}S (half-life = 87 days) is a cosmogenic isotope naturally produced by the bombardment of ^{40}Ar in the atmosphere by high energy cosmic rays. The flux of cosmic rays and the production rate of ^{35}S depends on both latitude and altitude (higher values at the polar region and the stratosphere and lower in the equatorial region and the planetary bouldary layer [PBL]) [*Lal and Peters*, 1967]. The physical chemical properties of cosmogenic ^{35}S are nearly identical to stable sulfur. Cosmogenic ^{35}S quickly becomes $^{35}SO_2$ after production, and is further oxidized to $^{35}SO_4^{2-}$ before wet and dry removal. Therefore, the variation of $^{35}SO_4^{2-}$ concentrations at ground level is controled by the SO_2 oxidation and SO_4^{2-} removel rates as well as air masses originating in the higher atmosphere. Specific activity (^{35}S atoms per nmol SO_4^{2-}) reported in this study incorporates both radiogenic and stable SO_4^{2-}, and its variation is mainly controlled by the relative contributions of high and low altitude air masses.

Two samples possessing exceptionally high ^{35}S SA (Oct 22-29 2014 and Jan 28 – Feb 4 2015, 30 and 35 atoms / nmol SO_4^{2-}), ~6σ greater than the average of other samples (8±4 atoms / nmol SO_4^{2-}, n = 45), offer a unique opportunity to investigate the triple oxygen isotopic compositions of SO_4^{2-} at high altitudes (Figure 7.2). The sample collected during Oct 22-29 2014 is characterized by a high absolute ^{35}S concentration (3150 atoms m^{-3}), which is ~10σ greater than the average of other samples (480±270 atoms m^{-3}, n=47). Our earlier study showed that the enhancement of cosmogenic ^{35}S in this period was due to strong downward transports of aged stratospheric air masses from the free troposphere (FT) and piling up of free tropospheric air masses in the PBL due to a subtropical anticyclone in this region [*Lin et al.*, 2016c]. The sample collected during Jan 28 – Feb 4 2015 is characterized by a low SO_4^{2-} concentration (1.1 μg m^{-3}) (Table 7.2 and Figure 7.6). In this sampling period, the concentrations of major air pollutants such as SO_2 and O_3 also dropped down significantly (Figure 7.6). The improvement of air quality over the East China region is because of the strong East Asian cold surge in late January (Figure 7.7), which can reduce air

pollutant concentrations by dilution/diffusion or wet removal in the PBL. Therefore, the low SO_4^{2-} concentration in this sample indicates that the isotopic signature of SO_4^{2-} in the FT is less diluted by the sulfur emission from the PBL in this sampling period. The sample collected in this period is mainly contributed by the tropospheric background aerosol in the FT over East China. In summary, it is reasonable to suggest that these two samples represent aerosols collected in air masses mainly originating from the FT.

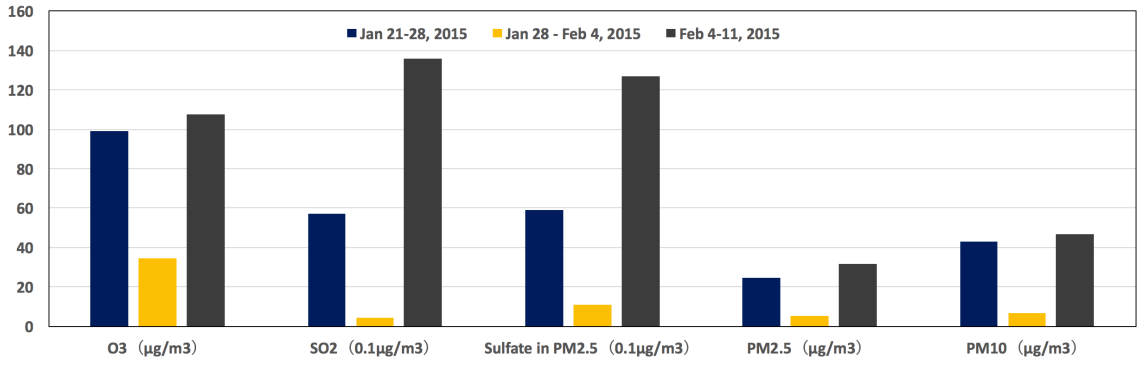

Figure 7.6 Concentrations of O_3, SO_2, sulfates, $PM_{2.5}$ and PM_{10} in Mount Wuyi in the periods of Jan 21-28, Jan 28-Feb 4 and Feb 4-11 in 2015. Concentrations of O_3, SO_2, $PM_{2.5}$ and PM_{10} were measured by an O_3 analyzer (model 49i, Thermo Fisher Scientific), a SO_2 analyzer (model 43i-TLE, Thermo Fisher Scientific) and two continuous PM monitors (TEOM 1405A, Thermo Fisher Scientific), respectively. Sulfate concentration was measured by an ion chromatography method described in Methods in the main text.

(A)

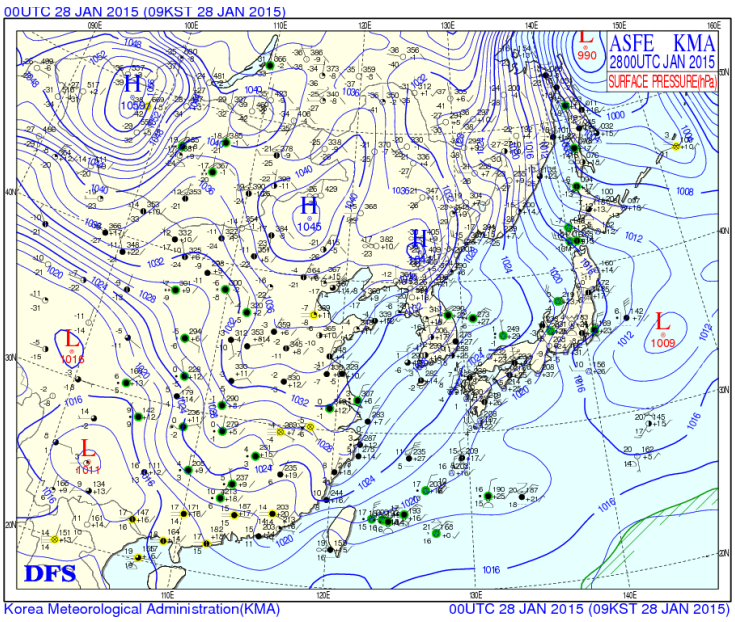

(B)

Figure 7.7 (A) Contour plot of surface pressure over East Asia at Jan 28 2015 provided the Korea Meteorological Administration. (https://web.kma.go.kr/eng/weather/images/analysischart.jsp) (B) Air Quality Index over China at Jan 28 2015 recorded by the Ministry of Environmental Protection of the People's Republic of China. In the color scale, green, yellow, brown, red, purple and maroon represent "Excellent", "Good", "Lightly Polluted", "Moderately Polluted", "Heavily Polluted" and "Severely Polluted", respectively. (http://datacenter.mep.gov.cn)

7.6.3 Simple Mixing Model - A First Proof-of-Concept Approximation

A simple isotope mass balance model shown in the main text is used for resolving the relative contributions by each end-member (SO_4^{2-} in the upwind region, upper troposphere and

PBL) for SO_4^{2-} in the FT. Since the sampling site is located at the downwind region of Tibetan Plateau (Figure 7.1), isotopic compositions of SO_4^{2-} collected at Tibetan Plateau may be deemed as end member values to solve the matrix. A previous study at Nam Co station (30.77°N, 90.98°E, 4730 m a.s.l.) at the central Tibetan Plateau showed that two groups of SO_4^{2-} are distinguished by their isotopic signatures [*Lin et al.*, 2016b]. One group is characterized by low $\Delta^{17}O(SO_4^{2-})$ (0.54-0.64‰). The low ^{35}S SA in this group (140-340 atoms / nmol SO_4^{2-}) indicates that these SO_4^{2-} samples are originated from the lower troposphere of the Tibetan Plateau. The other group possessed high $\Delta^{17}O(SO_4^{2-})$ (1.50-1.62‰) and ^{35}S SA (480-620 atoms / nmol SO_4^{2-}), which is mainly derived from the upper troposphere. In this first proof-of-concept approximation, the averages of these values are used as $\Delta^{17}O(SO_4^{2-})$ and ^{35}S SA endmembers (Figure 7.8). As discussed previously, two samples with exceptionally higher ^{35}S SA can represent aerosols collected in air masses mainly originating from the FT, while others (with ^{35}S SA less than 16 atoms / nmol SO_4^{2-}) are assumed to be SO_4^{2-} originating from the PBL (Figure 7.8). If we simply calculate averages as the isotopic compositions of SO_4^{2-} in the FT and the PBL, the matrix shown in the main text can be resolved and f_{UW}, f_{UT} and f_{BL} are estimated to be 3%, 3% and 94%, respectively.

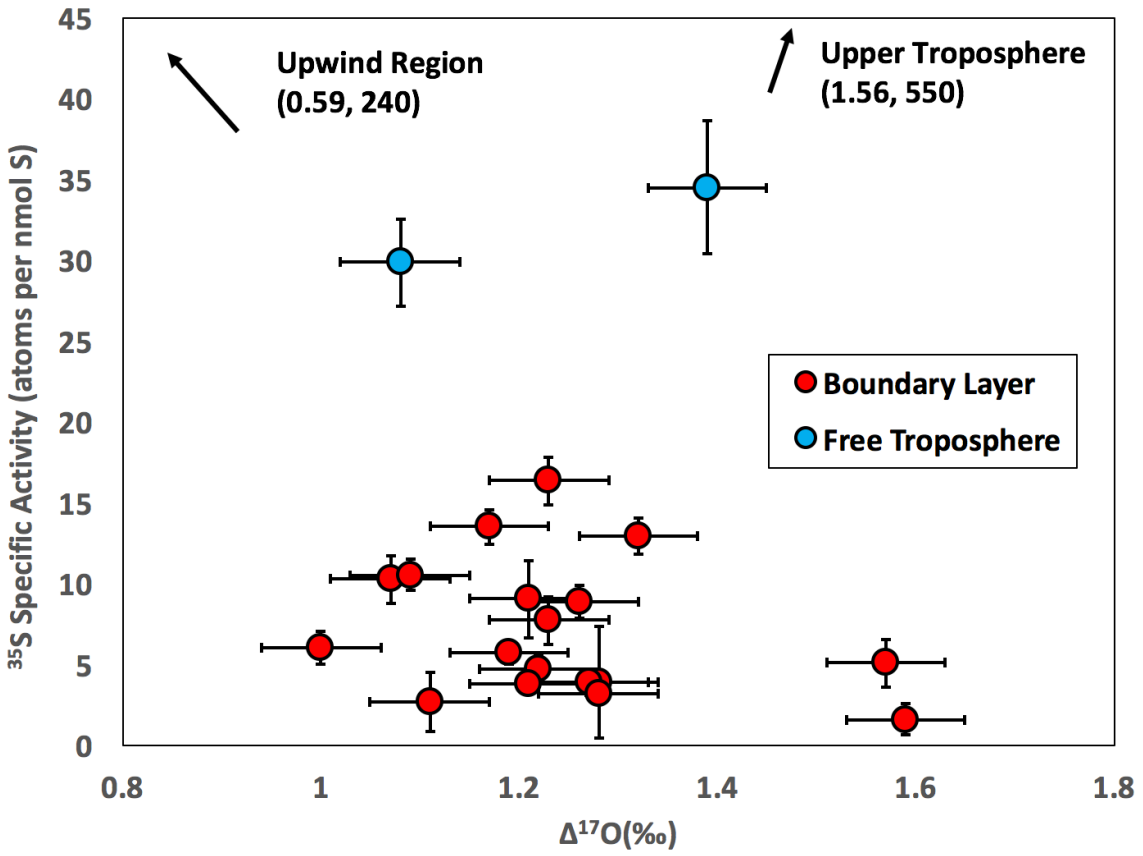

Figure 7.8. A summary of different groups of sulfate aerosols used for a simple mixing model in this study (see text for details). Error bars stand for one standard deviation. Isotopic compositions of sulfate aerosols in upwind regions and the upper troposphere were obtained from measurements at the central Tibetan Plateau [*Lin et al.*, 2016b].

7.7 Acknowledgement

This study was partially supported by the National Natural Science Foundation of China (grants 41475119 and 41501278). We gratefully acknowledge Teresa Jackson for technical advice and guidance in oxygen isotope analysis and Ritchie Hernandez and Haonan Huang for glassblowing. We thank two anonymous reviewers for their helpful comments that improved this manuscript. M. Lin acknowledges support from the Guangzhou Elite Project Fellowship (grant JY201303).

This chapter, in full, is a reprint of the material "Vertically uniform formation pathways of tropospheric sulfate aerosols in East China detected from triple stable oxygen and radiogenic sulfur isotopes" as it appears in Geophysical Research Letters 2017. Lin, Mang; Biglari, Saman; Zhang, Zhisheng; Crocker, Daniel; Jun, Tao; Su, Binbin; Liu, Lanzhong; Thiemens, Mark H., American Geophysical Union, 2017. The dissertation author was the primary investigator and author of this paper.

Chapter 8 Resolving the impact of stratosphere-to-troposphere transport on the sulfur cycle and surface ozone over the Tibetan Plateau using a cosmogenic ^{35}S tracer

8.1 Abstract

The Himalayas were recently identified as a global hotspot for deep stratosphere-to-troposphere transport (STT) in spring. Although the STT in this region may play a vital role in tropospheric chemistry, the hydrological cycle and aquatic ecosystems in Asia, there is no direct measurement of a chemical stratospheric tracer to verify and evaluate its possible impacts. Here, we use cosmogenic ^{35}S as a tracer for air masses originating in the stratosphere and transported downward. We measure concentrations of ^{35}S in fresh surface snow and river runoff samples collected from Mt. Everest in April 2013 to be more than 10 times higher than previously reported by any surface measurement, in support of the Himalayas as a gateway of springtime STT. In light of this result, measurements of $^{35}SO_2$ and $^{35}SO_4^{2-}$ at Nam Co in spring 2011 are reanalyzed to investigate the magnitudes of stratospheric air masses from the Himalayas to the tropospheric sulfur cycle and surface O_3 level over the Tibetan Plateau. A simple one box model reveals that the oxidative lifetime of SO_2 is reduced in aged STT plumes. Triple oxygen isotopic measurements of sulfate samples suggest that enhanced O_3 levels may shift the oxidation pathway of SO_2 in the troposphere, which may be constrained by further intensive sampling and measurements. Comparison with surface O_3 measurements and traditional meteorological tracing methods shows that ^{35}S is a potentially unique and sensitive tracer to quantify the contribution of stratospheric air to surface O_3 levels in fresh or aged STT plumes.

8.2 Introduction

Stratosphere-to-troposphere transport (STT) plays a crucial role in tropospheic chemistry because enriched ozone (O_3) in stratospheric air influences the tropospheric O_3 budget and participates in the tropospheric photochemical cycle [*Hsu et al., 2005*]. In direct STT plumes, O_3

of stratospheric origin may change the oxidizing capacity of the troposphere on a regional scale, which determines the lifetime of trace gases and evolution of aerosol [*Stohl et al.*, 2003]. As one of the most important atmospheric components, sulfate aerosol (SO_4^{2-}) affects the Earth's radiative budget by scattering light and affecting cloud formation. However, large uncertainties still remain because of incomplete knowledge of chemical transformation rates and pathways of sulfur dioxide (SO_2) to SO_4^{2-} [*Dupart et al.*, 2012]. For example, a faster SO_2 oxidation rate was found in east China due to large emissions of O_3 precursors in this region [*Bell et al.*, 2005], where the SO_2 oxidation pathway may be dominated by both aqueous O_3 oxidation and transition-metal-catalyzed O_2 oxidation [*Li et al.*, 2013]. Likewise, if levels of O_3 were enhanced from a stratospheric source, one can expect that tropospheric SO_2 oxidation rates and pathways may be also modulated.

The Tibetan Plateau and the Himalayas were recently identified as a global hotspot for deep STT in spring based on meteorological analysis [*Skerlak et al.*, 2014]. Such deep STT may affect tropospheric O_3 levels and the sulfur cycle in this region and downwind in east China (Figure 1a). The possible influences of STT on surface O_3 levels over the Tibetan Plateau and the Himalayas have been widely investigated [*Ding and Wang*, 2006], while studies of its impact on the tropospheric sulfur cycle are absent. These regions are unique and sensitive under the regime of climate change because glacier retreat and snow melting significantly influence the hydrological cycle and fresh water supply in Asia [*Xu et al.*, 2008]. It was shown that atmospheric aerosol deposition on the glaciers in this region can accelerate the snowmelt in a warming climate due to black carbon reduction of snow albedo [*Xu et al.*, 2009]. Since black carbon can form internal mixtures with sulfate, which strongly affect their optical and physical properties [*Cahill et al.*, 2012], it is also imperative to evaluate how STT contributes to the budget of tropospheric sulfate and its deposition on glacier. Although the STT frequency in this region was investigated via the analysis of surface O_3 data [*Cristofanelli et al.*, 2010], there is no direct measurement of a chemical tracer mainly originating in the stratosphere that determines its extent.

Recently, the cosmogenic radionuclide ^{35}S has been demonstrated to be an ideal tracer to study stratosphere-troposphere exchange processes [*Priyadarshi et al.*, 2011a]. Radioactive ^{35}S (half-life $t_{1/2}$ = 87 days) is naturally produced by high-energy cosmic ray spallation of ^{40}Ar in the atmosphere. The production rate of ^{35}S in the stratosphere is 1-2 orders of magnitude larger than in the troposphere [*Lal and Peters*, 1967]. Following production, ^{35}S is rapidly oxidized to $^{35}SO_2$ (gas phase) in ~1 s. $^{35}SO_2$ is oxidized to $^{35}SO_4^{2-}$ (solid phase) by gas phase homogenous (OH) or aqueous phase heterogeneous (O_3/H_2O_2) oxidation pathways in a few hours or days. These oxidation processes are relatively rapid in the lower troposphere. Owing to a long residence time of both gas and aerosols in the stratosphere (~1 year), $^{35}SO_2$ and $^{35}SO_4^{2-}$ produced in the stratosphere mostly decays to ^{35}Cl except during tropospheric downwelling. Therefore, considering the high production rate of ^{35}S in the stratosphere relative to the troposphere [*Lal and Peters*, 1967], most $^{35}SO_2$ and $^{35}SO_4^{2-}$ observed in the troposphere derives from the stratosphere during STT events. In addition, since the chemical properties of $^{35}SO_2$ and $^{35}SO_4^{2-}$ are identical to non-radiogenic SO_2 and SO_4^{2-}, simultaneous measurements of $^{35}SO_2$ and $^{35}SO_4^{2-}$ offer a new approach for tracing gas and aerosol lifetimes as well as turnover kinetics [*Brothers et al.*, 2010]. Overall, the single source, suitably short half-life and bimolecular partitioning of ^{35}S render it a sensitive tracer for quantifying the influx of stratospheric air into the troposphere and the sulfur cycle of short time scales.

Apart from ^{35}S, which can be utilized as a chronological tracer of sulfur oxidation, simultaneous triple oxygen isotopic measurement provides additional information on the impact of STT in terms of tropospheric sulfur oxidation pathway [*Hill-Falkenthal et al.*, 2012b]. Most atmospheric processes obey a mass-dependent isotopic relation as $\delta^{17}O$ and $\delta^{18}O$ vary proportionally to their reduced masses, yielding the relation $\delta^{17}O \approx 0.52 \times \delta^{18}O$, where $\delta = (R_{sample}/R_{standard} - 1) \times 1000$ and $R = {}^{17}O/{}^{16}O$ or ${}^{18}O/{}^{16}O$. Chemically produced mass-independent compositions with a ^{17}O anomaly ($\Delta^{17}O$), where $\Delta^{17}O = \delta^{17}O - 1000 \times [(1+\delta^{18}O/1000)^{0.52} - 1]$ quantifies the extent of a mass independent process and was first noted in the O_3 molecule [*Thiemens and Heidenreich*, 1983]. Laboratory experiments, field observations and model simulations have

demonstrated that this unique isotopic signature can be transferred to other molecular species such as sulfate during chemical transformation in nature [*Thiemens*, 2006]. Previous studies show that sulfate produced from SO_2+OH , S(IV)+H_2O_2, S(IV)+O_3 processes have the $\Delta^{17}O$ values of 0, 0.9 and 8.8, respectively [*Savarino et al.*, 2000], rendering triple oxygen isotopic measurements of ambient sulfate aerosols a unique tracer of the dominant oxidation pathway of sulfur [*Lee and Thiemens*, 2001].

In addition, identifying STT events and quantifying its contribution to surface O_3 levels has been a major scientific concern since the 1970s [*Stohl et al.*, 2003]. Recent studies suggest that naturally occurring STT might compromise high-altitude western U.S. regions in attaining U.S. national air quality standard for ground-level O_3, but the quantification are mainly based on model simulations, which differ by a factor of 2-3 [*Lin et al.*, 2012b]. Consequently, it is crucial to constrain model results by identifying and quantifying STT events using a sensitive chemical tracer. Along with meteorological simulation (e.g., potential velocity and specific humidity) and anthropogenic emission tracers (e.g., carbon monoxide (CO)), deep STT events and fresh stratospheric air from direct intrusions (hereafter referred to as fresh STT plumes) may be identified by unusually high surface O_3 concentration in background sites [*Langford et al.,* 2015], but the signatures of shallow STT events and aged and mixed air masses of semi-recent stratospheric origin (hereafter referred to as aged STT plumes) may be difficult to resolve. Ozonesondes and aircraft measurements provide high resolution information on vertical O_3 distributions [*Kim et al.*, 2002]. However, they are relatively expensive methods due to equipment costs and require experienced operators. Cosmogenic ^7Be (half-life $t_{1/2}$ = 53 days) is used as a tracer of both fresh and aged stratospheric air masses on the time scale of days to weeks [*Lee et al.*, 2007], but they readily attach to aerosol surfaces and behave as solids, suggesting they may not be a reliable tracer to define the physical and chemical processes of O_3 (gas phase) directly [*Zheng et al.*, 2011]. It was proposed that N_2O depletion could be utilized as a gas phase stratospheric tracer [*Boering et al.*, 2004]. It is limited in its application to trace gases with lifetimes significantly longer than O_3. These drawbacks

imply that finding a new stratospheric O_3 tracer is imperative. As stated earlier, $^{35}SO_2$, existing in the gaseous phase, is predominantly produced in the stratosphere. The flux of $^{35}SO_2$ in a STT event may be estimated from concurrent measurements of $^{35}SO_2$ and $^{35}SO_4^{2-}$ and proper modeling of SO_2 behavior that considers solubility and oxidative lifetime. The suitable half-life of ^{35}S also makes the quantification of aged stratospheric air masses possible. Consequently, it may be useful for identifying the influence of STT on surface O_3.

In this paper, we report the potential of cosmogenic ^{35}S as an effective stratospheric tracer to improve the understanding of the role of springtime STT from Himalayas in the tropospheric sulfur cycle and O_3 levels over the southern Tibetan Plateau. The paper is organized as follows. Section 8.3 briefly describes the methodologies for sampling, measurements, and model simulations. In Section 8.4, measurements of ^{35}S in snow/water samples collected at Mt. Everest in April 2013 are reported for the first time in support of the crucial role of springtime STT in this region. We then further investigate the possible impacts of springtime STT from Himalayas on atmospheric sulfur chemistry at the southern Tibetan Plateau. Specifically, located at the northern edge of the southern Tibetan Plateau, Nam Co (30.77ºN, 90.98ºE, 4730 m above sea level (a.s.l.), Figure 8.1a) is a clean continental background site less influenced by local anthropogenic pollution [*Cong et al.*, 2007]. Measurements of ^{35}S concentrations in SO_2 and aerosol samples collected at this site in spring 2011 are also presented in Section 8.4. Spring 2011 is selected because ^{35}S and O_3 peak at spring (Figure 8.1b-c) and both SO_2 and aerosol were collected in this period. To interpret these data, a 1-box model is established to constrain the stratospheric flux and its impact on the oxidative rate of SO_2. In addition, triple oxygen isotope measurements in these samples are reported for the first time to provide the extent to which STT may affect the SO_2 oxidation pathway. An additional goal of this study is to explore the potential of ^{35}S as a stratospheric O_3 tracer. We compare ^{35}S measurements with traditional stratospheric tracers (surface O_3 and humidity) and present a proof of concept method to estimate the contribution of stratospheric O_3 using ^{35}S measurements. This estimation is compared with a traditional quantification method (the

FLEXPART stratospheric O_3 tracer). We then briefly discuss the implication for springtime O_3 maximum in the southern Tibetan Plateau.

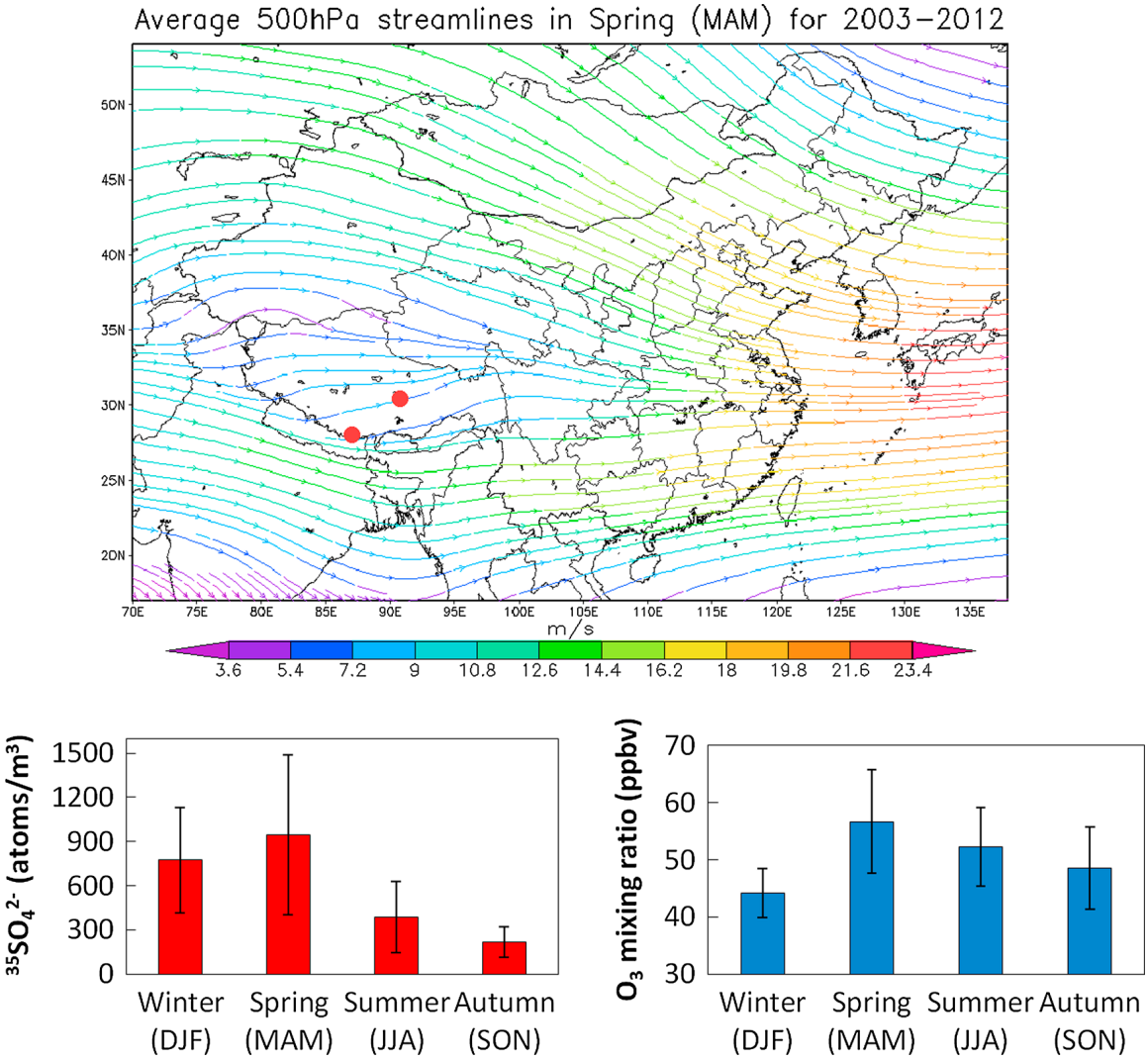

Figure 8.1 (a) Map showing the locations of Nam Co and Mt. Everest. The base map shows typical 500 hPa streamlines during spring (March, April and May) for 2003-2012. Arrows and color scale indicate prevailing wind directions and wind speed (unit: m/s) respectively. Springtime maximums of (b) $^{35}SO_4^{2-}$ concentrations (from October 2010 to August 2012) and (c) surface O_3 levels (from January 2011 to August 2013) measured at Nam Co are presented. Error bars stand for one standard deviation.

8.3 Methods

8.3.1 Sample collection

Samples of glacier surface snow, stream water under the serac and river water were collected at Mt. Everest (Figure 8.1a) during the 2013 Mt. Everest Scientific Expedition in spring 2013. Surface snow samples were collected at the East Rongbuk glacier col (28.02ºN, 86.96ºE, 6530 m a.s.l.) and melted in a water bath in field for further chemical processing. Stream water under a serac (28.04ºN, 86.94ºE, 6320 m a.s.l.) near the Advanced Base Camp, which is part of the East Rongbuk glacier, and runoff in a river located at the Mt. Everest Base Camp (28.14ºN, 86.85ºE, 5150 m a.s.l.), which is mainly supplied by the East Rongbuk glacier, were also collected. Three liters of each water sample were passed through an anion exchange resin column (BioRad X8) in the field to trap sulfate ions for further laboratory chemical processing.

Bulk aerosol and SO_2 samples were collected at Nam Co station during the springtime 2011 (from March 14 to June 1). A Hi-Vol aerosol sampler (Tisch Environmental Inc., Ohio, U.S.A.) was used to sample aerosol and SO_2 on quartz filter papers and KOH treated back up filter papers, respectively, at a typical flow rate of ~1 m^3 min^{-1}. Due to the harsh environment of the Tibetan Plateau, each set of samples was collected continuously for 5~10 days. Some days are missing due to operational issues.

8.3.2 Measurements of ^{35}S and triple oxygen isotopes

All samples were processed to determine ^{35}S concentration at the University of California San Diego using an ultra-low level liquid scintillation counting spectrometer (Wallac 1220 Quantulus) technique [*Brothers et al.*, 2010]. Sulfate was converted to aqueous Na_2SO_4 solution and mixed with Insta Gel Plus cocktail in a scintillation vial before counting. To improve the ratio of signal to noise, organic contaminants and chlorine salts were removed by a PVP (polyvinylpyrrolidone) resin and a Dionex Ag cartridge, respectively. The raw ^{35}S counting data was corrected for background activity and for the decay time.

Due to the pristine environment of Nam Co and sulfate sample requirement (~5 μmol) for triple oxygen isotope analysis ($\delta^{17}O$ and $\delta^{18}O$), only four bulk aerosol samples with sufficient sulfate concentrations were used to determine the triple oxygen isotopic composition following [*Savarino et al.*, 2001]. Sulfate was separated via ion chromatography and subsequently converted to Ag_2SO_4. The O_2 gas obtained from pyrolysis of Ag_2SO_4 in a quartz tube at a temperature of 1030°C was purified through a gas chromatograph and used for triple oxygen isotopes by an isotope ratio mass spectrometry (MAT253). The mass independent fractionation process of pyrolysis using quartz tube was corrected by the equation $\Delta^{17}O=\Delta^{17}O_{quartz}\times1.14+0.06$ as determined by [*Schauer et al.*, 2012].

8.3.3 Surface O_3 measurement

Continuous measurement of surface O_3 was done with a UV absorption analyzer (Thermo Model 49i). The 30-min average data used in this study have been subject to strict quality assurance and control procedures during monitoring and data processing. The O_3 analyzer was calibrated against a transfer standard (Thermo Electron 49i-PS) on a seasonal basis. When comparing to O_3 levels and ^{35}S concentrations, the O_3 data collected during the sampling period for each ^{35}S sample was averaged for temporal consistency with ^{35}S measurements.

8.3.4 Mesoscale meteorological simulation and FLEXPART stratospheric O_3 tracer

Mesoscale meteorological simulations were conducted using the Weather Research and Forecast (WRF) model [*Wang et al.*, 2014] from March 1 to May 31, 2011. The grid resolution for WRF simulations was 27 km and the total number of vertical layers was 39, with 28 between surface and 5000 m above ground level. The simulation domain stretched from 5°E to 140°E and from 0° to 60°N. In order to minimize integration errors, 4D-data assimilation (FDDA) was applied to WRF simulation domain using observational data from Global Telecommunication System (GTS). Based on hourly WRF output data, potential vorticity (PV) and specific humidity analyses, both of which are widely used to view the dynamics related to STT [*Gray et al.*, 1994], were

conducted in this study. The 72-hour back trajectories in the sampling periods were also calculated every 24 hours (starting location: 1000 m above ground level at Nam Co) to identify the source of air masses using the Hybrid Single-Particle Lagrangian Integrated Trajectory (HYSPLIT) model of version 4.8 and the Global Data Assimilation System (GDAS) data [*Draxler and Rolph*, 2015].

A relatively simple (compared to chemical transport models) but quantitative Lagrangian particle dispersion model [*Stohl et al.*, 1998] was utilized to identify the probability that air masses with observed high ^{35}S levels at Nam Co recently spent time in the stratosphere. Specifically, the FLEXPART-WRF version 3.2 driven by WRF output data was utilized [*Brioude et al.*, 2013]. The simulation domain covered the entire Tibetan Plateau from 80°E to 100°E and from 20° to 40°N, with horizontal resolution of 0.1 degree and 50 vertical layers from surface to 9000 m above ground level. Whether a particle is stratospheric or not is determined using the dynamical definition of the tropopause based on a threshold value for PV of 2.0 PVU [*Stohl et al.*, 2000]. In the calculation, stratospheric particles were assigned a mass according to the equation $M_{O3}=M_{air}\times PV\times C\times 48/29$, where $C=60\times10^{-9}$ PVU^{-1} is the average ratio between the O_3 mixing ratio and PV in the lower stratosphere in spring based on the ozonesonde data reported by [*Stohl et al.*, 2000]. The factor 48/29 converts from a volume to mass mixing ratio. Detailed description of the FLEXPART stratospheric O_3 tracer modeling is given by [*Cooper et al.*, 2005].

8.4 Results and discussion

8.4.1 High springtime ^{35}S concentrations at Mt. Everest

Concentrations of $^{35}SO_4^{2-}$ in glacier surface snow, stream water under serac and river water at Mt. Everest are determined as $1580\pm110\times10^3$, $252\pm99\times10^3$ and $2740\pm130\times10^3$ atoms L^{-1}, respectively. Considering the short lifetime of ^{35}S, concentration of $^{35}SO_4^{2-}$ in melted water from serac, mainly consisting of aged glacier ice, is assumed to be 0 atoms L^{-1}. Based on mass balance, our result suggests that at least 16% stream water under serac is contributed by the snow and/or ice melting on the top layers of glacier, providing valuable information for future modeling of glacier

stagnation *v.s.* glacier retreat in this region. The runoff is thought to be partly contributed by the snowmelt, and hence a smaller $^{35}SO_4^{2-}$ concentration compared to glacier surface snow is anticipated. The unexpectedly higher $^{35}SO_4^{2-}$ concentration in this study is possibly due to the limited sample size, strong wet deposition, and/or subtle evaporation on rivers before sampling. Intensive sampling in the future is recommended to improve our understanding on the glacier melt at Mt. Everest.

Since the source of ^{35}S in high altitude glacier surface snow is primarily atmospheric deposition of $^{35}SO_2$ and $^{35}SO_4^{2-}$, snow sample measurements provide critical information on ^{35}S concentrations in the free troposphere [*Priyadarshi et al.*, 2014]. Concentrations of ^{35}S at Mt. Everest as shown in this study are more than ten times higher than those measured in Zhadang glacier close to Nam Co at the southern Tibetan Plateau (Table 8.1), providing the first field-based measurement of stratospheric tracer at the Himalayas in support of this region as a global hotspot for deep STT in spring [*Skerlak et al.*, 2014]. Based on the scavenging ratio (ω) of sulfate on Mt. Everest [*Ming et al.*, 2007], the ^{35}S concentration in atmospheric aerosols is calculated according to the relationship $\omega=\rho_a \times C_s/C_a$, where ρ_a is air density (g m^{-3}) after correcting for standard temperature and pressure; C_s and C_a are ^{35}S concentrations in the surface snow (atoms g^{-1}) and aerosol samples (atoms m^{-3}), respectively. The estimated atmospheric $^{35}SO_4^{2-}$ concentration on Mt. Everest is ~4000 atoms m^{-3}, significantly higher than all aerosol measurements reported so far and close to the steady-state $^{35}SO_4^{2-}$ concentration in lower stratosphere (6316 atoms m^{-3}) calculated by a 4-box 1-D model for La Jolla at mid-latitudes [*Priyadarshi et al.*, 2012a]. Measurement of aerosol samples directly collected on Mt. Everest in the future will benefit constraining future estimations. The strong springtime STT over the Himalayas indicated by enhanced ^{35}S concentrations were suggested as normal based on a 33-year reanalysis data set [*Skerlak et al.*, 2014]. If these air masses transport to the southern Tibetan Plateau, enhancement of ^{35}S concentration is anticipated. In the ensuing sections, concurrent measurements of $^{35}SO_2$ and $^{35}SO_4^{2-}$ in Nam Co at 2011 spring are

presented to illustrate how springtime STT in the Himalayas influences the southern Tibetan Plateau.

Table 8.1. ^{35}S concentrations measured in snow and water samples collected from East Rongbuk glacier at Mt. Everest and Zhadang glacier near Nam Co

Sample	Collection Date	^{35}S Concentration (10^3 atoms L^{-1})	Altitude (m a.s.l.)
This Study			
Mt. Everest (Surface Snow)	04/28/2013	1580±110	6530
Mt. Everest (Serac)	05/01/2013	252±99	6320
Mt. Everest (River)	04/18/2013	2740±130	5150
Priyadarshi et al. [2014]			
Zhadang Col (Surface Snow)	09/10/2010	97±5	5800
Zhadang Col (Deep Snow)	09/10/2010	41±6	5800
Zhadang Terminal (Surface Snow)	09/10/2010	64±5	5500
Zhadang Terminal (Deep Snow)	09/10/2010	25±4	5500
Qugaqie River	09/10/2010	18±6	4800
Niyaqu River	09/07/2010	16±6	4750
Niyaqu River	12/16/2010	15±5	4750

8.4.2 Signature of stratospheric air at the southern Tibetan Plateau

In the present study period, nine sets of SO_2 and SO_4^{2-} samples were collected for ^{35}S measurement (Figure 8.2). The average concentrations of $^{35}SO_2$ and $^{35}SO_4^{2-}$ were 113±43 and 586±341 atoms m^{-3}, respectively (Table 8.2). These values are close to springtime averages measured at a coastal site of Southern California [*Priyadarshi et al.*, 2012a], which implies that Nam Co is generally affected by low altitude air masses and direct influence of air masses from the stratosphere on the boundary layer is infrequent. This result agrees well with the relatively low ^{35}S concentrations in glacier snow observed at this region (Table 8.1). Therefore, the enhancement of free tropospheric mixing and/or STT may be easily identified from an enhancement in ^{35}S concentrations.

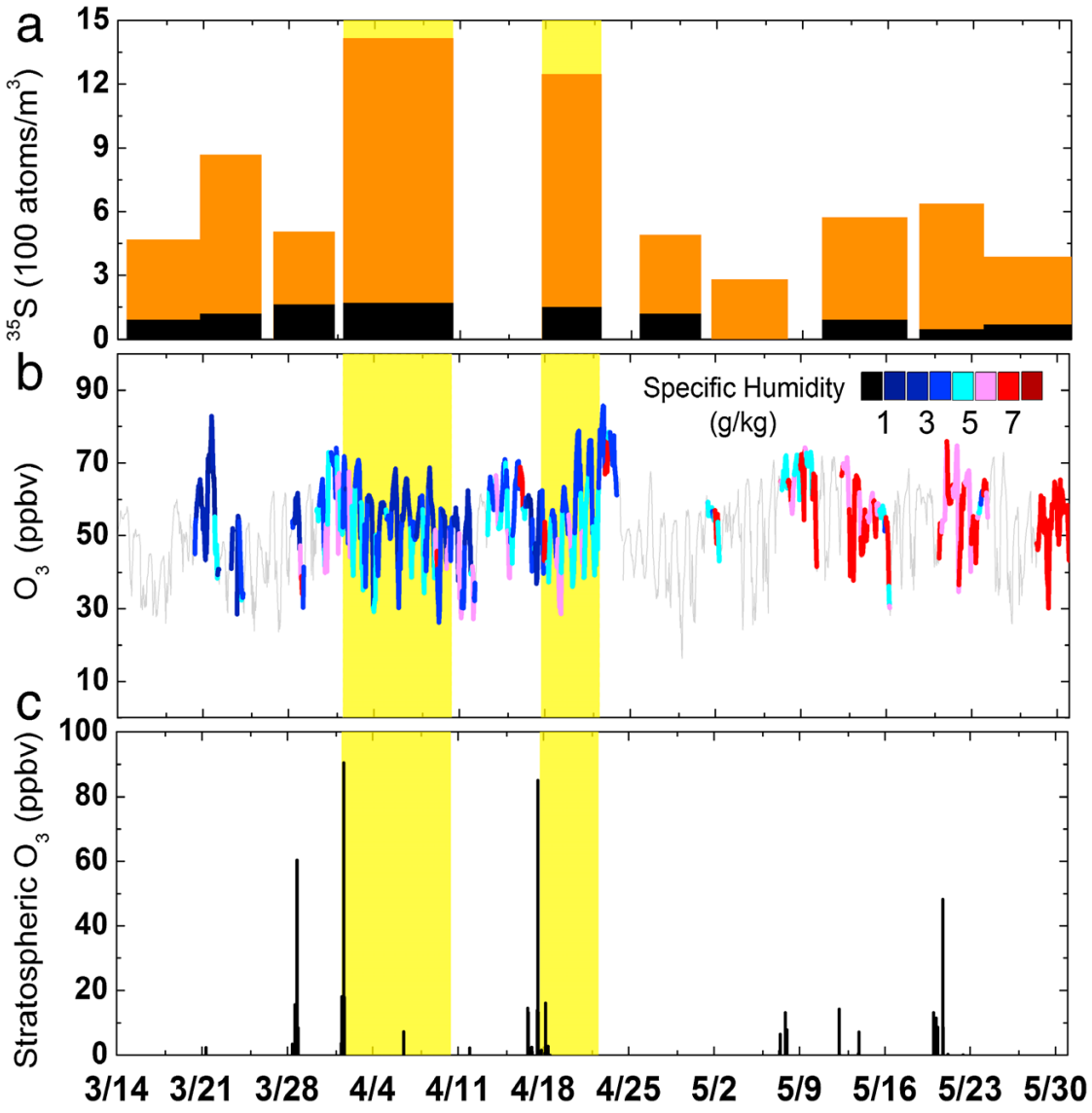

Figure 8.2. Time series of (a) total ^{35}S concentrations ($^{35}SO_2$ [black] + $^{35}SO_4^{2-}$ [orange]), (b) hourly surface ozone mixing ratio and corresponding specific humidity at 500hPa and (c) stratospheric O_3 tracer in the Himalayas air masses modeled by the FLEXPART at 50 m above ground level. Two periods with enhanced ^{35}S and F_{STT} are highlighted in yellow shades (see text for details).

Table 8.2. Summary of $^{35}SO_2$, $^{35}SO_4^{2-}$ concentrations (atoms/m^3) and $\Delta^{17}O$ (‰) measured in SO_4^{2-} samples collected at Nam Co in 2011, corresponding $^{35}SO_2$ flux of stratosphere-to-troposphere transport (F_{STT}) (atoms m^{-3} day^{-1}) and oxidative lifetime of SO_2 (τ_{ox}) (days) calculated by a box model (see text for details), surface O_3 mixing ratio (ppbv) and specific humidity (q) (g/kg).

Sample	$^{35}SO_2$	$^{35}SO_4^{2-}$	F_{STT}	τ_{ox}	$\delta^{18}O$	$\Delta^{17}O$	O_3	q
Mar 14-20	91	379	9.1	0.9	-	-	44.9	1.3
Mar 21-25	119	750	22.2	0.6	8.70	0.64	47.6	1.3
Mar 26-31	163	342	8.5	1.8	-	-	51.9	2.1
Apr 01-10	171	1246	39.8	0.5	9.26	1.50	53.3	1.6
Apr 17-22	150	1098	34.5	0.5	-	-	53.7	1.7
Apr 25-30	119	372	9.2	1.2	-	-	44.4	1.0
May 01-06	-	281	-	-	9.78	0.54	53.4	1.7
May 10-17	91	483	12.7	0.7	9.44	1.62	62.5	3.0
May 18-23	46	593	16.1	0.3	-	-	57.1	3.5
May 24-31	69	319	6.9	0.8	-	-	53.1	3.3
Average	113	586	17.7	0.8	9.30	1.08	52.2	2.0
± σ	43	341	12.1	0.4	0.45	0.56	5.5	0.0

The highest $^{35}SO_4^{2-}$ concentrations in the study period are found in April 1-10 (1246 atoms m^{-3}) and 17-22 (1098 atoms m^{-3}), comparable to that observed in aged STT plumes at coastal California (1095 atoms m^{-3}) [*Priyadarshi et al.*, 2012a]. In fresh STT plumes, a much higher $^{35}SO_4^{2-}$

concentration as that observed at Mt. Everest is anticipated. Consequently, we suggest that these two episodes are influenced by aged STT plumes, where fresh stratospheric air masses are mixed into the free troposphere, and the aged/diluted stratospheric air masses in the free troposphere subsequently transported to Nam Co and mixed into the boundary layer. Based on the snow ^{35}S concentrations made at Zhadang glacier (5800 m a.s.l.) close to Nam Co (4730 m a.s.l.) in autumn (Table 8.1), the springtime free troposphere $^{35}SO_4^{2-}$ concentration at this region can be predicted by ω as shown earlier and ^{35}S radioactive decay correction for the time elapsed. It yields a baseline of ~750 atoms m^{-3}, implying that the elevated $^{35}SO_4^{2-}$ concentration in boundary layer (1098-1246 atoms m^{-3}) in these two samples cannot be solely explained by the downwelling from the local free troposphere. Horizontal transport in the free troposphere, which brings aged stratospheric air from a region with greater STT flux and $^{35}SO_4^{2-}$ concentration, should be considered. A 72-hour backward trajectory analysis show that air masses in this period were exclusively from the Himalayas (Figure 8.3). If the $^{35}SO_4^{2-}$ concentration estimated earlier can represent a steady-state springtime condition of the free troposphere at the Himalayas, it is estimated that ~30% air masses at the Himalayas free troposphere were entrained to the boundary layer of Nam Co during April 1-10.

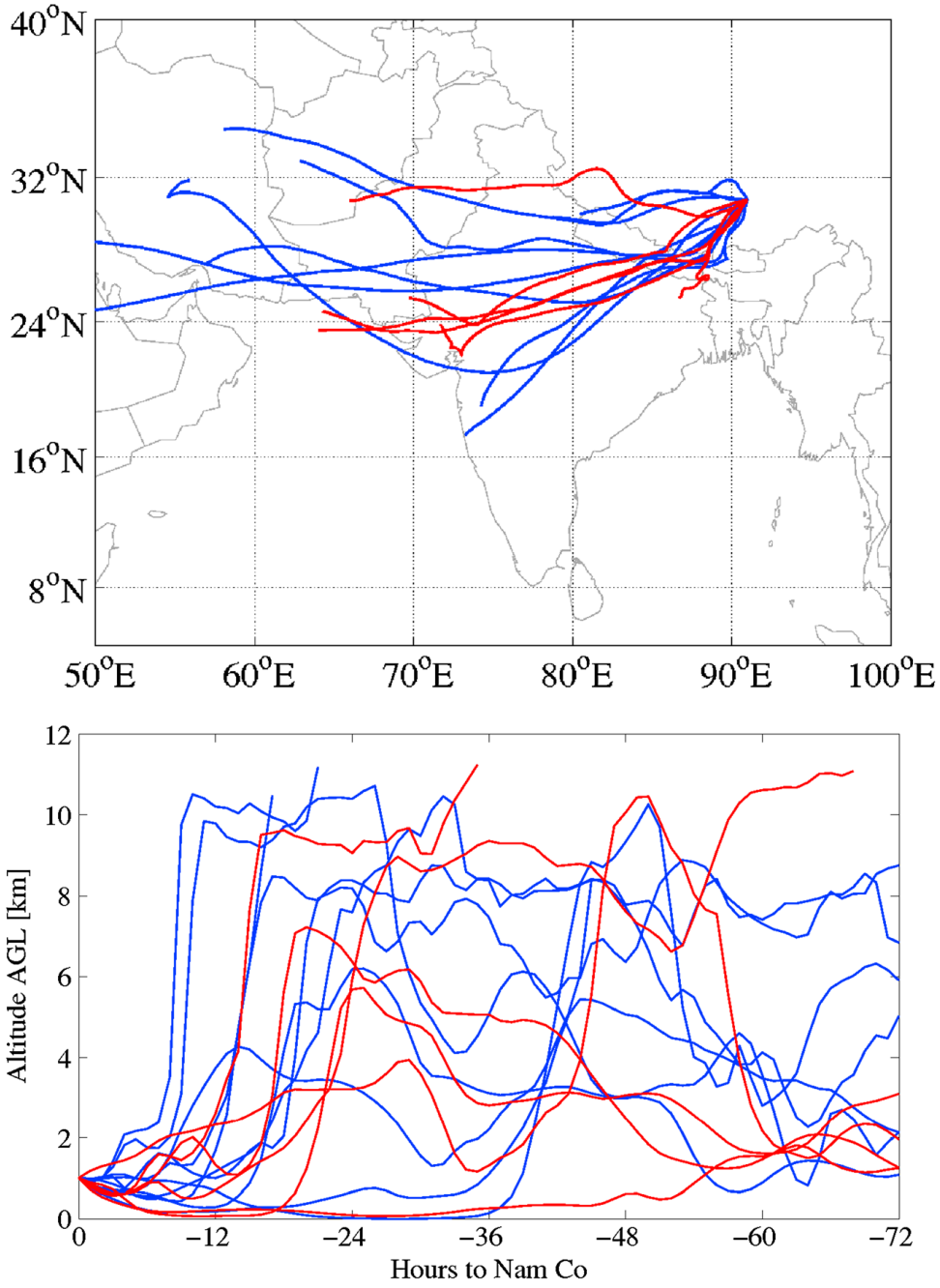

Figure 8.3. Daily backward trajectories during the sampling periods of April 1-10 (blue) and 17-22 (red)

To confirm that the observed high ^{35}S concentration is contributed by STT, eliminating any potential influence from other sources is crucial. The neutron leakage at the Fukushima nuclear plant is the only anthropogenic source of ^{35}S identified so far [*Priyadarshi et al.*, 2011b]. It is noted

that ^{131}I released from the Fukushima nuclear accident was detected in our aerosol sample collected in April 1-10 with an activity approximately one order of magnitude lower than observed in Northern California [*Hsu et al.*, 2012]. Enhanced $^{35}SO_4^{2-}$ concentration due to the Fukushima disaster was also observed in Southern California (1501 atoms m^{-3}) [*Priyadarshi et al.*, 2011b]. If we assume the transport speeds of these two nuclides are identical, transport of these radiation plumes from California to Nam Co requires ~8 days [*Hsu et al.*, 2012]. Considering only less than 1% of $^{35}SO_4^{2-}$ reached Southern California after 8 days transport from Japan [*Priyadarshi et al.*, 2011b], the ^{35}S contribution from Fukushima as a proportion of the total measured $^{35}SO_4^{2-}$ abundance is on the order of only 1%, which can be ignored. Because the lifetime of SO_2 is shorter than the transport time [*Priyadarshi et al.*, 2011b], the Fukushima contribution of $^{35}SO_2$ at Nam Co is also negligible.

8.4.3 Impact of STT on tropospheric sulfur cycle

Due to the insufficient $^{35}SO_2$ and $^{35}SO_4^{2-}$ data for the summer and fall [*Priyadarshi et al.*, 2014], it is difficult to establish a reliable 4-box 1-D model as suggested by [*Priyadarshi et al.*, 2011a]. In this study, a simple 1-box model of the boundary layer following the treatment similar to that of *Brothers et al.* [*Brothers et al.*, 2010] is applied to provide context to relate the ^{35}S measurements to the possible impacts of aged STT plumes on tropospheric sulfur cycle. If we consider STT as the only source outside the box, the time-dependent concentrations of $^{35}SO_2$ and $^{35}SO_4^{2-}$ in a stable boundary layer can be expressed as:

$$\frac{d[^{35}SO_2]}{dt} = P_{\mathrm{CR}} + F_{\mathrm{STT}} - \frac{[^{35}SO_2]}{\tau_{ox}} - \frac{[^{35}SO_2]}{\tau_d} - \frac{[^{35}SO_2]}{\tau_c} - \frac{[^{35}SO_2]}{\tau_\lambda}$$

$$\frac{d[^{35}SO_4^{2-}]}{dt} = nF_{\mathrm{STT}} + \frac{[^{35}SO_2]}{\tau_{ox}} - \frac{[^{35}SO_4^{2-}]}{\tau_r} - \frac{[^{35}SO_4^{2-}]}{\tau_\lambda}$$

where P_{CR} and F_{STT} is the cosmic ray production rates of $^{35}SO_2$ within the box and $^{35}SO_2$ flux of STT, respectively. The factor n expresses for the ratio of $^{35}SO_4^{2-}$ to $^{35}SO_2$ in the lower stratosphere outside the box. Since ^{35}S atom from cosmogenic production is rapidly oxidized to $^{35}SO_2$ (gas

phase) in ~1 s and then relatively slowly oxidized to $^{35}SO_4^{2-}$, production of $^{35}SO_4^{2-}$ within the box is determined by the oxidative lifetime of $^{35}SO_2$ (τ_{ox}). The time scales for sinks of $^{35}SO_2$ are represented by an oxidative lifetime (τ_{ox}), a dry deposition lifetime (τ_d), a cloud scavenging (wet removal) lifetime (τ_c) and the radioactive lifetime (λ) of ^{35}S (126 days), while those of $^{35}SO_4^{2-}$ are an aerosol removal lifetime (τ_r) and λ.

The P_{CR} is taken as 41.04 atoms m^{-3} day^{-1} adopted by [*Turekian and Tanaka*, 1992] and [*Brothers et al.*, 2010]. This value is mainly based on the canonical model developed by *Lal and Peters* [1967]. One should note that large uncertainties may exist in this term because the calculation of atmospheric productions of other cosmogenic isotopes (e.g., ^7Be) have been improved and are highly variable in space and time [*Usoskin and Kovaltsov*, 2008] while an updated estimation for ^{35}S production is still absent. The τ_d, τ_c and τ_r values are estimated to be 16, 102, and 3.5 days, respectively, which are the reported springtime mean of a single recent year at Nam Co simulated by the NCAR-CAM3.5 model in the Atmospheric Chemistry and Climate Model Intercomparison Project (ACCMIP) [Lamarque et al., 2013] (data available at http://browse.ceda.ac.uk/browse/badc/accmip/data/NCAR-CAM3.5/). Comparison of multiple models and years in the ACCMIP can assist in evaluating the variability in these terms, but such comprehensive analysis is beyond the scope of the present study. The ratio *n* is determined to be 8.5 based on the steady-state concentrations of $^{35}SO_4^{2-}$ and $^{35}SO_2$ in the UT/LS calculated by a 4-box 1-D model for La Jolla at mid-latitudes [*Priyadarshi et al.*, 2011a]. Based on these input parameters and steady-state assumption, F_{STT} and τ_{ox} are determined, providing information on the impacts of STT on the sulfur cycle in the troposphere. A sensitivity test shows that the F_{STT} is sensitive to τ_r and n, while τ_{ox} is only sensitive to τ_r (Table 8.3). Both of F_{STT} and τ_{ox} are insensitive to τ_c and τ_d, 10% changes of which do not alter most of the results presented here. This result suggests that the estimation of τ_{ox} is more reliable than F_{STT} in this study.

Table 8.3. Sensitivity Test of the Model

Calculated Parameters	Average	Changes of F_{STT} and τ_d with Model Parameter Values Varied by 10%									
		P_{RC} + 10%	P_{RC} - 10%	τ_d + 10%	τ_d - 10%	τ_c + 10%	τ_c - 10%	τ_r + 10%	τ_r - 10%	n + 10%	n - 10%
F_{STT} (atoms m^{-3} day^{-1})	17.7	-4%	+4%	-1%	+1%	0%	0%	-12%	+14%	-9%	+11%
τ_{ox} (days)	0.8	0%	0%	0%	0%	0%	0%	+9%	-9%	-1%	+1%

The highest $^{35}SO_2$ contributions of STT are found in two aged STT episodes (April 1-10 and 17-22), which are 34.5-39.8 atoms m^{-3} per day. Based on the stratospheric SO_2 mixing ratio [*Hopfner et al.*, 2015], sulfate concentration [*Sedlacek et al.*, 1983] and corresponding ^{35}S concentrations in a steady-state model [*Priyadarshi et al.*, 2012a], the contribution of stratospheric SO_2 and sulfate are determined as 2.7-3.2 pptv and 6.5-7.8 ng m^{-3} per day respectively in these two episodes, slightly higher than the estimated stratospheric flux on the Antarctica Plateau [*Minikin et al.*, 1998].

An average oxidation lifetime of SO_2 is calculated as 0.8±0.4 days (19±10 h), significantly lower than that on the Antarctic Plateau (4 days) [*Mauldin et al.*, 2004] and close to the overall lifetimes of tropospheric SO_2 over the eastern United States (19±7 h in summer) and the central China (38±7 h) [*Lee et al.,* 2011; *He et al.*, 2012] . This high oxidizing capacity in the troposphere is likely the result of elevated UV levels in the Tibetan Plateau [*Ren et al.*, 1999]. The variations in oxidation lifetime are not correlated with meteorological conditions, suggesting the changes in

atmospheric chemical components may be crucial. Relatively short oxidative lifetimes of SO_2 are found in two episodes described above (12 h), suggesting a more oxidative troposphere under the influence of O_3-rich stratospheric air masses. It is worthwhile to note that fresh STT plumes are depleted in NO_x, VOCs, water vapor and aerosol, in which conditions may act to suppress SO_2 oxidation, and therefore the mixing of anthropogenic pollution with stratospheric O_3 in aged STT plumes may play an important role in shortening the oxidative lifetime of SO_2. The lowest value of 8 h is found in a sample collected with insignificant stratospheric influence but relatively high O_3 concentration, which was likely affected by complex photochemistry due to anthropogenic emission and/or biomass burning. Since SO_2 oxidative lifetime may be shortened by stratospheric or photochemical O_3-rich air masses during entrainment process in the free troposphere, the relationship between surface O_3 mixing ratio and SO_2 oxidative lifetime is not simply linear. Although detailed chemical mechanisms and transport processes are not incorporated in this model, our results reasonably show that aged STT plumes may shorten the oxidative lifetime of SO_2 in the free troposphere. Measurements of other atmospheric species (e.g., NO_x, VOCs and CO) will assist in quantifying the kinetics. Using more realistic parameter values (e.g., values from field-based measurements or most recent localized model outputs) in the future is required to better estimate the oxidative lifetime of SO_2.

Under the influence of STT, high sulfate $\Delta^{17}O$ values are expected due to 1) increased transport of stratospheric or free tropospheric sulfate with high $\Delta^{17}O$ to the boundary layer, and 2) increased S(IV)+O_3 oxidation of SO_2 in the troposphere due to elevated O_3 level [*Hill-Falkenthal et al.*, 2013]. Previous studies revealed a strong correlation between ^{35}S specific activity and $\Delta^{17}O$ [*Lee and Thiemens*, 2001] because ^{35}S specific activity accounts for non-radioactively produced primary sulfate such as derived from biomass burning or dust with a zero $\Delta^{17}O$ value, which dilutes the values in bulk sulfate. A similar relationship is found in this study (Pearson correlation coefficient: 0.87, $p<0.13$) but should be interpreted with caution due to the small sample size (n=4).

The $\Delta^{17}O$ of the sample collected during an aged STT event (April 1-10) is close to the highest value observed in samples collected in a costal California site, which was affected by the increase of free tropospheric air mixing [*Hill-Falkenthal et al.*, 2012a]. This result highlights the influence of high altitude air masses as suggested previously. The highest $\Delta^{17}O$ value is observed in sample May 10-17 with a small STT flux. Since sulfate concentrations in Nam Co are mainly contributed by a regional crustal source [*Li et al.*, 2007], with $\Delta^{17}O \approx 0$, the lowest sulfate, sodium, magnesium and calcium concentrations detected in this sample (not shown) may imply a diminished dilution effect as suggested by [*Hill-Falkenthal et al.*, 2012b]. This hypothesis is supported by the highest sulfate, sodium, magnesium and calcium concentrations with lower $\Delta^{17}O$ values observed in the sample March 21-25, although the STT flux is relatively high.

Since the input of stratospheric sulfate as estimated earlier only accounts for ~1% of tropospheric sulfate, it is unlikely that higher $\Delta^{17}O$ value in aged STT plumes is due to the input of high $\Delta^{17}O$ stratospheric sulfate. Impact of O_3 levels on oxidation pathway shift may be a relevant factor controlling the variation of $\Delta^{17}O$ values. The higher $\Delta^{17}O$ values are observed in two samples with greater O_3 mixing ratios (April 1-10 and May 10-17), suggesting that enhanced O_3 levels may lead to a shift to a heterogeneous O_3 oxidation pathway. However, the lowest $\Delta^{17}O$ value is found in sample May 1-6 with a concomitant and relatively high O_3 mixing ratio, suggesting a complex nature for the sulfur oxidation process. The shift of oxidation pathway may involve several factors including ambient meteorological influences (e.g., relative humidity) [*Mcmurry and Wilson*, 1983], aerosol properties (e.g., pH) [*Lee and Thiemens*, 2001], uptake of SO_2 [*Li et al.*, 2006] and transition metal concentration [*Li et al.*, 2013]. Since the oxidation pathway of $S(IV)+O_3$ produces a higher $\delta^{18}O$ value (i.e., a positive correlation between $\delta^{18}O$ and $\Delta^{17}O$), the similar $\delta^{18}O$ values within these four samples may imply multiple sources rather than a distinct source [*Hill-Falkenthal et al.*, 2012a], though only four samples were measured. An intensive investigation on different sources and oxidation pathways of sulfur compounds on the Tibetan Plateau with a larger dataset of triple oxygen isotopic measurement will clarify and quantify contributing processes.

8.4.4 Potential of ^{35}S as stratospheric O_3 tracer and uncertainties

It was demonstrated that ^{35}S is a useful tracer to calculate the STT fluxes of SO_2 and SO_4^{2-} as well as the impact of STT on SO_2 oxidation lifetime. In this section, we evaluate the potential of ^{35}S as a stratospheric O_3 tracer by comparing our proof of concept approximation and traditional methods (surface O_3 measurements, specific humidity [*Gray et al.*, 1994] and FLEXPART stratospheric O_3 tracer [*Cooper et al.*, 2005]).

In two aged STT events identified above, the averaged O_3 mixing ratios are not significantly high (53.3 and 53.7 ppbv during April 1-10 and 17-22, respectively; Table 8.2). These values are slightly lower than the seasonal peaks observed in the northeast Tibetan Plateau (59 ppbv) [*Li et al.*, 2009b] and the Himalayas (61~67 ppbv) [*Bonasoni et al.*, 2008]. The relatively low O_3 mixing ratio in Nam Co reveals that this background site is often influenced by low altitude air masses, consistent with ^{35}S observations. Table 8.2 shows that O_3 mixing ratios are not simply correlated with ^{35}S concentrations, suggesting that photochemical production in the troposphere may be a dominant source of surface O_3 at this site and frequent influence of a fresh STT plume is highly unlikely. In two aged STT events (April 1-10 and 17-22), it is highly possible that the signature of stratospheric O_3 in aged STT plumes is largely erased during transport and therefore only accounts for a small portion of surface O_3. This result suggests that the signature of an aged STT plume is difficult to identify in surface O_3 measurement alone.

Comparison with specific humidity can provide additional information on the origin of surface O_3. Given that stratospheric air is expected to be dry and with a low humidity level, hourly specific humidity (at 500 hPa) data is utilized to identify the influence of stratospheric air masses. However, even though the lowest specific humidity in the sampling period is found at April 25-30, relative low ^{35}S concentrations and lowest O_3 mixing ratio are also observed (Table 2). A 72-hour backward trajectory analysis reveals that all air masses during this period were originated from the north (not shown), which passed through the desert areas of the Taklamakan Desert, the Loess Plateau and/or the Tibetan Plateau itself [*Li et al.*, 2012]. It implies that the variation of humidity

may also depend on the geographic origin of air masses apart from the altitude. Considering the air masses of two aged STT events (April 1-10 and 17-22) were exclusively from the south passing through the Himalayas (Figure 8.3), only this type of air masses (the Himalayas air masses) will be considered in this study. Figure 8.2 showed that water contents in these two periods were generally lower than other sampling periods like those in May, and most of O_3 peaks in these two periods were in tandem with low specific humidity, both of which suggested that the air masses were likely partly from the descending air of stratospheric origin, as revealed by ^{35}S measurements.

As model calculations may have large uncertainties, a sensitive tracer from field-based observation is needed to provide an additional way to resolve the impact of STT on surface O_3 and constrain the model results. A simple first order estimation is to relate ^{35}S and O_3 measurements at Nam Co and at Mt. Everest. As predicted in Section 3.2, ~30% air masses at the Himalayas were entrained to the boundary layer of Nam Co through horizontal transport and mixing from the free troposphere during April 1-10. There are limited surface O_3 measurements made at elevations above 6000 m on the north side of Mt. Everest, where we collected the $^{35}SO_4^{2-}$ samples. *Zhu et al.* [*Zhu et al.*, 2006] reported the highest O_3 mixing ratio (84 ppbv) at ~5000 m, where we collected river sample for ^{35}S measurement, while *Semple and Moore* [*Semple and Moore*, 2008] reported lower values (10-70 ppbv) from 5676 m to 8848 m. If it is assumed that both SO_4^{2-} and O_3 are inert and the transport of SO_4^{2-} and O_3 is identical, an upper limit of the contribution from the free troposphere of the Himalayas to surface O_3 at Nam Co is estimated as 25 ppbv (47%).

Although the enhanced O_3 levels observed by *Zhu et al.* [*Zhu et al.*, 2006] were likely from the stratosphere, the contribution was not quantitatively determined. A more reasonable approximation is using the STT flux of gas phase $^{35}SO_2$ as calculated in Section 3.3.1 to estimate the amount of O_3 exclusively originating from a stratospheric source. Even though SO_2 is influenced by wet removal process whereas O_3 is almost not, a complication noted in the interpretation of ^{7}Be (solid phase) as a tracer of stratospheric O_3 [*Zheng et al.*, 2011], gaseous $^{35}SO_2$ may reflect some O_3 transport processes better than solid phase tracers because wet removal lifetime of $^{35}SO_2$ is

significantly longer than airborne particulates and is incorporated in the model. The O_3 mixing ratio at ~17 km a.s.l. over the southern Tibetan Plateau as determined from ozonesondes was between ~100 and ~160 ppbv [*Zhu et al.*, 2006]. If $^{35}SO_2$ concentration at this altitude is adopted from steady-state model calculations occurred at mid-altitudes (746 atoms m^{-3}) [*Priyadarshi et al.*, 2012a], we can now estimate the upper and lower limits to the ratio between O_3 and $^{35}SO_2$ concentrations in the UT/LS (0.13-0.21 ppbv per atoms m^{-3}). A comparison with $^{35}SO_2$ STT flux shows a daily-averaged contribution of STT to surface O_3 mixing ratio of 5-8 ppbv during April 1-10. This value is lower than an estimation of 13 ppbv based on 30-min average data in a 2-year study conducted at a high altitude site in the Himalayas, which is directly influenced by fresh STT plumes [*Cristofanelli et al.*, 2010]. Since our estimation is based on the averaged ^{35}S concentration during a long sampling period (10 days), the signature of stratospheric air is diluted. With ^{35}S measurement of high temporal frequency, greater ^{35}S concentrations and estimated contributions of stratospheric O_3 should be observed in a specific day/hour when the air masses contain a pronounced amount of stratospheric air.

Because SO_2 can be oxidized by OH, H_2O_2, O_3 and/or O_2 through transition metal ion catalysis, if a fraction of SO_2 was oxidized by O_3, this reaction can be a sink of both SO_2 and O_3. In this first proof of concept approximation, the oxidation rate of SO_2 is considered but O_3 is assumed to be inert, meaning that the absence of detailed tropospheric photochemistry is a potential error source. It was suggested that the lifetime of O_3 over the Tibetan Plateau might be shorter than the surrounding area due to limited precursors and strong UV [*Lin et al.*, 2008c], but there is no literature reporting the exact O_3 lifetime at Nam Co. Although the estimation proposed here poses uncertainties, we provide an additional approach to resolve the contribution of STT to surface O_3 level that complements other techniques. High temporal resolution measurements of ^{35}S, further definition of the relationship between $^{35}SO_2$ and O_3 in the lower stratosphere, inclusion of tropospheric O_3 chemistry, establishment of a 4-box 1-D model [*Priyadarshi et al.,* [*Priyadarshi et*

al., 2011a] and relevant measurements constraining model parameters will improve future quantification of O_3 phenomena.

The FLEXPART stratospheric O_3 tracer at 50 m above ground level showed two notable peaks on April 1 and April 17, which reasonably agree with the enhanced ^{35}S concentrations (Figure 8.2). However, it is surprising to find that the surface O_3 mixing ratios observed at corresponding days are not exceptionally high. It is possibly because the enhanced stratospheric O_3 was compensated by a diminished amount of photochemical O_3 in low altitude air mass, further suggesting that the signature of stratospheric air masses may be difficult to resolve by surface O_3 measurement (without CO measurement) in a site dominated by tropospheric photochemical O_3. Although detailed meteorological analysis to understand the dynamic of STT is beyond the scope of this study, three-dimensional views of the 80 ppbv stratospheric O_3 isosurface are shown to better indicate the origin of two stratospheric O_3 peaks in the FLEXPART model (Figure 8.4). High altitude air masses from the Himalayas descending into the southern Tibetan Plateau as continuous bands are observed on both April 1 and 17, which may be due to the downward transport driven by the katabatic wind at the northern slope of Mt. Everest [*Zhu et al.*, 2006]. It is worthwhile to note the enhanced stratospheric O_3 level at the UT/LS of northern Tibetan Plateau, which may indicate that STT from that region should not be neglected. It was shown that polar stratospheric air can be transported to the middle troposphere above the Tibetan Plateau in winter [*Chen et al.*, 2011], but the backward trajectories (Figure 8.3) and discontinuities of stratospheric O_3 isosurfaces (Figure 8.4) suggest that this pathway is unlikely a key driver in these events. The ^{35}S measurement at northern Tibetan Plateau in the future is of interest to depict the geographical distribution of ^{35}S and an overall picture of STT over the Tibetan Plateau.

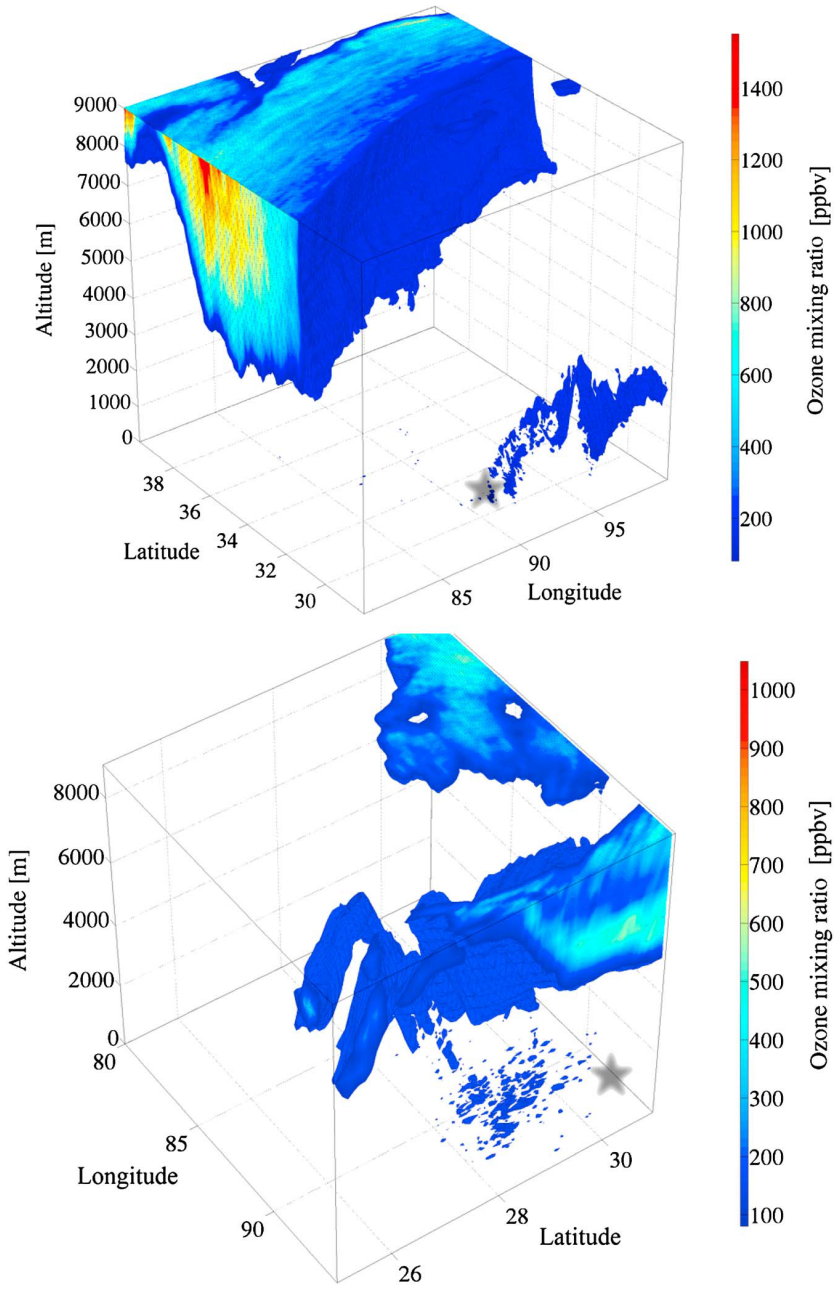

Figure 8.4 The FLEXPART 80 ppbv ozone isosurfaces at 1500 UTC, 1 April (upper) and 1300 UTC, 17 April (lower), with altitude above ground level and location of Nam Co (red star) for scale. Distributions of O_3 mixing ratio over the cross-sections are shown. Note the different perspective and scale.

The high positive PV values indicate a lowered tropopause height and the associated cutoff lows in the UT/LS [*Nieto et al.*, 2008], which may cause irreversible transfer of stratospheric air masses into the troposphere [*Beekmann et al.*, 1997]. *Cooper et al.* [*Cooper et al.*, 2007] suggested

that even regions of the troposphere with PV less than 1 PVU can still contain relatively notable amounts of aged stratospheric O_3, but the FLEXPART model excludes these aged stratospheric O_3 and may underestimate its contribution. In the periods (April 1-10 and 17-22) with elevated ^{35}S level and flux of STT, anomalous high positive PV values at the Himalayas or even Nam Co were frequently observed. For example, the PV contour maps at 400 hPa and wind field at 250 hPa show that notable PV anomalies swept over the Nam Co region from the Himalayas on the side of the strong westerly jet streams in April 6 and 22 (Figure 8.5), which likely indicates shallow types of STT bringing fresh stratospheric O_3 into the free troposphere (>3000 m above ground level) but not penetrating into the boundary layer immediately [*Skerlak et al.*, 2014]. In these two events, relatively low water content and high O_3 mixing ratio were observed, but the FLEXPART model failed to simulate a significant contribution of stratospheric O_3 (Figure 8.2). The average concentrations of the FLEXPART stratospheric O_3 tracer in April 1-10 and 17-22 (0.6 and 1.2 ppbv, respectively) are significantly smaller than our estimations stated earlier, implying that ^{35}S is a better diagnostic tracer for aged stratospheric plumes.

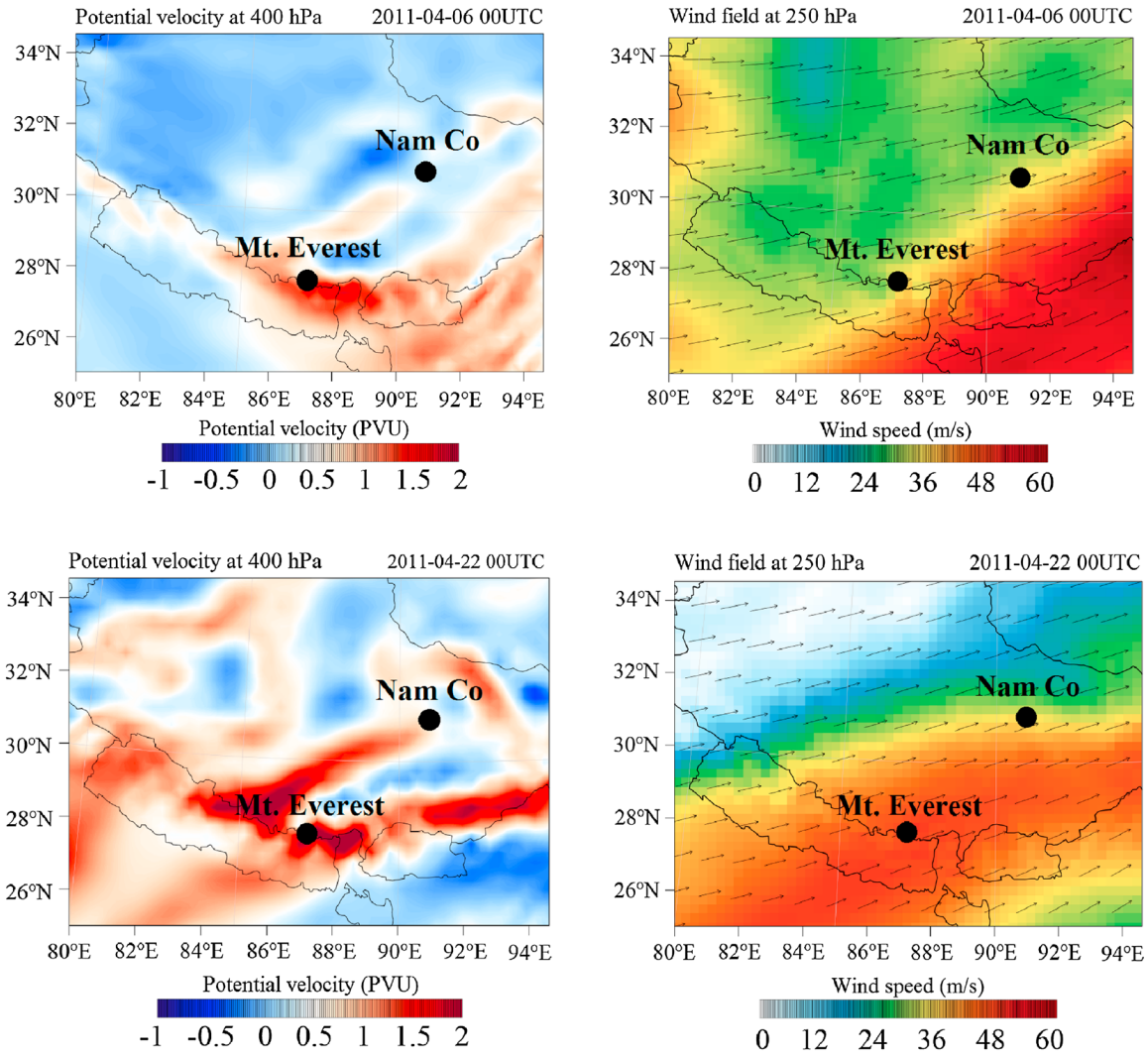

Figure 8.5 (a) The PV (Unit: PVU) at 400 hPa and (b) the wind field (Unit: m s^{-1}) at 250 hPa over the Tibetan Plateau at 0000 UTC, 6 April, based on the WRF simulation; (c) and (d) As in Figure 5a-5b but at 0000 UTC, 22 April. The black dots show the locations of Nam Co and Mt. Everest.

It's noted that two relatively small peaks of the FLEXPART stratospheric O_3 tracer occur at March 29 and May 21 when relatively high specific humidity are observed and relatively small flux of STT are estimated. The discrepancy may result from complex meteorological conditions of the boundary layer (e.g., limited resolution of sharp topography and mesoscale meteorology, inadequate representation of the boundary layer dynamics), uncertainty of parameterization in the ratio between O_3 mixing ratio and PV in the stratosphere, and the absence of chemistry in the FLEXPART model. Alternatively, if the model result is correct, it may suggest that 1) specific

humidity is not sufficiently sensitive when a small portion of high altitude air masses mixed with a large amount of low altitude air masses; 2) further constraining parameters in ^{35}S box model is imperative. However, due to the lack of relevant data, we are not able to conclude which reason is dominant. Further investigation using a 4-box model with parameters constrained by field-based measurement or more sophisticated chemical transport model can improve this method and provide deeper insight into this topic.

In summary, since Nam Co is often influenced by low altitude air masses, it is possible the mixing between polluted air masses from low altitude and the aged STT air masses from high altitude makes the signature of STT difficult to resolve using traditional O_3 and humidity measurements. Using a cosmogenic ^{35}S tracer, we are able to capture the stratospheric O_3 signals in aged STT plumes, even though most signals are quickly erased by tropospheric processes. We provide a first approximation to resolve these small impacts and suggest that ^{35}S can be a potentially useful tracer for stratospheric O_3.

8.4.5 Implication of springtime O_3 maximum in southern Tibetan Plateau

A springtime O_3 maximum is found at the Nam Co region (Figure 8.1c), coinciding with most high elevation sites globally [*Monks*, 2000; *Oltmans et al.,* 2012]. Owing to the pristine environment of Nam Co [*Cong et al.*, 2007], it is suggested that the day-to-day variation of surface O_3 level at this site is influenced by long range transport of tropospheric photochemical or stratospheric O_3 rather than local photochemical production [*Lin et al*., 2015]. In this study period, the O_3 mixing ratios observed in the Himalayas air masses (56.3±6.2 ppbv) are higher than others (48.8±6.0 ppbv) (Figure 8.2), which is statistically significant based on an independent sample t-test ($p<0.001$, i.e., confidential level of >99.9%). Previous studies have already suggested that anthropogenic emissions over the Indo-Gangetic Plain and biomass burning in South Asia can penetrate through the Himalayas and exert a crucial impact on the atmospheric composition of Tibetan Plateau [*Xia et al.*, 2011]. Our results may provide new insight for the frequent springtime

STT over the Himalayas [*Skerlak et al.*, 2014] and reveal that they not only enhance the O_3 concentration in that region [*Cristofanelli et al.*, 2010], but also bring aged stratospheric air to the southern Tibetan Plateau including Nam Co and influence the surface O_3 levels. Given that the pollution plume from the Indo-Gangetic Plain can reach up to 10 km a.s.l. under the influences of up-valley breezes [*Cristofanelli et al.*, 2010], extended research efforts involving field observations of O_3, ^{35}S and anthropogenic pollution tracer (e.g., CO) with high temporal resolution can bring us closer to quantifying the contributions of photochemical and stratospheric O_3 on the springtime O_3 maximum in southern Tibetan Plateau.

8.5 Concluding Remarks

Our measurements of ^{35}S concentrations in snow and water samples collected at Mt. Everest reveal strong springtime STT in the Himalayas. Comparison with simultaneous $^{35}SO_2$ and $^{35}SO_4^{2-}$ measurements at a background site (Nam Co) in the southern Tibetan Plateau during spring 2011 identify two periods with high ^{35}S concentration, which was affected by the aged stratospheric air masses originating from the Himalayas. A simple 1-box model shows that the oxidative lifetime of SO_2 under the influence of aged stratospheric air masses is 12 h. Triple oxygen isotopic measurements in sulfate samples suggest that the enhanced O_3 levels may shift the oxidation pathway. Along with surface O_3, meteorological simulations and FLEXPART stratospheric O_3 tracer, our results demonstrate that ^{35}S is an additional tracer to identify the influence of STT on surface O_3 levels, even in aged STT plumes. Although this first proof of concept approximation cannot provide a perfect quantification of stratospheric O_3 intrusion, it shows the potential and more detailed research into this topic is of importance.

Because of the short time scale of STT processes and unconstrained parameters in box model, a higher temporal resolution ^{35}S measurement (~1 day) and more relevant measurements constraining model parameters are needed. A thorough triple oxygen isotope measurement of sulfate in combination with ^{35}S measurements as shown in this study can provide more detailed

information regarding the influence of stratospheric O_3 on sulfur chemistry in the troposphere [*Hill-Falkenthal et al.*, 2012b]]. Quadruple stable sulfur isotope measurements were suggested as a tracer of stratospheric impact on the tropospheric sulfur cycle [*Romero and Thiemens*, 2003]. Most recent research on high resolution snow pit samples collected at the South Pole suggests that burning processes may also contribute the variation of quadruple stable sulfur isotope in tropospheric sulfate [*Shaheen et al.*, 2014]. Inclusion of such measurements may provide further information on the global sulfur cycle.

8.6 Acknowledgement

This study was supported by the National Science Foundation of China (40875075, 41225002, 41371088), the Fundamental Research Funds for Central Universities (2010380003161542), the Trans-Century Training Programme Foundation for the Talents offered by the Ministry of Education of China, and the "Strategic Priority Research Program (B)" of the Chinese Academy of Sciences (XDB03030504). Mang Lin acknowledges a fellowship from the Guangzhou Elite Project (JY201303). The authors gratefully acknowledge all members from 2013 Mt. Everest Scientific Expedition Team for field assistance and all staffs at Nam Co station for sample collection. The reviewers are graciously acknowledged for their insightful comments that greatly improved the manuscript.

This chapter, in full, is a reprint of the material "Resolving the impact of stratosphere-to-troposphere transport on the sulfur cycle and tropospheric ozone level over the Tibetan Plateau using a cosmogenic ^{35}S tracer" as it appears in Journal of Geophysical Research: Atmosphere, 2016. Lin, Mang; Zhang, Zhisheng; Su, Lin; Hill-Falkenthal, Jason; Priyadarshi, Antra; Zhang, Qianggong; Zhang, Guoshuai; Kang, Shichang; Chan, Chuen-Yu; Thiemens, Mark H., American Geophysical Union, 2016. The dissertation author was the primary investigator and author of this paper.

Chapter 9 Five-S-isotope evidence of two distinct mass-independent sulfur isotope effects and its consequence for the Archean record

9.1 Abstract

The signature of mass-independent fractionation of quadruple sulfur stable isotopes (S-MIF) in Archean rocks, ice cores, and Martian meteorites provides a unique probe of the oxygen and sulfur cycles in the terrestrial and Martian paleo-atmospheres. Its mechanistic origin however contains some uncertainties. Even for the modern atmosphere, the primary mechanism responsible for the S-MIF observed in nearly all tropospheric sulfates has not been identified. Here we present high-sensitivity measurements of a fifth sulfur isotope, stratospherically produced radiosulfur, along with all four stable sulfur isotopes in the same sulfate aerosols and a suite of chemical species to define sources and mechanisms on a field observational basis. The five-sulfur-isotope and multi chemical species analysis approach provides strong evidence that S-MIF signatures in tropospheric sulfates are concomitantly affected by two distinct processes: an altitude-dependent positive 33S anomaly, likely linked to stratospheric SO2 photolysis, and a negative 36S anomaly mainly associated with combustion. Our quadruple stable sulfur isotopic analysis in varying coal samples (formed in the Carboniferous, Permian, and Triassic periods) and SO2 emitted from combustion displays normal 33S and 36S, indicating that the observed negative 36S anomalies originate from a previously unknown S-MIF mechanism during combustion (likely recombination reactions) instead of coal itself. The basic chemical physics of S-MIF in both photolytic and thermal reactions and their interplay, which was not explored together in the past, may be another ingredient for providing deeper understanding of the evolution of Earth's atmosphere and life's origin.

9.2 Introduction

As the tenth most abundant element in the Universe, sulfur has stable (^{32}S, ^{33}S, ^{34}S and ^{36}S) and radioactive isotopes (e.g., ^{35}S and ^{38}S). The S-MIF or stable sulfur isotopic anomaly (quantified

by $\Delta^{33}S=\delta^{33}S-1000*[(1+\delta^{34}S/1000)^{0.515}-1]$ and $\Delta^{36}S=\delta^{36}S-1000*[(1+\delta^{34}S/1000)^{1.9}-1]$) observed in Archean (~4 to ~2.5 Ga) sediments has been interpreted as a proxy of the origin and evolution of atmospheric oxygen and early life on Earth [*Farquhar et al.*, 2000a; *Lyons et al.*, 2014]. Resolving all mechanistic origins of S-MIF has been a focus of active research for more than 20 years[*Thiemens*, 2006]. Photochemistry of sulfur-bearing gases (e.g., SO_2 and H_2S) in the short wavelength ultraviolet (UV) region accounts for much of the Archean record and is the currently most accepted mechanism responsible for S-MIF observed on the Earth [*Farquhar et al.*, 2000a; *Lyons et al.*, 2014; *Ono*, 2017], Mars [*Franz et al.*, 2014] and possibly achondritic meteorites [*Chakraborty et al.*, 2013].

In the modern Earth, only stratospheric sulfates are presumed to acquire S-MIF signatures because short (< ~290 nm) UV light is shielded by the stratospheric ozone layer. The presence of S-MIF in sulfates extracted from ice cores, snow pits, and ash beds is interpreted as deriving from massive volcanic eruptions with stratospheric SO_2 injection [*Baroni et al.*, 2007; *Martin and Bindeman*, 2009; *Savarino et al.*, 2003]. This assumption may not always be valid because sulfur isotopic anomalies not explicable by mass-dependent fractionation (MDF) [*Harris et al.*, 2013a] are widely found in tropospheric sulfates [*Guo et al.*, 2010; *Han et al.*, 2017; *Romero and Thiemens*, 2003] (Figure 9.1). Stratospheric influence on the unexpected S-MIF in tropospheric sulfates is not quantified [*Guo et al.*, 2010; *Han et al.*, 2017; *Romero and Thiemens*, 2003; *Shaheen et al.*, 2014] for lack of a measurable stratospheric tracer of the sulfate. Without a complete understanding for the origin of S-MIF in modern atmospheric sulfates, interpretation of S-MIF signals preserved in cryospheric, geological, and meteoritic samples possess embedded uncertainties.

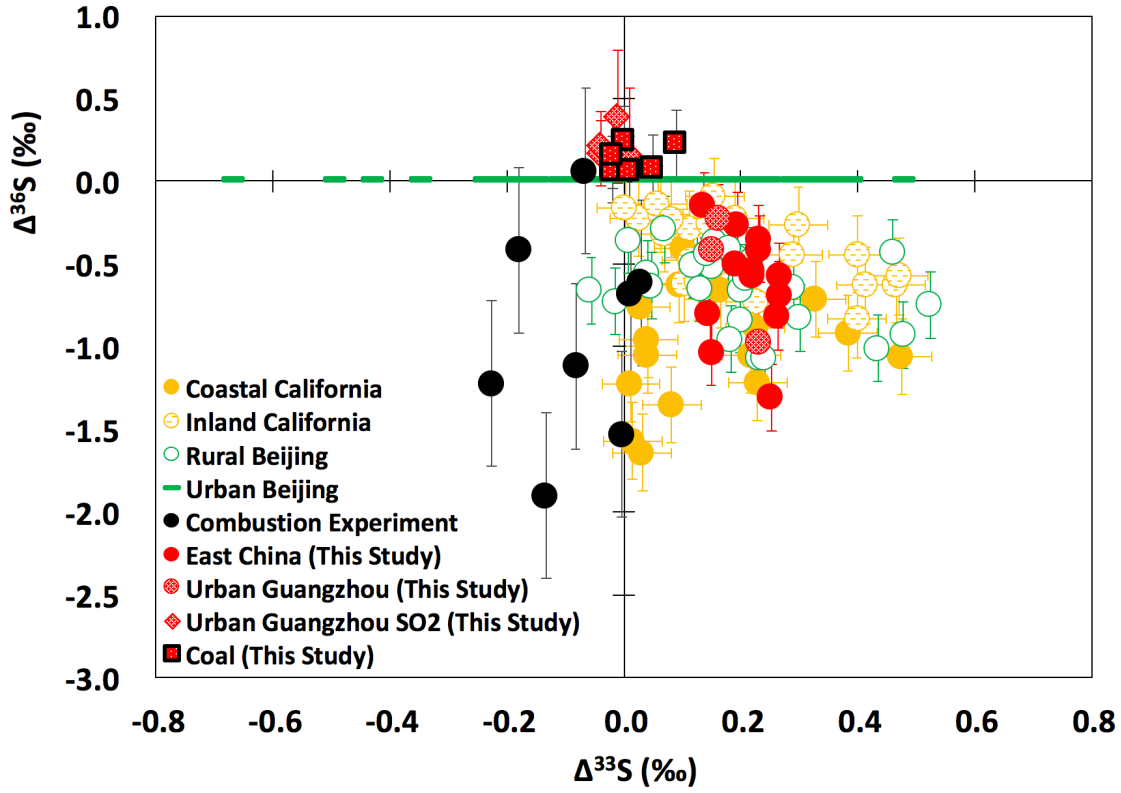

Figure 9.1. Quadruple stable sulfur isotopic compositions in modern tropospheric sulfates, SO_2 and coal. Atmospheric samples were collected from a background site at East China (the Mount Wuyi Station; this study), the third largest megacity in China (Guangzhou; this study), coastal California [*Romero and Thiemens*, 2003], inland California [*Romero and Thiemens*, 2003], rural Beijing [*Guo et al.*, 2010], and urban Beijing [*Han et al.*, 2017]. Note that $\Delta^{36}S$ for urban Beijing [*Han et al.*, 2017] is not available, and therefore $\Delta^{33}S$ data are shown on the x-axis as green bars. Chromium-reducible sulfur in coal (this study) and primary sulfates emitted from a chamber combustion experiment [*Lee et al.*, 2002] are also shown. Error bars stand for one standard deviation.

In this study, the high-sensitivity measurement [*Brothers et al.*, 2010] of a fifth sulfur isotope, ^{35}S (half-life: ~87 days), casts new light on the exploration of the origin of S-MIF in atmospheric sulfates on a field observational basis. Cosmogenic ^{35}S is the only radioactive sulfur isotope existing in nature with a half-life of ideal age to track atmospheric processes [*Brothers et al.*, 2010]. It is exclusively produced in the higher atmosphere by the spallogenical bombardment of ^{40}Ar by high-energy cosmic rays. The ability of ^{35}S to serve as a sensitive and unambiguous tracer in identifying sulfate aerosols originating from the higher atmosphere was recently

demonstrated [*Lin et al.*, 2016a] and has been utilized in understanding sulfate formation pathways at different altitudes [*Lin et al.*, 2017c]. Here we measured all five (four stable and one radioactive) sulfur isotopes along with all three stable oxygen isotopes (^{16}O, ^{17}O, and ^{18}O) in the same sulfate aerosols collected at a mid-latitude remote mountain site located in East China (see Methods and Figure 9.2).

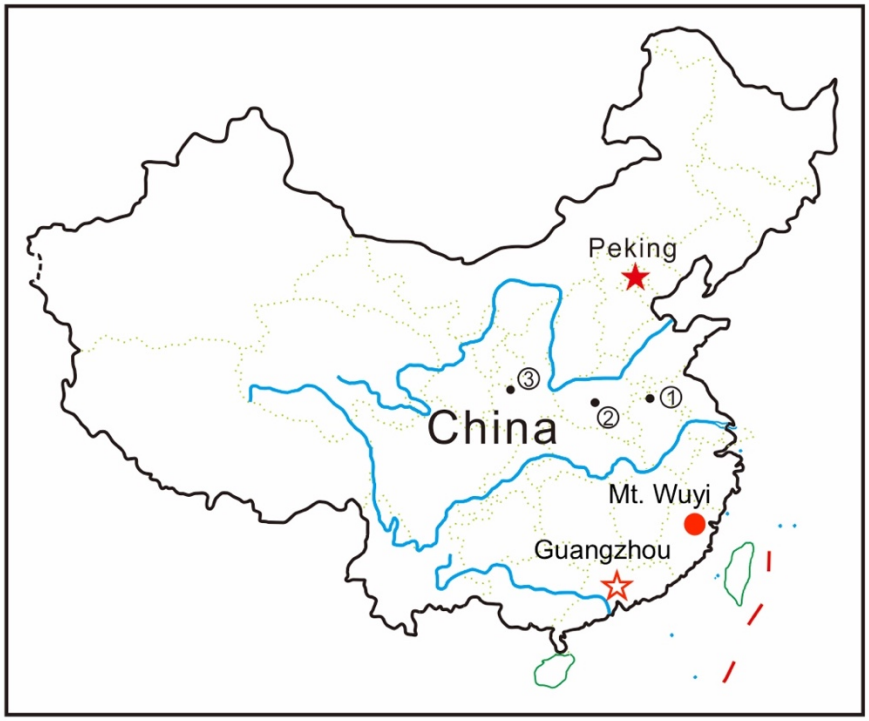

Figure 9.2. Map showing the sampling sites. $PM_{2.5}$ samples were collected at Mt. Wuyi; SO_2 and PM_{10} samples were simultaneous collected at Guangzhou (the third largest megacity in China); Black dots represent coal sampling sites (coal mines): 1) Zhuxianzhuang; 2) Pingdingshan; 3) Cuimu.

9.3 Quadruple sulfur isotope composition in sulfate aerosols, SO_2, and coal

All sulfate aerosols measured in this study possess non-zero $\Delta^{33}S$ and $\Delta^{36}S$ (Figure 9.1), consistent with previous measurements [*Guo et al.*, 2010; *Han et al.*, 2017; *Romero and Thiemens*, 2003]. Because coal burning accounts for ~95% of sulfur emissions in China [*Su et al.*, 2011], we

first measured quardurple stable sulfur isotopes in various representative Chinese coal samples (formed in the Carboniferous, Permian, and Triassic periods) and ambient SO_2 emitted from coal burning (see Methods and Figure 9.2) to evaluate their contribution to non-zero $\Delta^{33}S$ and $\Delta^{36}S$ values in atmospheric sulfates. Our data indicate that sulfur isotopic compositions in coal and SO_2 are essentially normal within error and their patterns in the $\Delta^{33}S$ *v.s.* $\Delta^{36}S$ scatter plot notably differ from tropospheric sulfates (Figure 9.2). It is therefore highly unlikely that non-zero $\Delta^{33}S$ and $\Delta^{36}S$ values in tropospheric sulfates directly originated from coal itself.

Slight differences in MDF exponents of varying SO_2 oxidation processes could accommodate small variations of $\Delta^{33}S$ in tropospheric-SO_2 derived sulfates (±0.1‰) [*Harris et al.*, 2013a], but cannot explain the relatively large non-zero $\Delta^{33}S$ and $\Delta^{36}S$ values in most atmospheric sulfates (including the data in this study) ($-0.7‰<\Delta^{33}S<0.6‰$; $-1.7‰<\Delta^{36}S<0.1‰$) (Figure 9.1). This view is partially supported by the poor correlation between $\Delta^{33}S$, $\Delta^{36}S$, and $\Delta^{17}O$ ($=\delta^{17}O-0.52\times\delta^{18}O$, an isotopic fingerprinting quantifying the relative contribution of SO_2 oxidation processes [*Thiemens*, 2006]) shown in this study (Supplementary Table 1) and by Romero and Thiemens [*Romero and Thiemens*, 2003]. Replicate analysis and inter-laboratory comparisons for the same atmospheric samples in this work demonstrate that the observed non-zero $\Delta^{33}S$ and $\Delta^{36}S$ values are independently reproducible and in agreement (see Methods), and further confirm that they are attributed to unknown S-MIF processes in nature which require identification.

9.4 Evidence for two distinct S-MIF processes

We observe that $\Delta^{33}S$ is correlated with ^{35}S specific activity (^{35}S-SA) (Figure 9.3 and Table 9.1). An extremely low ratio of ^{35}S in coarse to fine particles (0.04) supports the premise that sulfates collected in our remote mountain site were mainly affected by long-range horizontal and vertical transport (see Supplementary Discussion). The altitude-dependent variation of $\Delta^{33}S$ revealed by enrichment of stratospherically sourced ^{35}S indicates that sulfate aerosols originating from the higher atmosphere possess a greater $\Delta^{33}S$ value than the boundary layer and downward

transport of stratospheric sulfates is a likely source of $\Delta^{33}S$ to tropospheric sulfates. The stratospheric origin of non-zero $\Delta^{33}S$ values observed in most sulfate aerosols in East China and California (Figure 9.1) may be dynamically explained by a combination of the Asian monsoon anticyclone that efficiently transports SO_2 to the lower stratosphere [*Bourassa et al.*, 2012], the sulfate-enriched Asian Tropopause Aerosol Layer in the upper troposphere and lower stratosphere [*Yu et al.*, 2015], and frequent and active stratospheric intrusions at mid-latitudes of the Northern Hemisphere [*Lin et al.*, 2016a] (see Supplementary Discussion).

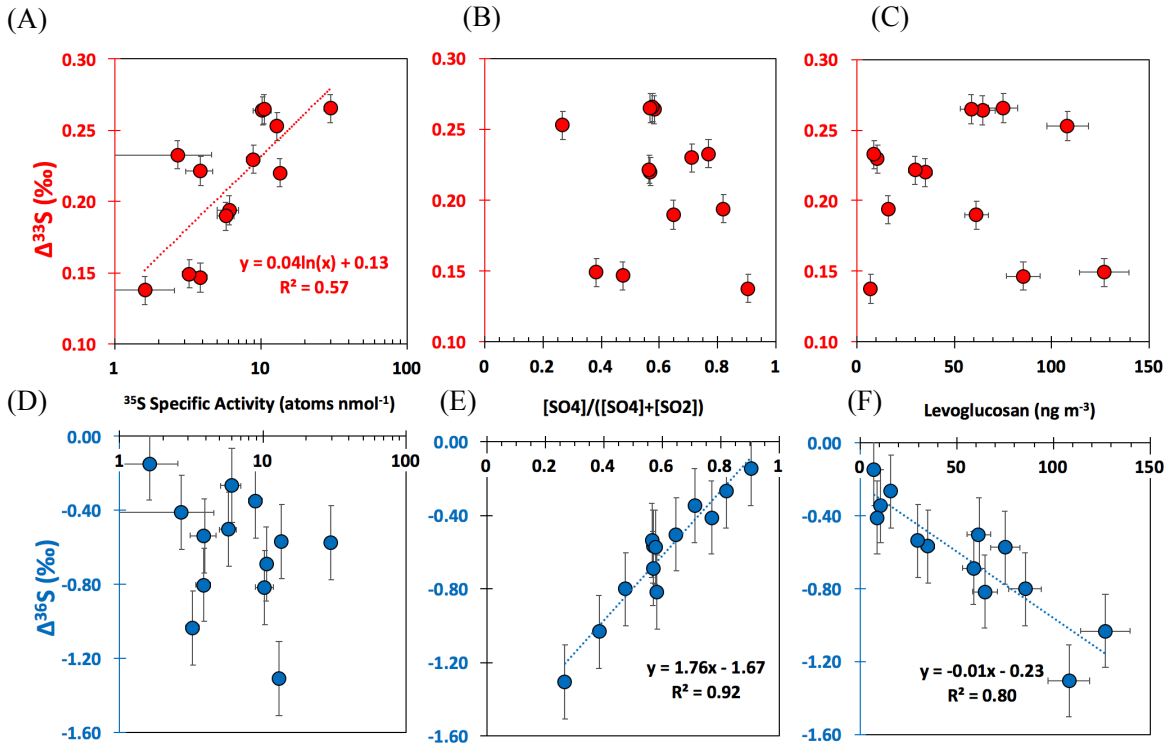

Figure 9.3. Scatter plots of S-MIF signatures versus stratospheric and combustion tracers. Upper panels: $\Delta^{33}S$ versus (A) ^{35}S specific activity, (B) SOR, and (C) levoglucosan concentrations; Lower panels: $\Delta^{36}S$ versus (D) ^{35}S specific activity, (E) SOR, and (F) levoglucosan concentrations. Error bars represent one standard deviation. If the Pearson correlation is significant at the 0.01 level (Supplementary Table S1), regression lines, equations, and coefficients of determination (R^2) are shown. The relationship between $\Delta^{33}S$ and ^{35}S specific activity appears non-linear because radioactive sulfates can produce or decay in the troposphere (see Supplementary Discussion).

Table 9.1. Pearson correlation coefficients between all five sulfur isotopes in sulfates and other variables including triple oxygen isotopes in sulfates, chemical compositions in the same aerosol samples, criteria air pollutant concentrations, and the ratios of $[SO_4]/([SO_2]+[SO_4])$ in the Mount Wuyi Station

	$\delta^{34}S$	$\Delta^{33}S$	$\Delta^{36}S$	^{35}S	^{35}S SA
$\delta^{34}S$	1.00	-0.08	-0.41	0.13	0.11
$\Delta^{33}S$	-0.08	1.00	-0.20	**0.60***	**0.68****
$\Delta^{36}S$	-0.41	-0.20	1.00	-0.09	-0.18
^{35}S	0.13	**0.60***	-0.09	1.00	**0.97****
^{35}S Specific Activity (SA)	0.11	**0.68****	-0.18	**0.97****	1.00
$\delta^{18}O$	**-0.65***	0.13	0.43	-0.13	-0.07
$\Delta^{17}O$	0.29	-0.53	0.04	-0.39	-0.37
Total Carbon	0.49	0.08	-0.84	0.36	0.34
Organic Carbon (OC)	0.39	0.07	**-0.80****	0.31	0.28
Element Carbon	0.41	0.06	-0.10	0.18	0.25
Water-soluble OC	0.41	0.18	**-0.72****	0.49	0.44
Chloride	0.33	0.03	**-0.82****	0.09	0.11
Nitrate	0.25	-0.38	**-0.69****	-0.16	-0.17
Sulfate (SO_4)	**0.60***	-0.20	-0.18	0.30	0.13

Table 9.1. Pearson correlation coefficients between all five sulfur isotopes in sulfates and other variables including triple oxygen isotopes in sulfates, chemical compositions in the same aerosol samples, criteria air pollutant concentrations, and the ratios of $[SO_4]/([SO_2]+[SO_4])$ in the Mount Wuyi Station (Continued)

	$\delta^{34}S$	$\Delta^{33}S$	$\Delta^{36}S$	^{35}S	^{35}S SA
Sodium	0.26	0.36	-0.36	0.44	0.37
Ammonium	**0.55***	-0.22	-0.40	0.24	0.09
Potassium	**0.57***	0.15	**-0.72****	0.41	0.36
Magnesium	**0.60***	-0.03	-0.34	0.09	0.03
Calcium	**0.58***	-0.10	**-0.55***	-0.03	0.01
Levoglucosan	0.42	-0.02	**-0.89****	0.23	0.24
Mannosan	0.37	-0.39	**-0.76****	-0.13	-0.10
SO_2	0.50	-0.11	**-0.89****	0.08	0.09
NO_2	**0.71****	0.06	**-0.81****	0.31	0.30
CO	0.28	-0.11	-0.25	0.26	0.21
O_3	**0.57***	0.33	0.03	0.48	0.42
$PM_{2.5}$	**0.65***	0.08	-0.51	0.42	0.32
$[SO_4]/([SO_2]+[SO_4])$	**-0.56***	-0.16	**0.96****	-0.19	-0.26

* Statistically significant at the 0.05 level.

** Statistically significant at the 0.01 level.

The most striking feature in the new data is that unlike $\Delta^{33}S$, $\Delta^{36}S$ is not clearly correlated with ^{35}S-SA (Figure 9.3 and Table 9.1). The poor correlation indicates that an additional process,

apart from SO_2 photochemistry [*Ono*, 2017], is required to fully explain S-MIF seen in atmospheric sulfates. The Sulfur Oxidation Ratio (SOR) is conventionally expressed as the molar ratio of sulfate to total sulfur (sulfate and SO_2) to quantify the degree of SO_2 oxidation (i.e., formation of secondary sulfate). A low SOR therefore indicates less secondary sulfates (i.e., a relatively large fraction of primary sulfates) in total sulfates. The excellent correlation between SOR and $\Delta^{36}S$ (Fig. 2) suggests that $\Delta^{36}S$ is likely linked to the formation of primary sulfate during fossil fuel and/or biomass combustion. The y-intercept (-1.7‰), representing $\Delta^{36}S$ in sulfates near the emission source (characterized by a near-zero SOR as a result of large amounts of SO_2), is close to the most negative $\Delta^{36}S$ (-1.9‰) in primary sulfate aerosols emitted from biomass and diesel combustion [*Lee et al.*, 2002] (Fig. 1). Alternatively, if the SOR equals to 1, the $\Delta^{36}S$ value in tropospheric secondary sulfate (0.1‰) is obtained, which matches SO_2 observations (Figure 9.1). This quantitative agreement therefore support the hypothesis that the large ^{36}S anomaly is associated with combustion processes rather than tropospheric SO_2 oxidation. Another independent verifying observation is that there are significant correlations between $\Delta^{36}S$ and various biomass burning tracers (levoglucosan, mannoson, and potassium) in the same samples (Figure 9.3 and Table 9.1).

Our five-sulfur-isotope observation points to a previously unknown non-photochemical channel for producing S-MIF (i.e., fossil fuel and/or biomass combustion). A recent theoretical study suggested that S-MIF can occur in recombination reactions of elemental sulfur (e.g., $S+S_2+M \rightarrow S_3+M$, an analogy of O_3 formation) as a result of the symmetry effect [*Babikov*, 2017], although the derived values should be quantitatively validated by laboratory experiments. The potential role of the symmetry effect in S-MIF has been noted since early studies [*Bainssahota and Thiemens*, 1989] but was generally not considered in SO_2 photolytic reactions because of the trace amount of gaseous S_2, S_3, and S_4 at ambient temperatures [*Lyons*, 2007] and the difficulty of experimental investigation [*Babikov*, 2017; *Babikov et al.*, 2017]. We argue that the elemental sulfur recombination reaction is strictly a thermal reaction because elemental sulfur vapor contains

sulfur allotropes with two to eight sulfur atoms [*Kumar and Francisco*, 2017]. In combustion processes, both S and S_2 are important short-lived intermediates [*Gardiner*, 2000]. There are a host of potentially relevant reactions (e.g., $SH+S \rightarrow S_2+H$) [*Gardiner*, 2000] may be crucial in producing these small sulfur allotropes and facilitating elemental sulfur recombination reactions, especially during slow smoldering combustion where large S-MIF would be emitted as primary sulfates ($\Delta^{36}S$=-1.9‰) [*Lee et al.*, 2002]. This unique isotopic fingerprinting may assist in quantifying the contribution of previously unappreciated sources of primate sulfates (e.g., incomplete residential coal combustion [*Du et al.*, 2016; *Han et al.*, 2017; *Yan et al.*, 2018]) to Earth's present-day atmosphere and its subsequent influences on public health and climate. The proposed hypothesis could be tested experimentally in the future to detail all parameters and mechanisms.

Significant correlations with SOR or biomass burning tracers are not observed with respect to $\Delta^{33}S$ (Figure 9.3 and Table 9.1), indicating that $\Delta^{33}S$ is less influenced by combustion processes than $\Delta^{36}S$ as shown in combustion experiments ($\Delta^{33}S$=-0.08±0.09‰, n=8) (Figure 9.1). Alternatively, the $\Delta^{33}S$ signatures of primary sulfates emitted from combustion processes may be masked by the apparent stratospheric signal because our samples were collected in a remote mountain site. On the basis of our new five-sulfur-isotope measurements, we identify an altitude-dependent process producing a gradual $\Delta^{36}S/\Delta^{33}S$ slope and a combustion-related process producing a steep slope. The finding explains why inland California, a region more affected by the stratospheric air [*Lin et al.*, 2016a], possesses more enriched ^{33}S (and less depleted ^{36}S) values than the more polluted coastal California [*Romero and Thiemens*, 2003] (Figure 9.1). These two MIF end-members, together with the MDF end-member (e.g., tropospheric secondary sulfates[*Harris et al.*, 2013a]), resolve a 15-year-old mystery: the “decoupled” relationship between $\Delta^{33}S$ and $\Delta^{36}S$ in atmospheric sulfates [*Romero and Thiemens*, 2003] (Figure 9.1).

9.5 Consequences for the understanding of the Archean S-MIF record

Using the y-intercepts of $\Delta^{33}S/^{35}S$-SA and $\Delta^{36}S$/levoglucosan fitted curves in Fig. 2 ($\Delta^{33}S$=0.13±0.02‰, $\Delta^{36}S$=-0.23±0.07‰, respectively), we estimate the $\Delta^{33}S/\Delta^{36}S$ ratio of background tropospheric sulfates at East Asia to be -1.8±0.6, a value close to the Archean array (from -0.9 to -1.5) [*Ono*, 2017]. We also note that the fitted $\Delta^{36}S/\Delta^{33}S$ slope (-4.0±1.0) in the measured samples (see Figure 9.4 and Supplementary Discussion) is compatible with a steep $\Delta^{36}S/\Delta^{33}S$ slope of -3.6±1.8 in Paleoarchean (3.6-3.2 Ga) pyrites [*Wacey et al.*, 2015] (Figure 9.5). This similarity implies that both photochemical and non-photochemical S-MIF processes identified in this study may also concomitantly occur in Archean.

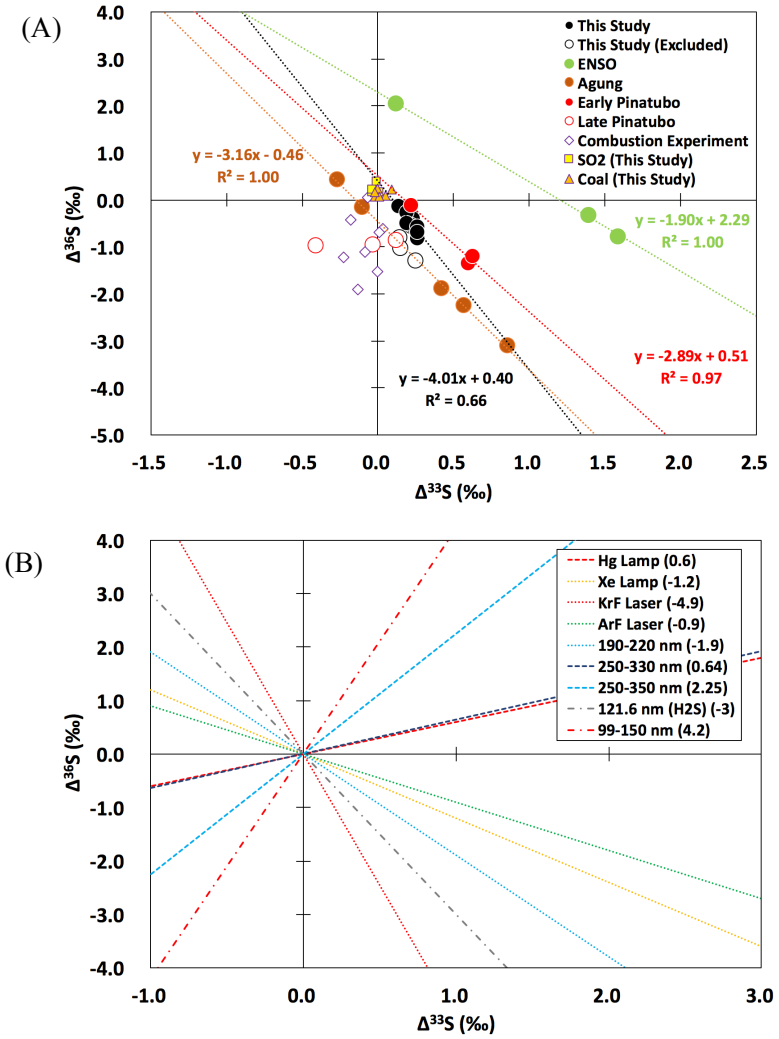

Figure 9.4. A wide range of $\Delta^{36}S/\Delta^{33}S$ slope in the field and laboratory. (A) Tropospheric sulfates in this study, and sulfate deposits in snow pits [*Baroni et al.*, 2007; *Shaheen et al.*, 2014]. Isotopic compositions shown in this figure are not corrected with background. Regression lines, equations and coefficients of determination (R^2) are shown. Empty symbols are excluded from regression analysis (see Supplementary Discussion). (B) Sulfur photochemistry experiments with various wavelengths [*Farquhar et al.*, 2001] [*Whitehill and Ono*, 2012] [*Whitehill et al.*, 2015] [*Chakraborty et al.*, 2013] [*Chakraborty et al.*, 2017]. Approximate values are shown in brackets. Readers are recommended to refer to the references for detailed information.

The variability of $\Delta^{36}S/\Delta^{33}S$ slopes in Archean sediments may be an indicator of a changing sulfur cycle on Earth during the appearance and evolution of early life [*Lyons et al.*, 2014], but corresponding biogeochemical processes remain elusive [*Halevy et al.*, 2010]. Because laboratory

photolysis experiments showed that the $\Delta^{36}S/\Delta^{33}S$ slope is sensitive to the wavelength (Figure 9.4), experimental and modeling efforts have been focused on tuning atmospheric composition to reproduce the observed Archean array [*Endo et al.*, 2016; *Ueno et al.*, 2009]. Based on laboratory experiments, the thermochemical sulfate reduction (a non-photochemical process) was proposed as an alternative or additional S-MIF mechanism to explain the Archean record [*Watanabe et al.*, 2009], but this process was attributed to magnetic isotope effects [*Oduro et al.*, 2011], which only lead to ^{33}S anomalies and contrast with observations in nature (e.g., Archean rocks, ice cores, present-day aerosols) (Figure 9.5).

Our study has shown that certainly for today, the isotopic anomalies in ^{33}S and ^{36}S appear decoupled in the measured samples and their corresponding processes can be identified by simultaneous measurements of radiosulfur and combustion indices. In the Archean, it is widely accepted that S-MIF signatures are from photochemistry of sulfur-bearing species emitted from volcanoes and volcanic activity is required in all Archean S-MIF models [*Halevy et al.*, 2010; *Lyons et al.*, 2014]. Venting and polymerization of gaseous S_2 is ubiquitous on Io (one of Galilean moons), the most volcanically active body in the solar system [*Spencer et al.*, 2000]. At terrestrial volcanic vents and fumaroles, elemental sulfur deposits formed in high-temperature sulfur-bearing gases are commonly found [*Kumar and Francisco*, 2017; *Taran et al.*, 1992]. Therefore, it is highly likely that basic reactions responsible for S-MIF in combustion (probably recombination reactions) [*Babikov*, 2017] can occur in both modern and primitive Earth's atmosphere and predominantly contribute to some notably depleted ^{36}S records in Paleoarchean (Figure 9.5), an era characterized by intense volcanic activity [*Philippot et al.*, 2012]. A pilot study observed a negative $\Delta^{36}S$ value (-0.9‰) in modern volcanogenic sulfate aerosols at the point of emission [*Mather et al.*, 2006], emphasizing the need for further sulfur isotopic measurements of present-day volcanic gases and solids formed in the gas phase. Given that both SO_2 photolysis and elemental sulfur polymerization are relevant to Archean volcanism, the Archean ^{33}S and ^{36}S anomalies could in fact come from the

same volcanoes but different reactions. With extended experimental and modeling efforts on providing the new chemical physics and atmospheric reactions, the Archean S-MIF record may potentially yield deeper insight in the future.

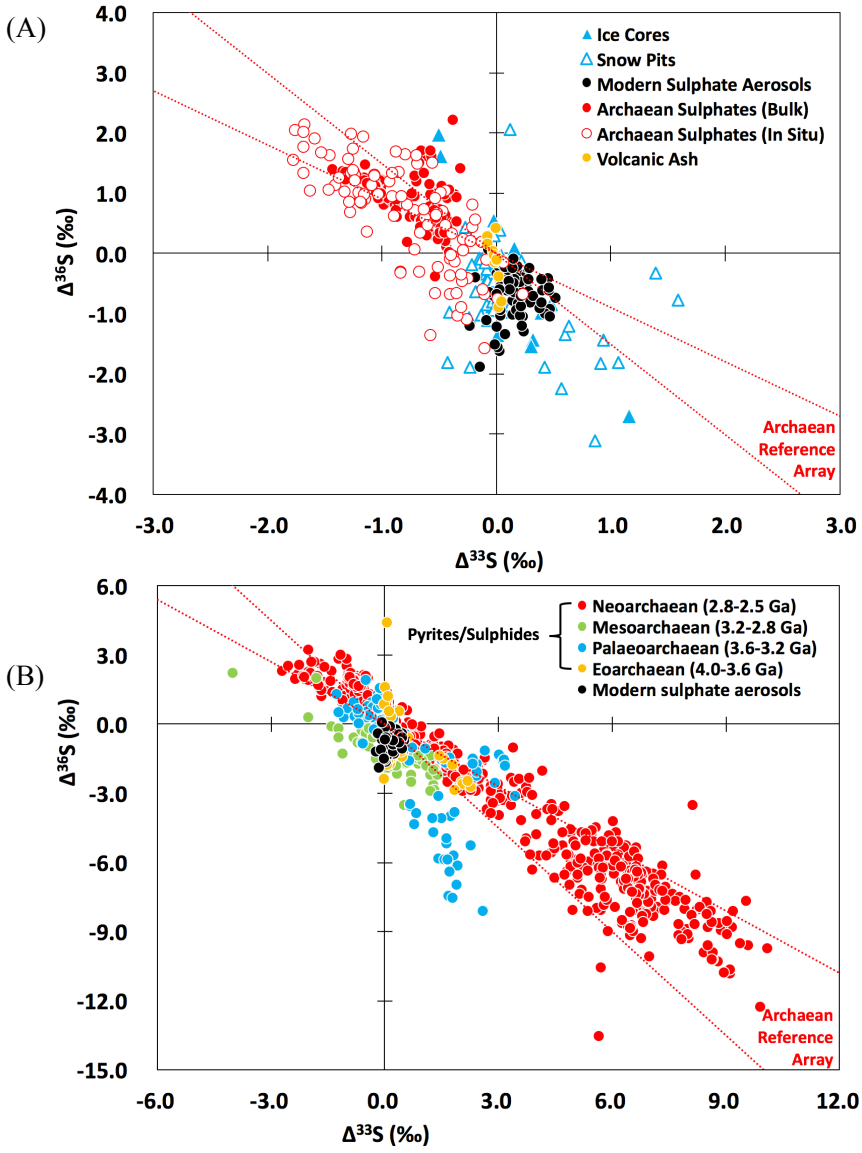

Figure 9.5. Similarity of S-MIF signatures in modern atmospheric sulfates and geological records. (A) Sulfates from modern aerosols (including the data in this study), ice cores, Archean sediments and volcanic ash; (B) Pyrites (FeS_2) and sulfides (S^{2-}) from different eras in Archean. Red dotted lines represent the Archean Reference Array (with slopes of -0.9 and -1.5). See supplementary discussion for the full list of references used for this compilation.

9.6 Methods

9.6.1 Sampling sites

Size-segregated aerosol samples ($PM_{2.5-10}$ and $PM_{2.5}$: particulate matter with aerodynamic diameters between 2.5 and 10 μm and less than 2.5 μm, respectively) were collected at a background mountain site (Mount Wuyi Station, 27.72°N, 117.68°E, 1139 m above sea level) in East China (Figure 9.2) using a high-volume air sampler (TE-6070DV-BLX, Tisch Environmental Inc., USA) equipped with a PM_{10} inlet and a $PM_{2.5}$ impactor. Quartz filters (Whatman, UK) were used and the flow rate was set at ~1.13 m^3 min^{-1}. Static field blanks were created every three months by loading fresh filters on the sampler for approximate one hour without turning on the pump, and were subsequently subjected to the same chemical analysis procedure. This site is a national atmospheric background monitoring station established and operated by the Ministry of Environmental Protection of the People's Republic of China to investigate regional atmospheric compositions in East China. Meteorological parameters (temperature, pressure, relative humidity, and precipitation) and criteria air pollutants (sulfur dioxide, nitrogen dioxide, carbon monoxide, ozone, PM_{10} and $PM_{2.5}$) are monitored and recorded routinely. This background site has negligible local emissions, and therefore, atmospheric and isotopic compositions at this locale represent regional characteristics of East China (see Supplementary Discussion).

Samples of sulfur dioxide (SO_2) and PM_{10} (particulate matters with aerodynamic diameters less than 10 μm) were simultaneously collected at an urban site (South China Institute of Environmental Sciences [SCIES], 23.17°N, 113.21°E, ~70 m above sea level) in Guangzhou, the third largest megacity in China, during the coal-burning season (Figure 9.2). The nearest coal-fired power plant (~1100 MW) is ~16 km from the SCIES. PM_{10} was collected on a quartz filter using a high-volume air sampler operated at a flow rate of ~1.13 m^3 min^{-1}. SO_2 was trapped by a KOH-impregnated quartz backup filter [*Lin et al.*, 2017a] installed in the same sampler.

Coal samples were collected from three coal mines across China: Zhuxianzhuang (site 1), Pingdingshan (site 2), and Cuimu (site 3) (Figure 9.2). The coal from these three sites was formed in three different geological periods (Permian, Carboniferous, and Jurassic, respectively). More than 90% of the total recoverable coal reserves across China were formed in these geological periods [*Dai et al.*, 2012].

9.6.2 Measurement of eight isotopes (^{32}S, ^{33}S, ^{34}S, ^{35}S, ^{36}S, ^{16}O, ^{17}O, and ^{18}O) in sulfates.

Soluble sulfates were extracted from half of each filter using Milli-Q deionized water (18.2 MΩ cm). Because the samples were analyzed approximately 7-8 months after collection (i.e. ~82-86% of ^{35}S atoms decayed), most (>90%) of the solution from each sample was immediately taken for radioactive ^{35}S analysis to assure high-precision determination, while the rest stored in a freezer for subsequent stable isotope measurements. The year-long measurements of ^{35}S in $PM_{2.5}$ were originally reported in our previous paper [*Lin et al.*, 2016c], and additional ^{35}S data for $PM_{2.5-10}$ is presented in this study for the first time to confirm the regional representativeness of the Mount Wuyi Station (see Supplementary Discussion). The ^{35}S analysis followed the aqueous solution method developed by [*Brothers et al.*, 2010] and quality assurance and control protocol described by [*Lin et al.*, 2016a; *Lin et al.*, 2017d]. Organic contaminants and chloride salts in sample solution were removed by a series of cleaning procedures including H_2O_2 oxidation, polyvinylpyrrolidone (PVP), and Ag-Cartridge purifications. The obtained aqueous sulfate solution was mixed with the Insta-Gel Plus scintillation gel (PerkinElmer) in a plastic scintillation vial for high-sensitivity ^{35}S determination using an ultra-low level liquid scintillation spectrometer (Wallac 1220 Quantulus) at the University of California San Diego (UCSD). Each sample was counted for 24 hours (12 cycles, 2-hour counting for each cycle) and their average and one standard deviation are reported. Raw ^{35}S counting data were corrected for background activity and for the decay time. In keeping with atmospheric ^{35}S literature [*Brothers et al.*, 2010; *Lin et al.*, 2017a; *Lin et al.*, 2017b; *Lin et al.*, 2016a; *Lin et al.*, 2016b; *Lin et al.*, 2016c; *Priyadarshi et al.*, 2011a; *Priyadarshi et al.*, 2012a], we

present ^{35}S data as ^{35}S concentration (atoms m^{-3}) and specific activity (atoms per nmol of stable sulfates). The ^{35}S concentration only accounts for radioactive sulfur from the higher atmosphere, while ^{35}S specific activity (^{35}S-SA) further incorporates nonradioactive sulfur emitted from combustion and other sources (e.g., Aeolian dust, sea-salt, and biological sources).

To minimize analytical error, samples with sufficient sulfates (>12 μmol for quadruple sulfur isotopes and >10 μmol for triple oxygen isotopes) were used for stable isotope (^{32}S, ^{33}S, ^{34}S, ^{36}S, ^{16}O, ^{17}O and ^{18}O) analysis. To prevent any inappropriate rejection of samples that have less sulfate but enriched (or depleted) ^{35}S, some samples with sulfates less than optimal amounts were also selected. Therefore, samples reported in this study cover all four seasons in the sampling period (Mar 2014 – Feb 2015) and the full range of ^{35}S variation. An aliquot of sample solution was transferred to a 50-mL boiling flask and organic impurities were removed by adding 2 mL of hydrogen peroxide (30%) [*Shaheen et al.*, 2013; *Shaheen et al.*, 2014]. Regarding SO_2, samples were oxidized to sulfates by dissolving a portion of filter paper in a H_2O_2 solution, and filtered solution was transferred to a 50-mL boiling flask. Subsequently, water-soluble sulfates in solution were quantitatively precipitated to $BaSO_4$ using $BaCl_2$ solution (1.3 M). The boiling flask was dried in a clean oven (120°C) overnight and solid $BaSO_4$ was subsequently reduced to gaseous H_2S in a gently boiling reduction solution (a mixture of 57% hydriodic acid, 50% hypophosphorous acid, and 12M hydrochloric acid). Evolved H_2S was carried by a high-purity nitrogen stream, washed through a Milli-Q deionized water trap, and reacted with cadmium acetate (0.2 M) to form CdS, which will be precipitated as Ag_2S by adding $AgNO_3$ (0.2 M). Ag_2S was subsequently filtered, rinsed with Milli-Q deionized water and NH_4OH (1.0 M), and dried. For coal samples, chromium-reducible sulfur (including monosulfide, pyrite, and elemental sulfur) was extracted and reduced to H_2S using chromium reduction solution, and the evolved H_2S was subsequently converted to Ag_2S following the standard procedure [*Zhang et al.*, 2017a].

Fluorination of Ag_2S and sulfur isotopic measurements were conducted in two independent laboratories: (i) the Stable Isotope Laboratory at the University of Science and Technology of China (USTC), and (ii) the Thiemens Lab at UCSD. In USTC, Ag_2S and a 10-fold excess of F_2 was loaded into a nickel reaction tube and reacted at 250°C for 8 hours to quantitatively convert Ag_2S to SF_6. The SF_6 product was cryogenically purified in a cold trap at -110°C, and further chromatographically purified by a gas chromatography equipped with a molecular sieve 5Å column and a Haysep Q column. The high-purity helium carrier flow was set at 20 mL min^{-1}. The SF_6 peak was registered on a thermal conductivity detector and then isolated by freezing into a liquid-nitrogen cooled trap. The isotopic abundance of the purified SF_6 was analyzed on an isotope ratio mass spectrometer (IRMS) (Thermo Finnigan MAT 253) at USTC. The isotope ratios of quadruple sulfur isotopes (^{32}S, ^{33}S, ^{34}S and ^{36}S) are defined as:

$$\delta^{33}S=[(^{33}S/^{32}S)_{sample}/(^{33}S/^{32}S)_{VCDT}-1]*1000$$

$$\delta^{34}S=[(^{34}S/^{32}S)_{sample}/(^{34}S/^{32}S)_{VCDT}-1]*1000$$

$$\delta^{36}S=[(^{36}S/^{32}S)_{sample}/(^{36}S/^{32}S)_{VCDT}-1]*1000$$

where VCDT stands for the international reference material Vienna Canyon Diablo Troilite and units of $\delta^{33}S$, $\delta^{34}S$ and $\delta^{36}S$ are parts per thousand or "per mil" (‰). Quadruple stable sulfur isotopic mass-independent fractation (S-MIF) or sulfur isotopic anomalies are presented as:

$$\Delta^{33}S=\delta^{33}S-1000*[(1+\delta^{34}S/1000)^{0.515}-1]$$

$$\Delta^{36}S=\delta^{36}S-1000*[(1+\delta^{34}S/1000)^{1.9}-1]$$

Ag_2S standards (International Atomic Energy Agency [IAEA] reference materials) were fluorinated and measured routinely at USTC during the study period. It is assumed that the IAEA S1 has a sulfur isotopic composition on the VCDT scale of $\delta^{34}S$=-0.3‰, $\Delta^{33}S$=0.10‰, and $\Delta^{36}S$=-0.80‰ [*Ueno et al.*, 2008]. Our results match these values as well as recent measurements made in

the University of Maryland [*Zhang et al.*, 2017a] (Table 9.2). Overall uncertainties (1 standard deviation) of $\delta^{34}S$, $\Delta^{33}S$, and $\Delta^{36}S$ in fluorination and isotopic measurements at USTC are less than ±0.2‰, ±0.01‰, and ±0.2‰, respectively. In UCSD, a BrF_5 method was used[*Baroni et al.*, 2007; *Chakraborty et al.*, 2013; *Farquhar et al.*, 2000a; *Shaheen et al.*, 2014]. Ag_2S was transferred to a commercial silver boat and loaded into a nickel tube for fluorination by BrF_5 at 580°C for 12 hours. The SF_6 product was separated from other byproducts and unreacted BrF_5 with 7-stage ethanol slush distillation at −119°C, and it was further purified by a gas chromatography. The purified SF_6 was measured by an IRMS (Thermo Finnigan MAT 253) in the Thiemens Lab at UCSD. Overall uncertainties (1 standard deviation) of $\delta^{34}S$, $\Delta^{33}S$, and $\Delta^{36}S$ in fluorination and isotopic measurements at UCSD are less than 0.2‰, 0.01‰, and 0.2‰, respectively, on the basis of long-term measurements of standard materials[*Shaheen et al.*, 2014]. The uncertainties of $\Delta^{36}S$ in two SO_2 samples (Feb 25 - Mar 1 and Mar 9-13, 2014) are estimated to be 0.4‰ (2 standard deviations) as a result of their small sample sizes.

Table 9.2. Quadruple stable sulfur isotopic compositions in laboratory and international Ag_2S standards measured in this study. Data obtained from University of Maryland (UMD) in a recent study is also included for comparison.

Standard	Amount (μmol)	$\delta^{33}S$ (‰)	$\delta^{34}S$ (‰)	$\delta^{36}S$ (‰)	$\Delta^{33}S$ (‰)	$\Delta^{36}S$ (‰)	Lab
A laboratory standard (commercial Ag_2S) from the Thiemens Lab							
Lab #2	5.3	2.47	4.76	9.08	0.02	0.01	UCSD
Lab #2	5.6	2.58	4.97	9.36	0.02	-0.11	UCSD
Lab #2	5.5	2.49	4.79	8.98	0.02	-0.14	UCSD
Lab #2	5.1	2.67	5.12	9.79	0.03	0.03	UCSD
Lab #2	5.4	2.63	5.06	9.54	0.02	-0.11	UCSD
Average±1σ		2.57±0.09	4.94±0.16	9.35±0.33	0.02±0.01	-0.06±0.08	UCSD
Lab #2	14.8	2.40	4.61	8.59	0.03	-0.18	USTC

Table 9.2. Quadruple stable sulfur isotopic compositions in laboratory and international Ag_2S standards measured in this study. Data obtained from University of Maryland (UMD) in a recent study is also included for comparison (Continued).

Standard	Amount (μmol)	$\delta^{33}S$ (‰)	$\delta^{34}S$ (‰)	$\delta^{36}S$ (‰)	$\Delta^{33}S$ (‰)	$\Delta^{36}S$ (‰)	Lab
International reference materials from the International Atomic Energy Agency (IAEA)							
S1	16.1	-0.08	-0.34	-1.54	0.09	-0.88	USTC
S1	12.1	-0.06	-0.30	-1.35	0.09	-0.79	USTC
S1	13.1	-0.06	-0.33	-1.40	0.11	-0.78	USTC
S1	15.8	-0.05	-0.30	-1.40	0.10	-0.83	USTC
S1	13.7	-0.05	-0.31	-1.28	0.11	-0.69	USTC
Average±1σ		-0.06±0.01	-0.32±0.02	-1.39±0.09	0.10±0.01	-0.79±0.07	USTC
S1		-0.15±0.02	-0.46±0.04	-1.64±0.13	0.09±0.01	-0.76±0.09	UMD

A laboratory Ag_2S standard from the Thiemens Lab was fluorinated and measured in both laboratories during the study period. Samples (one for SO_2 and one for sulfates) with sufficient sulfur were also replicated for full chemistry (reduction, fluorination and isotopic measurements) in both laboratories. The comparison of measured $\Delta^{33}S$ and $\Delta^{36}S$ values shows that differences between two laboratories and replicated experiments are within the analytical uncertainties (Tables 9.2 and 9.3). The high reproducibility of $\Delta^{33}S$ and $\Delta^{36}S$ for the same atmospheric sample in independent laboratories allow us to assure that the measured S-MIF signatures were not an experimental artifact resulted from any unknown S-MIF fractionation process due to the chemically complex matrix in the atmospheric samples.

Table 9.3. Quadruple stable sulfur isotopic compositions in atmospheric sulfate and SO_2 samples measured in this study

Sample	Amount (μmol)	$\delta^{33}S$ (‰)	$\delta^{34}S$ (‰)	$\delta^{36}S$ (‰)	$\Delta^{33}S$ (‰)	$\Delta^{36}S$ (‰)	Lab
Sulfate (in $PM_{2.5}$) collected at the Mount Wuyi Station (from April 2014 to February 2015)							
Apr 2-9	16.7	2.47	4.37	7.75	0.22	-0.57	USTC
May 22-28	8.6	1.50	2.66	4.90	0.14	-0.15	USTC
Jun 11-18	14.1	2.50	4.41	8.04	0.23	-0.35	USTC
Jul 9-16	14.2	0.69	0.88	1.27	0.23	-0.41	USTC
Sep 23-30	15.1	0.91	1.39	2.38	0.19	-0.27	USTC
Sep 30 - Oct 8	13.8	2.31	4.05	7.18	0.22	-0.54	USTC
Oct 8-15	13.7	2.23	3.97	7.08	0.19	-0.47	USTC
Oct 8-15 [a]	16.3	2.30	4.10	7.30	0.19	-0.50	USTC
Oct 8-15 [a]	6.2	2.67	4.80	8.72	0.20	-0.42	UCSD
Oct 15-22	11.2	1.99	3.36	5.57	0.26	-0.82	USTC
Oct 22-29	12.8	1.82	3.02	5.16	0.27	-0.57	USTC
Oct 29 - Nov 5	14.6	1.83	3.04	5.09	0.26	-0.69	USTC
Dec 18-25	11.6	2.22	3.83	5.99	0.25	-1.31	USTC

Table 9.3 Quadruple stable sulfur isotopic compositions in atmospheric sulfate and SO_2 samples measured in this study (Continued)

Sample	Amount (μmol)	$\delta^{33}S$ (‰)	$\delta^{34}S$ (‰)	$\delta^{36}S$ (‰)	$\Delta^{33}S$ (‰)	$\Delta^{36}S$ (‰)	Lab
Jan 14-21	16.6	2.46	4.50	7.76	0.15	-0.80	USTC
Feb 4-11	14.3	2.10	3.79	6.17	0.15	-1.03	USTC
SO_2 collected at Urban Guangzhou (from January to March 2014)							
Jan 21-25	8.8	2.79	5.50	10.65	-0.04	0.17	UCSD
Jan 21-25 [a]	8.0	2.85	5.55	10.89	-0.01	0.31	UCSD
Feb 25 - Mar 1	3.8	3.67	7.17	14.05	-0.01	0.39	UCSD
Mar 5-9	3.7	2.27	4.39	8.51	0.01	0.16	UCSD
Mar 9-13	4.9	2.17	4.22	8.26	-0.04	0.22	UCSD
Sulfate (in PM_{10}) collected at Urban Guangzhou (from January to March 2014)							
Jan 21-25	13.8	2.72	4.85	8.26	0.23	-0.97	USTC
Mar 5-9	5.2	3.08	5.68	10.62	0.16	-0.22	UCSD
Mar 9-13	13.3	2.33	4.24	7.67	0.15	-0.41	USTC

a. Replicate reductions, fluorinations and isotopic measurements.

Triple oxygen isotopic compositions have been recently reported [*Lin et al.*, 2017b], and were used in this study to investigate their possible relationships with quadruple sulfur isotopic compositions. Sulfates in pre-cleaned solution were separated via an ion chromatography and converted to Ag_2SO_4 for pyrolysis in a quartz tube at a temperature of 1030°C using the system developed by [*Savarino et al.*, 2001]. The O_2 gas evolved from the Ag_2SO_4 pyrolysis was purified through a gas chromatography, and its triple oxygen isotopic composition was measured by the IRMS at UCSD. The isotope ratios of triple oxygen isotopes are defined as:

$$\delta^{17}O=[(^{17}O/^{16}O)_{sample}/(^{17}S/^{16}S)_{SMOW}-1] *1000$$

$$\delta^{18}O=[(^{18}O/^{16}O)_{sample}/(^{18}S/^{16}S)_{SMOW}-1] *1000$$

where SMOW stands for the international reference material Standard Mean Oceanic Water and units of $\delta^{18}O$ and $\delta^{17}O$ are ‰. Triple stable oxygen isotopic mass-independent fractation (O-MIF) or oxygen isotopic anomalies are presented as: $\Delta^{17}O=\delta^{17}O-0.52*\delta^{18}O$. Raw $\delta^{18}O$ and $\Delta^{17}O$ data were corrected for the constant isotopic shift associated with the pyrolysis method [*Savarino et al.*, 2001; *Schauer et al.*, 2012]. Replicate analysis of mass-dependent laboratory standards (n=8) showed that the uncertainties (1 standard deviation) of $\delta^{18}O$ and $\Delta^{17}O$ were 0.8‰ and 0.06‰, respectively, through the course of our study period.

Assuming the molar ratio of sulfate to sodium (a sea salt tracer) to be 0.0604 in sea-salt spray, we estimated the sea-salt content in each fine sulfate sample to be less than 1.5% (with an average of 0.9±0.3%) [*Lin et al.*, 2017b]. Therefore, all isotopic compositions reported in this study are not corrected for non-sea-salt sulfates.

9.6.3 Measurements of water-soluble inorganic ions, saccharidic tracers, and carbonaceous species.

A small portion (2.66 cm^2) of each quartz filter for $PM_{2.5}$ was dissolved in Milli-Q deionized water in a glass vial. After ultrasonic agitation for 60 minutes, the filtered extracts were

used to determine concentrations of water-soluble inorganic ions and saccharidic compounds, respectively. Concentrations of cations (Na^+, NH_4^+, K^+, Ca^{2+} and Mg^{2+}) and anions (Cl^-, NO_3^- and SO_4^{2-}) were determined using two ion chromatographies (Dionex ICS-1600 and ICS-2100, respectively). Saccharidic tracers for biomass burning (levoglucosan and mannosan) in the same aerosol samples were quantified by a high-performance anion exchange chromatography with pulsed amperometric detection (HPAEC-PAD) method [*Engling et al.*, 2006; *Iinuma et al.*, 2009] using a Dionex ICS-3000 system with a Dionex CarboPac MA1 analytical column (250 X 4 mm) and a sodium hydroxide eluent. The analytical errors for these two saccharidic compounds are less than 10% (one standard deviation)[*Engling et al.*, 2006; *Iinuma et al.*, 2009]. A small portion (0.526 cm^2) of each quartz filter for $PM_{2.5}$ was punched for determining carbonaceous species using a DRI aerosol carbon analyzer (model 2001, Atmoslytic Inc., CA, USA) following the IMPROVE (Interagency Monitoring of PROtected Visual Environments) thermal/optical reflectance protocol [*Cao et al.*, 2004]. For the analysis of water-soluble organic carbon (WSOC), a punch (2.66 cm^2) was taken from each sample and extracted with 30 mL of Milli-Q deionized water in pre-baked glass bottles via 60-min sonication. The liquid extract was subsequently filtered using a 0.25 mm PTFE syringe filter and WSOC was quantified using a Total Organic Carbon Analyzer (Sievers Model 900, GE Analytical Instruments, USA). The instrument was calibrated with a series of sucrose standards during the analysis period. All measurements were corrected by field blanks.

9.7 Supplementary Discussion

9.7.1 Regional representativeness of the Mount Wuyi Station

A quantitative verification of the Mount Wuyi Station as an atmospheric background station in East China is important to understand the origins of $\Delta^{33}S$ and $\Delta^{36}S$ observed at this site. A previous study focusing on chemical compositions suggested that aerosols collected at this background site are mainly derived from long-range transport [*Su et al.*, 2015]. Here we provide additional isotopic evidence to support the regional representativeness of the Mount Wuyi Station.

Annual ^{35}S concentrations in fine sulfate aerosols in the Mount Wuyi Station (530±470 atoms m^{-3}) were statistically close to those at the Scripps Institution of Oceanography (SIO) pier in California (460±160 atoms m^{-3}) [*Priyadarshi et al.*, 2012a] and Dumont D'Urville (DD'U) in Antarctica (390±250 atoms m^{-3}) [*Priyadarshi et al.*, 2011a]. In contrast, concentrations of ^{35}S in coarse sulfate aerosols in Mount Wuyi Station (from March to June 2014 and from October 2014 to February 2015) are 20±20 atoms m^{-3} (n=29), notably lower than annual averages of SIO(140±60 atoms m^{-3}) [*Priyadarshi et al.*, 2012a] and DD'U (140±60 atoms m^{-3}) [*Priyadarshi et al.*, 2011a]. Because of the single source of cosmogenic ^{35}S in sulfate aerosols (i.e., the SO_2 oxidation) [*Lin et al.*, 2017a] and a shorter lifetime of coarse particles (minutes to days) than fine particles (days to weeks) in the troposphere, the lower ratios of ^{35}S in coarse to fine particles in our sampling site (0.04±0.06) than SIO (0.31±0.11) [*Priyadarshi et al.*, 2012a] and DD'U (0.58±0.50) [*Priyadarshi et al.*, 2011a] suggest that atmospheric sulfates in the Mount Wuyi Station are mainly contributed by long-range horizontal and vertical transport (instead of local primary or secondary formations).

9.7.2 Relationship between ^{35}S and $\Delta^{33}S$

The positive correlation between ^{35}S and $\Delta^{33}S$ suggests that the non-zero $\Delta^{33}S$ is likely originated from an altitude-dependent source. Prior to this study, radioactive and multiple stable sulfur isotopes in sulfate aerosols were only simultaneously measured by Romero and Thiemens[*Romero and Thiemens*, 2003] in two samples collected from White Mountain in California. The sample possessing a greater ^{35}S-SA in their pilot study displays a heavier $\Delta^{33}S$ (0.16‰) than the other (0.10‰), consistent with our higher-sensitivity ^{35}S measurements. Ion-induced binary nucleation of H_2SO_4 and H_2O galactic cosmic rays was recently identified as an important process of new particle formations in the free troposphere [*Kirkby et al.*, 2011]. This process was subsequently found to be mass-dependent in laboratory experiments [*Enghoff et al.*, 2012], and therefore, it could not explain the ^{35}S-$\Delta^{33}S$ relation observed in this study. Because enriched $\Delta^{33}S$ resulted from sulfates produced in the free troposphere is highly unlikely, SO_2

photochemistry in the stratosphere is the most possible mechanism responsible for the S-MIF. The relationship between ^{35}S and $\Delta^{33}S$ is likely non-linear because a portion of ^{35}S in troposphere sulfates is originated from the oxidation of radioactive SO_2 in the troposphere, which is not linked to S-MIF (i.e., enriched ^{35}S but low $\Delta^{33}S$). The age difference of air mass originated from the same altitude (i.e., decayed ^{35}S but the same $\Delta^{33}S$) may also lead to the complex relationship but would not affect our major finding (i.e., positive relationship between ^{35}S and $\Delta^{33}S$) beceause decay lifetime of ^{35}S (~126 days) is significantly longer than the sulfate lifetime in the troposphere (days to weeks).

The regression equation in Fig. 2a cannot be extrapolated to estimate $\Delta^{33}S$ in the stratosphere because (i) ^{35}S-$\Delta^{17}O$ relationships show distinct geographyical variations [*Lin et al.*, 2017b], and (ii) the actual relationship between ^{35}S and $\Delta^{33}S$ outside the range of this study remain unclear. In this study, the estimated fraction of sulfates originating from the UT/LS in samples with $\Delta^{33}S$ greater than 0.25‰ is on the order of <3% based on a mesoscale meteorology model [*Lin et al.*, 2016c] and a ^{35}S-$\Delta^{17}O$ isotopic mixing model [*Lin et al.*, 2017b]. If we assume the $\Delta^{33}S$ value in atmospheric background sulfates in our study region is 0.13‰ (see the main text), the $\Delta^{33}S$ value in stratospheric sulfates in the Asian Tropopause Aerosol Layer is ~4‰ based on linear isotopic mass balance. Romero and Thiemens [*Romero and Thiemens*, 2003] first measured quadruple sulfur isotopes in tropospheric sulfate aerosols and noted that $\Delta^{33}S$ in the stratosphere might be larger than previously thought. $\Delta^{33}S$ and $\Delta^{36}S$ measurements of collected stratospheric sulfate aerosols remain absent, but cryospheric records during stratospheric volcano eruptions extracted from polar regions reveal $\Delta^{33}S$ in stratospheric sulfate aerosols likely do not exceed ~2‰ (Fig. 3 and Supplementary Fig. 2). These $\Delta^{33}S$ values are significantly smaller than laboratory-based SO_2 photochemsitry experiments and were explained by model calculations, which showed that the OH oxidation (a MDF process) dominated over SO_2 photolysis and photo-oxidation (MIF processes) in the stratosphere[*Whitehill et al.*, 2015] and consequently dilute the anomaly.

It is worthwhile noting that the $\Delta^{33}S$ values after the 1997/1998 El Niño, a volcanically quiescence period, are significantly larger than stratospheric volcano eruptions, where volcanic SO_2 was directly injected to the lower stratosphere [*Baroni et al.*, 2007; *Shaheen et al.*, 2014] (Figure 9.5). A notably different $\Delta^{36}S/\Delta^{33}S$ slope (Figure 9.5) and enhanced potassium levels in the same cryogenic samples after the 1997/1998 El Niño indicate that SO_2 was likely produced *in situ* at a higher altitude via photodissociation of OCS emitted from intensive biomass burning (likely a MDF process) and conversion to SO_2 in the mid stratosphere where it was then photolyzed (a MIF process) [*Shaheen et al.*, 2014]. Therefore, a large sulfur isotope anomaly in the stratosphere may be linked to active combustion instead of stratospheric volcano eruption. Massive isotopic effect has been observed in the wavelength-dependent fractionation, which may be governed by electronic excited state perturbation and cannot be simulated by existing computational models [*Chakraborty et al.*, 2014]. It is currently unclear how fine structures of the spectral actinic solar flux at varying altitudes and regions, which is difficult to reproduce in laboratories [*Whitehill et al.*, 2015], affect S-MIF processes. In addition, estimations of $\Delta^{33}S$ of stratospheric sulfate aerosols based on cryospheric records limits in that all cryospheric records currently available are from polar regions, at least as a terminus in transport. Because (i) SO_2 photochemistry experiments (in the presence of O_2) display large positive $\Delta^{33}S$ values in sulfates and negative $\Delta^{33}S$ values in the residual SO_2 [*Whitehill et al.*, 2015], (ii) most SO_2 (and OCS) in the stratosphere were transported from the troposphere of the tropics and subtropics[*Bourassa et al.*, 2012], and (iii) stratospheric air is frequently transported downward at mid-latitudes[*Lin et al.*, 2016a], it is plausible that $\Delta^{33}S$ values of stratospheric sulfates deposited in polar regions (a terminus in poleward transport from the tropics) are much smaller than stratospheric sulfates entrained downward at mid-latitudes (where most of atmospheric sulfate measurements were made) as a result of Rayleigh fractionation of $\Delta^{33}S$ during poleward transport. This view is in consistence with results from a 2-D dynamical/chemical model [*Pavlov et al.*, 2005], although the different mechanism used in that model (SO_3 photolysis, in which the SO_2 acquires positive $\Delta^{33}S$ values) lead to an opposite trend. If this is true, the negative $\Delta^{33}S$ in most sulfates

deposited in the South Pole during volcanically quiescence times [*Shaheen et al.*, 2014] (Fig. 3) can be explained. This hypothesis is also consistent with the decrease of $\Delta^{33}S$ from positive to negative values found in cryospheric records during stratospheric volcano events [*Baroni et al.*, 2007] because more stratospheric SO_2 and sulfates can be transported to the polar regions during stratospheric volcano eruption than volcanically quiescence times. Furthermore, the time-dependent $\Delta^{33}S$ values in cyrospheric records imply that high-resolution samples may possess a greater S-MIF signature than low-resolution samples [*Baroni et al.*, 2007], and therefore, it is not impossible that stratospheric signatures of S-MIF preverved in the polar regions, even for snow-pit samples (time scale: months), were smaller than atmospheric samples (time scale: days).

Our findings highlight the need for further simultaneous measurements of all five isotopes of sulfur in the modern atmosphere at varying geographic locales, especially by aircraft or balloon collections, to understand the spatial sulfur isotopic heterogeneity, which may also have implication for constraining the structure and composition of the Archean atmosphere. The relationship between ^{35}S and $\Delta^{33}S$ in a larger spatial scale can also be investigated by a three-dimensional chemistry transport model incorporating all five sulfur isotopes. Such modeling is beyond the scope of this study.

9.7.3 Determination of $\Delta^{36}S/\Delta^{33}S$ slope

Similar to previous isotopic measurements in tropospheric sulfates (Figure 9.1), a clear relationship between $\Delta^{36}S$ and $\Delta^{33}S$ is not observed in this study (R^2=0.04, n=13) because combustion processes lead to profoundly negative $\Delta^{36}S$ in a portion of samples. It is difficult to fully parse out combustion influences of $\Delta^{36}S$ because the isotopic compositions and $\Delta^{36}S/\Delta^{33}S$ slopes of both S-MIF end-members have never been unambiguously determined. In this study, the annual means of levoglucosan ($PM_{2.5}$) concentrations and the SOR are 41±43 ng m^{-3} and 0.65±0.17, respectively (n=49). Three samples with concentrations of levoglucosan ($PM_{2.5}$) greater than 84 (average+σ) ng m^{-3} and SOR smaller than 0.48 (average-σ), representing aerosol significantly

affected by biomass burning and primary sulfates emitted from coal combustion, possess notably depleted $\Delta^{36}S$ (-1.0±0.2). If these three samples are excluded, a statistically significant $\Delta^{36}S$-$\Delta^{33}S$ relationship (R^2=0.66, n=10) is obtained (Figure 9.5) The $\Delta^{36}S/\Delta^{33}S$ slopes is suggested to be a function of wavelength [*Ono*, 2017] (Figure 9.5) and a direct indicator of the production altitude of mass-independent sulfates from SO_2 photolysis [*Romero and Thiemens*, 2003; *Shaheen et al.*, 2014]. The slope of -4.0 estimated in this study is different from other stratospheric volcano eruptions or massive biomass burning, suggesting a different production altitude of mass-independent sulfates and/or additional influences of combustion. It is noted that three data points during the beginning of the Pinatubo eruption were also exclused from the regression analysis (Figure 9.5) because these samples were affected by the tropospheric Cerro Hudson eruption [*Baroni et al.*, 2007].

The relationships between $\delta^{34}S$ and S-MIF signatures of in modern atmospheric sulfates and geological records are presented in Figures 9.6 and 9.7 but are not interpreted in this study because $\delta^{34}S$ variations in natural samples can be produced by many MDF processes, which are not the focus of this study. The data archive includes sulfates from modern aerosols (including the data in this study) [*Guo et al.*, 2010; *Han et al.*, 2017; *Lee et al.*, 2002; *Romero and Thiemens*, 2003], ice cores and snow pits [*Baroni et al.*, 2008; *Baroni et al.*, 2007; *Lanciki et al.*, 2012; *Shaheen et al.*, 2014], Archean sediments (barites) [*Bao et al.*, 2007; *Busigny et al.*, 2017; *Farquhar et al.*, 2000a; *Montinaro et al.*, 2015; *Muller et al.*, 2016; *Muller et al.*, 2017; *Roerdink et al.*, 2012; *Shen et al.*, 2009; *Ueno et al.*, 2008], volcanic ash [*Bindeman et al.*, 2007],and pyrites (FeS_2) and sulfides (S^{2-}) from different eras in Archean [*Cates and Mojzsis*, 2006; *Farquhar et al.*, 2013; *Farquhar et al.*, 2007; *Guy et al.*, 2012; *Kaufman et al.*, 2007; *Kurzweil et al.*, 2013; *Montinaro et al.*, 2015; *Ono et al.*, 2006a; *Ono et al.*, 2009a; *Ono et al.*, 2009b; *Philippot et al.*, 2007; *Philippot et al.*, 2012; *Shen et al.*, 2009; *Thomassot et al.*, 2015; *Thomazo et al.*, 2009; *Ueno et al.*, 2008; *Wacey et al.*, 2015; *Zerkle et al.*, 2012; *Zhelezinskaia et al.*, 2014].

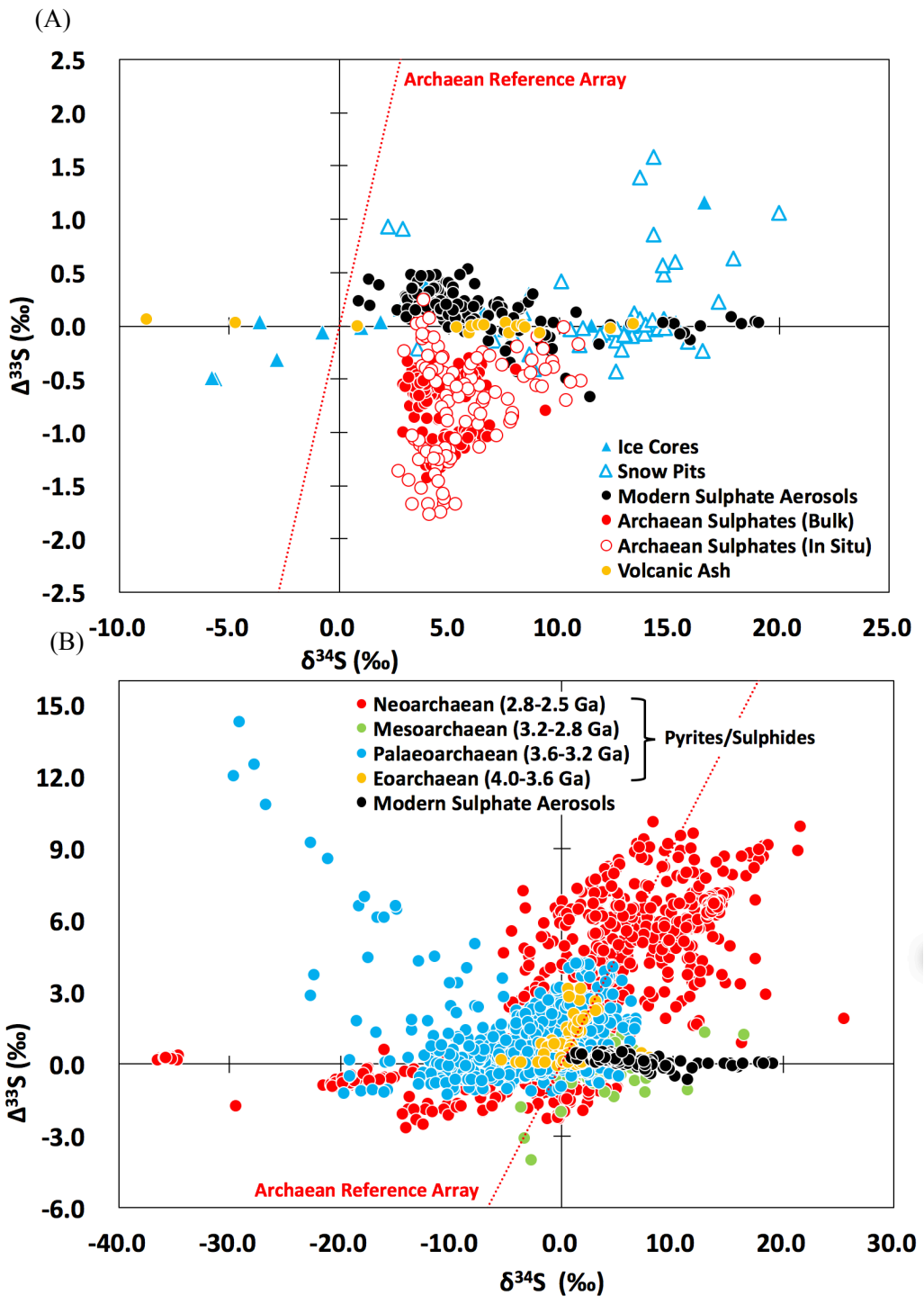

Figure 9.6. Sulfur isotopic compositions ($\Delta^{33}S$ versus $\delta^{34}S$) of a wide variety of terrestrial samples. The red dotted line represents the Archean Reference Array (slope: 0.9).

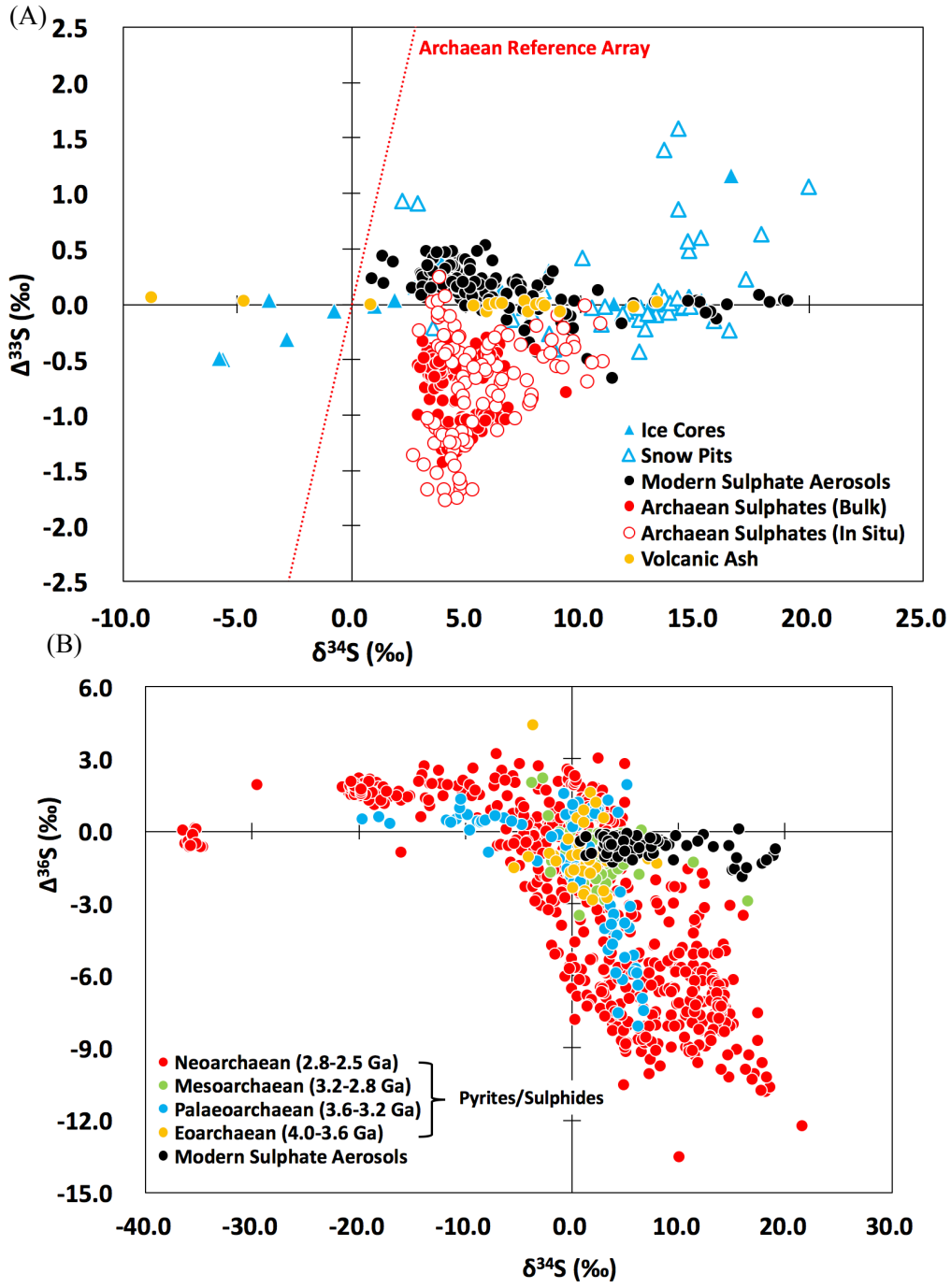

Figure 9.7. Same as Figure 9.6 but for $\Delta^{36}S$ and $\delta^{34}S$. Samples without $\Delta^{36}S$ data are not included.

9.8 Acknowledgements

This study was partially supported by the National Natural Science Foundation of China (41721002, 41475119 and 41603119), and Chinese Academy of Sciences (QYZDY-SSW-DQC031). We appreciate T. Jackson's technical advice and guidance in stable isotope analysis, K. Chen and X. Huang's assistance in stable sulfur isotopic analysis and compiling Archean data, and R. Zhang's assistance in the field work. M. Lin acknowledges a fellowship from the Guangzhou Elite Project (JY201303).

This chapter, in full, has been submitted for publication of the material "Five-S-isotope evidence of two distinct mass-independent sulfur isotope effects and its consequence for the Archean record" as it may appear. Lin, Mang; Zhang, Xiaolin; Li, Menghan; Xu, Yilun; Zhang, Zhisheng; Tao, Jun; Su, Binbin; Liu, Lanzhong; Shen, Yanan; Thiemens, Mark H. The dissertation author was the primary investigator and author of this paper.

Chapter 10 Atmospheric sulfur isotopic anomalies recorded at Mt. Everest across the Anthropocene and implications for the Archean sulfur isotopic record

10.1 Abstract

Anthropogenic induced aerosol concentration enrichment over the Himalayas and Tibetan Plateau in the last century has altered regional climate, accelerated snow/glacier melting, and influenced water supply and quality in Asia, yet the major source of sulfate, a predominant chemical component in aerosols and the hydrosphere, remain contentious. Here, we report multiple sulfur isotope composition of sedimentary sulfates from a remote freshwater alpine lake near the Mount Everest to reconstruct a two-century record of the atmospheric sulfur isotopic anomaly as a probe for sulfur source apportionment and chemical history. We found that sulfur isotopic anomalies surprisingly disappeared after 1930 when sulfate concentrations increased. Along with other elemental measurements, the isotopic proxy suggests that the increased trend of sulfate is mainly attributed to dust-associated sulfate aerosols and climate-induced weathering/erosion, which overprinted the anomalies originating from the background atmosphere. The unique $\Delta^{33}S$-$\delta^{34}S$ pattern in the 19th century, a period with active biomass burning around the globe, is similar to the Paleoarchean (3.6-3.2 Ga) barite record, providing a deeper insight into sulfur thermal reactions and volcanic influences on the Earth's earliest sulfur cycle.

10.2 Introduction

The Himalayas and Tibetan Plateau (HTP), the largest and highest plateau on the Earth, is climatically unique and important due to its location, topography, and teleconnection with other parts of the world [*An et al.*, 2001]. It hosts the largest number of glaciers outside the polar regions and thousands of lakes, and is commonly referred to as the "Third Pole". The ice and lake sediment cores from this mid-latitude region provide valuable paleo-climatic and paleo-atmospheric records

that cannot be obtained from polar regions [*Grigholm et al.*, 2015; *Kang et al.*, 2016b; *Kaspari et al.*, 2009; *Thompson et al.*, 2000]. The HTP is also known as the "Asian water tower" because snow and glacier melting in this region sustains water availability for major rivers in Asia and >1.4 billion people [*Immerzeel et al.*, 2010; *Pritchard*, 2017]. Significant increases in aerosol loading over this region have been altering the atmospheric/glacial chemical composition, snow/glacier melting rate, and glacial river water quality [*Immerzeel et al.*, 2010; *Kang et al.*, 2016b; *Li et al.*, 2016]. Sulfate is one of the major aerosol components but the relative contributions of varying sources (e.g., combustion, mineral dust) and its mixing state in aerosols remain uncertain because measurements of source-specific tracers in sulfates are absent. This fragmentary understanding limits our ability to accurately quantify the aerosol budget and evaluate its influences on climate and hydrological systems.

The sulfur isotopic anomaly (or mass-independent fractionation, MIF) is quantified by non-zero $\Delta^{33}S$ and/or $\Delta^{36}S$ values, where $\Delta^{33}S=\delta^{33}S-1000\times[(1+\delta^{34}S/1000)^{0.515}-1]$ and $\Delta^{36}S=\delta^{36}S-1000\times[(1+\delta^{34}S/1000)^{1.9}-1]$) (Materials and Methods). In the modern atmosphere, sulfate directly emitted from combustion or secondarily produced from photolytic oxidation of stratospheric SO_2 are the only two known types of isotopically anomalous sulfates [*Guo et al.*, 2010; *Han et al.*, 2017; *Lee et al.*, 2002; *Romero and Thiemens*, 2003; *Shaheen et al.*, 2014]. Other sulfates (e.g., terrigenous sulfate in mineral dust, secondary sulfate produced in the troposphere via SO_2 oxidation) are all isotopically normal ($\Delta^{33}S\approx0‰$) [*Guo et al.*, 2010; *Han et al.*, 2017; *Harris et al.*, 2013a; *Lee et al.*, 2002; *Romero and Thiemens*, 2003; *Shaheen et al.*, 2014]. This unique isotopic fingerprinting has been utilized in reconstructing changes in sources and chemical formation pathways of sulfates in the past atmosphere using ice/snow samples obtained from polar regions [*Shaheen et al.*, 2014], but the difficulty of drilling ice cores at Himalayas in terms of the harsh environment at high altitudes (>6500 m above sea level) [*Kaspari et al.*, 2009; *Thompson et al.*, 2000] hampers such studies in this region. Here we provide multiple sulfur isotopic analysis in a

200-year Himalayan lake sediment core (Materials and Methods) to gain insight into the change of sulfur source in this climatically sensitive and important region. As a part of the world's highest freshwater lake system, this remote lake is significantly different from many saline lakes on the HTP [*Sharma et al.*, 2012]. The low background sulfate concentration and low biological activity renders this alpine lake an ideal site to reconstruct regional atmospheric sulfur cycle and potentially to record climate-induced changes in weathering/erosion within the glacial hydrological system.

10.3 Atmospheric sulfur isotopic compositions in the central HTP

We first report $\Delta^{33}S$ (and $\Delta^{36}S$) values in sulfate aerosols (in total suspend particles, TSP) collected at the central HTP (Materials and Methods) to gain an overview of the atmospheric sulfur isotopic anomalies in this arid region (Figure 10.1). Because mineral dust or local soil accounts for ~3/4 of TSP at our sampling site [*Kang et al.*, 2016a] and sulfate derived from this terrigenous source is isotopically normal ($\Delta^{33}S$=0‰), the observed $\Delta^{33}S$ values (ranging from 0.05‰ to 0.12‰) are less than most sulfate aerosols collected at mid-latitudes [*Guo et al.*, 2010; *Han et al.*, 2017; *Romero and Thiemens*, 2003]. A first-order estimation based on isotopic mass balance yields a $\Delta^{33}S$ value of non-dust sulfate to be 0.36±0.12‰. This estimation is at the higher end of the $\Delta^{33}S$ range of currently measured tropospheric sulfate aerosols (maximum: ~0.6‰) [*Guo et al.*, 2010; *Han et al.*, 2017; *Romero and Thiemens*, 2003], likely because the HTP is frenquently affected by the downward transport of stratospheric air [*Lin et al.*, 2016b], which contains stratsopheric sulfates with positive $\Delta^{33}S$ values [*Guo et al.*, 2010; *Han et al.*, 2017; *Romero and Thiemens*, 2003]. Such a large anomaly cannot be explained by mass-dependent fractionation (MDF) processes resulting from slight differences in MDF exponents of varying SO_2 oxidation pathways in the troposphere, which only lead to small variations of $\Delta^{33}S$ (±0.1‰) [*Harris et al.*, 2013a]. Regression analysis of our data displays a $\Delta^{36}S/\Delta^{33}S$ slope of -1.9±0.8 (Figure 10.1), which is close to the Archean array (between 0.9 and 1.5) and therefore further confirms the predominant role of MIF processes.

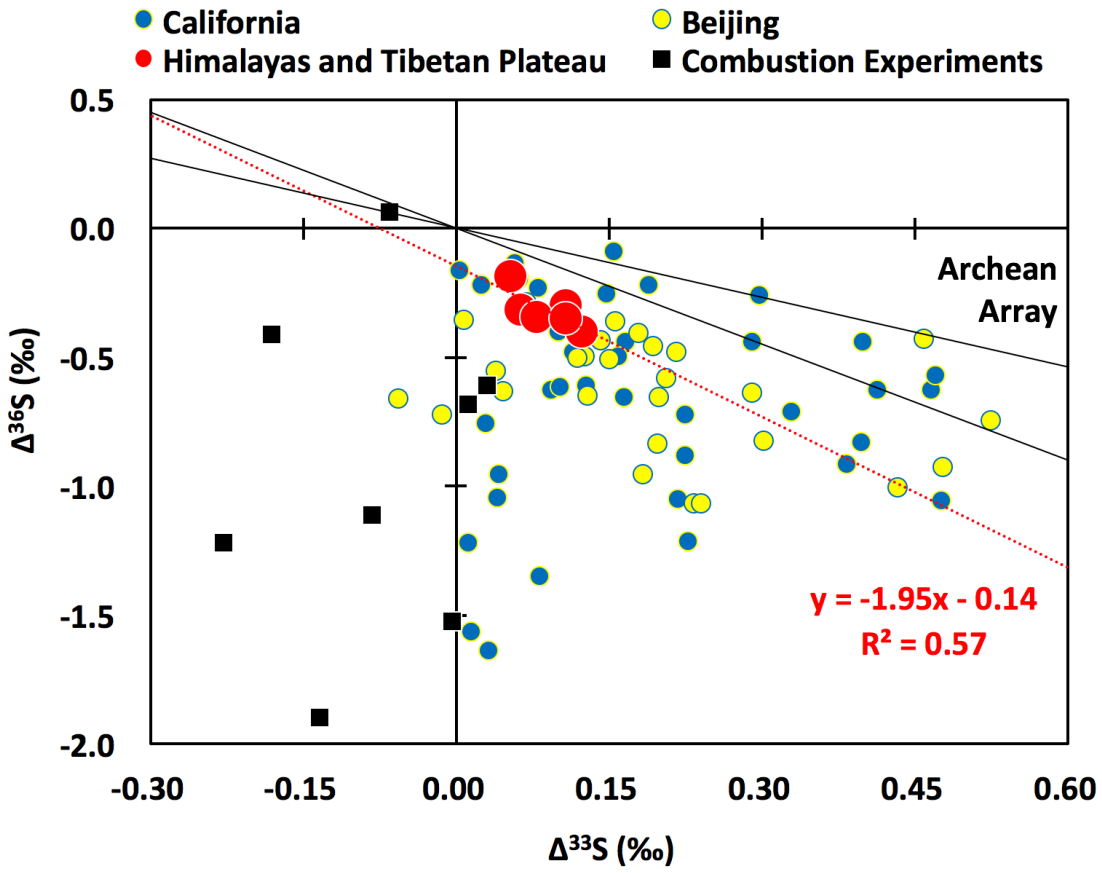

Figure 10.1. $\Delta^{33}S$ and $\Delta^{36}S$ in sulfate aerosols collected at the HTP. $\delta^{34}S$ values (ranging from 3.0‰ to 6.7‰) are reported in supplementary information. $\Delta^{33}S$ and $\Delta^{36}S$ values of tropospheric sulfate aerosols collected at California and Beijing, and primary sulfate aerosols emitted from biomass and fossil fuel combustion experiments are also shown in this figure. The red dotted and black solid lines represent the regression line of this study and the Archean array (slopes: 0.9-1.5), respectively.

10.4 Two-century record of atmospheric sulfur isotopic anomalies

The sulfur isotopic analysis of post-1930 lake sediments (n=8) display zero $\Delta^{33}S$ values within analytical error (±0.01‰) (Figure 10.2 and Materials and Methods), likely a result of a larger contribution of mineral dust to TSP in the Himalayas than the central HTP as noted by previous aerosol and ice core studies [*Grigholm et al.*, 2015; *Liu et al.*, 2017] and in part supported by near-zero $\Delta^{33}S$ values in glacial snow and river sulfates (0.03 and 0.02‰, respectively) collected at the Mt. Everest in this study (Materials and Methods). The isotopically normal sulfates may also originate from the weathering process of parent rocks, which is supported by (i) the low enrichment factors of major, trace, and rare earth elements, and (ii) the observed stable lead isotopic composition ($^{206}Pb/^{207}Pb$ and $^{208}Pb/^{207}Pb$) that is nearly identical to soils and river sediments over the HTP [*Cong et al.*, 2011; *Tan et al.*, 2014] (Figures 10.3 and 10.4).

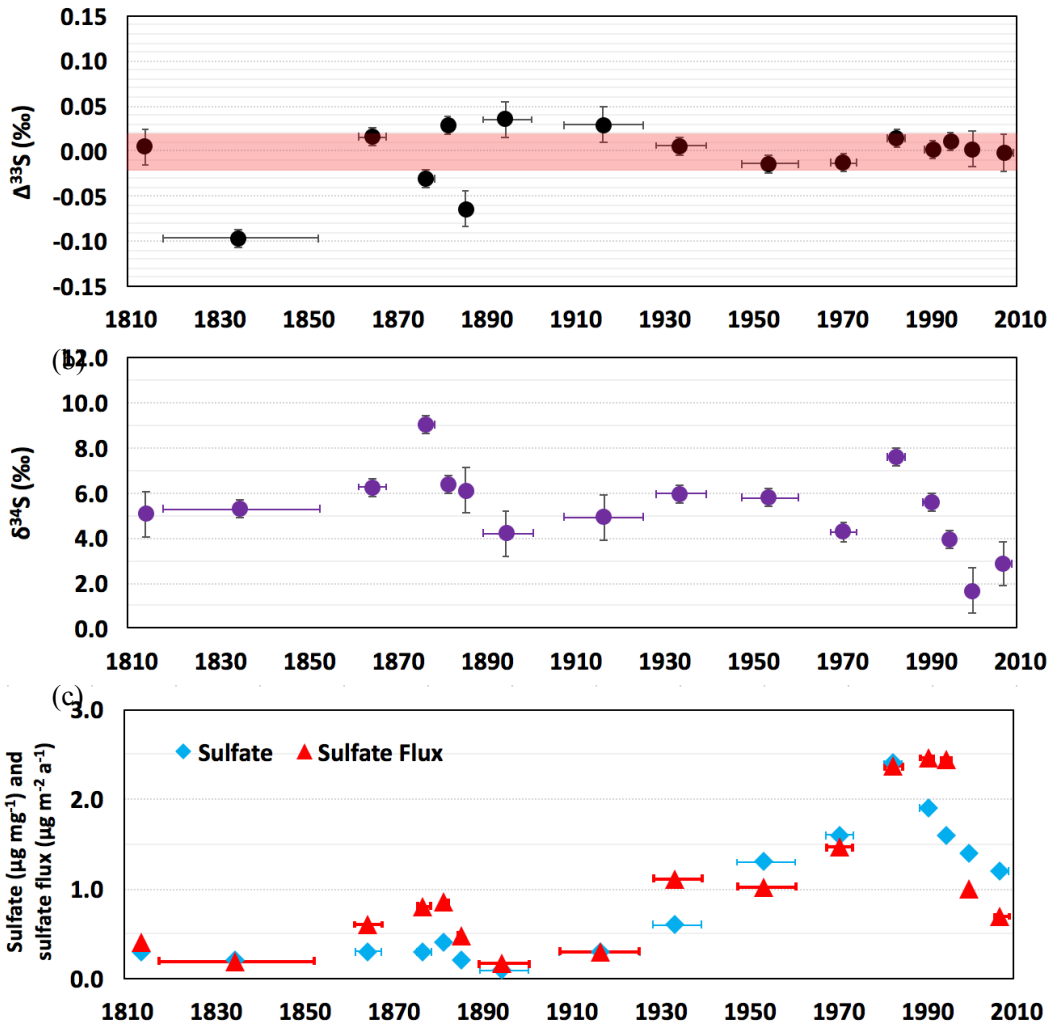

Figure 10.2. Time series of (a) $\Delta^{33}S$, (b) $\delta^{34}S$, and (c) sulfate concentration and flux. The ^{210}Pb-estimated age was obtained from Kang et al. Vertical errors bars represent one standard deviation uncertainties made on the basis of reproducibility of the laboratory standard with varying sample sizes (see Methods). Horizontal errors bars represent the ^{210}Pb-estimated age range of the combined sediment samples. The red shaded area between -0.02‰ and 0.02‰ in Figure 10.2a represents the mass-dependent field. Points distinguished from this field are interpreted to be sulfur isotopic anomalous (see text for details).

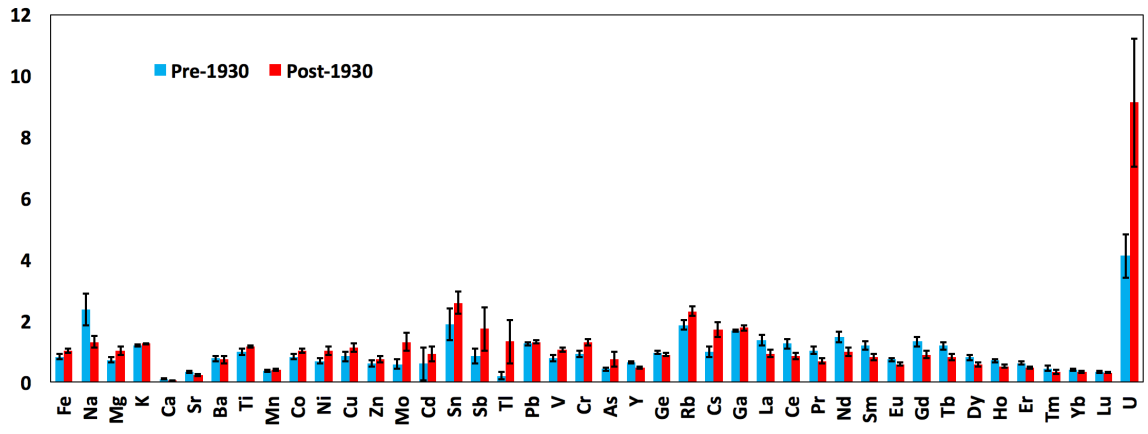

Figure 10.3. Enrichment factors of various elements measured in the sediment core. Error bars stand for one standard deviation.

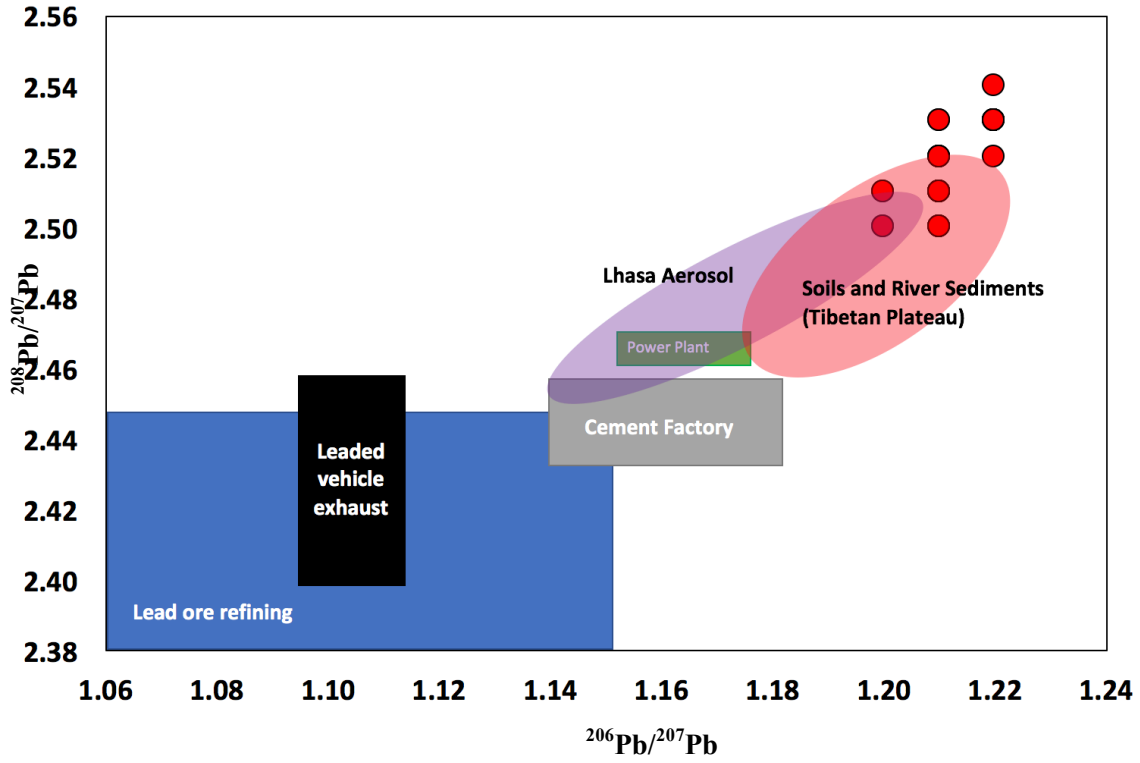

Figure 10.4. Multiple stable lead isotopic composition in the sediment core (red dots) and various sources. The lead isotopic composition of soils and river sediment are obtained from [*Cong et al.*, 2011; *Tan et al.*, 2014].

In contrast, most sulfate samples (6 of 8) deposited in the pre-1930 period display small but distinguishable non-zero $\Delta^{33}S$ values (at the 2σ level) (Figure 10.2), which may not be an

analytical artifact because multiple laboratory controls throughout the study period show that the measured $\Delta^{33}S$ values are highly reproducible (see Materials and Methods and Table 10.1). To attribute these small $\Delta^{33}S$ values to MIF processes, one should quantify the contribution from MDF processes. Slight differences in MDF exponents in various microbial sulfur reduction/disproportionation processes may produce small $\Delta^{33}S$ values (and large variations of $\delta^{34}S$) as those observed in geological samples of Phanerozoic age [*Ono et al.*, 2006b; *Zhang et al.*, 2017a]. However, the small $\delta^{34}S$ variation in our sedimentary sulfates (Figure 9.2), absence of acid volatile sulfide in all samples (Materials and Methods), and zero $\Delta^{33}S$ values (within ±0.01‰) in all post-1930 samples indicate that such MDF processes are negligible in this oligotrophic lake [*Sharma et al.*, 2012] and could not explain the observed non-zero $\Delta^{33}S$ values in the pre-1930 period. The origin of these non-zero $\Delta^{33}S$ values is therefore attributed to MIF signatures in atmospheric sulfates deposited in lake sediments.

Table 10.1. Replicated analysis of multiple sulfur isotopic composition of a UCSD laboratory Ag_2S during the course of this study. $\Delta^{33}S$ and $\Delta^{36}S$ values were calculated using raw data (three decimal places), and rounded to two decimal places and reported. Missing ^{36}S data arise from unreliable results for small sizes of samples.

Control ID	**Amount (μmol)**	**$\delta^{33}S$ (‰)**	**$\delta^{34}S$ (‰)**	**$\delta^{36}S$ (‰)**	**$\Delta^{33}S$ (‰)**	**$\Delta^{36}S$ (‰)**
1	5.6	2.63	5.06	9.51	0.03	-0.12
2	5.6	2.58	4.97	9.36	0.02	-0.11
3	5.5	2.49	4.79	8.98	0.02	-0.14
4	5.4	2.63	5.06	9.54	0.02	0.01
5	5.3	2.47	4.76	9.08	0.02	0.03
6	5.1	2.67	5.12	9.79	0.03	0.07
7	4.6	2.24	4.33	8.31	0.01	-0.15
8	2.9	2.46	4.74	8.87	0.01	-0.15
9	2.7	2.12	4.06	7.61	0.03	-0.11
10	2.7	2.27	4.36	8.40	0.03	0.10
Average	**(>2.5 umol)**	**2.45**	**4.72**	**8.95**	**0.02**	**-0.05**
STD	**(>2.5 umol)**	**0.19**	**0.36**	**0.67**	**0.01**	**0.10**

Table 10.1. Replicated analysis of multiple sulfur isotopic composition of a UCSD laboratory Ag_2S during the course of this study. $\Delta^{33}S$ and $\Delta^{36}S$ values were calculated using raw data (three decimal places), and rounded to two decimal places and reported. Missing ^{36}S data arise from unreliable results for small sizes of samples. (Continued)

Control ID	**Amount (μmol)**	**$\delta^{33}S$ (‰)**	**$\delta^{34}S$ (‰)**	**$\delta^{36}S$ (‰)**	**$\Delta^{33}S$ (‰)**	**$\Delta^{36}S$ (‰)**
11	2.4	2.86	5.51	-	0.03	-
12	2.2	2.26	4.42	-	-0.01	-
13	2.1	2.18	4.14	-	0.05	-
14	1.9	3.37	6.43	-	0.06	-
15	1.7	1.83	3.45	-	0.05	-
16	1.5	2.14	4.08	-	0.04	-
17	1.3	2.49	4.73	-	0.03	-
Average	**(<2.5 umol)**	**2.44**	**4.68**	**-**	**0.03**	**-**
STD	**(<2.5 umol)**	**0.52**	**1.00**	**-**	**0.02**	**-**

The most striking finding of this study is the disappearance of non-zero $\Delta^{33}S$ values in ~1930, when sulfate concentrations started to rise (>0.5 μg mg^{-1}) (Figure 10.2). Simultaneous increasing trends for Hg, U, Mo, Sb, and Tl (Figure 10.5) indicate that the increased sulfates are likely anthropogenic. The disappearance of the sulfur isotopic anomaly provides strong observational evidence that sulfate directly emitted from combustion (or secondarily produced from photolytic oxidation of stratospheric SO_2) is a highly unlikely source because they possess non-zero $\Delta^{33}S$ values as observed in the Pacific Rim [*Guo et al.*, 2010; *Han et al.*, 2017; *Romero and Thiemens*, 2003], South Pole [*Shaheen et al.*, 2014], and combustion experiments [*Lee et al.*, 2002]. As discussed, the Himalayas are strongly affected by dust aerosols [*Grigholm et al.*, 2015; *Liu et al.*, 2017], and the increased trend of sulfate is therefore likely attributed to two types of dust-associated sulfate aerosols ($\Delta^{33}S \approx 0‰$): (i) secondary sulfate produced from transition metal ion catalysis oxidation of anthropogenic emitted SO_2 on the surface of mineral dust [*Harris et al.*, 2013b], which is supported by declining $\delta^{34}S$ values in recent ~30 years (Figure 10.2), and/or (ii) terrigenous sulfate in anthropogenic emission of mineral particles from south Asia (Figure 10.6) [*Philip et al.*, 2017]. Another important source of isotopically normal sulfate that diluted/overprinted the MIF signature is strong weathering/erosion in this Himalayan glacial hydrological system in the post-1930 period as revealed by various weathering indices and Hf in the same sediment core (Figures 10.5 and 10.7), which is linked to pronounced warming trends, enhanced precipitation, and glacier melting [*Kaspar et al.*, 2008; *Rogora et al.*, 2003; *Salerno et al.*, 2016]. Our interpretation is independently supported by the Positive Matrix Factorization model (Materials and Methods): the relative contributions of background atmosphere to sediment samples decreased from 65±20% in the pre-1930 period to 10±11% in the post-1930 period; relatively contributions of anthropogenic influences and weathering/erosion (14±9% and 20±14%, respectively) in the pre-1930 period enhanced to 45±14% and 45±10%, respectively, in the post-1930 period (Figure 10.8 and 10.9).

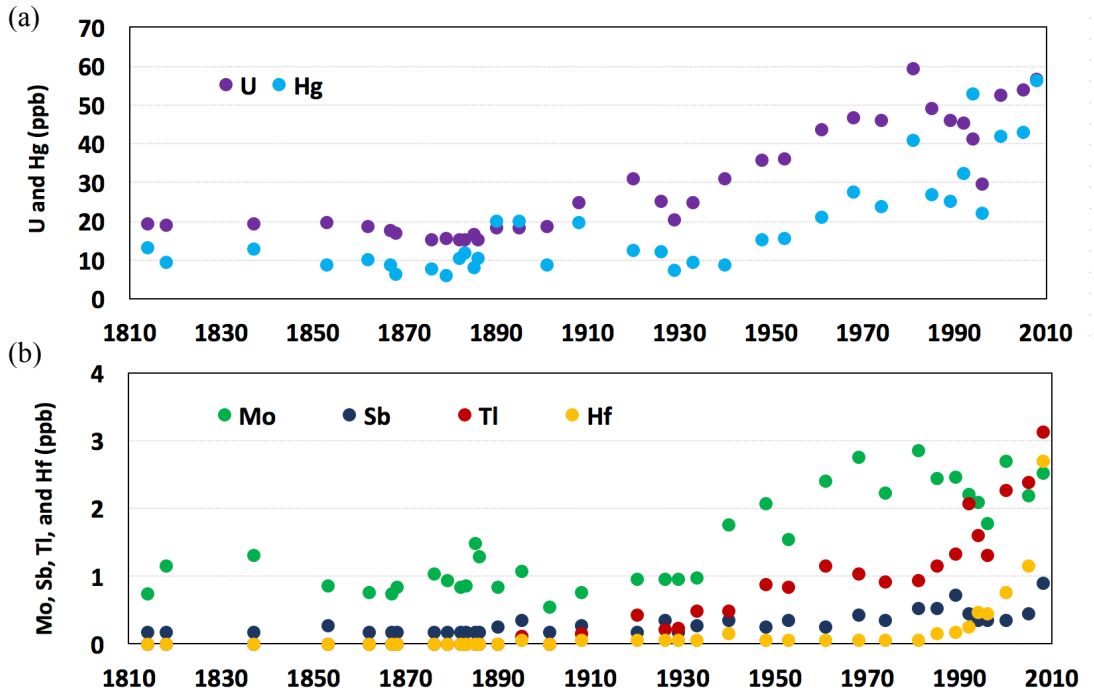

Figure 10.5. Time series of (a) U and Hg, (b) Mo, Sb, Tl and Hf. The ^{210}Pb-estimated age and Hg concentrations were obtained from Kang et al. These elements are selected out of 49 measured elements because their concentration ratios of the post-1930 to pre-1930 periods are greater than 2.

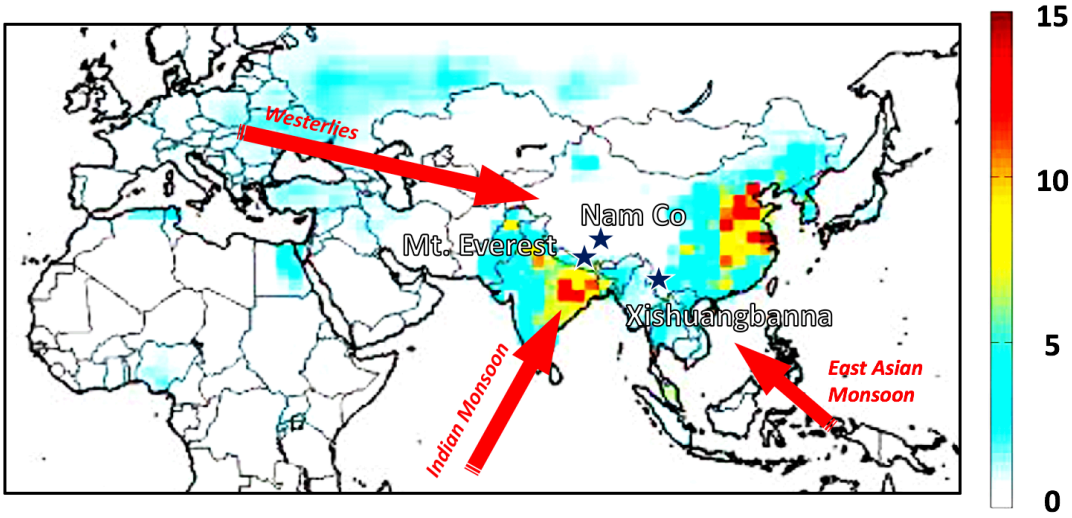

Figure 10.6. Locations of sampling sites (stars). The base map is reproduced from [Kaspari et al., 2009] and [Philip et al., 2017]. The color scales display concentrations of anthropogenic dust (in $PM_{2.5}$) (unit: $\mu g\ m^{-3}$) simulated by the GEOS-Chem global chemistry transport model [Philip et al., 2017]. The concentration of anthropogenic dust in coarse mode is expected to be greater. The arrows indicate the generalized atmospheric circulation in the study area [Kaspari et al., 2009].

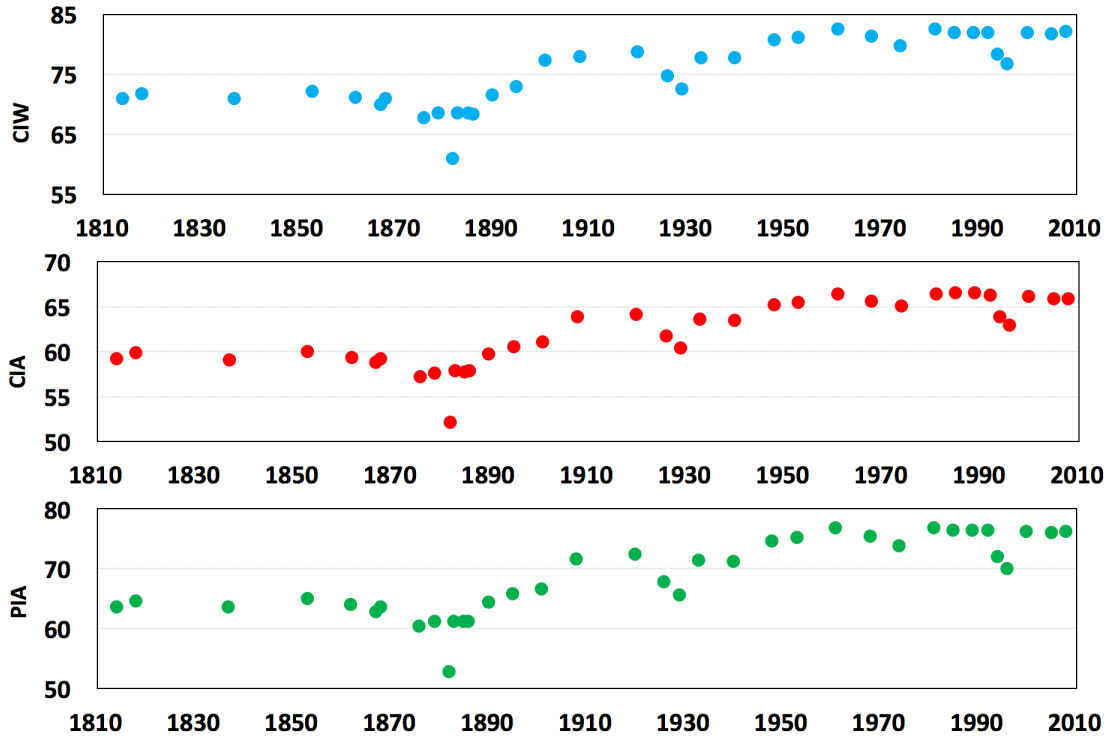

Figure 10.7. Time series of various weathering indices. CIW (Chemical Index of Weathering; upper panel), CIA (Chemical Index of Alteration; middle panel), and PIA (Plagioclase Index of Alteration; lower panel) were calculated using the equations $CIA=[Al_2O_3/(Al_2O_3+CaO+Na_2O+K_2O)]\times100$, $CIW=[Al_2O_3/(Al_2O_3+CaO+Na_2O)]\times100$, $PIA = [(Al_2O_3-K_2O)/(Al_2O_3+CaO+Na_2O-K_2O)]\times100$, respectively, where Al_2O_3, CaO, Na_2O and K_2O were given in molecular proportions.

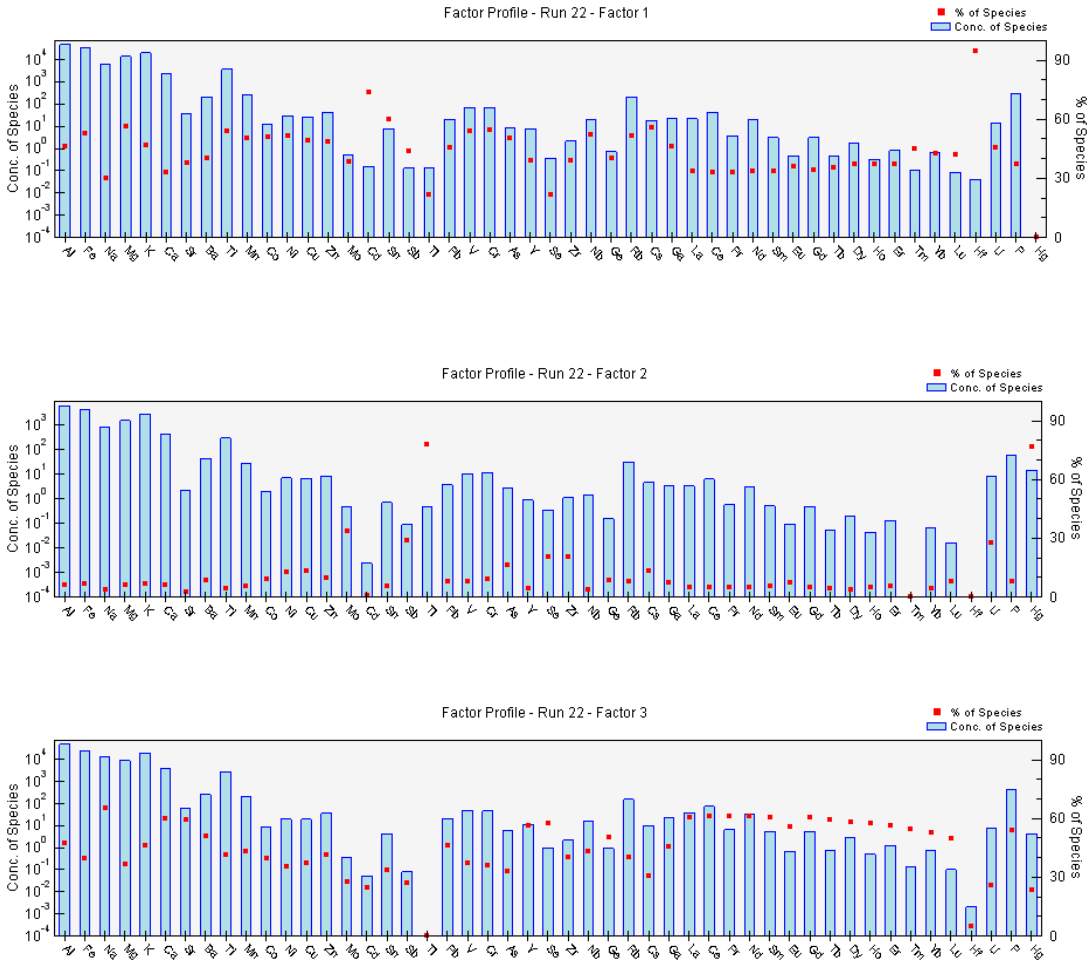

Figure 10.8. Three source profiles (blue bars; unit: ppb) and contribution percentages (red dots; unit: %) resolved by the PMF model. The upper, middle, and lower panels present factors 1 (weathering), 2 (anthropogenic influences), and 3 (background atmosphere), respectively.

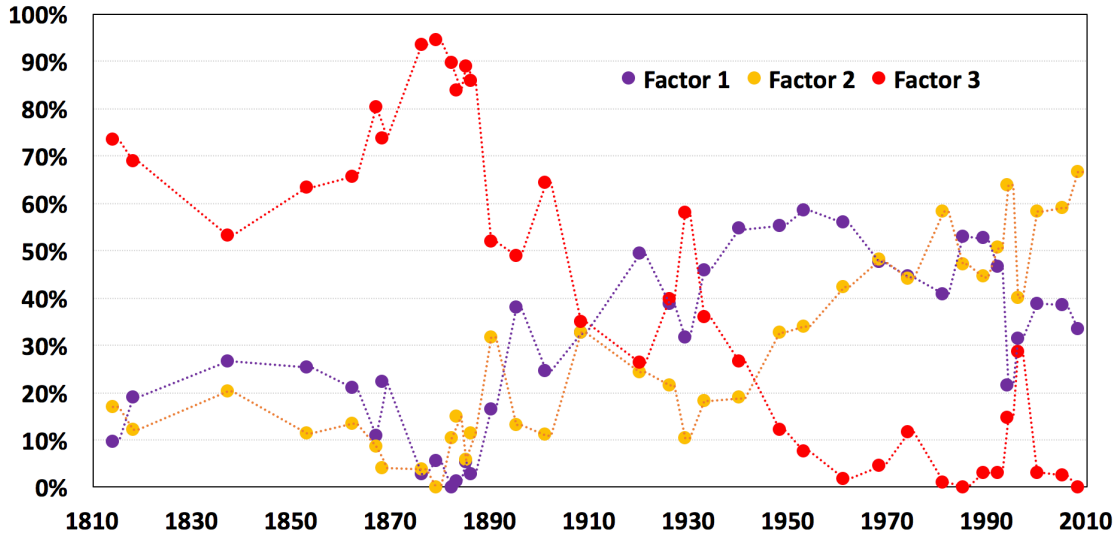

Figure 10.9. Three source profiles (blue bars; unit: ppb) and contribution percentages (red dots; unit: %) resolved by the PMF model. The purple, orange, and red dots present factors 1 (weathering), 2 (anthropogenic influences), and 3 (background atmosphere).

Dust-associated sulfates have been receiving increasing attention because of their ability to alter physical/chemical properties of dust [*Harris et al.*, 2013b]. The sulfur isotopic composition presented in this study highlights the role of dust-associated sulfate in enhancing sulfate levels in the Himalayas in the last century. This finding can improve our understanding how historical and future changes in the coupling of sulfur and dust emissions affect radiative forcing, glacier surface albedo, and snow/glacier melting over the HTP [*Duan et al.*, 2017; *Sokolik and Toon*, 1996; *Zhang et al.*, 2017b].

10.5 Possible origins of negative $\Delta^{33}S$ values

Three samples in the 19th century possess negative $\Delta^{33}S$ values and the largest anomaly ($\Delta^{33}S$=-0.10±0.01‰) is found in sulfates deposited from ~1818 to ~1853 (Figure 10.2). The negative values are surprising in that they contrast with positive $\Delta^{33}S$ values in most sulfate aerosols (101 of 118) collected at mid-latitudes (including the HTP) (Figure 10.10). Large positive $\Delta^{33}S$ values found in sulfates produced from laboratory SO_2 photochemistry experiments (in the presence of O_2) [*Ono*, 2017] indicate that the observed positive $\Delta^{33}S$ values in most tropospheric sulfate aerosols are likely attributed to the frequent downward transport of stratospheric sulfates at mid-latitudes, which have been noted by previous studies [*Guo et al.*, 2010; *Han et al.*, 2017; *Romero and Thiemens*, 2003]. However, negative $\Delta^{33}S$ values measured in this study and recently observed in urban Beijing during a highly polluted season with active industrial/residential coal combustion and minimal stratospheric influences (-0.21±0.19‰; minimum: -0.66‰) [*Han et al.*, 2017] are not expected, indicating that an additional MIF process may be required.

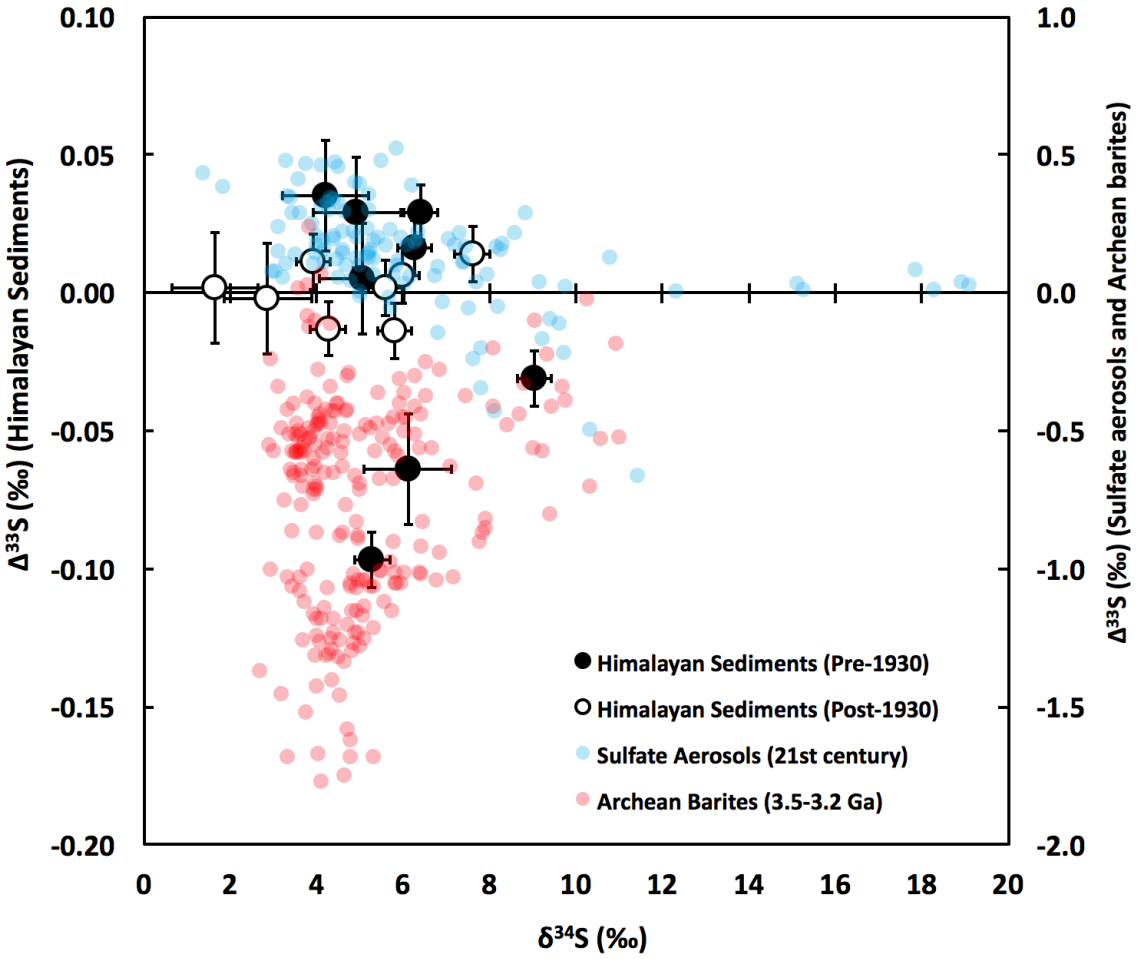

Figure 10.10. Stable sulfur isotopic compositions in sulfates extracted from the Himalayan sediment core, modern aerosols, and Archean barites. Modern aerosol data (Blue) is obtained from this study and [Guo et al., 2010; Han et al., 2017; Romero and Thiemens, 2003]. The Archean barite data (Red) is obtained from [*Bao et al.*, 2007; *Busigny et al.*, 2017; *Farquhar et al.*, 2000a; *Montinaro et al.*, 2015; *Muller et al.*, 2016; *Muller et al.*, 2017; *Roerdink et al.*, 2012; *Shen et al.*, 2009; *Ueno et al.*, 2008]. Note that the $\Delta^{33}S$ values for sediment samples are one order of magnitude smaller than aerosol and barite data because the signature of sulfur isotopic anomaly is greatly diluted by isotopically normal sulfates as discussed in the main text.

Combustion is a highly likely candidate [*Han et al.*, 2017; *Shaheen et al.*, 2014] because negative $\Delta^{33}S$ values (as low as -0.23‰) have been observed in the primary sulfates emitted from combustion [*Lee et al.*, 2002] (Figure 10.1). The fundamental chemical physics remain inadequately described, but recombination of elemental sulfur shown by a pilot theoretical study [*Babikov*, 2017] is the most likely mechanism because it is a strictly thermal reaction and in sulfur combustion there is a number of reactions relevant to this mechanism [*Gardiner*, 2000]. Global lake sedimentary charcoal records, including the one retrieved from the southeast HTP (Figure 10.11), have shown that the 19th century is a period with active biomass burning around the globe, especially in the northern hemisphere extra-tropics [*Marlon et al.*, 2008]. Therefore, it is highly likely that the negative $\Delta^{33}S$ values observed in the 19th century is attributed to primary sulfates directly emitted from intensive biomass burning. The active biomass burning may also provide consistent sources of carbonyl sulfide for producing stratospheric SO_2 that can be photolyzed and oxidized to isotopically anomalous sulfates [*Shaheen et al.*, 2014]. We do not rule out the possibility that this pathway may contribute in part to the observed non-zero $\Delta^{33}S$ values as the Himalayas are a global hotspot for stratospheric intrusions [*Lin et al.*, 2016b] though the detailed chemistry and transport mechanism required further modeling in the future. Alternatively, because deposition of isotopically anomalous sulfates of stratospheric volcanic origins occurs within several years after eruptions [*Shaheen et al.*, 2014], stratospheric volcanic events (e.g., Tambora in 1815, Cosigüina in 1835) only play a minor role, if any, in contributing to the most negative $\Delta^{33}S$ value observed from ~1818 to ~1853.

Figure 10.11. Quantity of charcoal particles in a sediment core drilled at an alpine lake located at the southeastern HTP. The location of this alpine lake (Xixiangbanna) is shown in Figure. 10.6**.** Data is obtained from the Global Charcoal Database (http://www.paleofire.org).

10.6 Implications for sulfur isotope records from 3.5–3.2-billion-year-old rocks

The sulfur isotopic anomaly in Archean (~4 to ~2.5 Ga) sediments is strong evidence of an anoxic atmosphere and a proxy for understanding the evolution of atmospheric oxygen and early life on primitive Earth [*Lyons et al.*, 2014], but corresponding biogeochemical processes are not fully understood [*Shaheen et al.*, 2014]. An interesting facet of our new data is that the unique $\Delta^{33}S$-$\delta^{34}S$ pattern in the pre-1930 period is similar to published Archean barite ($BaSO_4$) data (Figure 10.10), although the magnitude is smaller because present-day sediments contain a large amount of isotopically normal sulfates. Archean barites are only observed in a relatively short period (3.5-3.2 Ga) and are characterized by a narrow range of positive $\delta^{34}S$ values (from ~3‰ to ~11‰) and negative $\Delta^{33}S$ values of -0.75±0.39‰ (n=224) [*Bao et al.*, 2007; *Busigny et al.*, 2017; *Farquhar et al.*, 2000a; *Montinaro et al.*, 2015; *Muller et al.*, 2016; *Muller et al.*, 2017; *Roerdink et al.*, 2012; *Shen et al.*, 2009; *Ueno et al.*, 2008], notably different from the Archean pyrite (FeS_2) and sulfide

(S^{2-}) records (-40‰$\leqslant\delta^{34}S\leqslant$25‰; -4‰$\leqslant\Delta^{33}S\leqslant$15‰) [*Ono*, 2017]. It has been a mystery why the oxidized form of sulfur can exsit in the anoxic atmosphere and its unique isotopic composition may represent a combined result of atmospheric, oceanic and microbial processes [*Muller et al.*, 2016]. It is widely accepted that the Paleoarchean (3.6-3.2 Ga) was strongly affected by active volcanism [*Philippot et al.*, 2012] and negative $\Delta^{33}S$ values in barite deposits is likely an isotopic fingerprinting that sulfate is produced from photolytic reactions of SO_2 allowed by an anoxic atmosphere at that time [*Bao et al.*, 2007; *Busigny et al.*, 2017; *Farquhar et al.*, 2000a; *Montinaro et al.*, 2015; *Muller et al.*, 2016; *Muller et al.*, 2017; *Roerdink et al.*, 2012; *Shen et al.*, 2009; *Ueno et al.*, 2008]. However, the deviation of $\delta^{34}S$ from the expected photochemical array is debated and explained by various concept models such as microbial sulfate reduction [*Roerdink et al.*, 2012], different atmospheric composition (i.e., wavelength-dependent MIF effects) [*Muller et al.*, 2016], and/or mixing of varying sulfur reservoirs [*Ueno et al.*, 2008].

Our observation of Paleoarchean-barite-like $\Delta^{33}S$-$\delta^{34}S$ pattern in an oxygen-rich atmosphere (Figure 10.10) implies that basic reactions responsible for sulfur MIF in combustion as discussed previously may also occur in the Paleoarchean. Although biomass burning is not possible, it is plausible, and cannot be ruled out, that recombination reactions of elemental sulfur [*Babikov*, 2017] may be significant in the active Paleoarchean volcanism because formation of elemental sulfur related to volcanism are commonly observed on both Earth [*Kumar and Francisco*, 2017] and extraterrestrial bodies such as Io [*Spencer et al.*, 2000]. Therefore, the negative ^{33}S anomalies in Paleoarchean barites produced in the volcano plume could in fact come from a strictly thermal reaction instead of photolytic reactions, which may yield different $\Delta^{33}S$-$\delta^{34}S$ patterns. With extended experimental investigation and modeling efforts on providing the new chemical physics and atmospheric reactions, the relative roles of the dynamics, atmospheric chemistry, and microbial metabolisms on the formation and preservation of barites in the Paleoarchean can be further defined in the future.

10.7 Materials and Methods

10.7.1 Collection of aerosol, glacial snow and river samples.

TSP samples were collected at the Nam Co Station (30.77ºN, 90.98ºE, 4730 m above sea level) in the central HTP (Figure 10.6) from March to August in 2012. A high-volume (flow rate: ~1 m^3 min^{-1}) aerosol sampler (Tisch Environmental Inc., Ohio, U.S.A.) was used to collect TSP on a quartz filter paper. Glacial snow (fresh snow: 28.02ºN, 86.96ºE, 6530 m above sea level; melted snow/ice: 28.04ºN, 86.94ºE, 6320 m above sea level; these two samples were combined to obtain sufficient amounts of sulfur for isotopic analysis) and river (28°8'N, 86°51'E, 5150 m above sea level) samples were collected at the East Rongbuk Glacier (~5 km from the peak of Mount Everest) and the Mount Everest Base Camp (~15 km from the peak of Mount Everest), respectively, during the 2013 Mount Everest Scientific Expedition. Sulfate ions in each sample were trapped by an anion exchange resin column (BioRad X8) in the field, extracted by 1M HBr solution, and purified by Ag_2O in the Stable Isotope Laboratory at the University of California San Diego (UCSD).

10.7.2 Sediment core drilling and dating.

The Gokyo lake system (~4800 m above sea level, ~15 km from the peak of Mount Everest) in the Gokyo Valley at Nepal is the world's highest oligotrophic freshwater lake system including six main lakes. These lakes are intermorainic lateral lakes predominantly fed by precipitation and glacier and snowmelt runoff. The sediment core (length: 18.5 cm) was drilled at the center (the deepest basin: ~43 m) of Gokyo lake No.3 (27°57'N, 86°41'N, 4750 m above sea level) using a gravity coring system. Sectioned sediment samples (resolution: 0.5 cm) were freeze-dried and homogenized, and a portion of each sample was used for isotopic and chemical analysis in this study. The sediment chronology and sedimentary rates were determined by radioactive ^{210}Pb measurements carried out at the Chinese Academy of Science. Detailed information on sampling and dating of this sediment core was thoroughly described and reported by *Kang et al.* [2016b].

10.7.3 Sulfur content determination and stable sulfur isotope analysis.

The isotope ratios of quadruple sulfur isotopes (^{32}S, ^{33}S, ^{34}S and ^{36}S) defined as $\delta^{3x}S=[(^{3x}S/^{32}S)_{sample}/(^{3x}S/^{32}S)_{VCDT}-1]*1000$ (unit: ‰), where x=3, 4, and 6 and VCDT stands for the Vienna Canyon Diablo Troilite reference material, were determined in the Stable Isotope Laboratory at UCSD. Because of the pristine environment of Mount Everest, low sulfate concentrations in the freshwater lake, and the sample requirement (>1 μmol) for sulfur isotope analysis, some samples (up to 3) were combined to assure sufficient amounts of sulfur for successful measurements of multiple sulfur stable isotopes. Pre-dried and weighed samples were quantitatively transferred to a 50-mL boiling flask and reacted in a gently boiling 6 M HCl solution for 3 hours to extract acid volatile sulfide (AVS). Any H_2S produced in this reaction was carried by a high-purity nitrogen stream, washed through a Milli-Q deionized water trap, and reacted with cadmium acetate (0.2 M) to form CdS. In this study, AVS was not observed in all samples. Samples reacted with HCl were dried in an oil-bath (150°C) in a clean hood. Before drying, $BaCl_2$ solution (1.3 M) was added into the boiling flask to prevent any possible loss of sulfuric acid. Sample was subsequently reduced to gaseous H_2S in a gently boiling reduction solution (a mixture of 57% hydriodic acid, 50% hypophosphorous acid, and 12M hydrochloric acid). Evolved H_2S was converted to CdS and precipitated as Ag_2S by adding $AgNO_3$ (0.2 M). A portion of sulfates extracted from aerosol, glacial snow and river samples were precipitated using the same $BaCl_2$ solution, dried in a clean oven (120°C), and subject to the same reduction chemistry. Produced Ag_2S was subsequently filtered, rinsed with Milli-Q deionized water and NH_4OH (1.0 M), dried, and weighed for the determination of sulfate concentrations in sediment samples. The uncertainty of this gravimetric method is less than 10%. The weighed Ag_2S was subsequently transferred to a silver capsule, and loaded into a nickel tube for fluorination by BrF_5 at 580°C for 12 hours. The SF_6 product was separated from other byproducts and unreacted BrF_5 with 7-stage ethanol slush distillation at −119°C, and it was further purified by a gas chromatography (GC). The purified SF_6 was measured by an isotope ratio mass spectrometry (Thermo Finnigan MAT 253).

A laboratory Ag_2S standard of approximately the sample sizes comparable to environmental samples (1-6 μmol) was subjected to the same analytical procedure throughout out the study period to determine overall uncertainties of measurements (associated with extraction, fluorination, purification and mass spectrometer measurements) (Table 10.1). We noted that $\Delta^{36}S$ values in samples less than 2.5 μmol became artificially large (up to ~1‰; data not shown) during the study period (probably contaminated by trace amounts of carbon during fluorination or GC purification) and we therefore do not report and interpret the $\Delta^{36}S$ results in sediment samples because of their small sample sizes. For large sizes of samples (>2.5 μmol), the errors (one standard deviation) for $\delta^{34}S$, $\Delta^{33}S$, and $\Delta^{36}S$ values were less than 0.4‰, 0.01‰, and 0.1‰, respectively. For small sizes of samples (<2.5 μmol), the slightly greater standard deviations of $\delta^{34}S$ and $\Delta^{33}S$ (1.0‰ and 0.02‰, respectively) would not affect our interpretation and conclusion.

10.7.4 Elemental and stable lead isotope analysis.

Elemental and stable lead isotope analysis was carried out in the Trace Element Laboratory at the Academia Sinica. Pre-dried and weighed sediment samples were digested in an acid mixture (4 mL HNO_3 + 2 mL HF) using a microwave digestion system. The concentrations of major, trace, rare earth elements, and the ratios of $^{206}Pb/^{207}Pb$ and $^{208}Pb/^{207}Pb$ were subsequently determined by an inductively coupled plasma mass spectrometry (ICP-MS) (Perkin Elmer Elan 6100). Details on the microwave digestion, ICP-MS analysis, and quality assurance/control can be found in the literature [*Hsu et al.*, 2006; *Tao et al.*, 2014a]. Analytical error fraction for most elements are less than 10%, except for Se, As, Cs, Sb, and Rb (<15%). The relative standard deviation in stable lead isotope ratio measurements is less than 0.5%. Because elemental characteristics of top soils over the HTP are significantly different from the upper continental crust, enrichment factors of varying elements (=$[element/aluminum]_{sample}/[element/aluminum]_{reference}$) were calculated using the <20 μm fractions of top soils over the HTP as the reference material [*Li et al.*, 2009a].

10.7.5 Positive Matrix Factorization Model

The positive matrix factorization (PMF) model developed by the United States Environmental Protection Agency (EPA) is a source apportionment receptor model for estimating the contribution of each source to environment samples without knowing the source profiles and numbers. The detailed principles of the PMF model can be found elsewhere [*Tao et al.*, 2014a]. In this study, the EPA PMF version 5.0 was employed with 49 elements incorporated in the computation (Figure 10.8). Uncertainties of elemental concentrations were calculated using the equation: $Uncertainty = \sqrt{(Error\ Fraction \times Concentration)^2 + (0.5 \times Detection\ Limit)^2}$. For some samples with elemental concentrations less than or equal to detection limits, uncertainties of elemental concentrations were calculated as 5/6 times of the detection limit. To ensure the robustness of the statistics, 100 times of bootstrap runs with a minimum Pearson correlation coefficient of 0.6 were conducted. Three factors were resolved by the PMF model in this study (Figure 10.8 and 10.9). The first factor is characterized by enriched hafnium (Hf). Hf, a high field strength element, has very low solubility in aqueous fluids and has been utilized in terrestrial weathering and sediment transport studies. Therefore, this factor likely represents weathering/erosion processes. This interpretation is further confirmed by the time series of factor one (Figure 10.9), which closely matches the variation of weathering indices (Figure 10.7). The second factor is characterized by enriched thallium (Tl) and mercury (Hg). These two elements are highly relevant to anthropogenic activities such as ore mining and combustion, and this factor may thus present anthropogenic influences. The time series of factor two (Figure 10.9) is in consistence with the increasing trend of industrial production after the second industrial revolution. The factor three is not characterized by any particularly enriched elements, and may therefore present the background atmosphere.

10.8 Acknowledgement

This study was partially funded by National Natural Science Foundation of China (41630754, 41721091). The authors gratefully acknowledge Teresa Jackson, Shuen-Hsin Lin, Yi-Tang Huang, and Cheng-Ming Chou for technical assistance in isotopic and chemical analysis, and Qianggong Zhang for scientific discussion on the hydrology of the Gokyo Lake. Special thanks are due to Yanan Shen and the late Chih-An Huh for many interesting conversations on isotope biogeochemistry. M.L. acknowledges fellowships from the Guangzhou Elite Project (JY201303) and the visiting scholar program of Academia Sinica.

This chapter, in full, has been submitted for publication of the material "Atmospheric sulfur isotopic anomalies recorded at Mt. Everest across the Anthropocene" as it may appear. Lin, Mang; Kang, Shichang; Shaheen, Robina; Li, Chaoliu; Hsu, Shih-Chieh; Thiemens, Mark H. The dissertation author was the primary investigator and author of this paper.

REFERENCES

Aldahan, A., J. Hedfors, G. Possnert, A. Kulan, A. M. Berggren, and C. Soderstrom (2008), Atmospheric impact on beryllium isotopes as solar activity proxy, *Geophys Res Lett*, *35*(21).

Alexander, B., D. J. Allman, H. M. Amos, T. D. Fairlie, J. Dachs, D. A. Hegg, and R. S. Sletten (2012), Isotopic constraints on the formation pathways of sulfate aerosol in the marine boundary layer of the subtropical northeast Atlantic Ocean, *J Geophys Res-Atmos*, *117*.

Alexander, B., R. J. Park, D. J. Jacob, and S. L. Gong (2009), Transition metal-catalyzed oxidation of atmospheric sulfur: Global implications for the sulfur budget, *J Geophys Res-Atmos*, *114*, D02309.

Alexander, B., J. Savarino, K. J. Kreutz, and M. H. Thiemens (2004), Impact of preindustrial biomass-burning emissions on the oxidation pathways of tropospheric sulfur and nitrogen, *J Geophys Res-Atmos*, *109*(D8), doi:10.1029/2003jd004218.

Alkezweeny, A. J., and D. C. Powell (1977), Estimation of Transformation Rate of So2 to So4 from Atmospheric Concentration Data, *Atmos Environ*, *11*(2), 179-182.

An, Z. S., J. E. Kutzbach, W. L. Prell, and S. C. Porter (2001), Evolution of Asian monsoons and phased uplift of the Himalayan Tibetan plateau since Late Miocene times, *Nature*, *411*(6833), 62-66.

Arneth, A., S. P. Harrison, S. Zaehle, K. Tsigaridis, S. Menon, P. J. Bartlein, J. Feichter, A. Korhola, M. Kulmala, D. O'Donnell, G. Schurgers, S. Sorvari and T. Vesala (2010), Terrestrial biogeochemical feedbacks in the climate system, *Nat Geosci*, *3*(8), 525-532.

Assaf, E., L. Sheps, L. Whalley, D. Heard, A. Tomas, C. Schoemaecker, and C. Fittschen (2017), The Reaction between CH3O2 and OH Radicals: Product Yields and Atmospheric Implications, *Environ Sci Technol*, *51*(4), 2170-2177.

Ault, A. P., C. J. Gaston, Y. Wang, G. Dominguez, M. H. Thiemens, and K. A. Prather (2010), Characterization of the Single Particle Mixing State of Individual Ship Plume Events Measured at the Port of Los Angeles, *Environ Sci Technol*, *44*(6), 1954-1961.

Babich, L. (2017), Radiocarbon Production by Thunderstorms, *Geophys Res Lett*.

Babikov, D. (2017), Recombination reactions as a possible mechanism of mass-independent fractionation of sulfur isotopes in the Archean atmosphere of Earth, *P Natl Acad Sci USA*, *114*(12), 3062-3067.

Babikov, D., A. Semenov, and A. Teplukhin (2017), One possible source of mass-independent fractionation of sulfur isotopes in the Archean atmosphere of Earth, *Geochim Cosmochim Ac*, *204*, 388-406.

Bailey, H. P. (1966), *The climate of southern California*, Univ of California Press.

Bainssahota, S. K., and M. H. Thiemens (1989), A Mass-Independent Sulfur Isotope Effect in the Nonthermal Formation of S2F10, *J Chem Phys*, *90*(11), 6099-6109.

Bao, H. M., D. Rumble, and D. R. Lowe (2007), The five stable isotope compositions of Fig Tree barites: Implications on sulfur cycle in ca. 3.2 Ga oceans, *Geochim Cosmochim Ac*, *71*(20), 4868-4879.

Baroni, M., J. Savarino, J. H. Cole-Dai, V. K. Rai, and M. H. Thiemens (2008), Anomalous sulfur isotope compositions of volcanic sulfate over the last millennium in Antarctic ice cores, *J Geophys Res-Atmos*, *113*(D20).

Baroni, M., M. H. Thiemens, R. J. Delmas, and J. Savarino (2007), Mass-independent sulfur isotopic compositions in stratospheric volcanic eruptions, *Science*, *315*(5808), 84-87.

Barth, M. C., and A. T. Church (1999), Regional and global distributions and lifetimes of sulfate aerosols from Mexico city and southeast China, *J Geophys Res-Atmos*, *104*(D23), 30231-30239.

Baylon, P. M., D. A. Jaffe, R. B. Pierce, and M. S. Gustin (2016), Interannual Variability in Baseline Ozone and Its Relationship to Surface Ozone in the Western US, *Environ Sci Technol*, *50*(6), 2994-3001.

Beekmann, M., G. Ancellet, S. Blonsky, D. De Muer, A. Ebel, H. Elbern, J. Hendricks, J. Kowol, C. Mancier, R. Sladkovic, H. G. J. Smit, P. Speth, T. Trickl, Ph. Van Haver (1997), Regional and global tropopause fold occurrence and related ozone flux across the tropopause, *J Atmos Chem*, *28*(1-3), 29-44, doi:10.1023/A:1005897314623.

Bell, N., D. Koch, and D. T. Shindell (2005), Impacts of chemistry-aerosol coupling on tropospheric ozone and sulfate simulations in a general circulation model, *J Geophys Res-Atmos*, *110*(D14), doi:10.1029/2004jd005538.

Berresheim, H., M. Adam, C. Monahan, C. O'Dowd, J. M. C. Plane, B. Bohn, and F. Rohrer (2014), Missing SO2 oxidant in the coastal atmosphere? - observations from high-resolution measurements of OH and atmospheric sulfur compounds, *Atmos Chem Phys*, *14*(22), 12209-12223.

Bigeleisen, J., and M. G. Mayer (1947), Calculation of Equilibrium Constants for Isotopic Exchange Reactions, *J Chem Phys*, *15*(5), 261-267.

Bindeman, I. N., J. M. Eiler, B. A. Wing, and J. Farquhar (2007), Rare sulfur and triple oxygen isotope geochemistry of volcanogenic sulfate aerosols, *Geochim Cosmochim Ac*, *71*(9), 2326-2343.

Black, G., R. L. Sharpless, and T. G. Slanger (1982), Rate Coefficients at 298-K for So Reactions with O-2, O-3, and NO2, *Chem Phys Lett*, *90*(1), 55-58.

Boering, K. A., T. Jackson, K. J. Hoag, A. S. Cole, M. J. Perri, M. Thiemens, and E. Atlas (2004), Observations of the anomalous oxygen isotopic composition of carbon dioxide in the lower stratosphere and the flux of the anomaly to the troposphere, *Geophys Res Lett*, *31*(3), doi:10.1029/2003gl018451.

Bonasoni, P., Laj, P. Angelini, F. Arduini, J. Bonafè, U. Calzolari, F. Cristofanelli, P. Decesari, S. Facchini, M. C. Fuzzi, S. Gobbi, G. P. Maione, M. Marinoni, A. Petzold, A. Roccato, F. Roger, J.

C. Sellegri, K. Sprenger, M. Venzac, H. Verza, G. P. Villani, P. Vuillermoz, E. (2008), The ABC-Pyramid Atmospheric Research Observatory in Himalaya for aerosol, ozone and halocarbon measurements, *Sci Total Environ*, *391*(2-3), 252-261, doi:Doi 10.1016/J.Scitotenv.2007.10.024.

Bougiatioti, A., P. Nikolaou, I. Stavroulas, G. Kouvarakis, R. Weber, A. Nenes, M. Kanakidou, and N. Mihalopoulos (2016), Particle water and pH in the eastern Mediterranean: source variability and implications for nutrient availability, *Atmos Chem Phys*, *16*(7), 4579-4591.

Bourassa, A. E., A. Robock, W. J. Randel, T. Deshler, L. A. Rieger, N. D. Lloyd, E. J. Llewellyn, and D. A. Degenstein (2012), Large Volcanic Aerosol Load in the Stratosphere Linked to Asian Monsoon Transport, *Science*, *337*(6090), 78-81.

Bouvier, A., and M. Wadhwa (2010), The age of the Solar System redefined by the oldest Pb-Pb age of a meteoritic inclusion, *Nat Geosci*, *3*(9), 637-641.

Bowen, G. J. (2010), Isoscapes: Spatial Pattern in Isotopic Biogeochemistry, *Annu Rev Earth Pl Sc*, *38*, 161-187.

Bowen, G. J., L. I. Wassenaar, and K. A. Hobson (2005), Global application of stable hydrogen and oxygen isotopes to wildlife forensics, *Oecologia*, *143*(3), 337-348.

Brioude, J., D. Arnold, A. Stohl, M. Cassiani, D. Morton, P. Seibert, W. Angevine, S. Evan, A. Dingwell, J. D. Fast, R. C. Easter, I. Pisso, J. Burkhart, and G. Wotawa (2013), The Lagrangian particle dispersion model FLEXPART-WRF version 3.1, *Geosci Model Dev*, *6*(6), 1889-1904, doi:10.5194/Gmd-6-1889-2013.

Brothers, L. A., G. Dominguez, A. Abramian, A. Corbin, B. Bluen, and M. H. Thiemens (2010), Optimized low-level liquid scintillation spectroscopy of S-35 for atmospheric and biogeochemical chemistry applications, *P Natl Acad Sci USA*, *107*(12), 5311-5316, doi:10.1073/Pnas.0901168107.

Busigny, V., J. Marin-Carbonne, E. Muller, P. Cartigny, C. Rollion-Bard, N. Assayag, and P. Philippot (2017), Iron and sulfur isotope constraints on redox conditions associated with the 3.2 Ga barite deposits of the Mapepe Formation (Barberton Greenstone Belt, South Africa), *Geochim Cosmochim Ac*, *210*, 247-266.

Bytnerowicz, A., D. Cayan, P. Riggan, S. Schilling, P. Dawson, M. Tyree, L. Wolden, R. Tissell, and H. Preisler (2010), Analysis of the effects of combustion emissions and Santa Ana winds on ambient ozone during the October 2007 southern California wildfires, *Atmos Environ*, *44*(5), 678-687.

Cahill, J. F., K. Suski, J. H. Seinfeld, R. A. Zaveri, and K. A. Prather (2012), The mixing state of carbonaceous aerosol particles in northern and southern California measured during CARES and CalNex 2010, *Atmos Chem Phys*, *12*(22), 10989-11002.

Canfield, D. E., K. S. Habicht, and B. Thamdrup (2000), The Archean sulfur cycle and the early history of atmospheric oxygen, *Science*, *288*(5466), 658-661.

Cao, J. J., S. C. Lee, K. F. Ho, S. C. Zou, K. Fung, Y. Li, J. G. Watson, and J. C. Chow (2004), Spatial and seasonal variations of atmospheric organic carbon and elemental carbon in Pearl River Delta Region, China, *Atmos Environ*, *38*(27), 4447-4456.

Cao, Y., and R. G. Fovell (2016), Downslope Windstorms of San Diego County. Part I: A Case Study, *Mon Weather Rev*, *144*(2), 529-552.

Carlson, R. W., R. E. Johnson, and M. S. Anderson (1999), Sulfuric acid on Europa and the radiolytic sulfur cycle, *Science*, *286*(5437), 97-99.

Cates, N. L., and S. J. Mojzsis (2006), Chemical and isotopic evidence for widespread Eoarchean metasedimentary enclaves in southern West Greenland, *Geochim Cosmochim Ac*, *70*(16), 4229-4257.

Cecil, L. D., J. R. Green, S. Vogt, R. Michel, and G. Cottrell (1998), Isotopic composition of ice cores and meltwater from upper fremont glacier and Galena Creek rock glacier, Wyoming, *Geogr Ann A*, *80a*(3-4), 287-292.

Chakraborty, S., M. Ahmed, T. L. Jackson, and M. H. Thiemens (2008), Experimental test of self-shielding in vacuum ultraviolet photodissociation of CO, *Science*, *321*(5894), 1328-1331.

Chakraborty, S., M. Ahmed, T. L. Jackson, and M. H. Thiemens (2009), Response to Comments on "Experimental Test of Self-Shielding in Vacuum Ultraviolet Photodissociation of CO", *Science*, *324*(5934).

Chakraborty, S., T. Jackson, B. Rude, M. Ahmed, and M. Thiemens (2017), Sulfur Isotopic Fractionation in VUV Photodissociation of Sulfur Dioxide: Implications for Meteorite Data, paper presented at Lunar and Planetary Science Conference.

Chakraborty, S., T. L. Jackson, M. Ahmed, and M. H. Thiemens (2013), Sulfur isotopic fractionation in vacuum UV photodissociation of hydrogen sulfide and its potential relevance to meteorite analysis, *P Natl Acad Sci USA*, *110*(44), 17650-17655.

Chakraborty, S., B. H. Muskatel, T. L. Jackson, M. Ahmed, R. D. Levine, and M. H. Thiemens (2014), Massive isotopic effect in vacuum UV photodissociation of N-2 and implications for meteorite data, *P Natl Acad Sci USA*, *111*(41), 14704-14709.

Chan, C. Y., L. Y. Chan, W. L. Chang, Y. G. Zheng, H. Cui, X. D. Zheng, Y. Qin, and Y. S. Li (2003), Characteristics of a tropospheric ozone profile and implications for the origin of ozone over subtropical China in the spring of 2001, *J Geophys Res-Atmos*, *108*(D20).

Chan, C. Y., X. D. Zheng, L. Y. Chan, H. Cui, E. W. L. Ginn, Y. K. Leung, H. M. Lam, Y. G. Zheng, Y. Qin, C. S. Zhao, T. Wang, D. R. Blake, Y. S. Li (2004), Vertical profile and origin of wintertime tropospheric ozone over China during the PEACE-A period, *J Geophys Res-Atmos*, *109*(D23), doi:10.1029/2004jd004581.

Chan, L. Y., C. Y. Chan, and Y. Qin (1998), Surface ozone pattern in Hong Kong, *J Appl Meteorol*, *37*(10), 1153-1165.

Chen, Q. J., L. Geng, J. A. Schmidt, Z. Q. Xie, H. Kang, J. Dachs, J. Cole-Dai, A. J. Schauer, M. G. Camp, and B. Alexander (2016a), Isotopic constraints on the role of hypohalous acids in sulfate aerosol formation in the remote marine boundary layer, *Atmos Chem Phys*, *16*(17), 11433-11450.

Chen, X. L., Y. M. Ma, H. Kelder, Z. Su, and K. Yang (2011), On the behaviour of the tropopause folding events over the Tibetan Plateau, *Atmos Chem Phys*, *11*(10), 5113-5122, doi:10.5194/Acp-11-5113-2011.

Chen, X. L., B. Skerlak, M. W. Rotach, J. A. Anel, Z. Su, Y. M. Ma, and M. S. Li (2016b), Reasons for the Extremely High-Ranging Planetary Boundary Layer over the Western Tibetan Plateau in Winter, *J Atmos Sci*, *73*(5), 2021-2038.

Cheng, Y. F., Zheng, G. J., Wei, C., Mu, Q., Zheng, B., Wang, Z. B., Gao, M., Zhang, Q., He, K. B., . 325. Carmichael, G., Poschl, U., and Su, H. (2016), Reactive nitrogen chemistry in aerosol water as a source of sulfate during haze events in China, *Science Advances*, *2*(12).

Cho, H. M., Y. L. Hong, and G. Kim (2011), Atmospheric depositional fluxes of cosmogenic S-35 and Be-7: Implications for the turnover rate of sulfur through the biosphere, *Atmos Environ*, *45*(25), 4230-4234, doi:10.1016/j.atmosenv.2011.05.002.

Clapp, L. J., and M. E. Jenkin (2001), Analysis of the relationship between ambient levels Of O-3, NO2 and NO as a function of NO chi in the UK, *Atmos Environ*, *35*(36), 6391-6405.

Clark, J. F., S. H. Urióstegui, R. K. Bibby, B. K. Esser, and G. Tredoux (2016), Quantifying Apparent Groundwater Ages near Managed Aquifer Recharge Operations Using Radio-Sulfur (35S) as an Intrinsic Tracer, *Water*, *8*(11), 474.

Clayton, R. N., L. Grossman, and T. K. Mayeda (1973), Component of Primitive Nuclear Composition in Carbonaceous Meteorites, *Science*, *182*(4111), 485-488.

Colman, J. J., X. P. Xu, M. H. Thiemens, and W. C. Trogler (1996), Photopolymerization and mass-independent sulfur isotope fractionations in carbon disulfide, *Science*, *273*(5276), 774-776.

Cong, Z. Y., S. C. Kang, S. P. Gao, Y. L. Zhang, Q. Li, and K. Kawamura (2013), Historical Trends of Atmospheric Black Carbon on Tibetan Plateau As Reconstructed from a 150-Year Lake Sediment Record, *Environ Sci Technol*, *47*(6), 2579-2586.

Cong, Z. Y., S. C. Kang, X. D. Liu, and G. F. Wang (2007), Elemental composition of aerosol in the Nam Co region, Tibetan Plateau, during summer monsoon season, *Atmos Environ*, *41*(6), 1180-1187, doi:Doi 10.1016/J.Atmosenv.2006.09.046.

Cong, Z. Y., S. C. Kang, C. L. Luo, Q. Li, J. Huang, S. P. Gao, and X. D. Li (2011), Trace elements and lead isotopic composition of PM10 in Lhasa, Tibet, *Atmos Environ*, *45*(34), 6210-6215.

Cooper, L. W., C. R. Olsen, D. K. Solomon, I. L. Larsen, R. B. Cook, and J. M. Grebmeier (1991), Stable Isotopes of Oxygen and Natural and Fallout Radionuclides Used for Tracing Runoff during Snowmelt in an Arctic Watershed, *Water Resour Res*, *27*(9), 2171-2179.

Cooper, O. R., A. O. Langford, D. D. Parrish, and D. W. Fahey (2015), Challenges of a lowered US ozone standard, *Science*, *348*(6239), 1096-1097.

Cooper, O. R., A. Stohl, G. Hübler, E. Y. Hsie, D. D. Parrish, A. F. Tuck, G. N. Kiladis, S. J. Oltmans, B. J. Johnson, M. Shapiro, J. L. Moody, A. S. Lefohn (2005), Direct transport of midlatitude stratospheric ozone into the lower troposphere and marine boundary layer of the tropical Pacific Ocean, *J Geophys Res-Atmos*, *110*(D23), doi:10.1029/2005jd005783.

Cooper, O. R., M. Trainer, A. M. Thompson, S. J. Oltmans, D. W. Tarasick, J. C. Witte, A. Stohl, S. Eckhardt, J. Lelieveld, M. J. Newchurch, B. J. Johnson, R. W. Portmann, L. Kalnajs, M. K. Dubey, T. Leblanc, I. S. McDermid, G. Forbes, D. Wolfe, T. Carey-Smith, G. A. Morris, B. Lefer, B. Rappenglück, E. Joseph, F. Schmidlin, J. Meagher, F. C. Fehsenfeld, T. J. Keating, R. A. Van Curen, K. Minschwaner (2007), Evidence for a recurring eastern North America upper tropospheric ozone maximum during summer, *J Geophys Res-Atmos*, *112*(D23), doi:10.1029/2007jd008710.

Cortecci, G., and Longinel.A (1970), Isotopic Composition of Sulfate in Rain Water,Pisa, Italy, *Earth Planet Sc Lett*, *8*(1), 36.

Creamean, J. M., K. J. Suski, D. Rosenfeld, A. Cazorla, P. J. DeMott, R. C. Sullivan, A. B. White, F. M. Ralph, P. Minnis, J. M. Comstock, J. M. Tomlinson, K. A. Prather (2013), Dust and Biological Aerosols from the Sahara and Asia Influence Precipitation in the Western U.S., *Science*, *339*(6127), 1572-1578.

Cristofanelli, P., A. Bracci, M. Sprenger, A. Marinoni, U. Bonafè, F. Calzolari, R. Duchi, P. Laj, J.M. Pichon, F. Roccato, H. Venzac, E. Vuillermoz, and P. Bonasoni (2010), Tropospheric ozone variations at the Nepal Climate Observatory-Pyramid (Himalayas, 5079 m a.s.l.) and influence of deep stratospheric intrusion events, *Atmos Chem Phys*, *10*(14), 6537-6549, doi:10.5194/Acp-10-6537-2010.

Currie, L. A. (1968), Limits for Qualitative Detection and Quantitative Determination - Application to Radiochemistry, *Anal Chem*, *40*(3), 586-&.

Dai, S. F., D. Y. Ren, C. L. Chou, R. B. Finkelman, V. V. Seredin, and Y. P. Zhou (2012), Geochemistry of trace elements in Chinese coals: A review of abundances, genetic types, impacts on human health, and industrial utilization, *Int J Coal Geol*, *94*, 3-21.

Day, D. A., S. Liu, L. M. Russell, and P. J. Ziemann (2010), Organonitrate group concentrations in submicron particles with high nitrate and organic fractions in coastal southern California, *Atmos Environ*, *44*(16), 1970-1979.

De Bellevue, J. L., J. L. Baray, S. Baldy, G. Ancellet, R. Diab, and F. Ravetta (2007), Simulations of stratospheric to tropospheric transport during the tropical cyclone Marlene event, *Atmos Environ*, *41*(31), 6510-6526.

Ding, A. J., and T. Wang (2006), Influence of stratosphere-to-troposphere exchange on the seasonal cycle of surface ozone at Mount Waliguan in western China, *Geophys Res Lett*, *33*(3), doi:10.1029/2005gl024760.

Ding, A. J., T. Wang, and C. B. Fu (2013), Transport characteristics and origins of carbon monoxide and ozone in Hong Kong, South China, *J Geophys Res-Atmos*, *118*(16), 9475-9488.

Ding, A. J., T. Wang, V. Thouret, J. P. Cammas, and P. Nedelec (2008), Tropospheric ozone climatology over Beijing: analysis of aircraft data from the MOZAIC program, *Atmos Chem Phys*, *8*(1), 1-13.

Dominguez, G., T. Jackson, L. Brothers, B. Barnett, B. Nguyen, and M. H. Thiemens (2008), Discovery and measurement of an isotopically distinct source of sulfate in Earth's atmosphere, *P Natl Acad Sci USA*, *105*(35), 12769-12773.

Dorman, C. E., T. Holt, D. P. Rogers, and K. Edwards (2000), Large-scale structure of the June-July 1996 marine boundary layer along California and Oregon, *Mon Weather Rev*, *128*(6), 1632-1652.

Du, Q. Q., C. Zhang, Y. Mu, Y. Cheng, Y. Zhang, C. Liu, M. Song, D. Tian, P. Liu, J. Liu, C. Xue, C. Ye (2016), An important missing source of atmospheric carbonyl sulfide: Domestic coal combustion, *Geophys Res Lett*, *43*(16), 8720-8727.

Duan, J. P., J. Esper, U. Buntgen, L. Li, E. Xoplaki, H. Zhang, L. L. Wang, Y. J. Fang, and J. Luterbacher (2017), Weakening of annual temperature cycle over the Tibetan Plateau since the 1870s, *Nat Commun*, *8*.

Dufour, G., M. Eremenko, J. Cuesta, C. Doche, G. Foret, M. Beekmann, A. Cheiney, Y. Wang, Z. Cai, Y. Liu, M. Takigawa, Y. Kanaya, and J.-M. Flaud (2015), Springtime daily variations in lower-tropospheric ozone over east Asia: the role of cyclonic activity and pollution as observed from space with IASI, *Atmos Chem Phys*, *15*(18), 10839-10856.

Dupart, Y., S. M. King, B. Nekat, A. Nowak, A. Wiedensohler, H. Herrmann, G. David, B. Thomas, A. Miffre, P. Rairoux, B. D'Anna and C. George (2012), Mineral dust photochemistry induces nucleation events in the presence of SO2, *P Natl Acad Sci USA*, *109*(51), 20842-20847, doi:10.1073/Pnas.1212297109.

E.W. Rice, R. B. B., A.D. Eaton, L.S. Clesceri (2012), *Standard Methods for the Examination of Water and Wastewater*, 22nd ed., American Public Health Association, American Water Works Association, Water Environment Federation.

Endo, Y., S. O. Danielache, Y. Ueno, S. Hattori, M. S. Johnson, N. Yoshida, and H. G. Kjaergaard (2015), Photoabsorption cross-section measurements of S-32, S-33, S-34, and S-36 sulfur dioxide from 190 to 220 nm, *J Geophys Res-Atmos*, *120*(6), 2546-2557.

Endo, Y., Y. Ueno, S. Aoyama, and S. O. Danielache (2016), Sulfur isotope fractionation by broadband UV radiation to optically thin SO2 under reducing atmosphere, *Earth Planet Sc Lett*, *453*, 9-22.

Enghoff, M. B., N. Bork, S. Hattori, C. Meusinger, M. Nakagawa, J. O. P. Pedersen, S. Danielache, Y. Ueno, M. S. Johnson, N. Yoshida, and H. Svensmark (2012), An isotopic analysis of ionising radiation as a source of sulphuric acid, *Atmos Chem Phys*, *12*(12), 5319-5327.

Engling, G., C. M. Carrico, S. M. Kreldenweis, J. L. Collett, D. E. Day, W. C. Malm, E. Lincoln, W. M. Hao, Y. Iinuma, and H. Herrmann (2006), Determination of levoglucosan in biomass combustion aerosol by high-performance anion-exchange chromatography with pulsed amperometric detection, *Atmos Environ*, *40*, S299-S311.

Enoto, T., Y. Wada, Y. Furuta, K. Nakazawa, T. Yuasa, K. Okuda, K. Makishima, M. Sato, Y. Sato, and T. Nakano (2017), Photonuclear reactions triggered by lightning discharge, *Nature*, *551*(7681), 481.

Ervens, B. (2015), Modeling the Processing of Aerosol and Trace Gases in Clouds and Fogs, *Chem Rev*, *115*(10), 4157-4198.

Fakhraee, M., S. A. Crowe, and S. Katsev (2018), Sedimentary sulfur isotopes and Neoarchean ocean oxygenation, *Science advances*, *4*(1), e1701835.

Fang, T., H. Guo, L. Zeng, V. Verma, A. Nenes, and R. J. Weber (2017), Highly Acidic Ambient Particles, Soluble Metals, and Oxidative Potential: A Link between Sulfate and Aerosol Toxicity, *Environ Sci Technol*, *51*(5), 2611-2620.

Farquhar, J., H. M. Bao, and M. Thiemens (2000a), Atmospheric influence of Earth's earliest sulfur cycle, *Science*, *289*(5480), 756-758, doi:10.1126/Science.289.5480.756.

Farquhar, J., J. Cliff, A. L. Zerkle, A. Kamyshny, S. W. Poulton, M. Claire, D. Adams, and B. Harms (2013), Pathways for Neoarchean pyrite formation constrained by mass-independent sulfur isotopes, *P Natl Acad Sci USA*, *110*(44), 17638-17643.

Farquhar, J., M. Peters, D. T. Johnston, H. Strauss, A. Masterson, U. Wiechert, and A. J. Kaufman (2007), Isotopic evidence for Mesoarchaean anoxia and changing atmospheric sulphur chemistry, *Nature*, *449*(7163), 706-U705.

Farquhar, J., J. Savarino, S. Airieau, and M. H. Thiemens (2001), Observation of wavelength-sensitive mass-independent sulfur isotope effects during SO2 photolysis: Implications for the early atmosphere, *J Geophys Res-Planet*, *106*(E12), 32829-32839, doi:10.1029/2000je001437.

Farquhar, J., J. Savarino, T. L. Jackson, and M. H. Thiemens (2000b), Evidence of atmospheric sulphur in the martian regolith from sulphur isotopes in meteorites, *Nature*, *404*(6773), 50-52, doi:10.1038/35003517.

Federman, S. R., and E. D. Young (2009), Comment on "Experimental Test of Self-Shielding in Vacuum Ultraviolet Photodissociation of CO", *Science*, *324*(5934).

Fike, D. A., A. S. Bradley, and C. V. Rose (2015), Rethinking the Ancient Sulfur Cycle, *Annual Review of Earth and Planetary Sciences, Vol 43*, *43*, 593-622.

Forrest, J., and L. Newman (1973), Sampling and Analysis of Atmospheric Sulfur-Compounds for Isotope Ratio Studies, *Atmos Environ*, *7*(5), 561-573, doi:10.1016/0004-6981(73)90008-5.

Fountoukis, C., and A. Nenes (2007), ISORROPIA II: a computationally efficient thermodynamic equilibrium model for K+-Ca2+-Mg2+-Nh(4)(+)-Na+-SO42--NO3--Cl--H2O aerosols, *Atmos Chem Phys*, *7*(17), 4639-4659.

Franz, H. B., S. T. Kim, J. Farquhar, J. M. D. Day, R. C. Economos, K. D. McKeegan, A. K. Schmitt, A. J. Irving, J. Hoek, and J. Dottin (2014), Isotopic links between atmospheric chemistry and the deep sulphur cycle on Mars, *Nature*, *508*(7496), 364-368.

Froyd, K. D., S. M. Murphy, D. M. Murphy, J. A. de Gouw, N. C. Eddingsaas, and P. O. Wennberg (2010), Contribution of isoprene-derived organosulfates to free tropospheric aerosol mass, *P Natl Acad Sci USA*, *107*(50), 21360-21365, doi:10.1073/pnas.1012561107.

Gao, Y. Q., and R. A. Marcus (2001), Strange and unconventional isotope effects in ozone formation, *Science*, *293*(5528), 259-263.

Gardiner, W. C. (2000), *Gas-phase combustion chemistry*, Springer Verlag.

Gebel, M. E., B. J. Finlayson-Pitts, and J. A. Ganske (2000), The uptake of SO2 on synthetic sea salt and some of its components, *Geophys Res Lett*, *27*(6), 887-890.

Gijzeman, O. L., F. Kaufman, and G. Porter (1973), Oxygen Quenching of Aromatic Triplet-States in Solution .1., *J Chem Soc Farad T 2*, *69*(5), 708-720.

Goel, P. S. (1956), Radioactive Sulphur Produced by Cosmic Rays in Rain Water, *Nature*, *178*(4548), 1458-1459.

Goto, D., T. Nakajima, T. Dai, T. Takemura, M. Kajino, H. Matsui, A. Takami, S. Hatakeyama, N. Sugimoto, A. Shimizu, T. Ohara (2015), An evaluation of simulated particulate sulfate over East Asia through global model intercomparison, *J Geophys Res-Atmos*, *120*(12), 6247-6270.

Gray, L. J., M. Bithell, and B. D. Cox (1994), The Role of Specific-Humidity Fields in the Diagnosis of Stratosphere Troposphere Exchange, *Geophys Res Lett*, *21*(19), 2103-2106, doi:10.1029/94gl01909.

Grigholm, B., P. A. Mayewski, S. Kang, Y. Zhang, U. Morgenstern, M. Schwikowski, S. Kaspari, V. Aizen, E. Aizen, N. Takeuchi, K. A. Maasch, S. Birkel, M. Handley, S. Sneed (2015), Twentieth century dust lows and the weakening of the westerly winds over the Tibetan Plateau, *Geophys Res Lett*, *42*(7), 2434-2441.

Guo, H., L. Xu, A. Bougiatioti, K. M. Cerully, S. L. Capps, J. R. Hite Jr., A. G. Carlton, S.-H. Lee, M. H. Bergin, N. L. Ng, A. Nenes, and R. J. Weber (2015), Fine-particle water and pH in the southeastern United States, *Atmos Chem Phys*, *15*(9), 5211-5228.

Guo, J., Y. Wang, X. Shen, Z. Wang, T. Lee, X. Wang, P. Li, M. Sun, J.L. Collett Jr., W. Wang, and T. Wang (2012), Characterization of cloud water chemistry at Mount Tai, China: Seasonal variation, anthropogenic impact, and cloud processing, *Atmos Environ*, *60*, 467-476.

Guo, Z. B., Z. Q. Li, J. Farquhar, A. J. Kaufman, N. P. Wu, C. Li, R. R. Dickerson, and P. C. Wang (2010), Identification of sources and formation processes of atmospheric sulfate by sulfur isotope and scanning electron microscope measurements, *J Geophys Res-Atmos*, *115*.

Gustafsson, O., M. Krusa, Z. Zencak, R. J. Sheesley, L. Granat, E. Engstrom, P. S. Praveen, P. S. P. Rao, C. Leck, and H. Rodhe (2009), Brown Clouds over South Asia: Biomass or Fossil Fuel Combustion?, *Science*, *323*(5913), 495-498.

Guy, B. M., S. Ono, J. Gutzmer, A. J. Kaufman, Y. Lin, M. L. Fogel, and N. J. Beukes (2012), A multiple sulfur and organic carbon isotope record from non-conglomeratic sedimentary rocks of the Mesoarchean Witwatersrand Supergroup, South Africa, *Precambrian Res*, *216*, 208-231.

Guzman-Morales, J., A. Gershunov, J. Theiss, H. Q. Li, and D. Cayan (2016), Santa Ana Winds of Southern California: Their climatology, extremes, and behavior spanning six and a half decades, *Geophys Res Lett*, *43*(6), 2827-2834.

Haase, A. T., D. Gantz, B. Eble, D. Walker, L. Stowring, P. Ventura, H. Blum, S. Wietgrefe, M. Zupancic, W. Tourtellotte, C.J. Gibbs Jr., E. Norrby, and S. Rozenblatt (1985), Natural-History of Restricted Synthesis and Expression of Measles-Virus Genes in Subacute Sclerosing Panencephalitis, *P Natl Acad Sci USA*, *82*(9), 3020-3024.

Halevy, I., D. T. Johnston, and D. P. Schrag (2010), Explaining the Structure of the Archean Mass-Independent Sulfur Isotope Record, *Science*, *329*(5988), 204-207.

Han, X., Q. Guo, H. Strauss, C.-Q. Liu, J. Hu, Z. Guo, R. Wei, M. Peters, L. Tian, and J. Kong (2017), Multiple sulfur isotope constraints on sources and formation processes of sulfate in Beijing PM2.5 aerosol, *Environ Sci Technol*, *51*(14), 7794–7803, doi:10.1021/acs.est.7b00280.

Harris, E., B. Sinha, P. Hoppe, and S. Ono (2013a), High-Precision Measurements of S-33 and S-34 Fractionation during SO2 Oxidation Reveal Causes of Seasonality in SO2 and Sulfate Isotopic Composition, *Environ Sci Technol*, *47*(21), 12174-12183.

Harris, E., B. Sinha, D. van Pinxteren, A. Tilgner, K. W. Fomba, J. Schneider, A. Roth, T. Gnauk, B. Fahlbusch, S. Mertes, T. Lee, J. Collett, S. Foley, S. Borrmann, P. Hoppe, H. Herrmann (2013b), Enhanced Role of Transition Metal Ion Catalysis During In-Cloud Oxidation of SO2, *Science*, *340*(6133), 727-730, doi:10.1126/Science.1230911.

Harrison, R. M., and J. X. Yin (2000), Particulate matter in the atmosphere: which particle properties are important for its effects on health?, *Sci Total Environ*, *249*(1-3), 85-101.

Haywood, J., and O. Boucher (2000), Estimates of the direct and indirect radiative forcing due to tropospheric aerosols: A review, *Rev Geophys*, *38*(4), 513-543.

Haywood, J. M., and V. Ramaswamy (1998), Global sensitivity studies of the direct radiative forcing due to anthropogenic sulfate and black carbon aerosols, *J Geophys Res-Atmos*, *103*(D6), 6043-6058.

He, H., C. Li, C. P. Loughner, Z. Li, N. A. Krotkov, K. Yang, L. Wang, Y. Zheng, X. Bao, G. Zhao, R. R. Dickerson (2012), SO2 over central China: Measurements, numerical simulations and the tropospheric sulfur budget, *J Geophys Res-Atmos*, *117*.

Heidenreich, J. E., and M. H. Thiemens (1986), A Non-Mass-Dependent Oxygen Isotope Effect in the Production of Ozone from Molecular-Oxygen - the Role of Molecular Symmetry in Isotope Chemistry, *J Chem Phys*, *84*(4), 2129-2136.

Hill-Falkenthal, J. (2014), *Investigations of Atmospheric Sulfur Cycle Oxidation Using Stable and Radioactive Isotopes*, University of California, San Diego.

Hill-Falkenthal, J., A. Priyadarshi, J. Savarino, and M. Thiemens (2013), Seasonal variations in S-35 and Delta O-17 of sulfate aerosols on the Antarctic plateau, *J Geophys Res-Atmos*, *118*(16), 9444-9455, doi:10.1002/Jgrd.50716.

Hill-Falkenthal, J., A. Priyadarshi, and M. Thiemens (2012a), Differentiating sulfate aerosol oxidation pathways for varying source altitudes using S-35 and Delta O-17 tracers, *J Geophys Res-Atmos*, *117*, D18302, doi:10.1029/2012jd018242.

Hill-Falkenthal, J., A. Priyadarshi, and M. Thiemens (2012b), Differentiating sulfate aerosol oxidation pathways for varying source altitudes using S-35 and Delta O-17 tracers, *J Geophys Res-Atmos*, *117*, doi:10.1029/2012jd018242.

Hoag, K. J., C. J. Still, I. Y. Fung, and K. A. Boering (2005), Triple oxygen isotope composition of tropospheric carbon dioxide as a tracer of terrestrial gross carbon fluxes, *Geophys Res Lett*, *32*(2).

Hong, Y. L., and G. Kim (2005), Measurement of cosmogenic S-35 activity in rainwater and lake water, *Anal Chem*, *77*(10), 3390-3393.

Hou, X. L., L. F. Ostergaard, and S. P. Nielsen (2005), Determination of Ni-63 and Fe-55 in nuclear waste samples using radiochemical separation and liquid scintillation counting, *Anal Chim Acta*, *535*(1-2), 297-307.

Howarth, R. W., and B. B. Jorgensen (1984), Formation of S-35-Labeled Elemental Sulfur and Pyrite in Coastal Marine-Sediments (Limfjorden and Kysing Fjord, Denmark) during Short-Term (So42-)-S-35 Reduction Measurements, *Geochim Cosmochim Ac*, *48*(9), 1807-1818.

Hsu, S. C., C. A. Huh, C. Y. Chan, S. H. Lin, F. J. Lin, and S. C. Liu (2012), Hemispheric dispersion of radioactive plume laced with fission nuclides from the Fukushima nuclear event, *Geophys Res Lett*, *39*, doi:10.1029/2011gl049986.

Hsu, S. C., S. C. Liu, W. L. Jeng, C. C. K. Chou, R. T. Hsu, Y. T. Huang, and Y. W. Chen (2006), Lead isotope ratios in ambient aerosols from Taipei, Taiwan: Identifying long-range transport of airborne Pb from the Yangtze Delta, *Atmos Environ*, *40*(28), 5393-5404.

Huang, H. L., W. Chao, and J. J. M. Lin (2015a), Kinetics of a Criegee intermediate that would survive high humidity and may oxidize atmospheric SO2, *P Natl Acad Sci USA*, *112*(35), 10857-10862.

Huang, J., H. Liu, J. H. Crawford, C. Chan, D. B. Considine, Y. Zhang, X. Zheng, C. Zhao, V. Thouret, S. J. Oltmans, S. C. Liu, D. B. A. Jones, S. D. Steenrod, and M. R. Damon (2015b), Origin of springtime ozone enhancements in the lower troposphere over Beijing: in situ measurements and model analysis, *Atmos Chem Phys*, *15*(9), 5161-5179.

Huang, J. P., J. C. H. Fung, and A. K. H. Lau (2006), Integrated processes analysis and systematic meteorological classification of ozone episodes in Hong Kong, *J Geophys Res-Atmos*, *111*(D20).

Huang, R. J., Y. Zhang, C. Bozzetti, K. Ho, J. Cao, Y. Han, K. R. Daellenbach, J. G. Slowik, S. M. Platt, F. Canonaco, P. Zotter, R. Wolf, S. M. Pieber, E. A. Bruns, M. Crippa, G Ciarelli, A. Piazzalunga, M. Schwikowski, G. Abbaszade, J. Schnelle-Kreis, R. Zimmermann, Z. An, S. Szidat, U. Baltensperger, I. El Haddad and A. S. H. Prévôt (2014a), High secondary aerosol contribution to particulate pollution during haze events in China, *Nature*, *514*(7521), 218-222.

Huang, X., Y. Song, C. Zhao, M. M. Li, T. Zhu, Q. Zhang, and X. Y. Zhang (2014b), Pathways of sulfate enhancement by natural and anthropogenic mineral aerosols in China, *J Geophys Res-Atmos*, *119*(24), 14165-14179.

Hulston, J. R., and H. G. Thode (1965), Variations in S33 S34 and S36 Contents of Meteorites and Their Relation to Chemical and Nuclear Effects, *J Geophys Res*, *70*(14), 3475-&.

Hwang, C., A. J. Sinskey, and H. F. Lodish (1992), Oxidized Redox State of Glutathione in the Endoplasmic-Reticulum, *Science*, *257*(5076), 1496-1502.

Iinuma, Y., G. Engling, H. Puxbaum, and H. Herrmann (2009), A highly resolved anion-exchange chromatographic method for determination of saccharidic tracers for biomass combustion and primary bio-particles in atmospheric aerosol, *Atmos Environ*, *43*(6), 1367-1371.

Immerzeel, W. W., L. P. H. van Beek, and M. F. P. Bierkens (2010), Climate Change Will Affect the Asian Water Towers, *Science*, *328*(5984), 1382-1385, doi:10.1126/Science.1183188.

Ishino, S., S. Hattori, J. Savarino, B. Jourdain, S. Preunkert, M. Legrand, N. Caillon, A. Barbero, K. Kuribayashi, and N. Yoshida (2017), Seasonal variations of triple oxygen isotopic compositions of atmospheric sulfate, nitrate and ozone at Dumont d'Urville, coastal Antarctica, *Atmos. Chem. Phys.*, *17*, 14, doi:10.5194/acp-17-3713-2017.

Ivanov, M. V., and D. Babikov (2013), On molecular origin of mass-independent fractionation of oxygen isotopes in the ozone forming recombination reaction, *P Natl Acad Sci USA*, *110*(44), 17708-17713.

Jiang, Y. C., T. L. Zhao, J. Liu, X. D. Xu, C. H. Tan, X. H. Cheng, X. Y. Bi, J. B. Gan, J. F. You, and S. Z. Zhao (2015), Why does surface ozone peak before a typhoon landing in southeast China?, *Atmos Chem Phys*, *15*(23), 13331-13338.

Johannessen, M., and A. Henriksen (1978), Chemistry of Snow Meltwater - Changes in Concentration during Melting, *Water Resour Res*, *14*(4), 615-619.

Jordan, C. E., J. E. Dibb, and R. C. Finkel (2003), Be-10/Be-7 tracer of atmospheric transport and stratosphere-troposphere exchange, *J Geophys Res-Atmos*, *108*(D8).

Junkermann, W., and W. Roedel (1983), Evidence for Short SO2 Lifetimes in the Atmosphere - an Insitu Measurement of Atmospheric SO2 Lifetime Using Cosmic-Ray Produced Sulfur-38, *Atmos Environ*, *17*(12), 2549-2554.

Junkermann, W., and W. Roedel (1985), Evidence for Short So2 Lifetimes in the Atmosphere - an Insitu Measurement of Atmospheric SO2 Lifetime Using Cosmic-Ray Produced S-38 - Reply, *Atmos Environ*, *19*(7), 1206-1207.

Kang, S. C., P. F. Chen, C. L. Li, B. Liu, and Z. Y. Cong (2016a), Atmospheric Aerosol Elements over the Inland Tibetan Plateau: Concentration, Seasonality, and Transport, *Aerosol Air Qual Res*, *16*(3), 789-800.

Kang, S. C., J. Huang, F. Wang, Q. Zhang, Y. Zhang, C. Li, L. Wang, P. Chen, C. M. Sharma, Q. Li, M. Sillanpää, J. Hou, B. Xu, and J. Guo (2016b), Atmospheric Mercury Depositional Chronology Reconstructed from Lake Sediments and Ice Core in the Himalayas and Tibetan Plateau, *Environ Sci Technol*, *50*(6), 2859-2869.

Kaspar, S., R. L. Hooke, P. A. Mayewski, S. C. Kang, S. G. Hou, and D. H. Qin (2008), Snow accumulation rate on Qomolangma (Mount Everest), Himalaya: synchroneity with sites across the Tibetan Plateau on 50-100 year timescales, *J Glaciol*, *54*(185), 343-352.

Kaspari, S., P. A. Mayewski, M. Handley, E. Osterberg, S. C. Kang, S. Sneed, S. G. Hou, and D. H. Qin (2009), Recent increases in atmospheric concentrations of Bi, U, Cs, S and Ca from a 350-year Mount Everest ice core record, *J Geophys Res-Atmos*, *114*.

Kaufman, A. J., D. T. Johnston, J. Farquhar, A. L. Masterson, T. W. Lyons, S. Bates, A. D. Anbar, G. L. Arnold, J. Garvin, and R. Buick (2007), Late Archean biospheric oxygenation and atmospheric evolution, *Science*, *317*(5846), 1900-1903.

Kester, C. L., J. S. Baron, and J. T. Turk (2003), Isotopic study of sulfate sources and residence times in a subalpine watershed, *Environ Geol*, *43*(5), 606-613.

Kim, Y. K., H. W. Lee, J. K. Park, and Y. S. Moon (2002), The stratosphere-troposphere exchange of ozone and aerosols over Korea, *Atmos Environ*, *36*(3), 449-463, doi:10.1016/S1352-2310(01)00370-3.

Kirkby, J., J. Curtius, J. Almeida, E. Dunne, J. Duplissy, S. Ehrhart, A. Franchin, S. Gagné, L. Ickes, A. Kürten, A. Kupc, A. Metzger, F. Riccobono, L. Rondo, S. Schobesberger, G. Tsagkogeorgas, D. Wimmer, A. Amorim, F. Bianchi, M. Breitenlechner, A. David, J. Dommen, A. Downard, M. Ehn, R. C. Flagan, S. Haider, A. Hansel, D. Hauser, W. Jud, H. Junninen, F. Kreissl, A. Kvashin, A. Laaksonen, K. Lehtipalo, J. Lima, E. R. Lovejoy, V. Makhmutov, S. Mathot, J. Mikkilä, P. Minginette, S. Mogo, T. Nieminen, A. Onnela, P. Pereira, T. Petäjä, R. Schnitzhofer, J. H. Seinfeld, M. Sipilä, Y. Stozhkov, F. Stratmann, A. Tomé, J. Vanhanen, Y. Viisanen, A. Vrtala, P. E. Wagner, H. Walther, E. Weingartner, H. Wex, P. M. Winkler, K. S. Carslaw, D. R. Worsnop, U. Baltensperger and M. Kulmala (2011), Role of sulphuric acid, ammonia and galactic cosmic rays in atmospheric aerosol nucleation, *Nature*, *476*(7361), 429-U477.

Kuang, S., M. J. Newchurch, J. Burris, L. H. Wang, K. Knupp, and G. Y. Huang (2012), Stratosphere-to-troposphere transport revealed by ground-based lidar and ozonesonde at a midlatitude site, *J Geophys Res-Atmos*, *117*.

Kulmala, M., T. Petaja, M. Ehn, J. Thornton, M. Sipila, D. R. Worsnop, and V. M. Kerminen (2014), Chemistry of Atmospheric Nucleation: On the Recent Advances on Precursor Characterization and Atmospheric Cluster Composition in Connection with Atmospheric New Particle Formation, *Annual Review of Physical Chemistry, Vol 65*, *65*, 21-37.

Kumar, M., and J. S. Francisco (2017), Elemental sulfur aerosol-forming mechanism, *P Natl Acad Sci USA*, *114*(5), 864-869.

Kurzweil, F., M. Claire, C. Thomazo, M. Peters, M. Hannington, and H. Strauss (2013), Atmospheric sulfur rearrangement 2.7 billion years ago: Evidence for oxygenic photosynthesis, *Earth Planet Sc Lett*, *366*, 17-26.

Labidi, J., P. Cartigny, and M. Moreira (2013), Non-chondritic sulphur isotope composition of the terrestrial mantle, *Nature*, *501*(7466), 208.

Lal, D., and B. Peters (1967), Cosmic ray produced radioactivity on the earth, in *Kosmische Strahlung II/Cosmic Rays II*, edited, pp. 551-612, Springer.

Lamarque, J. F., F. Dentener, J. McConnell, C.-U. Ro, M. Shaw, R. Vet, D. Bergmann, P. Cameron-Smith, S. Dalsoren, R. Doherty, G. Faluvegi, S. J. Ghan, B. Josse, Y. H. Lee, I. A. MacKenzie, D. Plummer, D. T. Shindell, R. B. Skeie, D. S. Stevenson, S. Strode, G. Zeng, M. Curran, D. Dahl-Jensen, S. Das, D. Fritzsche, and M. Nolan (2013a), Multi-model mean nitrogen and sulfur deposition from the Atmospheric Chemistry and Climate Model Intercomparison Project

(ACCMIP): evaluation of historical and projected future changes, *Atmos Chem Phys*, *13*(16), 7997-8018.

Lamarque, J. F., D. T. Shindell, B. Josse, P. J. Young, I. Cionni, V. Eyring, D. Bergmann, P. Cameron-Smith, W. J. Collins, R. Doherty, S. Dalsoren, G. Faluvegi, G. Folberth, S. J. Ghan, L. W. Horowitz, Y. H. Lee, I. A. MacKenzie, T. Nagashima, V. Naik, D. Plummer, M. Righi, S. T. Rumbold, M. Schulz, R. B. Skeie, D. S. Stevenson, S. Strode, K. Sudo, S. Szopa, A. Voulgarakis, and G. Zeng (2013b), The Atmospheric Chemistry and Climate Model Intercomparison Project (ACCMIP): overview and description of models, simulations and climate diagnostics, *Geosci Model Dev*, *6*(1), 179-206.

Lanciki, A., J. Cole-Dai, M. H. Thiemens, and J. Savarino (2012), Sulfur isotope evidence of little or no stratospheric impact by the 1783 Laki volcanic eruption, *Geophys Res Lett*, *39*, doi:10.1029/2011gl050075.

Langford, A. O., J. Brioude, O. R. Cooper, C. J. Senff, R. J. Alvarez, R. M. Hardesty, B. J. Johnson, and S. J. Oltmans (2012), Stratospheric influence on surface ozone in the Los Angeles area during late spring and early summer of 2010, *J Geophys Res-Atmos*, *117*.

Langford, A. O., R. B. Pierce, and P. J. Schultz (2015a), Stratospheric intrusions, the Santa Ana winds, and wildland fires in Southern California, *Geophys Res Lett*, *42*(14), 6091-6097.

Langford, A. O., C.J. Senff, R.J. Alvarez, J. Brioude, O.R. Cooper, J.S. Holloway, M.Y. Lin, R.D. Marchbanks, R.B. Pierce, S.P. Sandberg, A.M. Weickmann, E.J. Williams (2015b), An overview of the 2013 Las Vegas Ozone Study (LVOS): Impact of stratospheric intrusions and long-range transport on surface air quality, *Atmos Environ*, *109*, 305-322.

Lee, C. (2000), Multiple Stable Oxygen Isotopic Studies of Atmospheric Sulfate: A New Quantitative Way to Understand Sulfate Formation Processes in the Atmosphere, University of California San Diego, San Diego.

Lee, C., R. V. Martin, A. van Donkelaar, H. Lee, R. R. Dickerson, J. C. Hains, N. Krotkov, A. Richter, K. Vinnikov, and J. J. Schwab (2011), SO2 emissions and lifetimes: Estimates from inverse modeling using in situ and global, space-based (SCIAMACHY and OMI) observations, *J Geophys Res-Atmos*, *116*, D06304, doi:10.1029/2010jd014758.

Lee, C. C. W., J. Savarino, H. Cachier, and M. H. Thiemens (2002), Sulfur (S-32, S-33, S-34, S-36) and oxygen (O-16, O-17, O-18) isotopic ratios of primary sulfate produced from combustion processes, *Tellus B*, *54*(3), 193-200, doi:10.1034/J.1600-0889.2002.01384.X.

Lee, C. C. W., J. Savarino, and M. H. Thiemens (2001), Mass independent oxygen isotopic composition of atmospheric sulfate: Origin and implications for the present and past atmosphere of earth and mars, *Geophys Res Lett*, *28*(9), 1783-1786, doi:10.1029/2000gl011826.

Lee, C. C. W., and M. H. Thiemens (2001), The delta O-17 and delta O-18 measurements of atmospheric sulfate from a coastal and high alpine region: A mass-independent isotopic anomaly, *J Geophys Res-Atmos*, *106*(D15), 17359-17373, doi:10.1029/2000jd900805.

Lee, D. C., and A. N. Halliday (1996), Hf-W isotopic evidence for rapid accretion and differentiation in the early solar system, *Science*, *274*(5294), 1876-1879.

Lee, H. N., L. Tositti, X. Zheng, and P. Bonasoni (2007), Analyses and comparisons of variations of Be-7, Pb-210, and Be-7/Pb-210 with ozone observations at two Global Atmosphere Watch stations from high mountains, *J Geophys Res-Atmos*, *112*(D5), doi:10.1029/2006jd007421.

Lee, T., D. A. Papanastassiou, and G. J. Wasserburg (1977), Al-26 in Early Solar-System - Fossil or Fuel, *Astrophys J*, *211*(2), L107-L110.

Lelieveld, J., J. S. Evans, M. Fnais, D. Giannadaki, and A. Pozzer (2015), The contribution of outdoor air pollution sources to premature mortality on a global scale, *Nature*, *525*(7569), 367-371.

Lelieveld, J., and J. Heintzenberg (1992), Sulfate Cooling Effect on Climate through in-Cloud Oxidation of Anthropogenic SO2, *Science*, *258*(5079), 117-120.

Li, C. L., C. Bosch, S. C. Kang, A. Andersson, P. F. Chen, Q. G. Zhang, Z. Y. Cong, B. Chen, D. H. Qin, and O. Gustafsson (2016), Sources of black carbon to the Himalayan-Tibetan Plateau glaciers, *Nat Commun*, *7*, 12574.

Li, C. L., S. C. Kang, and Q. G. Zhang (2009a), Elemental composition of Tibetan Plateau top soils and its effect on evaluating atmospheric pollution transport, *Environ Pollut*, *157*(8-9), 2261-2265.

Li, C. L., S. C. Kang, Q. G. Zhang, and S. P. Gao (2012), Geochemical evidence on the source regions of Tibetan Plateau dusts during non-monsoon period in 2008/09, *Atmos Environ*, *59*, 382-388, doi:10.1016/J.Atmosenv.2012.06.006.

Li, G., N. Bei, J. Cao, R. Huang, J. Wu, T. Feng, Y. Wang, S. Liu, Q. Zhang, and X. Tie (2017a), A possible pathway for rapid growth of sulfate during haze days in China, *Atmos Chem Phys*, *17*(5), 3301-3316.

Li, J., Z. F. Wang, H. Akimoto, J. Tang, and I. Uno (2009b), Modeling of the impacts of China's anthropogenic pollutants on the surface ozone summer maximum on the northern Tibetan Plateau, *Geophys Res Lett*, *36*, doi:10.1029/2009gl041123.

Li, L., Z. M. Chen, Y. H. Zhang, T. Zhu, J. L. Li, and J. Ding (2006), Kinetics and mechanism of heterogeneous oxidation of sulfur dioxide by ozone on surface of calcium carbonate, *Atmos Chem Phys*, *6*, 2453-2464.

Li, W., L. Xu, X. Liu, J. Zhang, Y. Lin, X. Yao, H. Gao, D. Zhang, J. Chen, and W. Wang (2017b), Air pollution–aerosol interactions produce more bioavailable iron for ocean ecosystems, *Science Advances*, *3*(3), e1601749.

Li, X. Q., H. M. Bao, Y. Q. Gan, A. G. Zhou, and Y. D. Liu (2013), Multiple oxygen and sulfur isotope compositions of secondary atmospheric sulfate in a mega-city in central China, *Atmos Environ*, *81*, 591-599, doi:10.1016/J.Atmosenv.2013.09.051.

Liang, M. C., and S. Mahata (2015), Oxygen anomaly in near surface carbon dioxide reveals deep stratospheric intrusion, *Sci Rep-Uk*, *5*.

Liang, M. C., J. Tang, C. Y. Chan, X. D. Zheng, and Y. L. Yung (2008), Signature of stratospheric air at the Tibetan Plateau, *Geophys Res Lett*, *35*(20).

Liao, J., L. G. Huey, D. J. Tanner, F. M. Flocke, J. J. Orlando, J. A. Neuman, J. B. Nowak, A. J. Weinheimer, S. R. Hall, J. N. Smith, A. Fried, R. M. Staebler, Y. Wang, J.-H. Koo, C. A. Cantrell, P. Weibring, J. Walega, D. J. Knapp, P. B. Shepson, C. R. Stephens (2012), Observations of inorganic bromine (HOBr, BrO, and Br-2) speciation at Barrow, Alaska, in spring 2009, *J Geophys Res-Atmos*, *117*, D00R16.

Lin, C. Y., F. Chen, J. C. Huang, W. C. Chen, Y. A. Liou, W. N. Chen, and S. C. Liu (2008a), Urban heat island effect and its impact on boundary layer development and land-sea circulation over northern Taiwan, *Atmos Environ*, *42*(22), 5635-5649.

Lin, J. T., D. Pan, S. J. Davis, Q. Zhang, K. B. He, C. Wang, D. G. Streets, D. J. Wuebbles, and D. B. Guan (2014a), China's international trade and air pollution in the United States, *P Natl Acad Sci USA*, *111*(5), 1736-1741.

Lin, M., S. Biglari, and M. H. Thiemens (2017a), Quantification of Gas-to-Particle Conversion Rates of Sulfur in the Terrestrial Atmosphere Using High-Sensitivity Measurements of Cosmogenic 35S, *ACS Earth and Space Chemistry*.

Lin, M., S. Biglari, Z. Zhang, D. Crocker, J. Tao, B. Su, L. Liu, and M. H. Thiemens (2017b), Vertically uniform formation pathways of tropospheric sulfate aerosols in East China detected from triple stable oxygen and radiogenic sulfur isotopes, *Geophys Res Lett*.

Lin, M., S. Biglari, Z. S. Zhang, D. Crocker, J. Tao, B. B. Su, L. Z. Liu, and M. H. Thiemens (2017c), Vertically uniform formation pathways of tropospheric sulfate aerosols in East China detected from triple stable oxygen and radiogenic sulfur isotopes, *Geophys Res Lett*, *44*(10), 5187-5196.

Lin, M., I. N. Chan, C. Y. Chan, G. Engling, and W. Bloss (2012a), Implications of regional surface ozone increases on visibility degradation in southeast China, *Tellus B*, *64*, 19625, doi:10.3402/Tellusb.V64i0.19625.

Lin, M., T. Holloway, G. R. Carmichael, and A. M. Fiore (2010), Quantifying pollution inflow and outflow over East Asia in spring with regional and global models, *Atmos Chem Phys*, *10*(9), 4221-4239.

Lin, M., L. Su, R. Shaheen, J. C. H. Fung, and M. H. Thiemens (2016a), Detection of deep stratospheric intrusions by cosmogenic S-35, *P Natl Acad Sci USA*, *113*(40), 11131-11136.

Lin, M., K. Wang, S. Kang, and M. H. Thiemens (2017d), Simple Method for High-Sensitivity Determination of Cosmogenic 35S in Snow and Water Samples Collected from Remote Regions, *Anal Chem*, *89*(7), 4116-4123, doi:10.1021/acs.analchem.6b05066.

Lin, M., Z. S. Zhang, L. Su, J. Hill-Falkenthal, A. Priyadarshi, Q. G. Zhang, G. S. Zhang, S. C. Kang, C. Y. Chan, and M. H. Thiemens (2016b), Resolving the impact of stratosphere-to-troposphere transport on the sulfur cycle and surface ozone over the Tibetan Plateau using a cosmogenic S-35 tracer, *J Geophys Res-Atmos*, *121*(1), 439-456.

Lin, M., Z. S. Zhang, L. Su, B. B. Su, L. Z. Liu, J. Tao, J. C. H. Fung, and M. H. Thiemens (2016c), Unexpected high S-35 concentration revealing strong downward transport of stratospheric air during the monsoon transitional period in East Asia, *Geophys Res Lett*, *43*(5), 2315-2322.

Lin, M. Y., A. M. Fiore, O. R. Cooper, L. W. Horowitz, A. O. Langford, H. Levy, B. J. Johnson, V. Naik, S. J. Oltmans, and C. J. Senff (2012b), Springtime high surface ozone events over the western United States: Quantifying the role of stratospheric intrusions, *J Geophys Res-Atmos*, *117*, doi:10.1029/2012jd018151.

Lin, M. Y., A. M. Fiore, L. W. Horowitz, A. O. Langford, S. J. Oltmans, D. Tarasick, and H. E. Rieder (2015), Climate variability modulates western US ozone air quality in spring via deep stratospheric intrusions, *Nat Commun*, *6*.

Lin, W. L., T. Zhu, Y. Song, H. Zou, M. Y. Tang, X. Y. Tang, and J. X. Hu (2008b), Photolysis of surface O-3 and production potential of OH radicals in the atmosphere over the Tibetan Plateau, *J Geophys Res-Atmos*, *113*(D2), D02309, doi:10.1029/2007jd008831.

Lin, W. L., T. Zhu, Y. Song, H. Zou, M. Y. Tang, X. Y. Tang, and J. X. Hu (2008c), Photolysis of surface O-3 and production potential of OH radicals in the atmosphere over the Tibetan Plateau, *J Geophys Res-Atmos*, *113*(D2), doi:10.1029/2007jd008831.

Lin, Y. C., C. A. Huh, S. C. Hsu, C. Y. Lin, M. C. Liang, and P. H. Lin (2014b), Stratospheric influence on the concentration and seasonal cycle of lower tropospheric ozone: Observation at Mount Hehuan, Taiwan, *J Geophys Res-Atmos*, *119*(6), 3527-3536, doi:10.1002/2013jd020736.

Liu, B., Z. Cong, Y. Wang, J. Xin, X. Wan, Y. Pan, Z. Liu, Y. Wang, G. Zhang, Z. Wang, Y. Wang, and S. Kang (2017), Background aerosol over the Himalayas and Tibetan Plateau: observed characteristics of aerosol mass loading, *Atmos Chem Phys*, *17*(1), 449-463.

Liu, H. Y., D. B. Considine, L. W. Horowitz, J. H. Crawford, J. M. Rodriguez, S. E. Strahan, M. R. Damon, S. D. Steenrod, X. Xu, J. Kouatchou, C. Carouge, and R. M. Yantosca (2016a), Using beryllium-7 to assess cross-tropopause transport in global models, *Atmos Chem Phys*, *16*(7), 4641-4659.

Liu, H. Y., D. J. Jacob, L. Y. Chan, S. J. Oltmans, I. Bey, R. M. Yantosca, J. M. Harris, B. N. Duncan, and R. V. Martin (2002), Sources of tropospheric ozone along the Asian Pacific Rim: An analysis of ozonesonde observations, *J Geophys Res-Atmos*, *107*(D21).

Liu, P. F., Y. J. Li, Y. Wang, M. K. Gilles, R. A. Zaveri, A. K. Bertram, and S. T. Martin (2016b), Lability of secondary organic particulate matter, *P Natl Acad Sci USA*, *113*(45), 12643-12648.

Liu, S. C., M. Trainer, F. C. Fehsenfeld, D. D. Parrish, E. J. Williams, D. W. Fahey, G. Hubler, and P. C. Murphy (1987), Ozone Production in the Rural Troposphere and the Implications for Regional and Global Ozone Distributions, *J Geophys Res-Atmos*, *92*(D4), 4191-4207.

Liu, T., F. Wang, G. Michalski, X. H. Xia, and S. D. Liu (2013), Using N-15, O-17, and O-18 To Determine Nitrate Sources in the Yellow River, China, *Environ Sci Technol*, *47*(23), 13412-13421.

Longin, R. (1971), New Method of Collagen Extraction for Radiocarbon Dating, *Nature*, *230*(5291), 241.

Longo, A. F., Y. Feng, B. Lai, W. M. Landing, R. U. Shelley, A. Nenes, N. Mihalopoulos, K. Violaki, and E. D. Ingall (2016), Influence of Atmospheric Processes on the Solubility and Composition of Iron in Saharan Dust, *Environ Sci Technol*, *50*(13), 6912-6920.

Lu, Z., D. G. Streets, Q. Zhang, S. Wang, G. R. Carmichael, Y. F. Cheng, C. Wei, M. Chin, T. Diehl, and Q. Tan (2010), Sulfur dioxide emissions in China and sulfur trends in East Asia since 2000, *Atmos Chem Phys*, *10*(13), 6311-6331, doi:10.5194/Acp-10-6311-2010.

Luck, J. M., J. L. Birck, and C. J. Allegre (1980), Re-187-Os-187 Systematics in Meteorites - Early Chronology of the Solar-System and Age of the Galaxy, *Nature*, *283*(5744), 256-259.

Luria, M., R. E. Imhoff, R. J. Valente, W. J. Parkhurst, and R. L. Tanner (2001), Rates of conversion of sulfur dioxide to sulfate in a scrubbed power plant plume, *J Air Waste Manage*, *51*(10), 1408-1413.

Luz, B., and E. Barkan (2005), The isotopic ratios O-17/O-16 and O-18/O-16 in molecular oxygen and their significance in biogeochemistry, *Geochim Cosmochim Ac*, *69*(5), 1099-1110.

Lyons, J. R. (2001), Transfer of mass-independent fractionation in ozone to other oxygen-containing radicals in the atmosphere, *Geophys Res Lett*, *28*(17), 3231-3234.

Lyons, J. R. (2007), Mass-independent fractionation of sulfur isotopes by isotope-selective photodissociation of SO2, *Geophys Res Lett*, *34*(22).

Lyons, J. R., R. S. Lewis, and R. N. Clayton (2009), Comment on "Experimental Test of Self-Shielding in Vacuum Ultraviolet Photodissociation of CO", *Science*, *324*(5934).

Lyons, T. W., and B. C. Gill (2010), Ancient Sulfur Cycling and Oxygenation of the Early Biosphere, *Elements*, *6*(2), 93-99.

Lyons, T. W., C. T. Reinhard, and N. J. Planavsky (2014), The rise of oxygen in Earth's early ocean and atmosphere, *Nature*, *506*(7488), 307-315.

Mahin, D. T., and R. T. Lofberg (1966), A Simplified Method of Sample Preparation for Determination of Tritium Carbon-14 or Sulfur-35 in Blood of Tissue by Liquid Scintillation Counting, *Anal Biochem*, *16*(3), 500.

Mandeville, C. W. (2010), Sulfur: A Ubiquitous and Useful Tracer in Earth and Planetary Sciences, *Elements*, *6*(2), 75-80.

Mao, H. T., and R. Talbot (2004), O-3 and CO in New England: Temporal variations and relationships, *J Geophys Res-Atmos*, *109*(D21).

Marlon, J. R., P. J. Bartlein, C. Carcaillet, D. G. Gavin, S. P. Harrison, P. E. Higuera, F. Joos, M. J. Power, and I. C. Prentice (2008), Climate and human influences on global biomass burning over the past two millennia, *Nat Geosci*, *1*(10), 697-702.

Martin, E., and I. Bindeman (2009), Mass-independent isotopic signatures of volcanic sulfate from three supereruption ash deposits in Lake Tecopa, California, *Earth Planet Sc Lett*, *282*(1-4), 102-114.

Masarik, J., and J. Beer (1999), Simulation of particle fluxes and cosmogenic nuclide production in the Earth's atmosphere, *J Geophys Res-Atmos*, *104*(D10), 12099-12111.

Masarik, J., and J. Beer (2009), An updated simulation of particle fluxes and cosmogenic nuclide production in the Earth's atmosphere, *J Geophys Res-Atmos*, *114*, D11103.

Masterson, A. L., J. Farquhar, and B. A. Wing (2011), Sulfur mass-independent fractionation patterns in the broadband UV photolysis of sulfur dioxide: Pressure and third body effects, *Earth Planet Sc Lett*, *306*(3-4), 253-260.

Mather, T. A., J. R. McCabe, V. K. Rai, M. H. Thiemens, D. M. Pyle, T. H. E. Heaton, H. J. Sloane, and G. R. Fern (2006), Oxygen and sulfur isotopic composition of volcanic sulfate aerosol at the point of emission, *J Geophys Res-Atmos*, *111*(D18).

Mauldin, R. L., E. Kosciuch, B. Henry, F. L. Eisele, R. Shetter, B. Lefer, G. Chen, D. Davis, G. Huey, and D. Tanner (2004), Measurements of OH, HO2+RO2, H2SO4, and MSA at the south pole during ISCAT 2000, *Atmos Environ*, *38*(32), 5423-5437, doi:10.1016/J.Atmosenv.2004.06.031.

McCabe, J. R., J. Savarino, B. Alexander, S. L. Gong, and M. H. Thiemens (2006), Isotopic constraints on non-photochemical sulfate production in the Arctic winter, *Geophys Res Lett*, *33*(5).

Mccrea, J. M. (1950), On the Isotopic Chemistry of Carbonates and a Paleotemperature Scale, *J Chem Phys*, *18*(6), 849-857.

McGrath, J. M., A. M. Betzelberger, S. W. Wang, E. Shook, X. G. Zhu, S. P. Long, and E. A. Ainsworth (2015), An analysis of ozone damage to historical maize and soybean yields in the United States, *P Natl Acad Sci USA*, *112*(46), 14390-14395.

McLinden, C. A., V. Fioletov, M. W. Shephard, N. Krotkov, C. Li, R. V. Martin, M. D. Moran, and J. Joiner (2016), Space-based detection of missing sulfur dioxide sources of global air pollution, *Nat Geosci*, *9*(7), 496.

Mcmurry, P. H., and J. C. Wilson (1983), Droplet Phase (Heterogeneous) and Gas-Phase (Homogeneous) Contributions to Secondary Ambient Aerosol Formation as Functions of Relative-Humidity, *J Geophys Res-Oc Atm*, *88*(Nc9), 5101-5108, doi:10.1029/Jc088ic09p05101.

Meagher, J. F., E. M. Bailey, and M. Luria (1983), The Seasonal-Variation of the Atmospheric SO2 to SO42- Conversion Rate, *J Geophys Res-Oc Atm*, *88*(Nc2), 1525-1527.

Meng, Z. Y., X. B. Xu, T. Wang, X. Y. Zhang, X. L. Yu, S. F. Wang, W. L. Lin, Y. Z. Chen, Y. A. Jiang, and X. Q. An (2010), Ambient sulfur dioxide, nitrogen dioxide, and ammonia at ten background and rural sites in China during 2007-2008, *Atmos Environ*, *44*(21-22), 2625-2631.

Michel, R. L., D. Campbell, D. Clow, and J. T. Turk (2000), Timescales for migration of atmospherically derived sulphate through an alpine/subalpine watershed, Loch Vale, Colorado, *Water Resour Res*, *36*(1), 27-36.

Ming, J., D. Q. Zhang, S. C. Kang, and W. S. Tian (2007), Aerosol and fresh snow chemistry in the East Rongbuk Glacier on the northern slope of Mt. Qomolangma (Everest), *J Geophys Res-Atmos*, *112*(D15), doi:10.1029/2007jd008618.

Minikin, A., M. Legrand, J. Hall, D. Wagenbach, C. Kleefeld, E. Wolff, E. C. Pasteur, and F. Ducroz (1998), Sulfur-containing species (sulfate and methanesulfonate) in coastal Antarctic aerosol and precipitation, *J Geophys Res-Atmos*, *103*(D9), 10975-10990, doi:Doi 10.1029/98jd00249.

Montinaro, A., H. Strauss, P. R.D. Mason, D. Roerdink, C. Münker, U. Schwarz-Schampera, N. T. Arndt, J. Farquhar, N. J. Beukes, J. Gutzmer, M. Peters (2015), Paleoarchean sulfur cycling: Multiple sulfur isotope constraints from the Barberton Greenstone Belt, South Africa, *Precambrian Res*, *267*, 311-322.

Muller, E., P. Philippot, C. Rollion-Bard, and P. Cartigny (2016), Multiple sulfur-isotope signatures in Archean sulfates and their implications for the chemistry and dynamics of the early atmosphere, *P Natl Acad Sci USA*, *113*(27), 7432-7437.

Muller, E., P. Philippot, C. Rollion-Bard, P. Cartigny, N. Assayag, J. Marin-Carbonne, M. R. Mohan, and S. Sarma (2017), Primary sulfur isotope signatures preserved in high-grade Archean barite deposits of the Sargur Group, Dharwar Craton, India, *Precambrian Res*, *295*, 38-47.

Newland, M. J., A. R. Rickard, L. Vereecken, A. Munoz, M. Rodenas, and W. J. Bloss (2015), Atmospheric isoprene ozonolysis: impacts of stabilised Criegee intermediate reactions with SO2, H2O and dimethyl sulfide, *Atmos Chem Phys*, *15*(16), 9521-9536.

Nier, A. O. (1947), A Mass Spectrometer for Isotope and Gas Analysis, *Rev Sci Instrum*, *18*(6), 398-411.

Nieto, R., M. Sprenger, H. Wernli, R. M. Trigo, and L. Gimeno (2008), Identification and Climatology of Cut-off Lows near the Tropopause, *Ann Ny Acad Sci*, *1146*, 256-290.

Oduro, H., B. Harms, H. O. Sintim, A. J. Kaufman, G. Cody, and J. Farquhar (2011), Evidence of magnetic isotope effects during thermochemical sulfate reduction, *P Natl Acad Sci USA*, *108*(43), 17635-17638.

Oltmans, S. J., B. J. Johnson, J. M. Harris, A. M. Thompson, H. Y. Liu, C. Y. Chan, H. Vömel, T. Fujimoto, V. G. Brackett, W. L. Chang, J.-P. Chen, J. H. Kim, L. Y. Chan, H.-W. Chang (2004), Tropospheric ozone over the North Pacific from ozonesonde observations, *J Geophys Res-Atmos*, *109*(D15).

Ono, S. (2017), Photochemistry of Sulfur Dioxide and the Origin of Mass-Independent Isotope Fractionation in Earth's Atmosphere, *Annual Review of Earth and Planetary Sciences*, *45*(1), 301-329.

Ono, S., N. J. Beukes, D. Rumble, and M. L. Fogel (2006a), Early evolution of atmospheric oxygen from multiple-sulfur and carbon isotope records of the 2.9 Ga Mozaan Group of the Pongola Supergroup, Southern Africa, *S Afr J Geol*, *109*(1-2), 97-108.

Ono, S., A. R. Whitehill, and J. R. Lyons (2013), Contribution of isotopologue self-shielding to sulfur mass-independent fractionation during sulfur dioxide photolysis, *J Geophys Res-Atmos*, *118*(5), 2444-2454.

Ono, S., B. Wing, D. Johnston, J. Farquhar, and D. Rumble (2006b), Mass-dependent fractionation of quadruple stable sulfur isotope system as a new tracer of sulfur biogeochemical cycles, *Geochim Cosmochim Ac*, *70*(9), 2238-2252.

Ono, S. H., N. J. Beukes, and D. Rumble (2009a), Origin of two distinct multiple-sulfur isotope compositions of pyrite in the 2.5 Ga Klein Naute Formation, Griqualand West Basin, South Africa, *Precambrian Res*, *169*(1-4), 48-57.

Ono, S. H., A. J. Kaufman, J. Farquhar, D. Y. Sumner, and N. J. Beukes (2009b), Lithofacies control on multiple-sulfur isotope records and Neoarchean sulfur cycles, *Precambrian Res*, *169*(1-4), 58-67.

Parrish, D. D., M. Trainer, J. S. Holloway, J. E. Yee, M. S. Warshawsky, F. C. Fehsenfeld, G. L. Forbes, and J. L. Moody (1998), Relationships between ozone and carbon monoxide at surface sites in the North Atlantic region, *J Geophys Res-Atmos*, *103*(D11), 13357-13376.

Patris, N., S. S. Cliff, P. K. Quinn, M. Kasem, and M. H. Thiemens (2007), Isotopic analysis of aerosol sulfate and nitrate during ITCT-2k2: Determination of different formation pathways as a function of particle size, *J Geophys Res-Atmos*, *112*(D23).

Pavlov, A. A., and J. F. Kasting (2002), Mass-independent fractionation of sulfur isotopes in Archean sediments: Strong evidence for an anoxic Archean atmosphere, *Astrobiology*, *2*(1), 27-41.

Pavlov, A. A., M. J. Mills, and O. B. Toon (2005), Mystery of the volcanic mass-independent sulfur isotope fractionation signature in the Antarctic ice core, *Geophys Res Lett*, *32*(12).

Pearl, J., R. Hanel, V. Kunde, W. Maguire, K. Fox, S. Gupta, C. Ponnamperuma, and F. Raulin (1979), Identification of Gaseous So2 and New Upper Limits for Other Gases on Io, *Nature*, *280*(5725), 755-758.

Pearson, G., F. Davies, and C. Collier (2010), Remote sensing of the tropical rain forest boundary layer using pulsed Doppler lidar, *Atmos Chem Phys*, *10*(13), 5891-5901.

Peng, C. T. (1960), Quenching of Fluorescence in Liquid Scintillation Counting of Labeled Organic Compounds, *Anal Chem*, *32*(10), 1292-1296.

PerkinElmer (2014), Application Note: Counting Aqueous Samples by LSC.*Rep.*, 7 pp.

Philip, S., R. V Martin, G. Snider, C. L. Weagle, A. van Donkelaar, M. Brauer, D. K. Henze, Z. Klimont, C. Venkataraman, S. K. Guttikunda and Q. Zhang (2017), Anthropogenic fugitive, combustion and industrial dust is a significant, underrepresented fine particulate matter source in global atmospheric models, *Environ Res Lett*, *12*(4).

Philippot, P., M. Van Zuilen, K. Lepot, C. Thomazo, J. Farquhar, and M. J. Van Kranendonk (2007), Early Archaean microorganisms preferred elemental sulfur, not sulfate, *Science*, *317*(5844), 1534-1537.

Philippot, P., M. van Zuilen, and C. Rollion-Bard (2012), Variations in atmospheric sulphur chemistry on early Earth linked to volcanic activity, *Nat Geosci*, *5*(9), 668-U100.

Pierce, D. W., D. R. Cayan, T. Das, E. P. Maurer, N. L. Miller, Y. Bao, M. Kanamitsu, K. Yoshimura, M. A. Snyder, L. C. Sloan, G. Franco, and M. Tyree (2013), The Key Role of Heavy Precipitation Events in Climate Model Disagreements of Future Annual Precipitation Changes in California, *J Climate*, *26*(16), 5879-5896.

Plummer, L. N., E. Busenberg, J. K. Bohlke, D. L. Nelms, R. L. Michel, and P. Schlosser (2001), Groundwater residence times in Shenandoah National Park, Blue Ridge Mountains, Virginia, USA: a multi-tracer approach, *Chem Geol*, *179*(1-4), 93-111.

Poluianov, S. V., G. A. Kovaltsov, A. L. Mishev, and I. G. Usoskin (2016), Production of cosmogenic isotopes Be-7, Be-10, C-14, Na-22, and Cl-36 in the atmosphere: Altitudinal profiles of yield functions, *J Geophys Res-Atmos*, *121*(13), 8125-8136.

Pritchard, H. D. (2017), Asia's glaciers are a regionally important buffer against drought, *Nature*, *545*(7653), 169-174.

Priyadarshi, A., G. Dominguez, J. Savarino, and M. Thiemens (2011a), Cosmogenic S-35: A unique tracer to Antarctic atmospheric chemistry and the polar vortex, *Geophys Res Lett*, *38*, doi:10.1029/2011gl047469.

Priyadarshi, A., G. Dominguez, and M. H. Thiemens (2011b), Evidence of neutron leakage at the Fukushima nuclear plant from measurements of radioactive S-35 in California, *P Natl Acad Sci USA*, *108*(35), 14422-14425, doi:10.1073/Pnas.1109449108.

Priyadarshi, A., J. Hill-Falkenthal, E. Coupal, G. Dominguez, and M. H. Thiemens (2012a), Measurements of S-35 in the marine boundary layer at La Jolla, California: A new technique for tracing air mass mixing during Santa Ana events, *J Geophys Res-Atmos*, *117*, L13808, doi:10.1029/2011jd016878.

Priyadarshi, A., J. Hill-Falkenthal, E. Coupal, G. Dominguez, and M. H. Thiemens (2012b), Measurements of S-35 in the marine boundary layer at La Jolla, California: A new technique for tracing air mass mixing during Santa Ana events, *J Geophys Res-Atmos*, *117*, D08301, doi:10.1029/2011jd016878.

Priyadarshi, A., J. Hill-Falkenthal, M. Thiemens, Z. S. Zhang, M. Lin, C. Y. Chan, and S. C. Kang (2014), Cosmogenic S-35 measurements in the Tibetan Plateau to quantify glacier snowmelt, *J Geophys Res-Atmos*, *119*(7), 4125-4135, doi:10.1002/2013jd019801.

Priyadarshi, A., J. Hill-Falkenthal, M. H. Thiemens, N. Yoshida, S. Toyoda, K. Yamada, A. Mukotaka, A. Fujii, M. Uematsu, S. Hatakeyama, I. Noguchi, Y. Nojiri, H. Tanimoto (2013), Detection of radioactive S-35 at Fukushima and other Japanese sites, *J Geophys Res-Atmos*, *118*(2), 1020-1027, doi:10.1029/2012jd018485.

Randerson, J. T., I. G. Enting, E. A. G. Schuur, K. Caldeira, and I. Y. Fung (2002), Seasonal and latitudinal variability of troposphere Delta(CO2)-C-14: Post bomb contributions from fossil fuels, oceans, the stratosphere, and the terrestrial biosphere, *Global Biogeochem Cy*, *16*(4).

Ren, P. B. C., Y. Gjessing, and F. Sigernes (1999), Measurements of solar ultra violet radiation on the Tibetan Plateau and comparisons with discrete ordinate method simulations, *J Atmos Sol-Terr Phy*, *61*(6), 425-446, doi:10.1016/S1364-6826(99)00005-X.

Ren, P. B. C., F. Sigernes, and Y. Gjessing (1997), Ground-based measurements of solar ultraviolet radiation in Tibet: Preliminary results, *Geophys Res Lett*, *24*(11), 1359-1362.

Riva, M., S. Tomaz, T. Q. Cui, Y. H. Lin, E. Perraudin, A. Gold, E. A. Stone, E. Villenave, and J. D. Surratt (2015), Evidence for an Unrecognized Secondary Anthropogenic Source of

Organosulfates and Sulfonates: Gas-Phase Oxidation of Polycyclic Aromatic Hydrocarbons in the Presence of Sulfate Aerosol, *Environ Sci Technol*, *49*(11), 6654-6664.

Roerdink, D. L., P. R. D. Mason, J. Farquhar, and T. Reimer (2012), Multiple sulfur isotopes in Paleoarchean barites identify an important role for microbial sulfate reduction in the early marine environment, *Earth Planet Sc Lett*, *331*, 177-186.

Rogora, M., R. Mosello, and S. Arisci (2003), The effect of climate warming on the hydrochemistry of Alpine Lakes, *Water Air Soil Poll*, *148*(1-4), 347-361.

Romero, A. B., and M. H. Thiemens (2003), Mass-independent sulfur isotopic compositions in present-day sulfate aerosols, *J Geophys Res-Atmos*, *108*(D16), doi:10.1029/2003jd003660.

Rosenfeld, D., S. Sherwood, R. Wood, and L. Donner (2014), Climate Effects of Aerosol-Cloud Interactions, *Science*, *343*(6169), 379-380.

Saiz-Lopez, A., and R. von Glasow (2012), Reactive halogen chemistry in the troposphere, *Chem Soc Rev*, *41*(19), 6448-6472.

Salerno, F., M. Rogora, R. Balestrini, A. Lami, G. A. Tartari, S. Thakuri, D. Godone, M. Freppaz, and G. Tartari (2016), Glacier Melting Increases the Solute Concentrations of Himalayan Glacial Lakes, *Environ Sci Technol*, *50*(17), 9150-9160.

Savarino, J., B. Alexander, V. Darmohusodo, and M. H. Thiemens (2001), Sulfur and oxygen isotope analysis of sulfate at micromole levels using a pyrolysis technique in a continuous flow system, *Anal Chem*, *73*(18), 4457-4462, doi:10.1021/Ac010017f.

Savarino, J., C. C. W. Lee, and M. H. Thiemens (2000), Laboratory oxygen isotopic study of sulfur (IV) oxidation: Origin of the mass-independent oxygen isotopic anomaly in atmospheric sulfates and sulfate mineral deposits on Earth, *J Geophys Res-Atmos*, *105*(D23), 29079-29088, doi:10.1029/2000jd900456.

Savarino, J., A. Romero, J. Cole-Dai, S. Bekki, and M. H. Thiemens (2003), UV induced mass-independent sulfur isotope fractionation in stratospheric volcanic sulfate, *Geophys Res Lett*, *30*(21), doi:10.1029/2003gl018134.

Savarino, J., and M. H. Thiemens (1999), Analytical procedure to determine both delta O-18 and delta O-17 of H2O2 in natural water and first measurements, *Atmos Environ*, *33*(22), 3683-3690.

Schauer, A. J., S. A. Kunasek, E. D. Sofen, J. Erbland, J. Savarino, B. W. Johnson, H. M. Amos, R. Shaheen, M. Abaunza, T. L. Jackson, M. H. Thiemens, B. Alexander (2012), Oxygen isotope exchange with quartz during pyrolysis of silver sulfate and silver nitrate, *Rapid Commun Mass Sp*, *26*(18), 2151-2157, doi:10.1002/Rcm.6332.

Scott, R. B., F. G. Brickwedde, H. C. Urey, and M. H. Wahl (1934), The Vapor Pressures and Derived Thermal Properties of Hydrogen and Deuterium, *J Chem Phys*, *2*(8).

Sedlacek, W. A., E. J. Mroz, A. L. Lazrus, and B. W. Gandrud (1983), A Decade of Stratospheric Sulfate Measurements Compared with Observations of Volcanic-Eruptions, *J Geophys Res-Oc Atm*, *88*(Nc6), 3741-3776, doi:Doi 10.1029/Jc088ic06p03741.

Seidel, D. J., Y. H. Zhang, A. Beljaars, J. C. Golaz, A. R. Jacobson, and B. Medeiros (2012), Climatology of the planetary boundary layer over the continental United States and Europe, *J Geophys Res-Atmos*, *117*, D17106.

Semple, J. L., and G. W. K. Moore (2008), First observations of surface ozone concentration from the summit region of Mount Everest, *Geophys Res Lett*, *35*(20), doi:10.1029/2008gl035295.

Shaheen, R., M. Abauanza, T. L. Jackson, J. McCabe, J. Savarino, and M. H. Thiemens (2013), Tales of volcanoes and El-Nino southern oscillations with the oxygen isotope anomaly of sulfate aerosol, *P Natl Acad Sci USA*, *110*(44), 17662-17667.

Shaheen, R., M. M. Abaunza, T. L. Jackson, J. McCabe, J. Savarino, and M. H. Thiemens (2014), Large sulfur-isotope anomaly in nonvolcanic sulfate aerosol and its implications for the Archean atmosphere, *P Natl Acad Sci USA*, *111*(33), 11979-11983, doi:10.1073/Pnas.1406315111.

Shaheen, R., A. Abramian, J. Horn, G. Dominguez, R. Sullivan, and M. H. Thiemens (2010), Detection of oxygen isotopic anomaly in terrestrial atmospheric carbonates and its implications to Mars, *P Natl Acad Sci USA*, *107*(47), 20213-20218.

Shao, M., X. Y. Tang, Y. H. Zhang, and W. J. Li (2006), City clusters in China: air and surface water pollution, *Front Ecol Environ*, *4*(7), 353-361.

Sharma, C. M., S. Sharma, R. M. Bajracharya, S. Gurung, I. Juttner, S. C. Kang, Q. G. Zhang, and Q. Li (2012), First results on bathymetry and limnology of high-altitude lakes in the Gokyo Valley, Sagarmatha (Everest) National Park, Nepal, *Limnology*, *13*(1), 181-192.

Shen, X. H., T. Lee, J. Guo, X. Wang, P. Li, P. Xu, Y. Wang, Y. Ren, W. Wang, T. Wang, Y. Li, S. A. Carn, J. L. Collett (2012), Aqueous phase sulfate production in clouds in eastern China, *Atmos Environ*, *62*, 502-511.

Shen, Y., J. Farquhar, A. Masterson, A. J. Kaufman, and R. Buick (2009), Evaluating the role of microbial sulfate reduction in the early Archean using quadruple isotope systematics, *Earth Planet Sc Lett*, *279*(3-4), 383-391.

Shen, Y. A., R. Buick, and D. E. Canfield (2001), Isotopic evidence for microbial sulphate reduction in the early Archaean era, *Nature*, *410*(6824), 77-81.

Sheng, J. X., D. K. Weisenstein, B. P. Luo, E. Rozanov, A. Stenke, J. Anet, H. Bingemer, and T. Peter (2015), Global atmospheric sulfur budget under volcanically quiescent conditions: Aerosol-chemistry-climate model predictions and validation, *J Geophys Res-Atmos*, *120*(1), 256-276.

Silva, S. R., C. Kendall, D. H. Wilkison, A. C. Ziegler, C. C. Y. Chang, and R. J. Avanzino (2000), A new method for collection of nitrate from fresh water and the analysis of nitrogen and oxygen isotope ratios, *Journal of Hydrology*, *228*(1-2), 22-36.

Skerlak, B., M. Sprenger, and H. Wernli (2014), A global climatology of stratosphere-troposphere exchange using the ERA-Interim data set from 1979 to 2011, *Atmos Chem Phys*, *14*(2), 913-937, doi:Doi 10.5194/Acp-14-913-2014.

Skoog, D. A., F. J. Holler, and S. R. Crouch (2007), *Principles of instrumental analysis*, Thomson Brooks/Cole.

Smith, G. J. (1994), Temperature-Dependence of Oxygen Quenching of Aromatic Hydrocarbon Triplet-States in Viscous Solution, *J Am Chem Soc*, *116*(11), 5005-5006.

Sofen, E. D., B. Alexander, and S. A. Kunasek (2011), The impact of anthropogenic emissions on atmospheric sulfate production pathways, oxidants, and ice core Delta O-17(SO42-), *Atmos Chem Phys*, *11*(7), 3565-3578.

Sokolik, I. N., and O. B. Toon (1996), Direct radiative forcing by anthropogenic airborne mineral aerosols, *Nature*, *381*(6584), 681-683.

Sommers, W. T. (1978), Lfm Forecast Variables Related to Santa-Ana Wind Occurrences, *Mon Weather Rev*, *106*(9), 1307-1316.

Spencer, J. R., K. L. Jessup, M. A. McGrath, G. E. Ballester, and R. Yelle (2000), Discovery of gaseous S-2 in Io's Pele plume, *Science*, *288*(5469), 1208-1210.

Sprenger, M., and H. Wernli (2003), A northern hemispheric climatology of cross-tropopause exchange for the ERA15 time period (1979-1993), *J Geophys Res-Atmos*, *108*(D12).

Squizzato, S., M. Masiol, A. Brunelli, S. Pistollato, E. Tarabotti, G. Rampazzo, and B. Pavoni (2013), Factors determining the formation of secondary inorganic aerosol: a case study in the Po Valley (Italy), *Atmos Chem Phys*, *13*(4), 1927-1939.

Stohl, A., P. Bonasoni, P. Cristofanelli, W. Collins, J. Feichter, A. Frank, C. Forster, E. Gerasopoulos, H. Gäggeler, P. James, T. Kentarchos, H. Kromp-Kolb, B. Krüger, C. Land, J. Meloen, A. Papayannis, A. Priller, P. Seibert, M. Sprenger, G. J. Roelofs, H. E. Scheel, C. Schnabel, P. Siegmund, L. Tobler, T. Trickl, H. Wernli, V. Wirth, P. Zanis, C. Zerefos (2003), Stratosphere-troposphere exchange: A review, and what we have learned from STACCATO, *J Geophys Res-Atmos*, *108*(D12), doi:10.1029/2002jd002490.

Stohl, A., M. Hittenberger, and G. Wotawa (1998), Validation of the Lagrangian particle dispersion model FLEXPART against large-scale tracer experiment data, *Atmos Environ*, *32*(24), 4245-4264, doi:10.1016/S1352-2310(98)00184-8.

Stohl, A., N. Spichtinger-Rakowsky, P. Bonasoni, H. Feldmann, M. Memmesheimer, H. E. Scheel, T. Trickl, S. Hubener, W. Ringer, and M. Mandl (2000), The influence of stratospheric intrusions on alpine ozone concentrations, *Atmos Environ*, *34*(9), 1323-1354, doi:Doi 10.1016/S1352-2310(99)00320-9.

Stutz, J., R. Ackermann, J. D. Fast, and L. Barrie (2002), Atmospheric reactive chlorine and bromine at the Great Salt Lake, Utah, *Geophys Res Lett*, *29*(10), 1380.

Su, B., Z. Zhang, J. Tao, J. Xu, X. Ji, X. Liu, and R. Zhang (2015), Characteristics of Water-soluble Inorganic Ions in PM2. 5 and PM2. 5-10 in Mountain Background Region of East China in Spring, *Environmental Science (in Chinese with English abstract)*, *36*(4), 1195-1201.

Su, S. S., B. G. Li, S. Y. Cui, and S. Tao (2011), Sulfur Dioxide Emissions from Combustion in China: From 1990 to 2007, *Environ Sci Technol*, *45*(19), 8403-8410.

Sullivan, J. T., T. J. Mcgee, A. M. Thompson, R. B. Pierce, G. K. Sumnicht, L. Twigg, E. Eloranta, and R. M. Hoff (2015), Characterizing the lifetime and occurrence of stratospheric-tropospheric exchange events in the rockymountain region using high-resolution ozone measurements, *J Geophys Res-Atmos*, *120*(24), 12410-12424.

Surratt, J. D., Y. Gómez-González, A. W. H. Chan, R. Vermeylen, M. Shahgholi, T. E. Kleindienst, E. O. Edney, J. H. Offenberg, M. Lewandowski, M. Jaoui, W. Maenhaut, M. Claeys, R. C. Flagan, and J. H. Seinfeld (2008), Organosulfate formation in biogenic secondary organic aerosol, *J Phys Chem A*, *112*(36), 8345-8378, doi:10.1021/jp802310p.

Tan, H. B., J. Chen, W. B. Rao, J. D. Yang, J. F. Ji, and A. R. Chivas (2014), Lead isotope variability of fine-grained river sediments in Tibetan Plateau water catchments: Implications for geochemical provinces and crustal evolution, *Lithos*, *190*, 13-26.

Tanaka, N., and K. K. Turekian (1991), Use of Cosmogenic S-35 to Determine the Rates of Removal of Atmospheric So2, *Nature*, *352*(6332), 226-228.

Tanaka, N., and K. K. Turekian (1995), Determination of the Dry Deposition Flux of So2 Using Cosmogenic S-35 and Be-7 Measurements, *J Geophys Res-Atmos*, *100*(D2), 2841-2848.

Tao, J., J. Gao, L. Zhang, R. Zhang, H. Che, Z. Zhang, Z. Lin, J. Jing, J. Cao, and S. C. Hsu (2014a), PM2.5 pollution in a megacity of southwest China: source apportionment and implication, *Atmos Chem Phys*, *14*(16), 8679-8699.

Tao, J., L. M. Zhang, K. F. Ho, R. J. Zhang, Z. J. Lin, Z. S. Zhang, M. Lin, J. J. Cao, S. X. Liu, and G. H. Wang (2014b), Impact of PM2.5 chemical compositions on aerosol light scattering in Guangzhou - the largest megacity in South China, *Atmos Res*, *135*, 48-58.

Taran, Y. A., V. P. Pilipenko, A. M. Rozhkov, and E. A. Vakin (1992), A Geochemical Model for Fumaroles of the Mutnovsky Volcano, Kamchatka, Ussr, *J Volcanol Geoth Res*, *49*(3-4), 269-283.

Thiemens, M. H. (2006), History and applications of mass-independent isotope effects, *Annual Review of Earth and Planetary Sciences*, *34*, 217-262.

Thiemens, M. H. (2013), Introduction to Chemistry and Applications in Nature of Mass Independent Isotope Effects Special Feature, *P Natl Acad Sci USA*, *110*(44), 17631-17637.

Thiemens, M. H., S. Chakraborty, and G. Dominguez (2012), The Physical Chemistry of Mass-Independent Isotope Effects and Their Observation in Nature, *Annu Rev Phys Chem*, *63*, 155-177, doi:Doi 10.1146/Annurev-Physchem-032511-143657.

Thiemens, M. H., S. Chakraborty, and T. L. Jackson (2014), Decadal Delta O-17 record of tropospheric CO2: Verification of a stratospheric component in the troposphere, *J Geophys Res-Atmos*, *119*(10), 6221-6229.

Thiemens, M. H., and J. E. Heidenreich (1983), The Mass-Independent Fractionation of Oxygen - a Novel Isotope Effect and Its Possible Cosmochemical Implications, *Science*, *219*(4588), 1073-1075.

Thodeandersen, S., and B. B. Jorgensen (1989), Sulfate Reduction and the Formation of S-35-Labeled Fes, Fes2, and S0 in Coastal Marine-Sediments, *Limnol Oceanogr*, *34*(5), 793-806.

Thomassot, E., J. O'Neil, D. Francis, P. Cartigny, and B. A. Wing (2015), Atmospheric record in the Hadean Eon from multiple sulfur isotope measurements in Nuvvuagittuq Greenstone Belt (Nunavik, Quebec), *P Natl Acad Sci USA*, *112*(3), 707-712.

Thomazo, C., M. Ader, J. Farquhar, and P. Philippot (2009), Methanotrophs regulated atmospheric sulfur isotope anomalies during the Mesoarchean (Tumbiana Formation, Western Australia), *Earth Planet Sc Lett*, *279*(1-2), 65-75.

Thompson, L. G., T. Yao, E. Mosley-Thompson, M. E. Davis, K. A. Henderson, and P. N. Lin (2000), A high-resolution millennial record of the South Asian Monsoon from Himalayan ice cores, *Science*, *289*(5486), 1916-1919.

Thomson, J. (2001), Use and preparation of quench curves in liquid scintillation counting, *Packard BioScience Company, Meriden, Connecticut*.

Turekian, K. K., and N. Tanaka (1992), The Use of Atmospheric Cosmogenic S-35 and Be-7 in Determining Depositional Fluxes of So2, *Geophys Res Lett*, *19*(17), 1767-1770, doi:10.1029/92gl01879.

Ueno, Y., M. S. Johnson, S. O. Danielache, C. Eskebjerg, A. Pandey, and N. Yoshida (2009), Geological sulfur isotopes indicate elevated OCS in the Archean atmosphere, solving faint young sun paradox, *P Natl Acad Sci USA*, *106*(35), 14784-14789.

Ueno, Y., S. Ono, D. Rumble, and S. Maruyama (2008), Quadruple sulfur isotope analysis of ca. 3.5 Ga Dresser Formation: New evidence for microbial sulfate reduction in the early Archean, *Geochim Cosmochim Ac*, *72*(23), 5675-5691.

Urey, H. C. (1947), The Thermodynamic Properties of Isotopic Substances, *J Chem Soc*(May), 562-581.

Urey, H. C., F. G. Brickwedde, and G. M. Murphy (1932a), A hydrogen isotope of mass 2, *Phys Rev*, *39*(1), 164-165.

Urey, H. C., F. G. Brickwedde, and G. M. Murphy (1932b), A hydrogen isotope of mass 2 and its concentration, *Phys Rev*, *40*(1), 1-15.

Uriostegui, S. H., R. K. Bibby, B. K. Esser, and J. F. Clark (2015), Analytical Method for Measuring Cosmogenic S-35 in Natural Waters, *Anal Chem*, *87*(12), 6064-6070.

Uriostegui, S. H., R. K. Bibby, B. K. Esser, and J. F. Clark (2016), Quantifying annual groundwater recharge and storage in the central Sierra Nevada using naturally-occurring 35S, *Hydrological Processes*.

Urióstegui, S. H., R. K. Bibby, B. K. Esser, and J. F. Clark (2016), Quantifying groundwater travel time near managed recharge operations using 35-S as an intrinsic tracer, *Journal of Hydrology*.

van Donkelaar, A., R. V. Martin, W. R. Leaitch, A. M. Macdonald, T. W. Walker, D. G. Streets, Q. Zhang, E. J. Dunlea, J. L. Jimenez, J. E. Dibb, L. G. Huey, R. Weber, and M. O. Andreae (2008), Analysis of aircraft and satellite measurements from the Intercontinental Chemical Transport

Experiment (INTEX-B) to quantify long-range transport of East Asian sulfur to Canada, *Atmos Chem Phys*, *8*(11), 2999-3014.

Verstraeten, W. W., J. L. Neu, J. E. Williams, K. W. Bowman, J. R. Worden, and K. F. Boersma (2015), Rapid increases in tropospheric ozone production and export from China, *Nat Geosci*, *8*(9), 690.

Vicars, W. C., and J. Savarino (2014), Quantitative constraints on the O-17-excess (Delta O-17) signature of surface ozone: Ambient measurements from 50 degrees N to 50 degrees S using the nitrite-coated filter technique, *Geochim Cosmochim Ac*, *135*, 270-287.

Voulgarakis, A., P. J. Telford, A. M. Aghedo, P. Braesicke, G. Faluvegi, N. L. Abraham, K. W. Bowman, J. A. Pyle, and D. T. Shindell (2011), Global multi-year O-3-CO correlation patterns from models and TES satellite observations, *Atmos Chem Phys*, *11*(12), 5819-5838.

Wacey, D., N. Noffke, J. Cliff, M. E. Barley, and J. Farquhar (2015), Micro-scale quadruple sulfur isotope analysis of pyrite from the similar to 3480 Ma Dresser Formation: New insights into sulfur cycling on the early Earth, *Precambrian Res*, *258*, 24-35.

Wang, G. H., R. Zhang, M. E. Gomez, L. Yang, M. L. Zamora, M. Hu, Y. Lin, J. Peng, S. Guo, J. Meng, J. Li, C. Cheng, T. Hu, Y. Ren, Y. Wang, J. Gao, J. Cao, Z. An, W. Zhou, G. Li, J. Wang, P. Tian, W. Marrero-Ortiz, J. Secrest, Z. Du, J. Zheng, D. Shang, L. Zeng, M. Shao, W. Wang, Y. Huang, Y. Wang, Y. Zhu, Y. Li, J. Hu, B. Pan, L. Cai, Y. Cheng, Y. Ji, F. Zhang, D. Rosenfeld, P. S. Liss, R. A. Duce, C. E. Kolb and M. J. Molina (2016), Persistent sulfate formation from London Fog to Chinese haze, *P Natl Acad Sci USA*, *113*(48), 13630-13635.

Wang, L., A. F. Khalizov, J. Zheng, W. Xu, Y. Ma, V. Lal, and R. Y. Zhang (2010), Atmospheric nanoparticles formed from heterogeneous reactions of organics, *Nat Geosci*, *3*(4), 238-242.

Watanabe, Y., J. Farquhar, and H. Ohmoto (2009), Anomalous Fractionations of Sulfur Isotopes During Thermochemical Sulfate Reduction, *Science*, *324*(5925), 370-373.

Whitehill, A. R., B. Jiang, H. Guo, and S. Ono (2015), SO2 photolysis as a source for sulfur mass-independent isotope signatures in stratospehric aerosols, *Atmos Chem Phys*, *15*(4), 1843-1864.

Whitehill, A. R., and S. Ono (2012), Excitation band dependence of sulfur isotope mass-independent fractionation during photochemistry of sulfur dioxide using broadband light sources, *Geochim Cosmochim Ac*, *94*, 238-253.

Whitehill, A. R., C. J. Xie, X. X. Hu, D. Q. Xie, H. Guo, and S. H. Ono (2013), Vibronic origin of sulfur mass-independent isotope effect in photoexcitation of SO2 and the implications to the early earth's atmosphere, *P Natl Acad Sci USA*, *110*(44), 17697-17702.

Winiger, P., A. Andersson, S. Eckhardt, A. Stohl, and O. Gustafsson (2016), The sources of atmospheric black carbon at a European gateway to the Arctic, *Nat Commun*, *7*.

Xia, X. G., X. M. Zong, Z. Y. Cong, H. B. Chen, S. C. Kang, and P. C. Wang (2011), Baseline continental aerosol over the central Tibetan plateau and a case study of aerosol transport from South Asia, *Atmos Environ*, *45*(39), 7370-7378, doi:10.1016/J.Atmosenv.2011.07.067.

Xie, L. H., B. Spiro, and G. J. Wei (2016), Purification of BaSO4 precipitate contaminated with organic matter for oxygen isotope measurements (delta O-18 and Delta O-17), *Rapid Commun Mass Sp*, *30*(14), 1727-1733.

Xu, B. Q., J. Cao, J. Hansen, T. Yao, D. R. Joswia, N. Wang, G. Wu, M. Wang, H. Zhao, W. Yang, X. Liu and J. He (2009), Black soot and the survival of Tibetan glaciers, *P Natl Acad Sci USA*, *106*(52), 22114-22118, doi:10.1073/Pnas.0910444106.

Xu, X. D., C. G. Lu, X. H. Shi, and S. T. Gao (2008), World water tower: An atmospheric perspective, *Geophys Res Lett*, *35*(20), doi:10.1029/2008gl035867.

Xu, Y. W., and G. R. Carmichael (1998), Modeling the dry deposition velocity of sulfur dioxide and sulfate in Asia, *J Appl Meteorol*, *37*(10), 1084-1099.

Yan, C., M. Zheng, A. P. Sullivan, G. Shen, Y. Chen, S, Wang, B. Zhao, S. Cai, Y. Desyaterik, X. Li, T. Zhou, Ö. Gustafsson, and J. L. Collett, Jr. (2018), Residential Coal Combustion as a Source of Levoglucosan in China, *Environ Sci Technol*, *52*(3), 1665-1674, doi:10.1021/acs.est.7b05858.

Yin, Q. Z., X. Y. Shi, C. Chang, and C. Y. Ng (2009), Comment on "Experimental Test of Self-Shielding in Vacuum Ultraviolet Photodissociation of CO", *Science*, *324*, 5934.

Yin, X., S. Kang, B. de Foy, Z. Cong, J. Luo, L. Zhang, Y. Ma, G. Zhang, D. Rupakheti, and Q. Zhang (2017), Surface ozone at Nam Co (4730 m a.s.l.) in the inland Tibetan Plateau: variation, synthesis comparison and regional representativeness, *Atmos. Chem. Phys. Discuss.*, *2017*, 1-32, doi:10.5194/acp-2017-175.

Yu, P. F., O. B. Toon, R. R. Neely, B. G. Martinsson, and C. A. M. Brenninkmeijer (2015), Composition and physical properties of the Asian Tropopause Aerosol Layer and the North American Tropospheric Aerosol Layer, *Geophys Res Lett*, *42*(7), 2540-2546.

Zak, B. D. (1981), Lagrangian Measurements of Sulfur-Dioxide to Sulfate Conversion Rates, *Atmos Environ*, *15*(12), 2583-2591.

Zerkle, A. L., M. Claire, S. D. Domagal-Goldman, J. Farquhar, and S. W. Poulton (2012), A bistable organic-rich atmosphere on the Neoarchaean Earth, *Nat Geosci*, *5*(5), 359-363.

Zhang, G. J., X. Zhang, D. Hu, D. Li, T. J. Algeo, J. Farquhar, C. M. Henderson, L. Qin, M. Shen, D. Shen, S. D. Schoepfer, K. Chen and Y. Shen (2017a), Redox chemistry changes in the Panthalassic Ocean linked to the end-Permian mass extinction and delayed Early Triassic biotic recovery, *P Natl Acad Sci USA*, *114*(8), 1806-1810.

Zhang, R. Y., G. H. Wang, S. Guo, M. L. Zarnora, Q. Ying, Y. Lin, W. G. Wang, M. Hu, and Y. Wang (2015), Formation of Urban Fine Particulate Matter, *Chem Rev*, *115*(10), 3803-3855.

Zhang, X., M. C. Liang, F. Montmessin, J. L. Bertaux, C. Parkinson, and Y. L. Yung (2010), Photolysis of sulphuric acid as the source of sulphur oxides in the mesosphere of Venus, *Nat Geosci*, *3*(12), 834-837.

Zhang, Y. L., S. Kang, Z. Cong, J. Schmale, M. Sprenger, C. Li, W. Yang, T. Gao, M. Sillanpää, X. Li, Y. Liu, P. Chen, X. Zhang (2017b), Light-absorbing impurities enhance glacier albedo reduction in the southeastern Tibetan plateau, *J Geophys Res-Atmos*, *122*(13), 6915-6933.

Zhang, Y. Q., H. Y. Liu, J. H. Crawford, D. B. Considine, C. Y. Chan, S. J. Oltmans, and V. Thouret (2012), Distribution, variability and sources of tropospheric ozone over south China in spring: Intensive ozonesonde measurements at five locations and modeling analysis, *J Geophys Res-Atmos*, *117*, doi: 10.1029/2012jd017498.

Zhao, T. L., S. L. Gong, X. Y. Zhang, J. P. Blanchet, I. G. McKendry, and Z. J. Zhou (2006), A simulated climatology of Asian dust aerosol and its trans-Pacific transport. Part I: Mean climate and validation, *J Climate*, *19*(1), 88-103.

Zhelezinskaia, I., A. J. Kaufman, J. Farquhar, and J. Cliff (2014), Large sulfur isotope fractionations associated with Neoarchean microbial sulfate reduction, *Science*, *346*(6210), 742-744.

Zheng, B., Q. Zhang, Y. Zhang, K. B. He, K. Wang, G. J. Zheng, F. K. Duan, Y. L. Ma, and T. Kimoto (2015a), Heterogeneous chemistry: a mechanism missing in current models to explain secondary inorganic aerosol formation during the January 2013 haze episode in North China, *Atmos Chem Phys*, *15*(4), 2031-2049.

Zheng, X. D., C. D. Shen, G. J. Wan, K. X. Liu, J. Tang, and X. B. Xu (2011), Be-10/Be-7 implies the contribution of stratosphere-troposphere transport to the winter-spring surface O-3 variation observed on the Tibetan Plateau, *Chinese Sci Bull*, *56*(1), 84-88, doi:10.1007/S11434-010-4211-3.

Zheng, X. Y., Y. F. Fu, Y. J. Yang, and G. S. Liu (2015b), Impact of atmospheric circulations on aerosol distributions in autumn over eastern China: observational evidence, *Atmos Chem Phys*, *15*(21), 12115-12138.

Zhu, T., W. L. Lin, Y. Song, X. H. Cai, H. Zou, L. Kang, L. B. Zhou, and H. Akimoto (2006), Downward transport of ozone-rich air near Mt. Everest, *Geophys Res Lett*, *33*(23), doi:10.1029/2006gl027726.